Non Uniform Magnetization Dynamics of Antidot Arrays: Experimental and Numerical Investigations of Domain Patterns and Spin Waves

DISSERTATION

SUBMITTED IN PARTIAL FULFILLMENT OF

THE REQUIREMENTS FOR THE DEGREE OF

DOCTOR OF ENGINEERING

FARZANEH KARIMIAN JAZI

SUPERVISOR: PROF. DR.-ING. JEFFREY McCORD

FACULTY OF ENGINEERING

CHRISTIAN-ALBRECHTS-UNIVERSITÄT ZU KIEL

29 April, 2021

Declaration

I hereby declare that all the contents of this dissertation have been written based on my own knowledge and I have not used any reference other than what has been mentioned. Furthermore, this dissertation is submitted first to Kiel University and has not been presented to any other institute or university. I declare that this dissertation has been prepared subject to the Rules of Good Scientific Practice of the German Research Foundation.

Farzaneh Karimian Jazi
Christian-Albrechts-Universität zu Kiel

Date: Signature:

Reviewers:

1. Prof. Dr.-ing. Jeffrey McCord
2. Prof. Dr. Martina Gerken

Date for the oral exam: 29.04.2021

To My Great Family

Abstract

In this work, the static and dynamic magnetization behaviour of non-uniform magnetization distributions in single and antiferromagnetically coupled bi-layer $Co_{40}Fe_{40}B_{20}$ films, which are patterned in a square array of circular antidots, is investigated. The static and dynamic magnetization configurations of the samples are recorded via static and time-resolved wide-field magneto-optical Kerr effect microscopy. The latter one as a unique technique allows for the detection of domain wall emitted magnetic and elastic waves. The dynamic magnetic behaviour is modelled numerically via micromagnetic simulations. The magnetic structure is exposed to a pulse and a harmonic sinusoidal field excitation. For the first case, a method is developed which is capable of mapping the spatial distributions of the local magnetic resonance frequencies $f_{r,l}$. For the single layer structure, backward volume spin waves are detected. For the bi-layer structures, magnetization states with antiparallel aligned domains are investigated, which display a non-reciprocity of spin wave propagation as well as an asymmetric dispersion at low magnetic fields. It is shown how to enable a manipulation of the dispersion relation via the antiferromagnetic coupling and the anisotropy field. The frequency splitting in a low magnetic field and exhibited additional resonance frequencies can be used when an operation frequency higher than the natural resonance frequency of the material is required. It is further shown that domain walls in an antidot array can act as magnetic antennas while the shape and the propagation direction of the created waves are tunable via bias and uniaxial anisotropy fields, as well as frequency and amplitude of the excitation field. The layering of the magnetic structures and antiferromagnetic interlayer coupling give rise to an additional tunability.

Zusammenfassung

In dieser Arbeit wird das statische und dynamische Magnetisierungsverhalten einer ungleichmäßigen Magnetisierungsverteilung in $Co_{40}Fe_{40}B_{20}$ Einzel- und Zweilagenschichten untersucht. Die Schichten sind dabei mit quadratisch verteilten kreisförmigen Löchern in sogenannte Antidots strukturiert. Die statische und dynamische Magnetisierungskonfiguration der Proben wird mittels abbildender statischer und zeitaufgelöster magnetooptischer Kerreffektmikroskopie analysiert. Letztere stellt eine einzigartige Technik dar, mit welcher von Domänenwänden ausgehende magnetische und elastische Wellen direkt detektiert werden können. Das magnetodynamische Verhalten der Strukturen wurde mithilfe mikromagnetischer Simulationen im Detail analysiert. Die Magnetisierungsstruktur wurde numerisch mit einem magnetischen Anregungsfeld in Form eines Puls- und eines harmonischen Sinusfelds angeregt. Für den ersten Fall wurde eine Methode entwickelt, welche in der Lage ist, die Verteilung der lokalen Resonanzfrequenz abzubilden. Darüber hinaus wird die dynamische Magnetisierungsantwort auf einen harmonischen magnetischen Stimulus simuliert, um den Ursprung der magnetischen Wellen aufzuzeigen. Für die Einzelschicht sind Backward-Volume Spinwellen werden detektiert.Im Fall der Doppelschicht werden Magnetisierungszustände mit antiferromagnetisch gekoppelten Magnetisierungsausrichtung untersucht, welche eine nicht reziproke Spinwellenausbreitung und eine asymmetrische Dispersion in einem niedrigen Magnetfeld zeigen. Es wird weiterhin gezeigt, wie die Manipulation der Dispersionsrelation durch antiferromagnetische Kopplung und einachige Anisotropie möglich ist. Die Frequenzaufspaltung in einem niedrigeren Magnetfeld und die zusätzlichen Resonanzfrequenzen können genutzt werden, um eine Anregungfrequenz oberhalb der natürlichen Resonanzfrequenz des Materials zu erzielen. Es wird zusätzlich gezeigt, dass in einem Antidotarray formende Domänenwände als magnetische Antennen fungieren können, wobei die Form und die Ausbreitungsrichtung der erzeugten Wellen über die Schichtlaminierung, das Stütz- und das uniaxiale Anisotropiefeld, sowohl als auch über die Frequenz und Amplitude des Anregungsfeldes einstellbar sind.

Contents

Abbreviation

BVW	Backward Volume Wave
CPW	Coplanar Waveguide
DFT	Discrete Fourier Transformation
DW	Domain Wall
FFT	Fast Fourier Transformation
FMR	Ferromagnetic Resonance
IP	In Plan
LLG	Landau-Lifshitz-Gilbert equation
LS-PIMM	Locally Simulated PIMM
MOKE	Magneto-Optical Kerr Effect
MSW	Magnetostatic Spin Waves
OOP	Out of PLan
PIMM	Pulsed Inductive Microwave Magnetometer
PSSW	Perpendicular Standing Spin Wave
SW	Spin Wave
TR-MOKE	Time Resolved Magneto-Optic Kerr Effect
VNA	Vector Network Analyzer

Chapter 1

Introduction

The precessional excitation of ordered spins inside a magnetic material creates a wave that is called spin wave. The approaches to control and manipulate spin waves in ferromagnetic materials is the subject of magnonics [1]. It is getting more attention lately as its results may be used in computing and microwave signal processing [2]. Spin wave (SW) based technology has been developed recently by intensive research on filters [3], magnonic beam splitters [4] and logic gates [5]. The SW-based logic device is not just a proposed idea since 2005, when for the first time such device was made [6]. This device was attractive because it operates at room temperature and in the GHz frequency range [6]. Afterwards, other logic devices have been proposed [7, 8] or experimentally demonstrated [9, 10]. These SW-based devices, either phase [9, 10, 8], or amplitude of SWs [7, 6, 11] was used as a state variable to make logic decision. Examples are the prototype controlled phase shifters (CPSs) which were fabricated based on backward volume magnetostatic, and magnetostatic surface SWs propagation. The backward volume waves (BVWs) and surface waves correspond to parallel or perpendicular orientation of in plane wave vector k and magnetization M, respectively. These SW modes differ in their dispersion relation $\omega(k)$, which is the utilized point in fabrication of such logical gates. The input signal with initial value k_0 and ω_0 delivers into magnetic medium (for example yttrium iron garnet (YIG) in Ref. [6]). Any perturbation along the signal path toward the output microwave transducer changes the wave vector's amplitude k and based on the dispersion relation, the perturbation can be detected via measuring the wave vector variation [6]:

$$\begin{aligned} \text{Backward Volume Waves: } & k(z)-k_0=\frac{(\gamma H)^2+\omega_0^2}{2\pi\gamma^2 M_S H L}\frac{\delta H(z)}{H}, \Delta\phi=\int[k(z)-k_0]dz \\ \text{Surface Waves: } & \frac{\Delta\phi}{\delta H(I)}=-\frac{\ell}{L}\frac{\gamma^2(H+2\pi M_S)}{\omega_0^2-\gamma^2 H(H+4\pi M_S)} \end{aligned} \tag{1.1}$$

where L,l are the geometrical parameter, M_s, H are the saturation magnetization and the applied field, respectively, and δH indicates the perturbation field. In the first case, CPS based on backward volume SWs, **H**, **M** and δ**H** are along one axis, but in the case of CPS based on surface waves H and δH are perpendicular. The total field increase or decrease is based on δH direction which is controlled by the current direction. For instance, in the case of BVWs, dispersion branch shifts upward or downward, respectively. Therefore, at a given carrier frequency ω_0, the wave vector varies and $\Delta\phi$ is measured. To make a π phase difference in the case of BVWs propagation, since the relation between current ($\delta H \propto$ I) and $\delta\phi$ is a direct one, a larger current (1 A) than CPS based on surface waves (0.3 A) is needed [6]. This was a short description of the first logic device using a Mach-Zehnder-type current controlled interferometer based on SWs propagation.

In magnonic logic circuits [12, 13], information is transmitted via spin waves, SWs. The unique feature of these circuits is that SWs propagate in the magnetic waveguides without electrical current usage. To enhance the functionality of the magnonic circuit, it is favourable that their operating wavelengths are reduced well below 1 μm. The scalability of the logic device, that relies on SWs propagation, depends on SWs' wavelength. This can be tuned by different factors such as magnetic material which is used as a waveguide and its geometry. The attractive materials such as NiFe [8], YIG [6, 14, 15] are already studied. The low damping parameter of Permalloy and YIG around 0.008 [16] and 0.00006 [17], respectively, make them preferable media to transmit SWs. In this work, our samples are made of $Co_{40}Fe_{40}B_{20}$ because of its high saturation magnetization $\mu_0 M_s$=1.48 T [18] and relatively low damping parameter [19] that can be changed thermally [20]. Besides, this material is amorphous which means that there is no magnetocrystalline anisotropy. So magnetic anisotropy can be avoided or induced along an arbitrary axis during deposition or changed post-production. The SW emittance in CoFeB is investigated already [20, 21, 22]. The high velocity of SWs propagation, from 3.5 to 25 km/s, in $Co_{20}Fe_{60}B_{20}$ has been measured [22]. SWs emission from magnetic domain walls, DWs, in $Co_{40}Fe_{40}B_{20}$ and their propagation with a phase velocity of 6.45 km/s have been reported [21]. The magnetic DWs not only can be a SW emitter but also can be used as reconfigureable nanochannels to transfer SWs [23].

In addition to SWs emittance from DWs or (even) their propagation though DWs inside a full film [23], it is shown that the different shapes of magnetic materials such as rectangular and triangle [24], square permalloy islands [25] or diamond shape NiFe [26] can create SWs from the edges mostly because of variations in the local effective fields. Besides changing material to obtain desirable magnetic properties, the micromagnetic structure can be manipulated by artificial crystals, their crystal size ranges from nanometer to centimeter. Since these materials' magnetic properties change, they are called metamaterials. A choice to pattern a magnetic thin film and create a

specific microstructure to provide SW emittance is a antidot or dot pattern [27, 28]. An antidot is a zero-magnetization area or physically empty area inside a magnetic full film. Because of a demagnetizing field variation around every antidot, the effective field and f_r distribution are non-uniform [29] and several resonance frequencies are detected [30]. Because of the periodic feature of such magnetic structures, they are called magnonic crystals if the periodicity and antidot (dot) size is in the nanometer range. In this work creation and propagation of SWs in an antidot array is discussed where the antidot diameter and lattice parameter are 4 and 16 μm, respectively. In such an antidot array, we are able to use a unique technique, time-resolved wide field MOKE [31, 32] to directly observe microstructure, dynamic magnetization behaviour and SWs propagation. These direct observations confirm the numerical simulation method. This accuracy of calculation on the μm scale provides a high degree of reliability to investigate any other array with the same approach, where the optical resolution restricts the range of detection. Besides magnetic spin waves detection, the propagation of elastic waves from DWs is observed, which can be an alternative to carry energy or a signal at low frequencies of excitation field not high enough to excite SWs.

Another advantage of a SW-based device is the possibility of waves superposition that provides different operating frequencies and therefore the device can be used as an independent channel to transmit information [12]. In addition, the microwave devices such as tunable microwave filters [33, 34, 35, 36, 37, 38, 39, 40, 41, 42], phase shifters [41, 33] and circulators [33, 43] operate based on magnetic energy absorption in a microwave cavity in the materials' ferromagnetic resonance [44]. This highlights the importance of methods to calculate the resonance frequency, f_r, of a system during design before a sample is produced. Considering the above discussion about DWs and their potential as SWs emitters, such simulation method should be capable of f_r calculation in the magnetization configuration consisting of DWs. In this work, we develop a numerical method to calculate and map resonance frequency distribution in every system which is also capable of predicting dynamic magnetization patterns. Besides, the calculated results are compared with a previously introduced approach [29].

Furthermore, we should be able to adjust the operation frequency range in a magnetic material. There are some possibilities. First, like in every design, the magnetic material selection plays a role, for instance magnetic insulators YIG [36, 33], Fe-based [41, 39] can be proper choices. Furthermore, it is shown that laminating a magnetic material can change the dispersion relation [45, 46, 47, 48] although both layers have the same magnetic material. This variation is sometimes a consequence of introducing antiferromagnetic coupling, bilinear J_1 and biquadratic J_2, between two ferromagnetic layers [46, 47] or the dispersion variation can be seen even if an interlayer exchange coupling is not taken into consideration [45]. Also, an antidot array makes a difference via

introducing a non-uniform magnetization [49, 50].

The non-reciprocity of SWs propagation [51] makes them unique when unidirectional transmission [52, 53] or asymmetric propagation of waves [54] is preferable. The non-reciprocity means that the waves propagation and so their dispersion relation $\omega(\mathbf{k})$ ($\omega(\mathbf{H}_0)$) depends on the wave vector $\mathbf{k}$ (magnetic field $\mathbf{H}_0$) direction and so it is not symmetric relative to a line of k=0 (H_0=0).

In this work, we report the non-reciprocity of SWs propagation from DWs. These walls are formed by applying a low magnetic field (-0.48< H_0 <0.48 kA/m) to a double-layer with antiferromagnetic coupling between layers. As it is a method that can be utilized post-production with the ability to adjust and change DWs via applied field's direction and amplitude or the history of magnetization, therefore, it can be preferable in comparison with other methods such as writing DWs in a synthetic antiferromagnet [55] via thermally assisted magnetic scanning probe lithography.

Chapter 2

An Overview of Micromagnetics

2.1 Micromagnetism

The first step in any micromagnetic calculation is finding the system's total energy and then minimizing this energy in order to predict the magnetization structure. The total energy consists of several terms:

$$E_t = E_{ext} + E_{exch} + E_{an} + E_{dem} \quad \text{with} \quad E_i = \int_V e_i \, dv \tag{2.1}$$

where E_i and e_i represent energy and volume energy densities, respectively.

In equation(2.1), the Zeeman energy or external field energy E_{ext} is the potential energy of a magnetic material after an external magnetic field is exerted. The exchange energy E_{exch} originates from a quantum mechanical effect between indistinguishable particles' spins since their total wave function should be antisymmetric. In ordered magnetic materials, for instance ferromagnetic or antiferromagnetic materials, every variation in spin orientation of the equilibrium state causes an energy penalty, described by an exchange energy between neighbouring spins. Another term in equation(2.1), the anisotropy energy E_{an} shows how much energy is needed to align all of the magnetic moments in one specific direction.

The last term in equation(2.1) refers to the demagnetizing, magnetostatic or magnetic stray field. This depends on the sample shape. For example, elongated materials tend to be magnetized along the longer dimension. Surface and volume magnetic charges decrease and so the stray field. For a magnetized body, an external field is applied to reduce the total magnetization moment, which is called the stray field.

In the following these energy contributions are discussed in detail.

It is straightforward to find the magnetic field corresponding to every energy term by consid-

ering their relation as follows:

$$\mathbf{H}_{eff} = -\frac{1}{\mu_0 M_s}\nabla_m(\frac{dE}{dv}) = -\frac{1}{\mu_0 M_s}\nabla_m e, \tag{2.2}$$

where $\mathbf{H}_{eff}$ and M_s indicate the effective field (correlated to energy term E) and the saturation magnetization, respectively.

2.1.1 Zeeman Energy

By applying an external magnetic field to a sample, every magnetic moment experiences a torque equal to

$$\mathbf{T} = M_s\mathbf{m}\times\mathbf{B} \quad \text{with} \quad \mathbf{m} = \frac{\mathbf{M}}{M_s} \tag{2.3a}$$

$$\mathbf{B} = \mu_0\mathbf{H} \tag{2.3b}$$

where **T** indicates the magnetic torque and **m** corresponds to the normalized magnetization relative to the saturation magnetization M_s. **B** and **H** are the magnetic flux density and the magnetic field, respectively, while their proportional coefficient is the vacuum permeability μ_0 or in general the permeability of material, μ[56]. This permeability (μ) can be a real number, a complex number or a complex tensor.

The torque exerts force on the magnetic moments and tends to align them in the same direction as the magnetic field. Therefore, an equilibrium state exists when the torque is zero and the magnetic energy

$$E_{ext} = -M_s\mathbf{m}\cdot\mathbf{B} \tag{2.4}$$

is minimum[57, 58].

2.1.2 Exchange Energy

In ferromagnetic materials, there is a tendency to align all magnetic moments along one direction. So every change in magnetization direction between neighbouring moments causes a non-zero magnetization gradient, increasing the exchange energy. This enhancement depends on the materials character and is called volume stiffness energy *A*. However, in general, it can be site-dependent, in most simulations it is considered as constant.

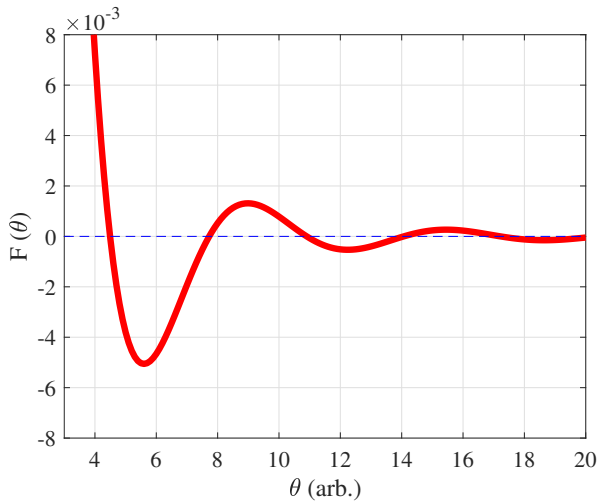

Figure 2.1: The RKKY function, $F(\theta)$, shows how effective exchange coupling fluctuates versus distance between two magnetic moments originate from spins. As it can be seen, the effective exchange coupling has the highest value before $\theta = 4$[61].

The formulated exchange energy by Kittel shows the relation

$$E = A \int (\nabla \mathbf{m})^2 dv = A \int ((\nabla m_x)^2 + (\nabla m_y)^2 + (\nabla m_z)^2) dv, \tag{2.5}$$

where m_x, m_y and m_z are the normalized magnetization components in Cartesian coordinates. They are dimensionless. Additionally, the gradient is the spatial derivitive of magnetization. The exchange integral is calculated over the volume dv[59].

The interlayer exchange energy can be used to describe antiferromagnetic coupling between two ferromagnetic layers with one non-magnetic metallic layer as a spacer. The thickness of spacer layer can vary ferro- to antiferromagnetic coupling between layers from or change the intensity of this coupling. This layer is usually in the order of nanometer to angstrom. Ruderman, Kittel, Kasuya and Yosida (RKKY) proved that a single magnetic impurity leads to fluctuation in spin polarity of electrons in the conduction band of metals. The Hamiltonian, quantum mechanics's energy operator, correspond to two spins' interaction is:

$$H = \sum_{i>j} -J \mathbf{S}_i \mathbf{S}_j, \tag{2.6}$$

where $\mathbf{S}_{i,j}$ and J indicate the spin operators for the nearest neighbours and the exchange integral[60]. The corresponding RKKY function can be shown as

$$F(\theta) = \frac{\sin(\theta) - \theta cos(\theta)}{\theta^4} \quad \text{with} \quad \theta = k_f r \tag{2.7}$$

where k_f and r show the Fermi wave vector and the distance between two spins, respec-

tively[62]. Since the effective exchange coupling is proportional to the RKKY function $J \propto F(\theta)$), the Hamiltonian as an energy operator has the same dependency ($H \propto$ F(θ). If equation (2.7) is substituted in equation (2.6), it can be seen that for $F(\theta)$ and so J<0 the magnetic moments tend to align antiparallel or antiferromagnetic, and for J>0 a parallel alignment of neighbouring spins and so a ferromagnetic configuration is preferable [61].

2.1.3 Anisotropy Energy

Based on the Hamiltonian introduced above, the energy for every magnetic moment is considered as $\mu H\ M\ cos(\theta)$, where θ is the angle between the magnetization and the applied field. Therefore for a system of atoms at low temperature the average of this energy term depends on $\cos(\theta)\exp(x\cos(\theta)$, while the exponential term shows the probability of finding a magnetic moment under an angle θ and the average of $cos(\theta)$ is calculated as

$$< \cos(\theta) >= L(x) = \coth(x) - \frac{1}{x} \quad \text{with} \quad x = \frac{\mu H}{k_B T} \tag{2.8}$$

where k_B and T indicate the Boltzmann constant and temperature, respectively, and L(x) is the Langevin function. Furthermore, $\cos(\theta)$ is as follows

$$\mathbf{M} \cdot \mathbf{H} = HM\cos(\theta) = HM_H \Rightarrow \cos(\theta) = \frac{M_H}{|\mathbf{M}|} \tag{2.9}$$

where M_H displays the magnetization component in the direction of applied field. From comparison between equation(2.8) and(2.9), it can be concluded that $< \cos(\theta) >= M_H / \mid \mathbf{M} \mid = L(x)$. Therefore, in zero magnetic field, the average of $\cos(\theta)$ is zero as the Langevin function reaches zero. It means that the angle θ has random orientation similar to paramagnetic materials. If this is the case, the magnetization of ordered magnetic materials like ferromagnetic materials in zero field cannot described.

There are different types of anisotropy that will be discussed shortly in the following.

2.1.3.1 Magnetocrystalline Anisotropy

This intrinsic anisotropy is the most common one in single crystalline materials as a result of the spin-orbit interaction[63]. To change the orientation of magnetization in a magnetic field, every spin direction coupled to the orbit and orbit itself coupled to the lattice should be rotated. Since the coupling between lattice and orbit is strong, breaking this coupling is not possible from an energy point of view. The solution is to break the coupling between spin-orbit which have a week in-

teraction. The energy consumed for this is called magnetocrystalline anisotropy energy. Based on the crystalline structure, there are different kinds of magnetocrystalline anisotropies, for instance cubic and hexagonal anisotropy in single crystalline Iron and Cobalt, respectively. In a hexagonal lattice structure, like Co, the easy axis is along the crystal's c axis and all other directions in the basal plane are equally hard[64]. These materials have a crystalline uniaxial anisotropy whose energy density is defined as

$$E_u = \int (K_0 + K_1 \sin^2(\theta) + K_2 \sin^4(\theta) + ...) \, dv \tag{2.10}$$

where θ indicates the angle between magnetization direction and easy axis (c axis in the hexagonal case). If $K_{0,1,2}$(anisotropy constant) is positive, the material has easy axis. Thus, the anisotropy energy is minimum for $\theta = 0°$ and $\theta = 180°$, where the magnetization aligns either up or down regarding to the easy direction. The elemental Co and Ba-ferrite have this kind of anisotropy[65].

2.1.3.2 Stress-induced Anisotropy

When a material is exposed to a magnetic field, its length l changes by Δl and the fraction between these two is a dimensionless parameter called the material's magnetostriction,λ_m:

$$\lambda_m = \frac{\Delta l}{l} \tag{2.11}$$

The measured λ_m in saturation is called saturation magnetostriction λ_s. However, it is small in strong magnetic materials, for instance 10^{-5} and even smaller in weak magnetic substances[66]. It can lead to significant practical consequences. For instance if sample is annealed and then cooled down, as there is a difference between the thermal expansion coefficient of the magnetic material and its substrate, the substrate imposes force to magnetic materials, leading to a magnetostriction effect in the magnetic layers. The magnetoelastic energy, $E_{mag,e}$, contribution corresponding to the magnetostriction effect can be described as

$$E_{mag,e} = \int K_\sigma \sin^2(\theta) \, dv \tag{2.12a}$$

$$K_\sigma = \frac{3}{2}\lambda_s \sigma \quad \text{for uniaxial anisotropy,} \quad \sigma = Y \Delta l \quad \text{Y=Young's modulus,} \tag{2.12b}$$

in which the applied stress σ is less than the elastic stress limitation of the material or the yield stress[61] and Young's modulus is one material feature. In addition, in equation (2.12a), θ shows the angle between saturation magnetization and stress. Therefore, stress alone can induce

anisotropy which is uniaxial and it should be considered with any other type of anisotropy. The easy axis for this anisotropy is defined depending on the sign of $\lambda_s\sigma$. If it is positive, the easy axis will be parallel to the applied stress axis. If it is negative, the easy plane will be normal to the stress axis.

2.1.3.3 Magnetization Induced Anisotropy

The induced anisotropy differs from intrinsic anisotropy like the magnetocrystalline anisotropy. There are several methods to induce anisotropy in a preferred direction by applying a magnetic field. The examples are magnetic annealing, plastic deformation and irradiation[65]. Furthermore, anisotropy can be induced during deposition of the sample by applying a magnetic field strong enough to saturate the sample along a preferred axis or direction. This is the method that we used to introduce an anisotropy in the $Co_{40}Fe_{40}B_{20}$ samples used for this work. In this way, a uniaxial anisotropy is induced to the amorphous samples ($K_1 = 0$ in every magnetocrystalline anisotropy term), which obeys to the similar equation as the magnetocrystalline uniaxial anisotropy (2.10) introduced before

$$E_u = \int (K_0 + K_u \sin^2(\theta))\, dv \tag{2.13}$$

Here, we shortly talk about magnetic annealing. Details about other methods can be found in reference[65].

The annealing in magnetic field can change the shape of the magnetization curve (the hysteresis) and so the anisotropy based on the temperature, the application of fast or slow cooling, material's components, annealing time [67]and the direction of applied field during annealing[68, 69].

2.1.4 Demagnetizing Energy

One important difference between electrical and magnetic fields is that magnetic monopoles do not exist. Therefore, there are only dipole magnetic charges. At the edges of a material, every boundary between the material and its surrounding might induce sudden field changes and magnetic charges accumulate. These charges act like an extra source of magnetic field inside the substance. This field is opposite to the main direction of magnetization and is therefore called the demagnetizing field.

Based on Maxwell's equation

$$\nabla \times \mathbf{H} = \mathbf{J} \quad \text{with} \quad \mathbf{J}\text{=Current density} \tag{2.14}$$

when there is no free current ($J = 0$) we can define a scalar magnetic potential ϕ [70]

$$\mathbf{H} = -\nabla\phi \tag{2.15}$$

because based on mathematics the curl of every divergence is zero. If we consider the relation between **M** and **H** as

$$\mathbf{H} = \frac{1}{\mu_0}\mathbf{B} - \mathbf{M} \quad \text{leads to} \quad \bigtriangledown \cdot \mathbf{H} = -\bigtriangledown \cdot \mathbf{M} \tag{2.16}$$

by substitution equation 2.16 in equation 2.15, a Poisson equation is obtained

$$\triangle \phi = -\bigtriangledown \cdot \mathbf{M} \tag{2.17}$$

By solving this equation for the scalar potential

$$\phi(r) = -\frac{1}{4\pi}\int_V \frac{\nabla \cdot \mathbf{M(r)}'}{\mid \mathbf{r} - \mathbf{r}' \mid} dv' + \frac{1}{4\pi}\oint_S \frac{\mathbf{n}' \cdot \mathbf{M}(r)'}{\mid \mathbf{r} - \mathbf{r}' \mid} ds' \tag{2.18}$$

in which **r** and $\mathbf{r}'$ display the observation (magnetization calculation) point and charge source point, respectively. In addition, dv' and ds' point out the volume and surface charge element. The equation(2.18) allows to define the effective magnetic charge density ρ and the effective magnetic surface charge density σ,

$$\rho = -\nabla \cdot \mathbf{M} \quad \text{and} \quad \sigma = \mathbf{M} \cdot \mathbf{n} \tag{2.19}$$

when **n** shows a unity vector perpendicular to the outside surface [71]. Based on the equation (2.19), a discontinuity at the surface causes surface charges, while nonhomogeneous magnetization results in volume magnetic charges [72].

Therefore, an elongated sample like a long cylinder tends to be magnetized along its longer dimension and has a minimum stray field with two magnetic poles at the two ends by magnetizing the sample along the perpendicular direction, the magnetic charges are all at the sides and the stray field significantly increases. For materials with a higher symmetry like a cylindrical disk with very small thickness, in-plane orientations of the magnetization direction are equally preferred and the demagnetizing factor N will have the same value in-plane and will be usually very small. Out-of-plane N has the maximum value. The mentioned demagnetizing factors can be constant

for instance for an ellipsoid, or can vary in more complicated structures. Generally, they correlate magnetization and demagnetizing field

$$H_{dem,i} = -N_i M_i \quad \text{with} \quad i = x, y, z \tag{2.20}$$

where N_i represents the demagnetizing factors along the three different directions of the Cartesian coordination system. For the highest symmetry in a sphere, all of N_i are equal. In addition, as a general rule summation of these factors should be unity. So, for a sphere in a uniform magnetic field $N_x = N_y = N_z = \frac{1}{3}$ and therefore

$$\mathbf{H}_{dem} = -\frac{1}{3}\mathbf{M} \quad , \quad \mathbf{H}_{in} = \mathbf{H}_{out} - \frac{1}{3}\mathbf{M} \tag{2.21}$$

where $\mathbf{H}_{in}$ and $\mathbf{H}_{out}$ indicate the magnetic fields inside and outside of the sphere [73]. The corresponding demagnetizing energy for every system can be achieved after finding the demagnetizing field by this relation [74]:

$$E_{dem} = -\frac{1}{2}\int_V \mathbf{M}\cdot\mathbf{H}_{dem}\, dv. \tag{2.22}$$

An isolated sphere is completely symmetric in 3-dimensional space that makes it a straightforward example. But in other cases, like for example patterned antidot arrays in magnetic thin films, a more complicated calculation is needed. Because of the competition between different energy terms, such as exchange and demagnetizing energy causing interaction and coupling between the antidots, demagnetizing factors in different directions (demagnetizing tensor's elements N_{ij}) should be individually calculated [29].

2.2 Magnetic Domains

In magnetic materials with specific order and shape surface, the exchange field aligns the magnetic moments parallel or antiparallel. On the other hand, it costs demagnetizing energy enhancement. The solution for this competition is the formation of magnetic domains. These are areas where the magnetization orientation for all moments is the same, parallel to the local easy axis of magnetization and so lessening the exchange energy. In addition, this division of magnetic materials into different domains with different orientation of magnetization reduces the magnetostatic or stray field around the materials. As a simple example, Fig. (2.2) illustrates how emergence of domains reduces the stray field around the sample.

Between two domains, magnetization can not vary suddenly because it imposes high exchange

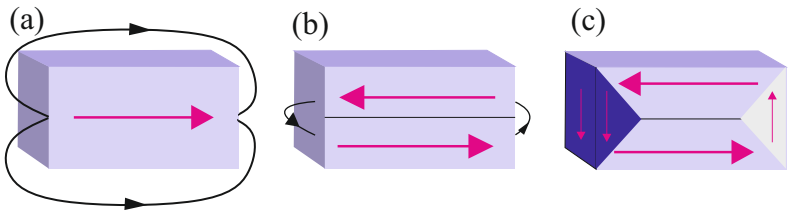

Figure 2.2: In the exemplary sample, uniform magnetization in (a) leads to a stray field around it while dividing it into two domains in b) significantly decreases magnetostatic field and in (c) closure domains or a Landau configuration makes a complete loop of magnetization variation and therefore reduction in magnetic charges, thus there is not any stray field around the sample any more.

energy to the system. Therefore, the magnetization vector rotates uniformly and gradually from one domain to the neighbouring one. The area needed for this variation is called a domain wall (DW). Based on in-plane (IP) or out-of-plane (OOP) rotation of magnetization, two different types of DWs are defined Néel walls and Bloch walls, respectively. This is a most generalized category and there are other types of domain walls which will be discussed in the following sections.

2.2.1 Symmetric Domain Walls

Bloch walls usually occur in bulk samples. In thin films, where the OOP demagnetizing factor is maximum and so any OOP rotation of magnetization needs very high external field and energy, Bloch walls are seldom. For the simplest model, one dimension walls, these equations are used to define magnetization around Bloch and Néel walls:

$$\begin{aligned} m_x(x) &= \frac{\delta^2 cos(\phi)}{\delta^2 + x^2} \\ m_y(x) &= \frac{x\sqrt{2\delta^2 + x^2}}{\delta^2 + x^2} \\ m_z(x) &= \frac{\delta^2 \sin(\phi)}{\delta^2 + x^2} \end{aligned} \tag{2.23}$$

where x and y are the IP components and z defines the OOP one. In these equations, δ is an adjustable parameter determining the wall width and m_i stands for normalized magnetization components. The parameter ϕ is zero in the case of symmetric Néel walls with vanishing OOP component m_z. For Néel walls, there is not any surface charge, while magnetic charges are distributed inside the substance' s volume. In contrast, for Bloch walls, where surface magnetic charges exist, volume charges can not be found. In this case, ϕ is 90° in equation(2.23) and one of the IP components (m_x) is zero [75].

Using equation (2.23) and considering magnetostatic, exchange and anisotropy energies cor-

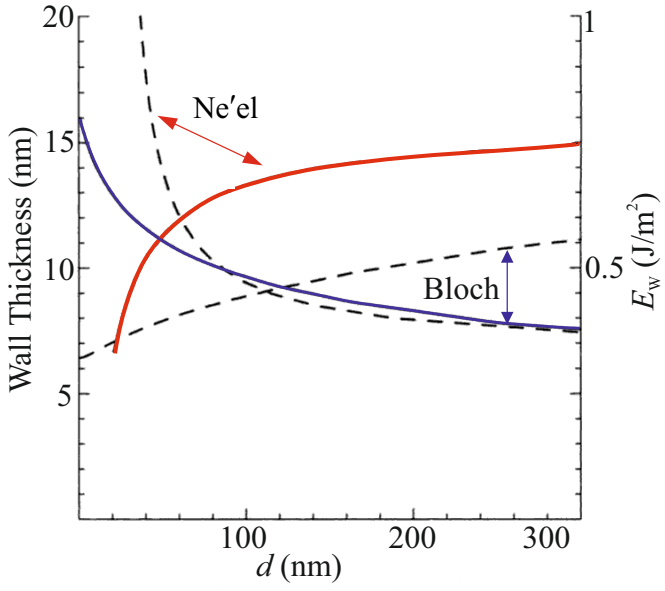

Figure 2.3: The relation between wall energy and film thickness are illustrated for Néel (solid red line) and Bloch (solid blue line) walls. The dashed lines show wall thickness for both mentioned type of domain walls. The plot has been adopted from [77].

respondingly Bloch and Néel wall energies are calculated

$$\begin{aligned} E_{BW} &= \frac{\pi A}{\delta}(\sqrt{2}-1) + \frac{\pi\delta}{2}K_1 + \frac{(\pi\delta M_s)^2}{d}\log(1+\frac{d}{\delta}) \\ E_{NW} &= \frac{\pi A}{\delta}(\sqrt{2}-1) + \frac{\pi\delta}{2}K_1 + (\pi M_s)^2\delta[1-\frac{\delta}{d}]\log(1+\frac{d}{\delta}) \end{aligned} \tag{2.24}$$

where E_{BW} and E_{NW} denote energy per unit wall area corresponding to Bloch and Néel walls. In addition, A and K_1 are material features, exchange stiffness and anisotropy constant, respectively. Furthermore, the substance and wall thickness are shown with d and δ. The first terms in equation (2.24) display the exchange energy contribution in domain wall formation while the second and third terms account for the anisotropy and the magnetostatic energy parts, respectively [76].

Now, the wall width can be achieved by minimization of the wall energy in equation (2.24). The solution can be found easily if we ignore magnetostatic energy terms. This assumption imposes specific limitations to the specimen thickness d. Therefore, for Néel walls in extremely thin films ($d \to 0$) and for Bloch walls in extremely thick substance ($d \to \infty$) the obtained wall widths are [77]:

$$\delta_{BW} = \delta_{NW} = \sqrt{\frac{2A}{K_u}(\sqrt{2}-1)} = 0.9\sqrt{\frac{A}{K_u}} \tag{2.25}$$

As can be seen in Fig. (2.3), in thin films Néel wall energy is lower than for Bloch walls and so Néel walls are the preferable profile. In contrast to thick films with 300 nm in thickness, Bloch wall

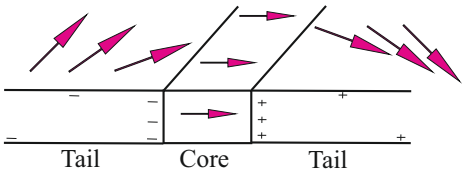

Figure 2.4: A Néel wall separated from one core and two extremely wide tails are shown.The magnetic charge density is much higher inside the core rather than the tails, adapted from[79].

formation is a better option from an energy minimization point of view. It should be mentioned that the plots reported in Fig. (2.3) were calculated for a Permalloy with $A = 2\times 10^{-11}$ J/m , $K_u = 100$ J/m^3 and $M_s = 0.8$ J/T [77].

It should be further mentioned that what was discussed above is applicable for materials with zero magnetostriction such as permalloy but is not applicable to calculate domain wall energies in magnetostrictive samples.

There is another approach, introduced by Riedel and Seeger [78], which considers symmetric Néel walls consisting of a core and a long tail on every side of the core. The core is like a magnetic dipole and every tail has a very low density of single polarity charges as it is indicated in Fig. (2.4). Based on this method, the core width (W_{core}) and the tail width (W_{tail}) can be obtained as follows

$$\begin{aligned} W_{core} &= 2\sqrt{\frac{A(1-p^2)}{(K_u+K_d)(1-c_0)^2}} \quad \text{with} \quad p=\frac{HM_s}{2K_u} \quad K_d=\frac{\mu_0 M_s^2}{2} \\ W_{tail} &= e^{-\gamma} D\frac{K_d}{K_u} \\ \text{with} \quad \gamma &= 0.577\ldots \text{ Euler's constant and } D = 12.5\sqrt{\frac{A}{K_d}} \end{aligned} \tag{2.26}$$

where K_u shows the uniaxial anisotropy constant. In addition, K_d represents the stray field energy's density and $\sqrt{A/K_d}$ indicates the exchange length of the stray field. However, the core-tail boundary, c_0, in the equilibrium (with minimum amount of energy) is principally between p (defined in equation(2.26)) and 1, assumed to be in the middle of its interval. Furthermore, H indicates the applied magnetic field magnitude. From equation (2.26) it can be concluded that in soft magnetic materials with small anisotropy, the core width scales with A/K_d as K_d is much larger than K_u inside the core because of the high charge density. Therefore, inside the core the exchange energy (via A) and the magnetostatic energy (via K_d) balance each other. On the other hand, for the Néel tails, the magnetostatic energy is balanced by the anisotropy energy.

In ferromagnetic materials with higher saturation magnetization and anisotropy in comparison with Permalloy, the Néel wall core is smaller and the tail length is larger [80].

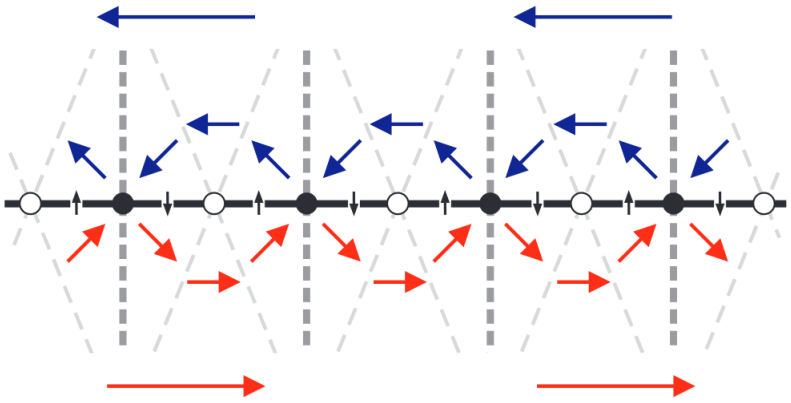

Figure 2.5: The cross-tie domain walls. The vortex and antivortex are illustrated by filled and empty circles. Furthermore, the dashed line should be replaced by continous rotation of magnetization from one domain to another. This structure is more favourable from an energy point of view, because it contains mostly 90° walls in comparison 180° walls [82].

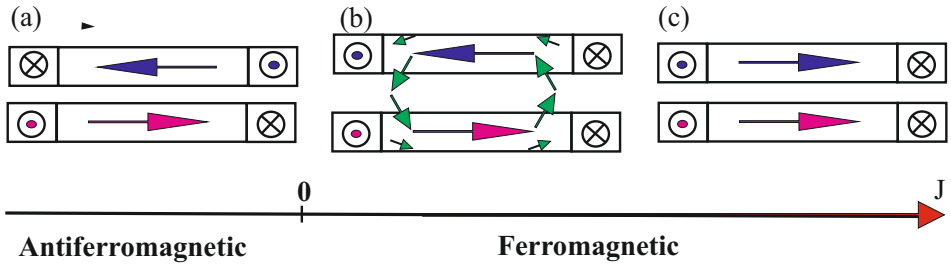

Figure 2.6: The superimposed 180° Néel walls for a double layer structure with antiferromagnetic ($J < 0$) in (a) and ferromagnetic ($J > 0$) in (b) are shown. For stronger interlayer exchange coupling (J introduced in equation(2.6)) , between two ferromagnetic layers, parallel Néel walls in (c) are predicted [83].

What is mentioned above in equation (2.24) is denoted for symmetric 180° walls. It means that the magnetization at two sides of the walls is antiparallel. But walls with lower angles have a smaller energy. For instance the magnetic wall energy decreases by 78% when one 180° Néel wall is replaced by a 90° wall [79], [81]. This is the reason that another type of combined walls called cross-tie walls, illustrated in Fig. (2.5), which consist of 90° Néel walls is more favourable in spite of the fact that they are longer than the usual 180° walls. In thin film with double layers and antiferromagnetic coupling between layers, 180 degree Néel walls as introduced before are preferred. The reason is that in double layers, the stray field because of antiferromagnetic coupling between layers decreases significantly as a result of the reduction in volume magnetic charges. In Fig. (2.6), three different Néel wall structures formed because of different interlayer exchange coupling corresponding to the displayed antiferro- and ferromagnetic coupling between layers [83].

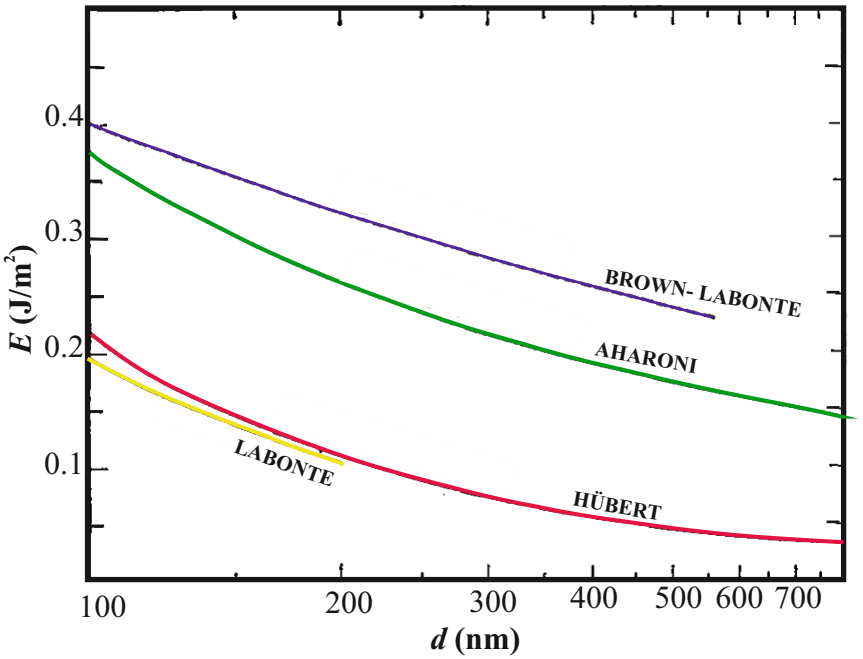

Figure 2.7: The historical development of two-dimension Bloch wall energy, *E*, versus film thickness is shown. The purple curve indicates the lowest calculated energy for one-dimension Bloch walls, while the other curves represents two-dimension calculation. It is adopted from [84].

2.2.2 Asymmetric Walls

In our single layer thin film $Co_{40}Fe_{40}B_{20}$ with 50 nm thickness mostly another type of walls called asymmetric walls is expected. Thus, in the following this type of wall will be considered.

For some time, there was a common feeling that there should be a method to reduce energy of one dimension Bloch walls by accounting for variation of OOP magnetization component. This variation leads to a decrease in magnetostatic energy and as a result the total wall energy. The general idea was that by consideration of second magnetization component, the magnetization vector can form a close loop. In this way volume magnetic charges disappear and there will be a small area hit by surface charges. Therefore, this reduction in charges decreases the corresponding magnetostatic energy. Fig. (2.7) illustrates how this idea developed by different researchers changed the resulting wall energy. The first idea came from Brown and Labonte [85], who introduced the exact numerical solution to calculate one dimensional wall energy and then Labonte extended it for two-dimensional walls. The new method showed that wall energy can be decreased by 30%, while the wall stays still symmetric. Afterwards, Aharoni tried to relax the system by introducing a transition part into the center of closed-loop magnetization [86], confirmed by the yellow lines in Fig. (2.8) in order to reduce the high exchange energy in the center of loop. Because in the center of the wall, when the magnetization tends to change drastically in a very small area, high exchange energy is imposed to the system. Nevertheless, Aharoni's method could not decrease the energy contribution more than Labonte's model. Finally, Labonte [87] and Hubert [88, 89] independently

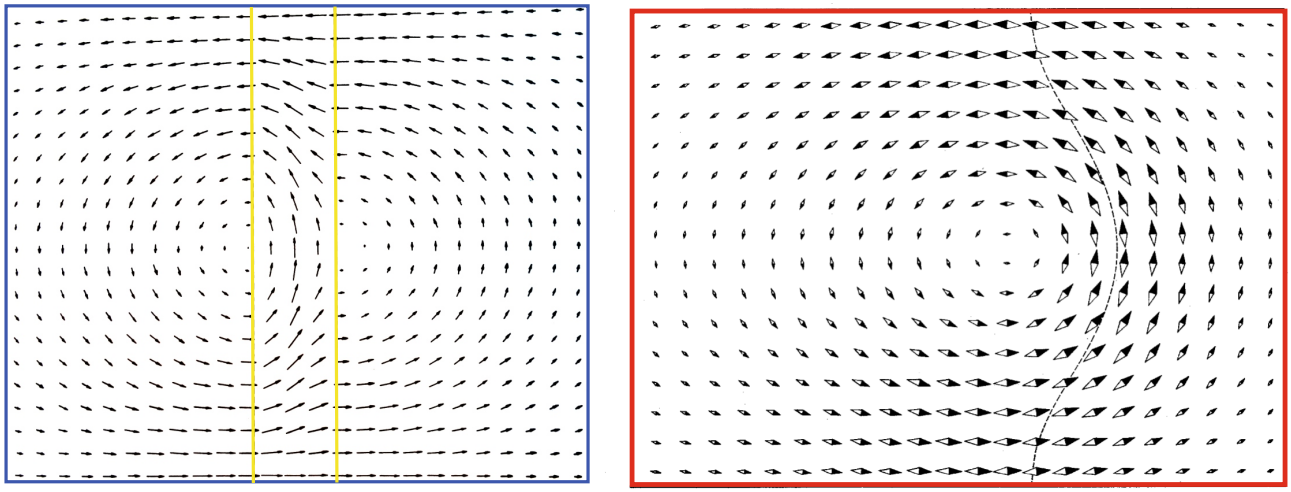

Figure 2.8: The Aharoni model on left side of the Fig. [77] suggesting a transition region(marked with two yellow lines) is compared to an asymmetric Bloch wall model on the right side [87].

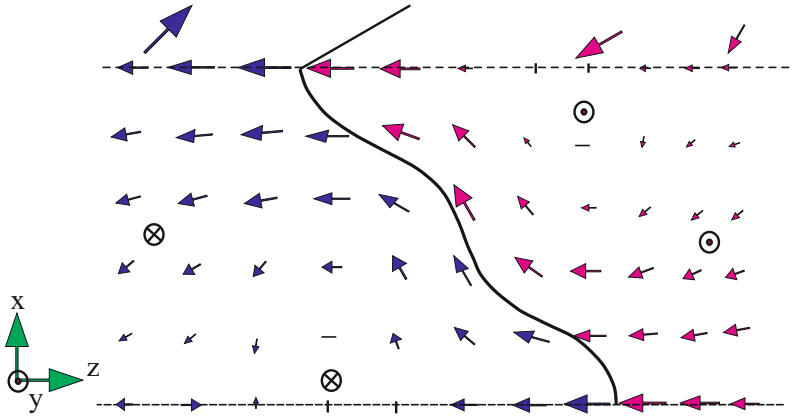

Figure 2.9: The stray field free asymmetric Néel wall as a vortex wall is shown. The center of the wall is illustrated by a contour line. This line is where the y-component of magnetization passes zero [79].

introduced a complete stray field free model, which was asymmetric. The Labonte's asymmetric Bloch wall and Aharoni's model are illustrated in Fig. (2.8).

As can be distinguished in Fig. (2.8), the asymmetric Bloch wall has antiparallel magnetization vectors in the top and bottom surfaces while for asymmetric Néel walls both sides have the same magnetization direction, which is the same direction as the applied field. Therefore without any magnetic field or with small field application, asymmetric Bloch walls are favourable while the application of a higher field causes asymmetric Néel walls (with lower angles and so lower energy) to emerge. In Fig. (2.9), an asymmetric Néel wall profile is shown.

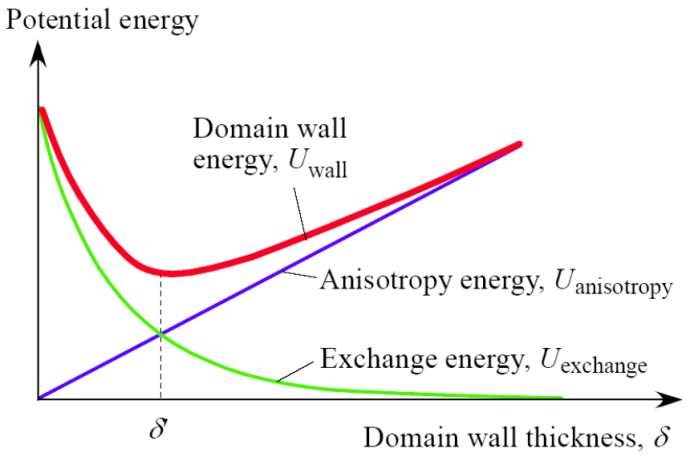

Figure 2.10: Thickness of DW depends on magnetic anisotropy and exchange energy [91].

2.2.3 Exchange Length

In any micromagnetic simulation, one of first important concerns is the cell size in griddling. If it is coarse, there is the possibility of inducing an error in the calculations for instance the collapsing of a Néel wall as a result of overriding the exchange energy by the magnetostatic energy [90]. Therefore, it is needed to define a special length as maximum allowed grid size. This is called exchange length and shows the range in which exchange interaction is considered.

In magnetic materials with spontaneous magnetization, the exchange field tries to keep the magnetic moment neighbours parallel in order to decrease the corresponding energy, but this will increase the anisotropy energy tending to align all magnetic moments parallel to the easy axis or easy plane of magnetization. In hard magnetic materials with magnetocrystalline anisotropy mostly Bloch walls form. Their shape and thickness as mentioned above is a result of competition between the anisotropy trying to reduce wall thickness and the exchange energy trying to increase it, as it can be seen in Fig. (2.10). Finally, the DW thickness δ is scaling with the relation between this two energy densities:

$$\delta_{Bloch} \propto \sqrt{\frac{A}{K_u}} = l_{exch} \tag{2.27}$$

where A represents the exchange stiffness and K_{u} indicates the uniaxial anisotropy constant. In the equation (2.27) , l_{exch} is called magnetocrystalline exchange length.

In thin film soft magnetic materials, with small anisotropy, the typical domain wall profile is the Néel wall whose thickness scales with by

$$\delta_{Néel} \propto \sqrt{\frac{A}{K_d}} = l_{exchange} \quad \text{with} \quad K_d = \frac{\mu_0 M_s^2}{2} \tag{2.28}$$

where l_{exch} is the magnetostatic exchange length [92]. It should be mentioned that the exchange

length is somehow different from the characteristic length because it has unrelated to the DWs thickness and is independent of the anisotropy. It was introduced for the first time as

$$R = \frac{\sqrt{A}}{M_s} \quad \text{in cgs system} \tag{2.29}$$

and describes the critical size for single domain behaviour. It is the largest size (radius for cylindrical shapes) of an ideal magnetic particle, in which the magnetization reversal takes place by rotation rather than nucleation [93].

2.3 Magnetization Dynamics

Above, we discussed the static magnetization, where a static magnetic field is applied. The magnetization will be in non equilibrium (transition time) shortly until it arranges itself via new domain nucleation or DWs movement throughout the magnetic sample and reaches a new equilibrium alignment by minimization of total energy. If a time dependent excitation magnetic field is applied to the magnetic material, based on the frequency of excitation, the magnetization response can be different. For instance, when the period of the excitation field is much higher than the transition time ($t_{exc} >> t_{\text{trans}}$) the magnetization behaviour is considered as static because the magnetization will relax fast enough towards the energetic equilibrium state. By increasing the excitation frequency (f_{exc}) to the MHz and GHz regime, the magnetization obeys the laws of magnetization dynamics, which will be discussed in this section. Magnetization dynamics at different time scales are illustrated in Fig. (2.11).

Subsequently, we will consider one single spin and then extend our discussion to an ensemble of particles with the same magnetization orientation, one single domain. The analytical discussion for a multi domain magnetic state is not so clear but there are powerful simulation programs such as Mumax3 [94] and Micromagus [95]. They use the finite differences method to calculate the dynamic response of magnetization numerically by integrating between the responses averaging on the sample. In this work, Micromagus is used to simulate magnetization dynamics and the corresponding details will be discussed later .

In a magnetic flux density **B**, the magnetic moment $\boldsymbol{\mu}$ experiences a torque $\boldsymbol{\tau}$

$$\boldsymbol{\tau} = \boldsymbol{\mu} \times \mathbf{B} = \mu_0 \boldsymbol{\mu} \times \mathbf{H} \quad \text{with} \quad \mu_0 = \text{ vacuum permeability} \tag{2.30}$$

In addition, a moving charge has angular momentum **J** related to its magnetic moment by a con-

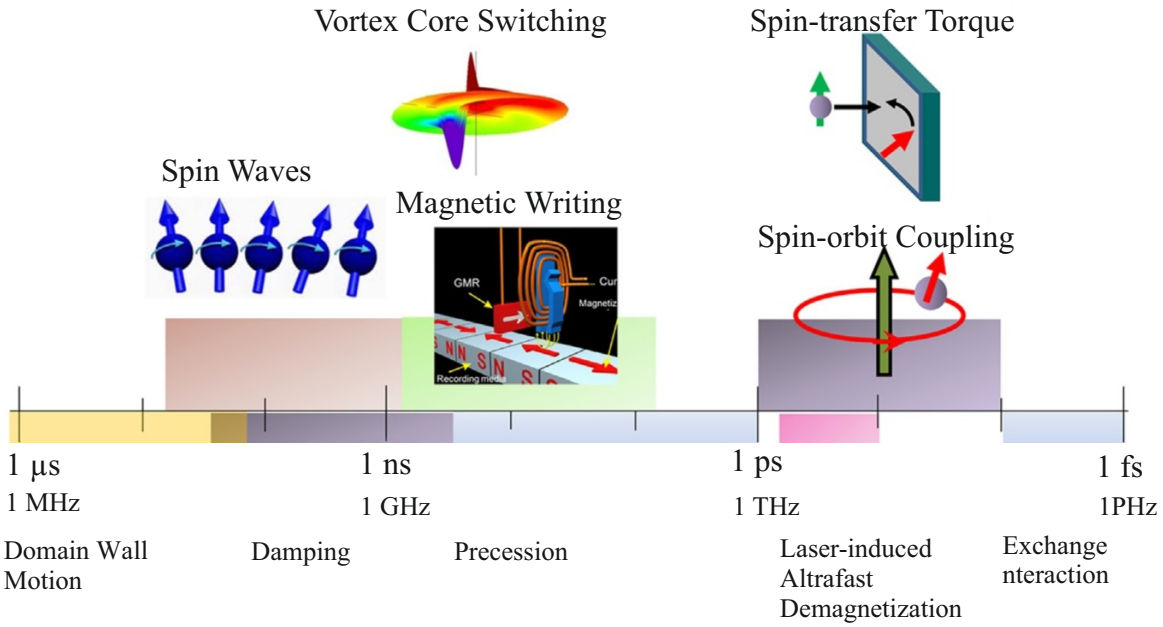

Figure 2.11: The different types of magnetization responses depend on the excitation field's frequency. For instance, the fastest phenomenon is exchange interaction and the slowest process is DWs movement. The diagram has been adopted from [96].

stant

$$\boldsymbol{\mu} = \gamma \mathbf{J} \quad \text{with} \quad \gamma = \text{ gyromagnetic ratio} \tag{2.31}$$

where the gyromagnetic ratio γ as the name suggests, shows the ratio between the magnetic moment and the angular momentum for every particle. It has a negative value for electrons [97] and is equal to $1.760859644 \times 10^{11}$ rad/sT. Now, we are able to write the equation of motion for a magnetic moment. In this equation the dynamic variation in the angular momentum equals to the applied torque from equation (2.30)

$$\frac{\mathrm{d}\mathbf{J}}{\mathrm{d}t} = \boldsymbol{\mu} \times \mathbf{B} = \gamma \mathbf{J} \times \mathbf{B} = \gamma \mu_0 \mathbf{J} \times \mathbf{H} \tag{2.32}$$

For a system of N magnetic moment when an effective magnetic field is applied, $\mathbf{H}_{eff}$, equation (2.32), is written as

$$\begin{gathered} \frac{\mathrm{d}\mathbf{M}}{\mathrm{d}t} = \gamma \mu_0 \mathbf{M} \times \mathbf{H}_{eff} \quad \text{with} \quad \mathbf{M} = N\boldsymbol{\mu} = N\gamma \mathbf{J} \\ \mathbf{H}_{eff} = \mathbf{H}_{ext} + \mathbf{H}_{exch} + \mathbf{H}_{an} + \mathbf{H}_{dem} \end{gathered} \tag{2.33}$$

where H_{eff} denotes the superposition of all fields exerted on the particles. In addition, $\mathbf{H}_{ext}$, $\mathbf{H}_{exch}$, $\mathbf{H}_{an}$, $\mathbf{H}_{dem}$ indicate respectively the external, exchange, anisotropy and demagnetizing field. This equation is the lossless Landau-Lifshitz equation [98] since damping has not been considered yet.

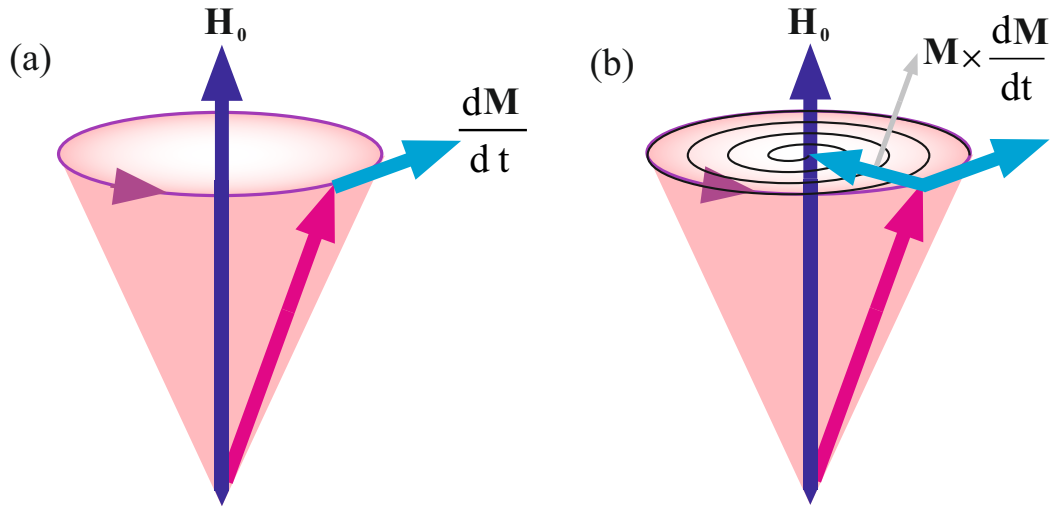

Figure 2.12: (a)The Landau-Lifshitz equation by with damping ignorance is illustrated. Without damping, the magnetization vector precesses around the local effective magnetic field and the angular momentum for this rotation depends on d**M**/dt. (b) The precession of magnetization based on Landau-Lifshitz-Gilbert equation is illustrated. It indicates that magnetization will precess around magnetic field, but the radius of precession decreases because of damping which scales by angular momentum, d**M**/dt , and magnetization, **M**. The magnetization will be relaxed when it aligned completely parallel to the magnetic field.

2.3.1 Ferromagnetic Resonance (FMR)

The ferromagnetic resonance is defined as the condition in which a ferromagnetic material absorbs the maximum energy from an alternating excitation magnetic field. In this situation spins receive energy from the field and transfer it to a lattice via spin-lattice coupling. This causes lattice vibrations. From an analytical point of view, FMR happens when either the magnetic field amplitude H_{res} or its frequency f_{res} satisfy special conditions, in which the permeability of the material reaches a peak. The FMR depends on magnetic features of the materials such as anisotropy, exchange interaction and demagnetizing field in addition to the frequency and the field amplitude. Therefore, it can be used to estimate anisotropy and magnetic inhomogeneity [99]. In the next section, firstly we start with an analytically simple model. This ignores damping and other fields except the externally applied field. They will be added to the system gradually to obtain a more general model.

2.3.1.1 Bias Field Contribution

If the exchange, anisotropy and demagnetizing field can be ignored, the differential equation (2.33) has a simple solution, which means the permeability can be obtained easily. The external magnetic field in this case comprises a static field $\mathbf{H}_0$ and a time dependent excitation field **h**(t) , and therefore the magnetization is supposed, correspondingly, to have a static $\mathbf{M_0}$ and a time depen-

dent response **m**(t) :

$$\mathbf{H}_{eff} = \mathbf{H}_0 + \mathbf{h}(t) \quad \text{with} \quad \mathbf{h}(t) = \mathbf{h}\exp(-i\omega t) \tag{2.34a}$$

$$\mathbf{M} = \mathbf{M}_0 + \mathbf{m}(t) \quad \text{with} \quad \mathbf{m}(t) = \mathbf{m}\exp(-i\omega t) \tag{2.34b}$$

in which $f = 2\pi\omega$ shows the frequency of the excitation field, **h**(t). Furthermore, **h** and **m** display the time independent part of the excitation field and the magnetization response, respectively. It is supposed that they have both z (IP) and y (OOP) components, which lead to obtaining the susceptibility tensor. In addition, the time dependency is assumed to be $\exp(-i\omega t)$. If definitions for **M** and $\mathbf{H}_{eff}$ is substituted in the differential equation (2.33), after ignoring higher orders and assuming that the static magnetization does not change by applying a small amplitude excitation field ($M_0 = M_s$), this relation is achieved

$$-i\omega\mathbf{m} = \hat{\mathbf{z}} \times [\omega_M \mathbf{h} - \omega_0 \mathbf{m}] \tag{2.35a}$$

$$\text{with} \quad \omega_M = \gamma\mu_0 M_s \quad \text{and} \quad \omega_0 = \gamma\mu_0 H_0 \tag{2.35b}$$

in which γ shows gyromagnetic ratio and ω_0 is the natural resonance of the frequency material. In addition, $\hat{\mathbf{z}}$ is the unit vector parallel to bias field. From this equation, the susceptibility or permeability tensor is found since it connects the dynamic magnetization and the excitation field:

$$\mathbf{h} = \overleftrightarrow{\chi}^{-1} \cdot \mathbf{m} \Rightarrow \overleftrightarrow{\chi}^{-1} = \frac{1}{\omega_M} \begin{bmatrix} \omega_0 & -i\omega \\ -i\omega & \omega_0 \end{bmatrix} \tag{2.36a}$$

$$\mathbf{m} = \overleftrightarrow{\chi} \cdot \mathbf{h} \Rightarrow \overleftrightarrow{\chi} = \begin{bmatrix} \chi & -i\kappa \\ -i\kappa & \chi \end{bmatrix} \tag{2.36b}$$

$$\text{with} \quad \chi = \frac{\omega_0\omega_M}{\omega_0^2 - \omega^2} \quad \text{and} \quad \kappa = \frac{\omega\omega_M}{\omega_0^2 - \omega^2} \tag{2.36c}$$

where $\overleftrightarrow{\chi}$ denotes Polder's susceptibility tensor. As it can be seen, generally, the susceptibility of materials can be complex [100]. In addition, from equations (2.36), it is concluded that when the frequency of the excitation field and natural resonance frequency of the material are equal ($\omega_0 \rightarrow \omega$), the susceptibility tensor's components are infinite. This is called lossless ferromagnetic resonance in a harmonic excitation field. The magnetization precession around the effective field is illustrated in Fig. (2.12 a).

2.3.1.2 Bias and Exchange Field Contribution

To consider the exchange field H_{exch}, the effective magnetic field in equation(2.34a) should be replaced by

$$\mathbf{H}_{eff} = \mathbf{H}_0 + \mathbf{H}_{0,exch} + \mathbf{h}(t) \tag{2.37}$$

By exactly the same procedure leading to equations (2.36), $\overleftrightarrow{\chi}^{-1}$ can be obtained:

$$\overleftrightarrow{\chi}^{-1} = \frac{1}{\omega_M} \begin{bmatrix} \omega_0 - \omega_M \lambda_{exch} \triangle & -i\omega \\ -i\omega & \omega_0 - \omega_M \lambda_{exch} \triangle \end{bmatrix} \tag{2.38}$$

In comparison to equations (2.36), ω_0 is replaced by $\omega_0 - \omega_M \lambda_{exch} \triangle$. Furthermore, $\triangle$ indicates the second spatial derivitive of **m**. Besides, λ_{exch} represents a sample parameter relating magnetization and exchange field

$$\mathbf{H}_{exch} = \lambda_{exch} \triangle \mathbf{M} \tag{2.39}$$

The relation between λ_{exc} and the stiffness constant is obtained from substitution of equation (2.5) in equation (2.2) and then comparing the result to equation(2.39). Therefore, it is obtained

$$\lambda_{exch} = \sqrt{\frac{2A}{\mu_0 (M_s)^2}} \tag{2.40}$$

For our sample with the stiffness constant $A = 2.24 \times 10^{-5}$ J/m and $\mu_0 M_{\text{s}} = 1.5$ T, λ_{exch} is equal to 2.5×10^{-17} m^2.

2.3.1.3 Analogy with Mechanical Oscillator

To illustrate the similarity between a magnetization dynamic oscillation and its mechanical counterpart, we consider a spring whose spring constant is k_s. It is connected to a body whose mass is m_s and oscillates in x direction inside a fluid with damping factor c_d after applying a force $F(t)$. The equation of motion is written as

$$\underbrace{m_s x''}_{\text{Force}} + \underbrace{c_d x'}_{\text{Damping Force}} + \underbrace{k_s x}_{\text{Restoring Force}} = \underbrace{F(t)}_{\text{Applied Force}} \tag{2.41}$$

where x'' and x' are the second and first time derivation of position function x(t). The above mentioned forces and their magnetic equivalent are shown in Fig. (2.13), while the spring tries to restore the body to its equilibrium position $x_{eq} = 0$. In addition, *F(t)* represents the applied force to

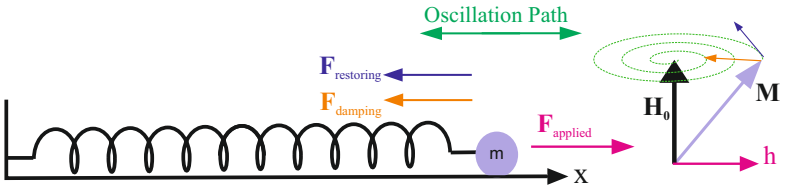

Figure 2.13: The exerted forces on a spring connected to a body and their counterparts in a magnetic material system are illustrated with the same colours.

the system. It can be zero all times except $t = t_0$ or a harmonic driven force such as

$$F(t) = F_0 \exp(i\omega t + \varphi) = F_0(\cos(\omega t + \varphi) + i \sin(\omega t + \varphi)) \tag{2.42}$$

where F_0 and $f = \omega/2\pi$ represent the amplitude and the frequency of the driving force and φ indicates the phase differences between the driving force and the mass position's function $x(t)$.

For a pulse force with $F = 0$ in $t \neq t_0$, equation (2.41) is a homogeneous second order differential equation with an exponential decay solution. Based on how the strong damping parameter in comparison with the spring constant and mass is, for a general answer *x(t)* (introduced below in 2.43a), there are three possibilities (b-d) [101]

$$x(t) = x_0 e^{-\gamma_d t} e^{\pm\sqrt{\gamma_d^2 - \omega_0^2}t} \tag{2.43a}$$

$$\gamma_d^2 < \omega_0^2 \Rightarrow \text{Underdamped Oscillator} \Rightarrow x(t) = x_0 e^{-\gamma_d t} \sin\sqrt{\omega_0^2 - \gamma_d^2}\, t \tag{2.43b}$$

$$\gamma_d^2 = \omega_0^2 \Rightarrow \text{Critically Damped Oscillator} \Rightarrow x(t) = x_0 e^{-\gamma_d t} \tag{2.43c}$$

$$\gamma_d^2 > \omega_0^2 \Rightarrow \text{Overdamped Oscillator} \Rightarrow x(t) = x_0 \exp(-\gamma_d t - \sqrt{\gamma_d^2 - \omega_0^2}\, t) \tag{2.43d}$$

where $\omega_0 = \sqrt{k/m}$ is called the natural resonance or fundamental frequency of the oscillator and $\gamma_d = c_d/2m$ depends on the damping. The underdamped oscillator is a periodic function (harmonic excitation) which damps exponentially. In the case of the overdamped oscillator, damping is high enough to damp the movement before any oscillation. Furthermore, from an exponential decay modulation plot over an underdamped plot, γ_d and thus the damping parameter c can be calculated.

Another important case is the oscillator reaction to a driven periodic force like the force in equation (2.42). In this case, there is a general solution that comprises the transition and the steady-state solution. To find the transition solution, it is supposed that $F(t) = 0$ and, therefore, the solution is the same as equation (2.43a). To find the steady state term, which is a solution for non homogeneous differential equation and depends on driven force, a solution such as x_1 exp(iω t)

is assumed and substituted in equation (2.41) where x_1 is the dynamic response amplitude. After solving this equation we have:

$$x(t) = \underbrace{x_0 \exp(-\gamma_d t)\, \exp(\pm i\sqrt{\omega_0^2 - \gamma_d^2})}_{\text{Transition Solution}} + \underbrace{x_1 \exp(-i\omega t + \varphi)}_{\text{Steady State Solution}} \tag{2.44a}$$

$$\text{where } x_1 = \frac{F_0/m}{\sqrt{(\omega_0^2 - \omega^2) + (2\omega\gamma_d)^2}} \tag{2.44b}$$

$$\text{and } \varphi = \arctan\frac{2\gamma_d\omega}{\omega_0^2 - \omega^2} \tag{2.44c}$$

This states that the oscillator starts to oscillate immediately after the application of excitation force with frequency $(\omega_0^2 - \gamma_d^2)/2\pi$, less than its natural frequency. However, it damps exponentially (because of the exp(-$\gamma_d t$) dependency of transition solution) at the end of transition time (this time is approximately a few $1/\gamma_d$). Afterwards, the body oscillates in the same frequency as the excitation frequency.

Furthermore, from equation (2.44) it can be concluded that the amplitude of the dynamic response x_1 to the harmonic driving force has a peak when the frequency of the driving force matches with the natural resonance frequency $\omega = \omega_0$. For other frequencies far from this x_1 decreases significantly.

2.3.1.4 Damping Contribution

Further discussion of magnetization dynamic, we introduced an idealized case without any magnetic damping. After applying an excitation field, the magnetization vector would precess around effective magnetic field permanently, and it never will reach the minimum energy state by aligning parallel to this field (Fig. (2.12) a). Therefore, Landau-Lifshitz [102] and then Gilbert [103] suggested adding a damping term to the lossless equation of motion for magnetization:

$$\frac{d\mathbf{M}}{dt} = \gamma\mu_0(\mathbf{M}\times\mathbf{H}_{eff}) + \frac{\lambda\gamma\mu_0}{M_s}\mathbf{M}\times(\mathbf{M}\times\mathbf{H}_{eff}) \qquad \text{Landau-Lifshitz} \tag{2.45a}$$

$$\frac{d\mathbf{M}}{dt} = \gamma\mu_0(\mathbf{M}\times\mathbf{H}_{eff}) + \frac{\alpha}{M_s}(\mathbf{M}\times\frac{d\mathbf{M}}{dt}) \qquad \text{Landau-Lifshitz-Gilbert} \tag{2.45b}$$

where α is a dimensionless damping factor. It can be measured by ferromagnetic resonance method which will be discussed later, α and λ are usually both small, for instance for our sample $Co_{40}Fe_{40}B_{20}$ the measured α is between 0.008 and 0.01. Therefore, the direction of $d\mathbf{M}/dt$ will be perturbed slightly toward the center of the cone, illustrated in Fig. (2.12 b), and at the end of the transition time, the magnetization damps on $\mathbf{H}_{eff}$.

The mentioned equations (2.45a) and (2.45b) are mathematically equivalent, but there are some differences in their application. For instance, damping throughout the sample is supposed to be isotropic for the Gilbert damping term, while it is assumed to be anisotropic in the LL equation [104]. Furthermore, in materials with a high damping parameter, the LL equation does not lead to meaningful results in some materials such as Permalloy sheets with big damping where there is not loss because of eddy currents [103].

Now, we are able to obtain the susceptibility for magnetic materials by considering the LLG equation. By substitution of equations (2.34) in equation (2.45b) and by taking into account the same assumptions as the earliest assumptions leading to equation (2.35), it is found that the Polder tensor and its components in equations (2.36) can be used again for the damping case provided that ω_0 is replaced by $\omega_0 - i\omega\alpha$.

In our experimental measurement, it is tried to align the static bias field H_0 parallel to the sample's easy axis of magnetization (in -$\hat{\mathbf{z}}$ direction). Therefore, H_0 (or its equivalent in susceptibility calculation ω_0) can be replaced by $H_0 + H_k$ ($\omega_0 + \omega_k$) in order to take the uniaxial anisotropy into account. Furthermore, the sample is assumed to be dynamically isotropic and thus the susceptibility tensor is reduced to a scalar χ.

In addition, the excitation field is applied IP and perpendicular to H_0 (in x direction). The dynamic response of the magnetization can have generally both IP and OOP components. However, the OOP component of M most likely is really small. The reason is the high OOP demagnetizing factor close to 1. This means that a very high OOP field is needed to magnetize the material normally to its surface plane. Therefore, the susceptibility is approximated as a complex IP parameter in the y direction. To find out χ or the permeability, after the LLG equation is solved and higher orders are ignored, the following equation is obtained [105]:

$$\chi_x(\omega) = \frac{\omega_M(\omega_M + \omega_k + \omega_0 + i\omega\alpha)}{-\omega^2 + (\omega_k + \omega_0)\omega_M + i\omega\alpha\omega_M} \quad \text{with: } \omega_k = \gamma\mu_0 H_k \tag{2.46a}$$

$$\text{OR in terms of fields: } \chi_x(\omega) = \frac{M_s(M_s + H_k + H_0 + i\beta\alpha\omega)}{-(\alpha\omega)^2 + (H_k + H_0)M_s + i\beta\alpha M_s\omega} \quad \text{with: } \beta = \frac{1}{\gamma\mu_0} \tag{2.46b}$$

where ω_M and ω_0 have the same definition as in equation (2.35). It should be mentioned that the index x denotes the measured susceptibility in x direction parallel to the excitation field.

For magnetization dynamic, the critical damping criteria is found when the susceptibility denominator in equation (2.46) has degenerate roots. Therefore, the dynamic magnetization oscillation shown by dM/dt in analogy to equations (2.43) can have three different behaviours based on

the relation between damping parameter and effective field ($H_{eff} = H_0 + H_k$) [105]:

$$0 < \alpha < 2\sqrt{\frac{\omega_k + \omega_0}{\omega_M}} \Rightarrow \text{Underdamped} \tag{2.47a}$$

$$\alpha = 2\sqrt{\frac{\omega_k + \omega_0}{\omega_M}} \Rightarrow \text{Critically damped} \tag{2.47b}$$

$$\alpha > 2\sqrt{\frac{\omega_k + \omega_0}{\omega_M}} \Rightarrow \text{Overdamped} \tag{2.47c}$$

The calculated real (Re), imaginary (Im), and magnitude of susceptibility are plotted in Fig. (2.14) for a sample of $Co_{40}Fe_{40}B_{20}$ by substitution of the applied static field $H_0 = 2$ kA/m , saturation magnetization $M_s = 12\times10^5$ A/m, anisotropy field $H_k = 923$ A/m and damping parameter $\alpha = 0.008$, in the equation(2.46).

This is one example to find f_r for an underdamped magnetization precession. The imaginary part's peak frequency, highlighted by a dashed line, shows a resonance frequency of the material of 2.02 GHz. The zero-crossing frequency of Re and the peak frequency of Im occur at about the same frequency, if the damping parameter is so small [105]:

$$f_i = \frac{\gamma\mu_0}{2\pi}\sqrt{M_s(H_k + H_0 - M_s\frac{\alpha^2}{4})} \tag{2.48a}$$

$$f_r = \frac{\gamma\mu_0}{2\pi}\sqrt{M_s(H_k + H_0)} \tag{2.48b}$$

where f_i and f_r demonstrate Im's peak frequency and Re's zero-crossing frequency. For our sample the damping factor is small and so $f_i \approx f_r$. The equation (2.48b) is called the Kittel formula and is valid for a single domain state [106]. In addition, in Fig. (2.14) the magnitude is obtained as the $\sqrt{\text{Re}^2 + \text{Im}^2}$. Furthermore, by tracing the dash of line, it can be concluded that the resonance frequency happens while the phase difference reaches its largest angle in $\pi/2$. The phase difference is calculated as arctan(Im/Re) and denotes the phase difference between the excitation field and the dynamic magnetization response.

Furthermore, the above equations were obtained under the assumption that H_0 is applied in an easy axis. For H_0, along the hard axis direction, the Kittel formula is different [107]

$$f_r = \frac{\gamma\mu_0}{2\pi}\sqrt{M_s(H_0 - H_k)} \quad \text{when } H_0 > H_k \tag{2.49}$$

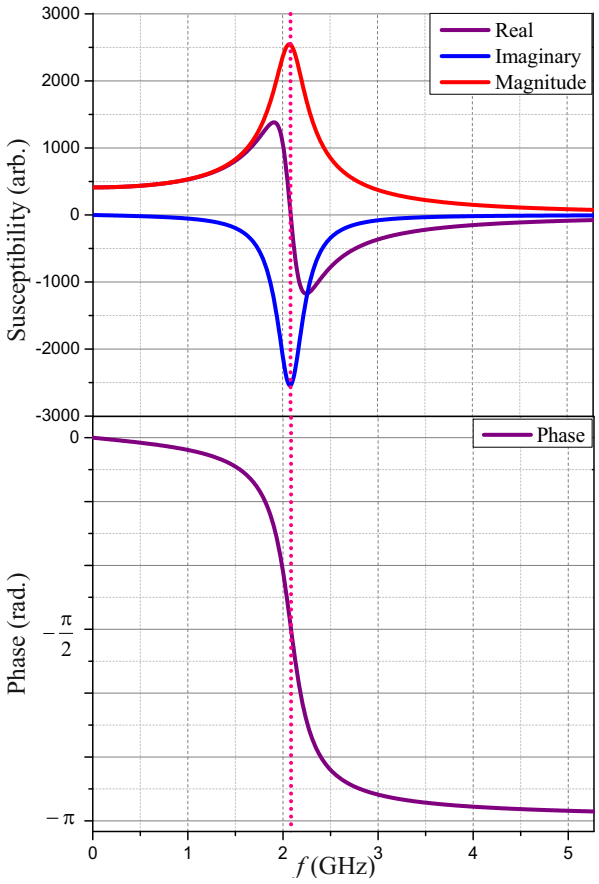

Figure 2.14: The real, the imaginary part, amplitude and phase of susceptibility after substitution of the corresponding value for a sample of $Co_{40}Fe_{40}B_{20}$ are shown in equation (2.46) .

2.3.1.5 Demagnetizing Tensor

If the anisotropic demagnetizing field is involved, the Kittel formula by considering a bias field in the easy axis can be written as [108]:

$$f(r) = \frac{\mu_0 \gamma}{2\pi} \sqrt{(H_0 + H_k + (N_{xx} - N_{zz})M_s)(H_0 + H_k + (N_{yy} - N_{zz})M_s) - M_s^2 (N_{xy} N_{yx})}$$
$$\overleftrightarrow{N} = \begin{bmatrix} N_{xx} & N_{xy} & N_{xy} \\ N_{yx} & N_{yy} & N_{yz} \\ N_{zx} & N_{zy} & N_{zz} \end{bmatrix} \tag{2.50}$$

where $\overleftrightarrow{N}$ is the demagnetizing tensor. Furthermore, index y indicates OOP direction and the bias field is applied in z direction. For thin films, usually the OOP component of the demagnetization field is much larger in comparison to the IP ones.

As an example of utilizing this formula, we will obtain the demagnetization tensor and then calculate the resonance frequency for an array of antidots, when a static field equal to 1.6 kA/m is applied along the easy axis of a 50 nm thick $Co_{40}Fe_{40}B_{20}$ film with a uniaxial anisotropy K_u = 1300 J/m^3. This field is high enough to keep the magnetization close to saturation (in 4 kA/m). The

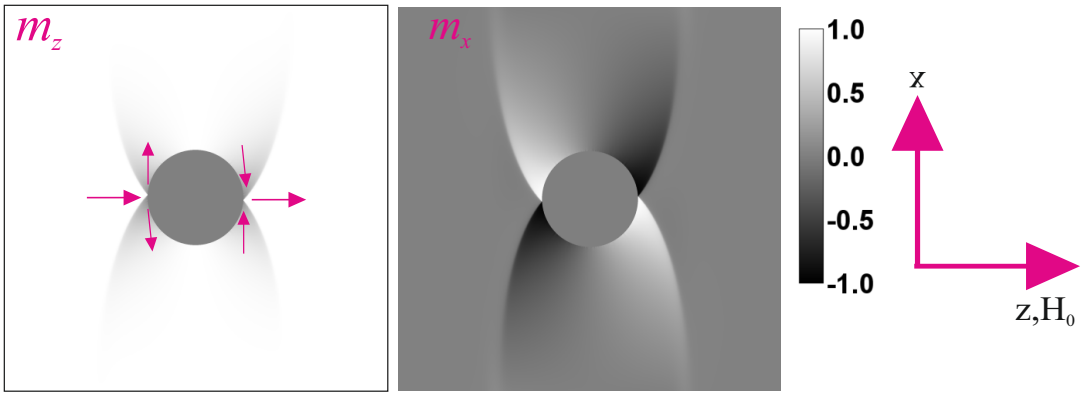

Figure 2.15: The calculated static state for the antidot array after applying 1.6 kA/m bias field. The bias field is parallel to the easy axis and the colour code shows the amplitude of magnetization in every pixel for its IP components. The similar calculation around a hole with the help of another micromagnetic simulation using OOMMF confirms these results [109].

matrix (positions far from the dot's edge) is saturated as can be seen in Fig. (2.15). It is obvious that the magnetization component in the direction of $\hat{\mathbf{z}}$ has highest value 1.

One method to calculate all demagnetizing factors has been introduced in [29]. The N_{zz} can be calculated by projection of the saturation magnetization vector on the demagnetizing field

$$N_{zz} = -\frac{1}{M_s^2}(\mathbf{H}_{dem} \cdot \mathbf{M}_s) \tag{2.51}$$

The demagnetizing, exchange and anisotropy fields for the static state shown in Fig. (2.15) are calculated and displayed in Fig. (2.16) with the help of a numerical micromagnetic simulator.

In order to calculate other factors, firstly one IP and OOP component are defined. Afterwards, the local $\mathbf{M}_s$ is deviated from its ground state (which is the equilibrium state before any variation or perturbation) with very small perturbation of saturation magnetization in each newly defined direction:

$$\hat{\mathbf{n}}_{IP} = \frac{\mathbf{M}_s \times \hat{\mathbf{n}}}{M_s} \quad \text{and} \quad \hat{\mathbf{n}}_{OOP} = \frac{\hat{\mathbf{n}}_{IP} \times \mathbf{M}_s}{M_s^2} \tag{2.52a}$$

$$\mathbf{M}' = \mathbf{M}_s + \frac{M_s}{1000}\hat{\mathbf{n}}_{IP} \quad \text{and} \quad \mathbf{M}'' = \mathbf{M}_s + \frac{M_s}{1000}\hat{\mathbf{n}}_{OOP} \tag{2.52b}$$

where, $\hat{\mathbf{n}}$ indicates the unit vector of the local coordination system perpendicular to the sample surface and other auxiliary vectors. In addition, $\mathbf{M}'$ and $\mathbf{M}''$ represent the perturbed magnetization by a small IP and OOP distortion, respectively. Afterwards, the effective field for each IP and OOP distortion is numerically calculated and the results are subtracted from the obtained data for the ground state. This eventuates in finding the pure distortion components of the effective field.

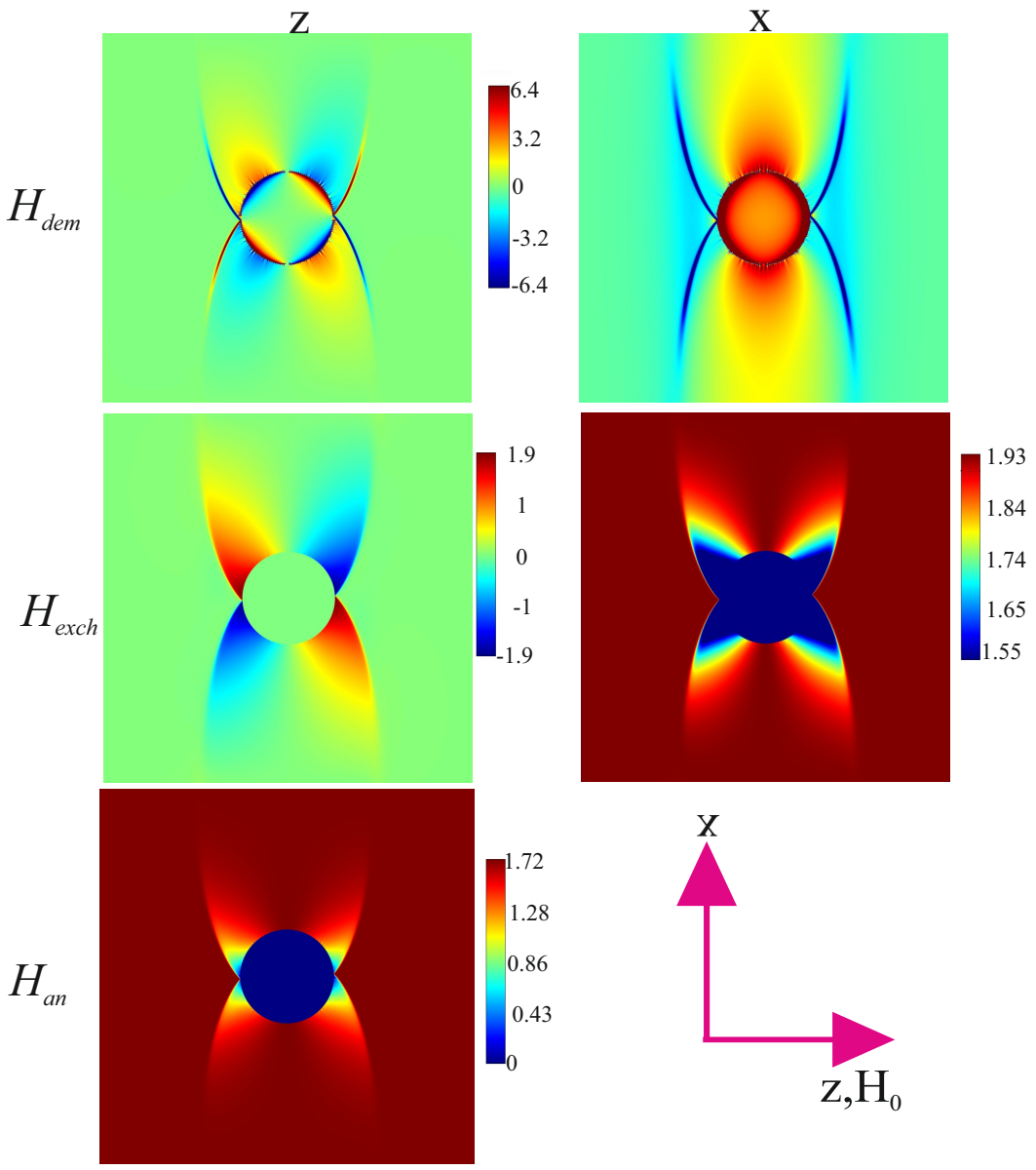

Figure 2.16: The calculated demagnetizing field in kA/m and exchange field in MA/m are illustrated for the static pattern in Fig. (2.15 a) . It can be seen that the exchange energy is almost 300 times higher than the demagnetizing field around the antidots. In addition, the anisotropy field applied along the easy axis of the magnetization $\hat{\mathbf{z}}$ is shown, therefore the other component $\hat{\mathbf{x}}$ is zero everywhere.

Therefore, it is possible to extract the demagnetizing factors N_{ij} as they satisfy these equations:

$$\begin{bmatrix} h''_{dem,x} \\ h''_{dem,y} \end{bmatrix} = \begin{bmatrix} N_{xx} & N_{xy} \\ N_{yx} & N_{yy} \end{bmatrix} \begin{bmatrix} 0 \\ m''_{y} \end{bmatrix} \tag{2.53a}$$

$$\begin{bmatrix} h'_{dem,x} \\ h'_{dem,y} \end{bmatrix} = \begin{bmatrix} N_{xx} & N_{xy} \\ N_{yx} & N_{yy} \end{bmatrix} \begin{bmatrix} m'_{x} \\ 0 \end{bmatrix} \tag{2.53b}$$

where m'_x and m''_y display the pure perturbed IP and OOP magnetization component, respectively. By solving above equations, all demagnetizing factors in x and y direction are achieved [29]. However, in the paper, it is mentioned that exchange energy is accounted. Here, we found out the same result as mentioned in Ref. [29] provided that the exchange energy is ignored in the calculations.

The demagnetizing factors are calculated for the antidot array, via the method introduced by equations (2.53) and (2.52), and are shown in Fig. (2.17). It can be seen that far from the antidot edge, the demagnetizing factor for both IP components x and z are ignorable in contrast to the OOP factor, which is nearly one. This behaviour is similar to full films. In contrast, at the antidot's edge, a variation of the demagnetizing factor leads to IP demagnetization enhancement as it is shown for N_{xx} and N_{zz} . However, $-10^{-4} \leq N_{xy} \leq 10^{-4}$ is non-zero, another non-diagonal element of the demagnetization tensor, N_{yx} is zero everywhere which makes the last term in the equation (2.50) zero. After all demagnetizing factors are obtained, they are inserted into the Kittel formula (equation (2.50)) to obtain the local resonance frequencies pixel by pixel.

2.3.2 Spin Waves

Before we discuss about spin waves (SWs), it is essential to explain some terms used in this section.

Linear medium: If the magnetization inside materials depends on just the first order of the magnetic field, the medium is called linear, $\mathbf{B} = \mu\mathbf{H} = (\chi+1)\mathbf{H}$.

Dispersive medium: If the material does not respond to an applied magnetic field instantaneously, it is concluded that the material has a memory. For instance, specimen with a non-zero magnetization has a different magnetization behaviour in the same fields with different magnetic history. These mediums are dispersive. In the linear and non dispersive medium, the instantaneous response is $\mathbf{m}(t) = \overleftrightarrow{\chi}\ \mathbf{h}(t)$, but for a dispersive medium, either the integral over all $\chi(t)$ in the time domain should be accounted for or a steady state in f-domain is considered without integrating, $\mathbf{m}(\omega) = \overleftrightarrow{\chi}(\omega)\mathbf{h}(\omega)$.

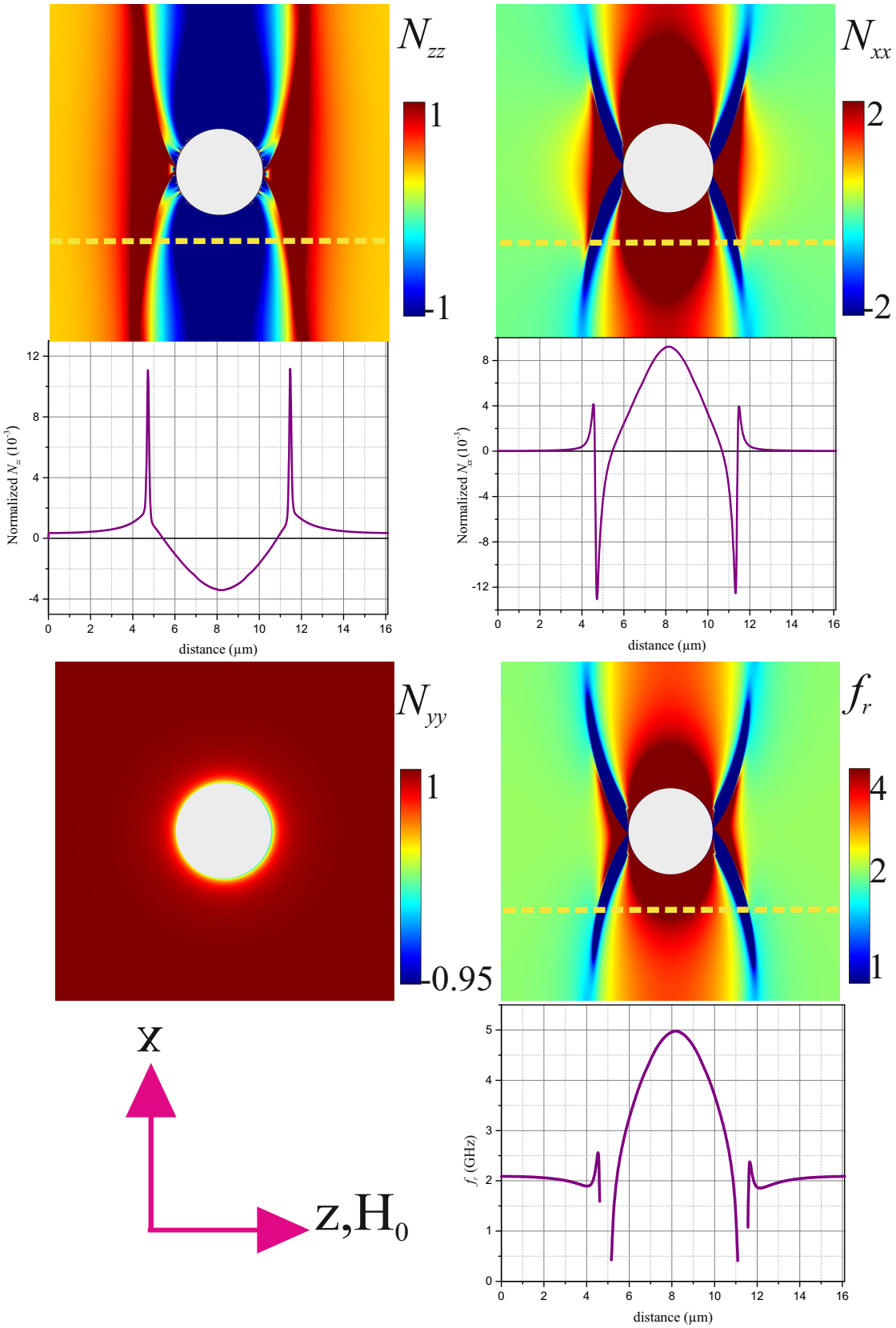

Figure 2.17: Demagnetizing factors calculated through perturbation of a ground state and corresponding local resonance frequencies from equation (2.50) are shown. As it is indicated, out of plane demagnetizing factor N_{yy} is maximum. The number next to colour calibration for the first row has a 10^{-3} factor. The plots display the N_{xx} and N_{zz} variation along the dashed line indicated in the images. Two extrema in these plots correspond to DWs around antidots where there are two discontinuities in the resonance frequency plot. The reason of these discontinuities will be discussed later in section 4.3.1.

2.3.2.1 Walker's Equation

Consider two Maxwell equations as

$$\bigtriangledown \times \mathbf{H} = \frac{\partial \mathbf{D}}{\partial t} + \mathbf{J}_I \quad \text{where} \quad \mathbf{D} = \varepsilon \mathbf{E} \tag{2.54a}$$

$$\bigtriangledown \cdot \mathbf{B} = 0 \tag{2.54b}$$

where $\mathbf{J}_I$, $\mathbf{D}$ and $\mathbf{E}$ indicate the electric current density, the electric flux density and the electrical field, respectively [110]. ε is the dielectric constant. Moreover, $\mathbf{h}$ is the magnetic field of the propagating wave inside the material. Therefore, $\mathbf{H}$ in equation (2.54a) comprises two parts, $\mathbf{H}_0$ and $\mathbf{h}$, with

$$\mathbf{H} = \mathbf{H}_{0,z} + \mathbf{h} \tag{2.55}$$

the effective static field is applied along $\hat{z}$. When there is not any electrical source inside the material, $\mathbf{J}$ is zero. In the static condition, the electric field does not vary in time, so the second term in the equation (2.54a) is also neglected. Therefore, the above equations are reduced to magnetostatic form:

$$\bigtriangledown \times \mathbf{h} = 0 \tag{2.56a}$$

$$\bigtriangledown \cdot \mathbf{b} = 0 \tag{2.56b}$$

$$\mathbf{b} = \overleftrightarrow{\mu}\mathbf{h} \quad \text{and} \quad \overleftrightarrow{\mu} = \mu_0(\overleftrightarrow{\chi} + I) \quad \text{with} \quad \overleftrightarrow{\chi} = \begin{bmatrix} \chi & -i\kappa & 0 \\ -i\kappa & \chi & 0 \\ 0 & 0 & 0 \end{bmatrix} \tag{2.56c}$$

where $\overleftrightarrow{\chi}$ and $\overleftrightarrow{\mu}$ denote the susceptibility and permeability tensor and I displays the identity matrix.

While the curl of a function is zero like $\mathbf{h}$ in equation (2.56a), mathematically, this function can be written as the gradient of another scalar function. Therefore, $\mathbf{h}$ is defined as the gradient of the magnetostatic's scalar potential (ψ), $\mathbf{h} = -\bigtriangledown\psi$. By substitution of equation(2.56c) ($\mathbf{b} = \overleftrightarrow{\mu} \bigtriangledown\psi$) in equation (2.56b), one obtains:

$$(1+\chi)(\frac{\partial^2\psi}{\partial^2 x} + \frac{\partial^2\psi}{\partial^2 y}) + \frac{\partial^2\psi}{\partial^2 z} = 0 \tag{2.57}$$

This is called the Walker's equation and it is the principle equation for magnetostatic modes inside of homogenenous materials [111]. The frequency dependency of Walker's equation is via χ. This

equation is used to predict the dynamic behaviour (such as the dispersion relation) of magnetic waves. Thus, the magnetostatic term does not refer to the static state. The magnetostatic terminology comes from the fact that in order to obtain Walker's equation, the Maxwell equations in static modes were utilized. From Walker's equation, when the spatial dependency of the scalar potential is clear, the corresponding dispersion relation for propagation of waves in magnetic materials is obtained.

2.3.2.2 Magnetostatic Mode and Exchange Mode

It is supposed that spatial dependency of a propagating wave in an infinitely large magnetic material is in the form of $\exp(i\mathbf{k}\cdot\mathbf{r})$ (similar to the plane waves), where $\mathbf{k}$ is the wave number's vector and $\mathbf{r}$ is the position vector. Therefore, by solving Walker's equation for plane waves, this dispersion relation is obtained:

$$\omega = \sqrt{\omega_0(\omega_0 + \omega_M \sin^2\theta)} \tag{2.58}$$

where θ represents the angle between the effective field and the propagation direction. We assume that the effective field and the magnetization direction are parallel, since the bias field is high enough to saturate the material.

To take the exchange energy into account, equation (2.38), which defines the susceptibility of a lossless medium in the presence of exchange, is utilized . Due to the spatial dependency as $e^{i\mathbf{k}\cdot\mathbf{r}}$, $\triangle\mathbf{m}$ in equation (2.38) is substituted by k^2. From comparison between the susceptibility tensor without and with exchange energy in equations (2.36a) and (2.38), it is concluded that ω_0 with $\omega_0+\omega_M\lambda_{exc}k^2$ in equation (2.58) should be replaced. Therefore, the following equation predicting the propagation behaviour of plane waves inside an infinitely large magnetic medium without damping is obtained [112]:

$$\omega = \sqrt{(\omega_0 + \omega_M\lambda_{exc}k^2)(\omega_0 + \omega_M(\lambda_{exc}k^2 + \sin^2\theta))} \tag{2.59}$$

If $\lambda_{exc}k^2 \ll 1$ the exchange term can be neglected and the corresponding mode is called the magnetostatic mode (as Walker's equation obtained from the "static" form of Maxwell equations has been used) or the dipolar mode. On the other hand, the k enhancement (for low wavelengths) leads to highlight exchange interaction, which mode is called the exchange mode [113].

2.3.2.3 Magnetostatic Boundary Condition

At every interface between a magnetic material and another magnetic or non magnetic material, the normal component of magnetic flux density in addition to the tangential component of the magnetic field must be continuous:

$$\mathbf{b}_{n,in} = \mathbf{b}_{n,out} \tag{2.60a}$$

$$\mathbf{h}_{t,in} = \mathbf{h}_{t,out} \tag{2.60b}$$

where n and t in indexes represent the normal and tangential components, respectively. Moreover, in and out indicate inside and outside of the film [114].

In the last section (ferromagnetic resonance) the situation was discussed in which all spins have uniform in-phase precession in response to an external magnetic excitation. Consider every spin where its neighbour has the same phase difference in precession around the effective field. This forms waves are called spin waves. Furthermore, the material is magnetically linear and dispersive. Moreover, in order to keep the discussion general, it is assumed that the material's susceptibility is considered to be a tensor and so the material's permeability can be anisotropic. The goal is to find the dispersion relation representing possible SWs' wavelengths for different excitation frequencies.

The approach is to utilize Walker's equation to obtain a relation connecting wave vectors inside and outside of the film and then applying the magnetostatic boundary conditions to the magnetic field and the flux density to find the coefficients defining the scalar potential ψ corresponding to waves in the magnetic field $\mathbf{h}$. Depending on the angle between the wave's propagation direction and magnetization orientation, different magnetostatic waves are categorized. The features of these waves are characterized here by evaluating their corresponding dispersion relation.

2.3.3 Backward Volume Waves

These waves propagate in-plane, IP, and parallel or antiparallel to the magnetization direction.

Based on the coordination and geometry shown in Fig. (2.18), the applied field magnetizes the sample in $\hat{\mathbf{z}}$ direction. We assume that the wave vector does not have any other IP component and so $k_x = 0$. From the Walker equation (2.57) , the relations between the wave vectors inside and

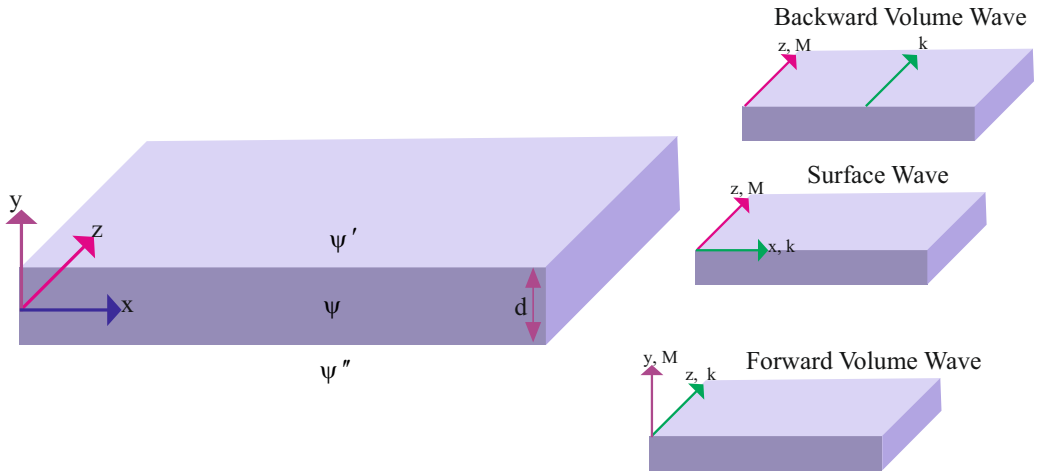

Figure 2.18: The geometry and coordination used to define magnetostatic waves are shown. The origin is in the middle of the film thickness (d) and scalar potentials for three different regions are indicated as ψ', ψ and ψ''. On the right side, three different modes of SWs are shown based on the relative direction of magnetization.

outside the material are obtained[100]

$$(1+\chi)k_y^2 + k_z^2 = 0 \qquad \text{Inside magnetic material} \tag{2.61a}$$

$$k_y'^2 + k_z'^2 = 0 \qquad \text{Outside magnetic material} \tag{2.61b}$$

where k_i and k_i' indicate the wave vector along i direction inside and outside the magnetic material, respectively. For the non-magnetic region in equation (2.61b), the susceptibility outside is zero ($\chi = 0$). Moreover, from equation (2.61a) the wave vectors inside the magnetic material are real provided that $\chi < -1$ mathematically. The scalar potentials in the three areas denoted in Fig. (2.18) are written as:

$$\psi_0(\mathbf{r}) = e^{\pm i k_z z} \tag{2.62a}$$

$$\psi'(\mathbf{r}) = A\psi_0 e^{-k_z y} \tag{2.62b}$$

$$\psi(\mathbf{r}) = \psi_0 \sin(k_y y) \tag{2.62c}$$

$$\psi"(\mathbf{r}) = B\psi_0 e^{k_z y} \tag{2.62d}$$

where ψ_0 indicates the plane wave propagating in the magnetization direction[100]. Furthermore, ψ' and ψ" represent scalar potential functions associated to the magnetic field outside of the material. Far from magnetic material, these potentials should be zero. This is satisfied through the exponential decay function $\exp(k_z\, y)$ and $\exp(\text{-}k_z\, y)$ for the − and + side of $\hat{\mathbf{y}}$, respectively. Furthermore, A and B are coefficients independent of position vector $\mathbf{r}$ and are determined from the

boundary conditions introduced in equation (2.60a, 2.60b), where $y = \pm d/2$

$$\psi'(y = d/2) = \psi(y = d/2) \Rightarrow Ae^{-k_z d/2} = \sin(k_y d/2) \tag{2.63a}$$

$$\psi"(y = -d/2) = \psi(y = -d/2) \Rightarrow Be^{-k_z d/2} = \sin(-k_y d/2) \tag{2.63b}$$

$$\Rightarrow A = -B \tag{2.63c}$$

Furthermore, equation (2.56c) provides the OOP component of b, b_y. It is substituted in the other boundary condition in equation (2.60b)[100]:

$$b_y = i\kappa h_x + (1+\chi)h_y = i\kappa \frac{\partial \psi}{\partial x} + (1+\chi)\frac{\partial \psi}{\partial y} \tag{2.64a}$$

$$\text{for } y = \frac{d}{2} \Rightarrow -Ak_z e^{-k_z d/2} = (1+\chi)k_y \cos(k_y d/2) \tag{2.64b}$$

$$\text{for } y = \frac{-d}{2} \Rightarrow Bk_z e^{-k_z d/2} = (1+\chi)k_y \cos(k_y d/2) \tag{2.64c}$$

Since ψ is independent from x, the first term in equation (2.64a) is cancelled. However, equation (2.64b) and (2.64c) do not provide extra information about A and B. From two divisions, equation (2.64c) and (2.63b) and then (2.63a) and (2.64b), two relations are obtained. The k_y is substituted from equation (2.61a) and the susceptibility dependency to frequency is found from equation (2.36c). Therefore, the relation between wave number and frequency of the excitation field is obtained [115], [100], [116]:

$$f = \frac{1}{2\pi}\sqrt{\omega_0(\omega_0 + \omega_M \frac{1 - e^{-k_z d}}{k_z d})} \tag{2.65a}$$

$$f = \frac{1}{2\pi}\sqrt{(\omega_0 + \omega_M \lambda_{exch} k_z^2)((\omega_0 + \omega_M \lambda_{exch} k_z^2) + \omega_M \frac{1 - e^{-k_z d}}{k_z d})} \tag{2.65b}$$

While the first equation shows the dispersion relation of BVWs by considering only magnetostatic interaction, the second one accounts exchange interaction as well. The second equation is obtained by replacing ω_0 with $\omega_0 + \omega_M \lambda_{exch} k_z^2$ where λ_{exch} was introduced in equation 2.40. The exemplary solution of these two equations are plotted in Fig. (2.19). The solid curves indicated dispersion relation based on equation (2.65a) in which the exchange interaction is ignored and the dash curves illustrate the exchange distribution plus to magnetostatic one.

Consider a pattern such as an antidot array shown in the Fig. (2.15). There are regions with different magnetization and effective fields (different domains) as it was indicated in Fig. (2.16). From the equations (2.48), different effective fields lead to different local resonance frequencies, $f_{r,l} = \omega_0 \,/\, 2\,\pi$. Therefore, by substituting ω_0 with different local resonance frequencies in equation

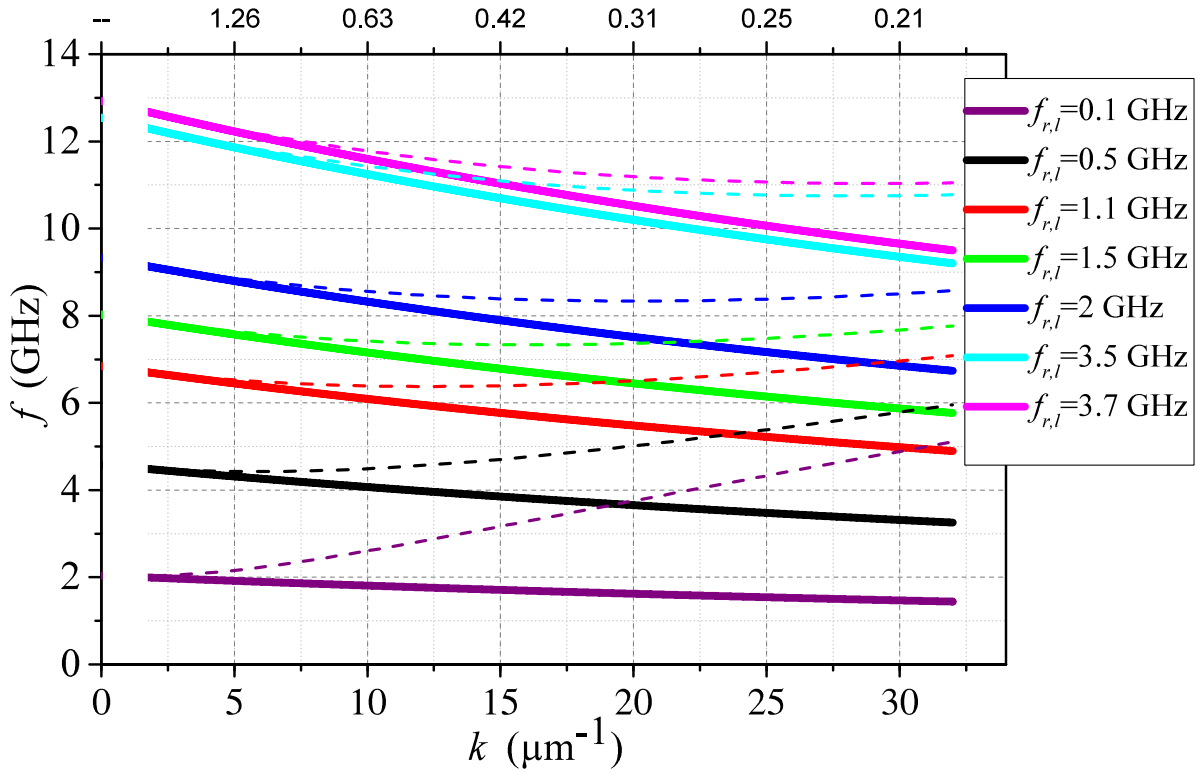

Figure 2.19: The dispersion relation for the backward volume waves are plotted for some selected $f_{r,local} = \omega_0 / 2\,\pi$. The solid curves are exemplary solution of equation (2.65a) while dash one indicate the solution of equation (2.65b) that considers exchange interaction as well.

(2.65), corresponding backward volume wave numbers are obtained. In Fig. (2.19), for several $f_{r,l}$, BVWs are plotted while the saturation magnetization is $M_s = 12 \times 10^5$ A/m. The thickness is 50 nm of a single layer $Co_{40}Fe_{40}B_{20}$ and a static bias field of 4 kA/m is applied to reach saturation. In Fig. (2.19), if an area's local resonance frequency is $\omega_0 = 2\,\pi$ ($f_{r,l} = 0.1$) GHz, indicated by the dash purple line, it is expected to see backward volume waves' propagation by a wavelength around 500 nm, when the sample is excited with $f = 3$ GHz. If the excitation frequency is lower about 2 GHz, the backward volume waves are emitted with the wavelength higher than 2.5 μm from the same region. Furthermore, the dispersion relation for backward volume waves and correspondingly Fig. (2.19) predict to excite domains with local resonance frequencies above 1 GHz, the required excitation field is above 6.5 GHz in a time resolved magneto-optic Kerr effect, TR-MOKE, experiment.

2.3.4 Surface Waves

In this section, the waves are considered which propagate normal to the magnetization direction while both waves and magnetization are IP. They are called "Surface Waves" or "Damon-Eshbach" waves [117]. By looking at the geometry used before in Fig. (2.18), now the propagation direction is assumed to be in $\hat{\mathbf{x}}$, while the effective field and the magnetization are still in the $\hat{\mathbf{z}}$ direc-

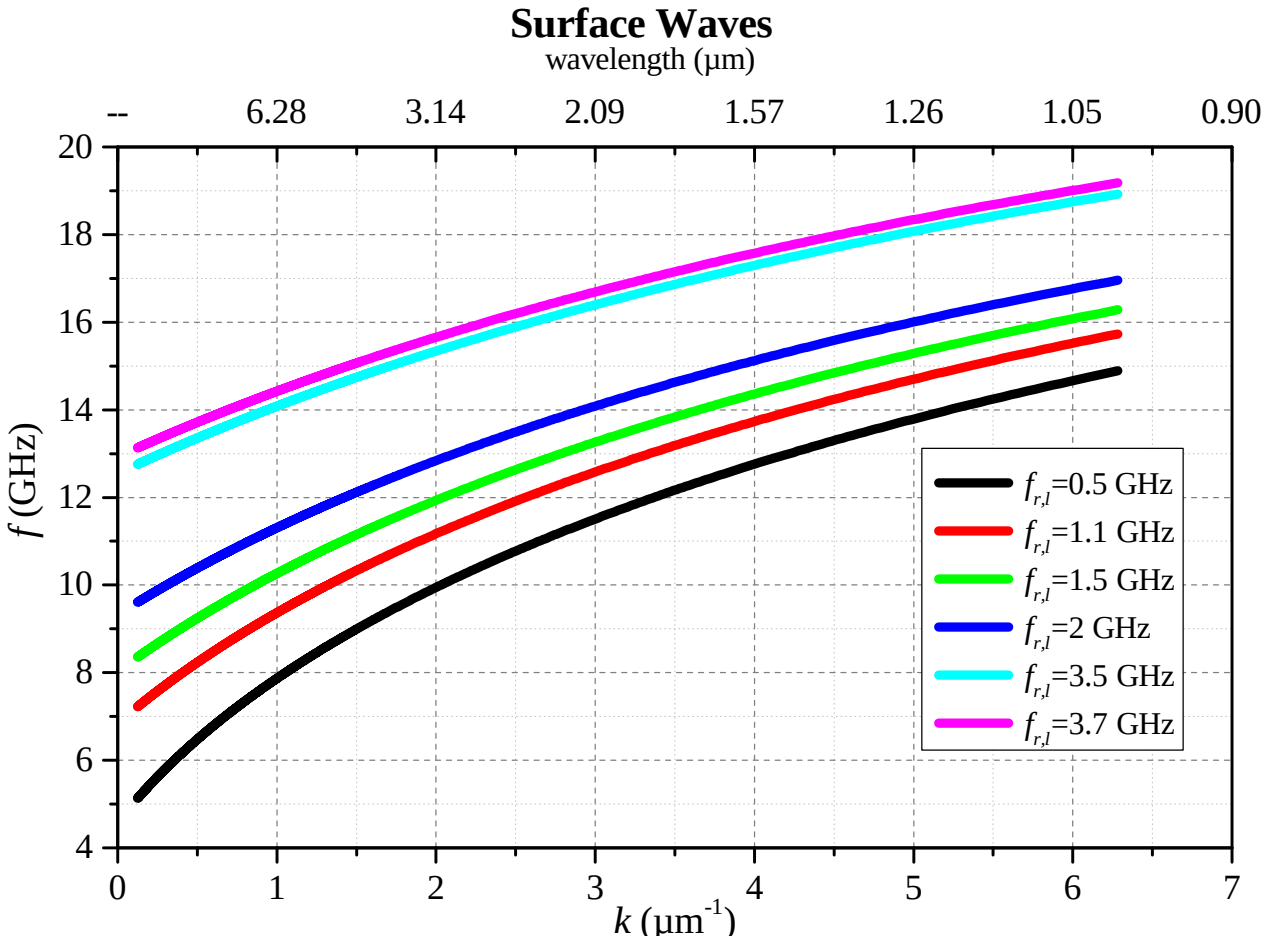

Figure 2.20: The dispersion relation for waves propagating normal to their magnetization direction, the surface waves, at the same local frequencies as Fig. (2.19) are shown.

tion. Therefore, in equations (2.62), k_z should be replaced by k_x. By seeking the same analytical approach leading to the equation (2.65) for the backward volume waves, the dispersion relation describing surface waves is obtained [118]:

$$f = \frac{1}{2\pi}\sqrt{\omega_0(\omega_0+\omega_M)+\frac{\omega_M^2}{4}[1-e^{-2kd}]} \tag{2.66}$$

The exemplary solutions to this equation are plotted in Fig. (2.20). In contrast to the backward volume waves, there is a direct relation between the frequency of excitation field and the wave numbers. Therefore, the group velocity V_{group} is positive.

To compare these two types of magnetostatic waves consider the area in the sample which local resonance frequency is $f_{r,l}$ = 0.5 GHz , shown by black lines in Fig. (2.19) and (2.20). If this area is excited by f = 3 GHz, backward volume waves with k = 10 μm^{-1} (wavelength=420 nm) are expected, while no surface wave is produced as there is not any crossing point between the plot according to $f_{r,local}$ = 0.5 GHz and the horizontal line from f = 3 GHz in Fig. (2.20). To excite surface waves inside the mentioned area with $f_{r,local}$ =0.5 GHz, an excitation frequency higher

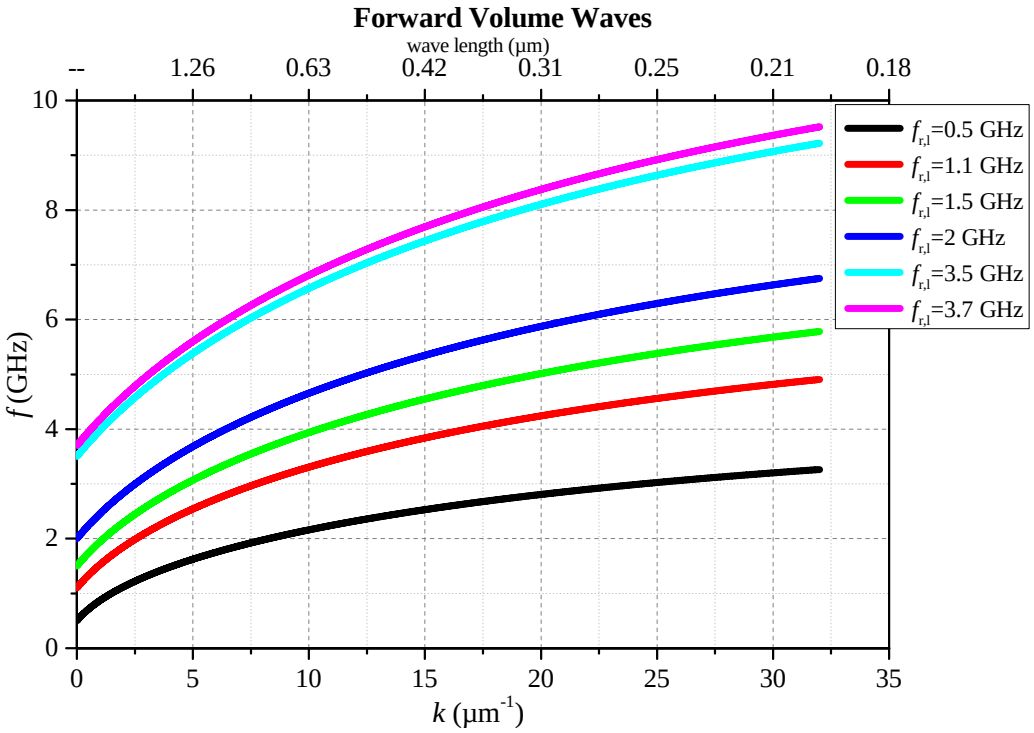

Figure 2.21: The dispersion relation for the forward volume waves propagating IP and normal to their OOP magnetization direction for some local frequencies are plotted.

than 6 GHz is needed. For instance, by f = 8 GHz, the surface waves with k = 1 μm^{-1} (wavelength = 6.28 μm) are observed.

To excite surface waves with the same wavelength as backward volume waves, a higher frequency of excitation is required.

2.3.5 Forward Volume Waves

This mode of magnetostatic waves propagates IP while the sample is magnetized OOP illustrated in Fig. (2.18). These waves are mentioned here regarding a complete discussion. However, either in our experimental or in the simulated data, a pronounced OOP magnetization is not expected. The reason is that a small and IP magnetic field (maximum 4 kA/m) applied to the samples is not suited to overcome the high OOP demagnetizing factor ($N_{yy} \approx 1$) shown for our sample in Fig. (2.17). The relation between the excitation field frequency and the **k** vector of forward volume waves is written as [115]:

$$f = \frac{1}{2\pi}\sqrt{\omega_0(\omega_0 + \omega_M(1 - \frac{1 - e^{-k_z d}}{k_z d}))} \tag{2.67}$$

where the sample is magnetized in the $\hat{\mathbf{y}}$ direction and the waves propagate in the $\hat{\mathbf{z}}$ direction based on the geometry shown in Fig. (2.18). This relation is plotted in Fig. (2.21) for some local resonance

frequencies. As it can be seen, similar to surface waves, the relation between k and f_{exc} is direct.

2.3.6 Spin Waves in Double Layers

What we discussed above is applicable to the propagation of SWs in single layer ferromagnetic thin films, but laminating a magnetic sample leads to variation in its overall magnetic responses in comparison with every layer's magnetic character [119]. If two layers are separated by a spacer in the range of a few angstroms to nanometers, the interlayer exchange coupling J plays a role depending on its value and sign. For instance, the analytical discussion by Grünberg and his numerical calculation [45] show that in the presence of a gap between two ferromagnetic layers the dispersion relation for the Damon-Eshbach mode depends on the gap's thickness in addition to other factors which were mentioned before in equation (2.66) such as each layer's thickness, saturation magnetization and effective field. Two ferromagnetic layers with d_A and d_B as thickness and spacer thickness d_s are assumed, based on Grünberg's approach. First the parameter C in the following equation is found and then the second equation provides the dispersion relation for propagating waves:

$$1 - e^{-2kd_B} - e^{2kd_A} + e^{2k(d_A-d_B)} - e^{2kd_s}[1 + Ce^{-2kd_B} + \frac{1}{C}e^{2kd_A} + e^{2k(d_A-d_B)}] = 0 \tag{2.68a}$$

$$f = \frac{\omega_M}{2\pi}\sqrt{\frac{C}{4} + (\frac{\omega_H}{\omega_M} + \frac{1}{2})^2} \tag{2.68b}$$

These equations are applicable while the magnetization resides in the plane[45].

Since the equation (2.68a) provides two possible answers for parameter C, therefore, two types of waves are anticipated by equation (2.68b). Moreover, this study predicts that by increasing the distance between two layers, two surface modes in addition to one volume mode can be distinguished. The figures (2.22) and (2.23) indicate results for some different local frequencies while two layers are separated by a non-magnetic spacer with 0.8 nm thickness. The other used parameters are the same as what mentioned before for the single layer sample plotted in Fig. (2.19) except the every layer's thickness is equal to 25 nm.

In addition, Grünberg calculated the Damon-Eshbach mode under the assumption that the saturation magnetization of both layers is dissimilar [120]. There are experimental evidences clarifying how exchange coupling across a non-magnetic layer can be measured by Brillouin Light Scattering, BLS [121].

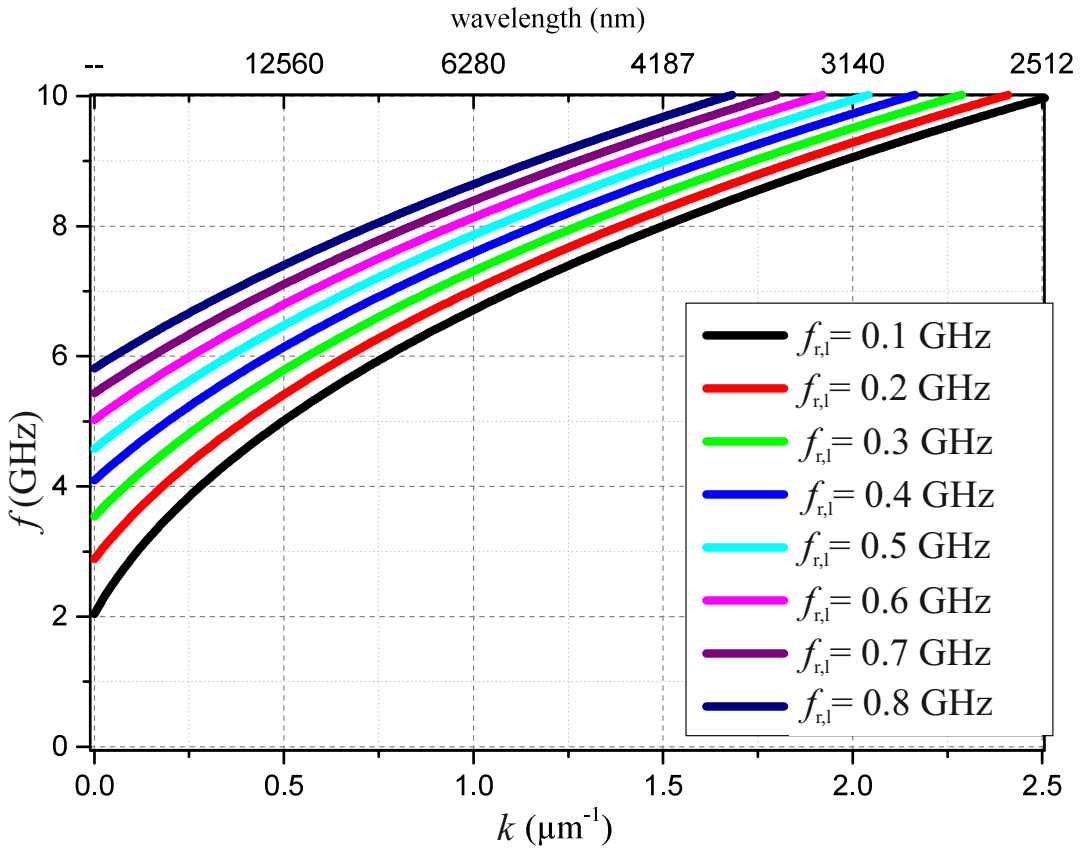

Figure 2.22: The calculated data from the Grünberg theory for a double layer ferromagnetic material with a non-magnetic spacer between them. In this calculation, the first answer of the equation (2.68a) is taken and substituted in the equation (2.68b).

2.3.7 Optical and Acoustical Modes

The interlayer exchange coupling between two layers is defined by strength and sign of the bilinear J_1 and the biquadratic interlayer exchange coupling J_2. Therefore, the total energy of this system is written as [119, 122, 123]:

$$e = d_A e_A + d_B e_B - J_1 \frac{\mathbf{M}_A \cdot \mathbf{M}_B}{M_A M_B} - J_2 (\frac{\mathbf{M}_A \cdot \mathbf{M}_B}{M_A M_B})^2 \tag{2.69}$$

where the indices A and B indicate the two individual layers and e is the energy density. If the J_1 dominates, depending on its sign, antiferromagnetic or ferromagnetic alignment of magnetization, in the two layers leads to minimization of energy. On the other hand, if J_2 term dominates, the magnetization of layer A is perpendicular to the magnetization of layer B in equilibrium. It should be mentioned that this analysis is independent of the physical origin of the coupling since it is phenomenological [46].

If we consider the Zeeman energy and an uniaxial IP anisotropy energy (it can be tilted in one layer relative to the other layer's anisotropy by angle δ) and magnetization is IP, a fourth order equation in ω can be obtained by a method of Smith and Beljers. With the assumptions that the

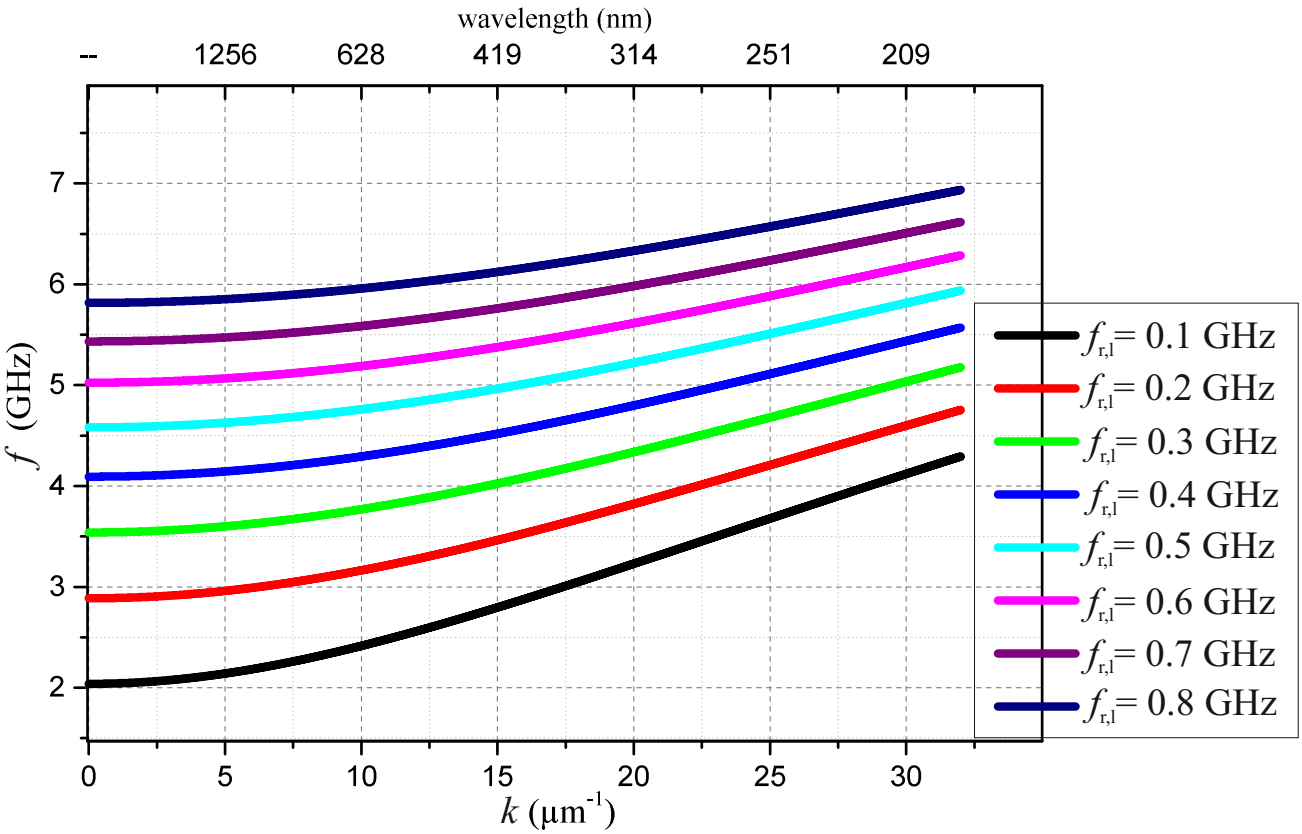

Figure 2.23: The same calculation as Fig. (2.22) is shown, except in this calculation the second answer of equation (2.68a) for parameter C is considered and substituted in equation (2.68b).

gyromagnetic ratio, the thickness and the saturation magnetization are the same for both layers, it can be found that [46]:

$$\omega^4(\frac{a}{\gamma})^4 - \omega^2\frac{a^2}{\gamma^2}[a^2\sum_{i,j}H_1^iH_2^i + c_1a\sum_{i,j}H_2^i + c_2a\sum_{i,j}H_1^i + 2c_1c_2 + 2c_0c_2] + D = 0 \tag{2.70a}$$

$$D = [a^2H_2^AH_2^B + c_2a\sum_{i,j}H_2^i][a^2H_1^AH_1^B + c_1a\sum_{i,j}H_1^i + c_1^2 - c_0^2] \tag{2.70b}$$

$$H_1^i = H\cos\varphi_i - H_{K,eff,i} + H_{K,i}\cos^2(\varphi_i - \delta_i) \tag{2.70c}$$

$$H_2^i = H\cos\varphi_i + H_{K,i}\cos 2(\varphi_i - \delta_i) \tag{2.70d}$$

$$c_0 = J_1 + 2J_2\cos\alpha \quad , c_1 = J_1\cos\alpha + 2J_2cos^2\alpha \quad , c_2 = J_1\cos\alpha + 2J_2\cos(2\alpha) \tag{2.70e}$$

$$H_{K,eff,i} = 2K_{u,eff,i}/M_i \quad \text{with} \quad K_{u,eff,i} = K_{u,i,o} - 2\pi M_i^2 \tag{2.70f}$$

$$H_{K,i} = 2K_{u,i}/M_i \quad \text{and} \quad a = M \times d \tag{2.70g}$$

where i indicates layers A or B. The φ_i denotes the magnetization angle relative to the applied magnetic field **H**. Furthermore, α is the angle between the magnetizations in layer A and B. Above a critical magnetic field, the magnetization in both layers is aligned parallel, while below it the magnetization orientation in each individual layer depends on the absolute value of the coupling

and its sign. Moreover, $K_{u,i,o}$ indicates the OOP anisotropy constant. It is zero for our sample.

If there is no coupling between the layers, $c_{0,1,2}$ are all zero and the resonance frequency for each layer is calculated individually. The double layer structure even without coupling between layers has two peaks or one degenerate peak in its FMR measurement. For the full film sample with $\mu_0 M_s$ = 1.48 T and uniaxial anisotropy K_u = 700 J/m^3, resonance frequencies of uncoupled layers in the saturation magnetization (H = 3.2 kA/m) are ±2.482 and ±2.481 GHz and in the remanence magnetization has degenerate frequency at ±1.1743 GHz and ± 1.1738, where OOP magnetization is neglected. This result is independent of the layers' thickness.

If a small bilinear antiferromagnetic coupling between layers equal to J_1 = -10 μJ/m^2 is assumed, f_r=± 2.48 and ± 2.32 GHz in saturation (3.2 kA/m) and f_r=±1.17 and ± 0.76 GHz in remanent magnetization are anticipated. When the coupling between layers is taken into account , there should be two resonance frequencies in FMR corresponding to optical and acoustical modes.

To validate this method of calculation, we evaluated them with experimentally measured data. The induced anisotropy is higher than in above examples and is considered to be K_u = 1300 J/m^3, in saturation (3.2 kA/m) calculation results ± 2.7 and ± 2.6 GHz and from measurement 2.8 GHz is obtained which is in agreement. In antiferromagnetic coupling and at the higher fields, optical mode frequencies are lower than acoustic mode, in contrast to ferromagnetic coupling. In addition, for such coupling between layers, the saturation field increases by the coupling strength enhancement [46]. The critical field is calculated as:

$$H_{crit} = -(J_1 - 2J_2)[\frac{1}{d_A M_{s,A}} - \frac{1}{d_B M_{s,B}}] - H_K \tag{2.71}$$

Therefore, for our sample with very small bilinear coupling J_1 = -10 μJ/m^2, in absence of biquadratic one, H_{crit} is equal to the anisotropy field, 960 A/m [46].

The resonance frequencies of laminated materials can be found through a macrospin calculation. In this method the exchange energy is defined the same as in equation (2.69), where e_A and e_B consist of other energy distributions, Zeeman, uniaxial anisotropy and demagnetizing energy for every layer. Then, the equilibrium state for every applied field is calculated numerically. Furthermore, the dynamic response of this static state to an alternative magnetic field is calculated by finding numerical solutions of the LLG equation (2.45b). The effective field in equation (2.45b) comprises the applied magnetic field, anisotropy and demagnetizing field in addition to

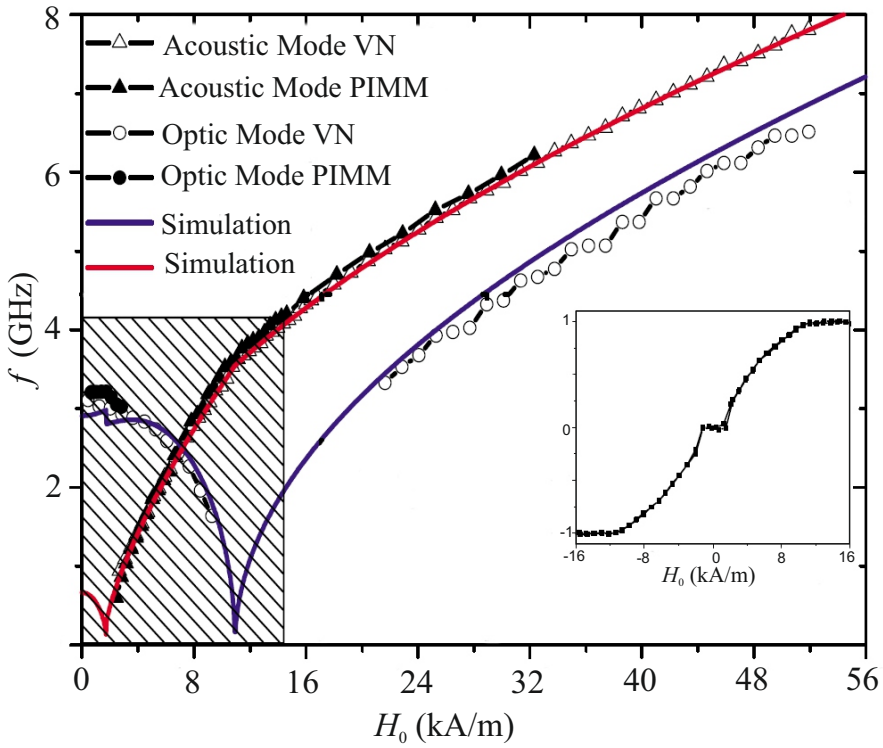

Figure 2.24: The measured resonance frequencies via two methods, VNA and PIMM are compared with calculated data for Si/Ta/NiFe (30 nm)/Ru (1.48 nm)/ NiFe (30 nm). There is antiferromagnetic coupling between layers which is illustrated by the normalized hysteresis in the inset. The additional simulation result shown by the red curve are based on the discussion from Ref.[46]. Adopted from [47].

the exchange fields which are defined as follows [47]:

$$H_{J_1,i} = \frac{J_1}{\mu_0 M_s d_i}\mathbf{m}_j(t) \tag{2.72a}$$

$$H_{J_2,i} = \frac{2J_2}{\mu_0 M_s d_i}\begin{bmatrix} m_{i,x}m_{j,x}^2 + m_{j,x}(m_{i,y}m_{j,y} + m_{i,z}m_{j,z}) \\ m_{i,y}m_{j,y}^2 + m_{j,y}(m_{i,x}m_{j,y} + m_{i,z}m_{j,z}) \\ m_{i,z}m_{j,z}^2 + m_{j,z}(m_{i,y}m_{j,y} + m_{i,x}m_{j,x}) \end{bmatrix} \tag{2.72b}$$

where $i \neq j$ denote the layers A and B. Furthermore, $m_{i,j,k}$ indicates normalized components of magnetization. The simulated results are summarized in Fig. (2.24) for two layers NiFe with each 30 nm thickness. These are separated by 1.48 nm thick layer of Ru as a non-magnetic spacer which provides antiferromagnetic coupling between the two ferromagnetic layers. In this case, the bilinear coupling between the layers is J_1 = -140 μ J/m^2 and the biquadratic coupling is J_2 = -15 μ J/m^2. In Fig. (2.24), two different methods of FMR measurements, the vector network analyser FMR (VNA) and pulsed inductive microwave magnetometer (PIMM), are compared. It can be seen that in the low field regime the optic mode is higher than the acoustic mode and this is reversed in higher fields. Moreover, the acoustic mode at fields lower than 2 kA/m is not detectable by PIMM method, however, VNA measurement shows the results in agreement with simulation [47].

Moreover, it can be seen from Fig. (2.24) at low fields the optical mode frequencies and for higher fields the acoustical mode has higher frequencies. This is explained with the calculated relation between these modes and the magnetization direction in the layers[124], [125]:

$$(\frac{\omega}{\gamma})^2_{Optic} - (\frac{\omega}{\gamma})^2_{Acoustic} = -\frac{1}{M_s^2}(2e_{\varphi_A\varphi_B}e_{\theta_A\theta_B}) \tag{2.73a}$$

$$e_{\varphi_A\varphi_B} = -J_1\cos(\varphi_A - \varphi_B) \tag{2.73b}$$

where $\varphi_{A,B}$ indicates the IP angle of magnetization in layer A and B. In addition, $\theta_{A,B}$ refer to the magnetization angle relative to the normal of the sample surface and is always positive. In the low field regime, the magnetization in antiferromagnetically coupled layers is aligned antiparallel and so $e_{\varphi_A\,\varphi_B}$ based on equation (2.73b) is negative. Therefore, from equation (2.73a) the optical mode is higher in comparison to the acoustic mode. On the other hand, by increasing the static field above the critical field, the angle between individual layer magnetization is less than $\pi/2$ and thus a positive $e_{\varphi_A\,\varphi_B}$ leads to the higher frequency of the acoustic mode.

Chapter 3

Measurement Techniques and Materials

To measure the ferromagnetic resonance FMR, there are two main classes. The first one is the conventional FMR utilizing a resonant cavity. The sample inside the cavity is irradiated by an excitation field in the microwave range. In this method, the excitation frequency is fixed while the bias field changes within a range of fields [126]. These cavity-based systems are useful methods for instance in electron spin resonance spectrometers, since it is possible to apply high frequencies up to 200 GHz [127]. In addition, FMR in single or multilayer structures [128] at high bias fields in the range of kOe is measured. But to measure the FMR phenomenon in thin films, where a low static field is needed, the second category is highly preferred.

The second group of FMR techniques consists of striplines and coplanar waveguides (CPW) [126]. Through stripline, the static field changes at a fixed microwave frequency while via Vector Network Analyser (VNA) a fixed magnetic field (fixed frequency) is applied when the frequency (bias field) varies in a range.

In this work, a Pulsed Inductive Magnetometer, PIMM, is used to measure the dynamic features of thin film. This method is explained in detail in the following section and in the end it is evaluated in comparison with other methods.

3.1 Pulsed Inductive Microwave Magnetometry

3.1.1 Theoretical Explanation

The magnetic flux,Φ, for a loop in a magnetic flux density, $\mathbf{B}$, defines as

$$\Phi = \oint_s \mathbf{B} \cdot d\mathbf{S} \quad \text{and } S = \text{The surface confined by loop} \tag{3.1}$$

where $d\mathbf{S}$ indicates the surface vector normal to each element of loop surface and the integral should be calculated all over the loop surface. Based on Faraday's law of induction, every time-dependent variation of magnetic flux density in this loop leads inducing a voltage V in the loop. However, this inductive voltage is the so called electromotive force, emf.

$$V = -\frac{\mathrm{d}\Phi}{\mathrm{d}t} = -\frac{\mathrm{d}}{\mathrm{d}t}\oint_s \mathbf{B}\cdot\mathbf{S} \tag{3.2a}$$

$$\frac{\mathrm{d}\Phi}{\mathrm{d}t} = -\frac{\mathrm{d}\mathbf{B}}{\mathrm{d}t}\cdot\mathbf{S} - \mathbf{B}\cdot\frac{\mathrm{d}\mathbf{S}}{\mathrm{d}t} \tag{3.2b}$$

$$\frac{d\Phi}{\mathrm{d}t} = -\frac{\mathrm{d}B}{\mathrm{d}t}S\cos(\theta) - B\frac{\mathrm{d}S}{\mathrm{d}t}\cos(\theta) - BS\sin(\theta)\frac{\mathrm{d}\theta}{\mathrm{d}t} \tag{3.2c}$$

The equation (3.2a) shows the Faraday Law in general form [57]. The negative sign comes from Lenz's law. Based on this, inductive voltage (and its corresponding current and magnetic field) opposes its own source [129]. In addition, in equation (3.2c), θ represents the angle between the magnetic flux density $\mathbf{B}$ and the normal vector on the surface $\mathbf{S}$ [130]. The second and third term in equation (3.2c) denote , respectively, that the induced voltage comes from the loop surface variation by time or the loop's angle rotation (for example loop motion with a linear or angular velocity). Therefore, on the assumption of a fixed loop, the mentioned terms are ignored. Therefore, the induced voltage originates only from any time-dependent variation of magnetic flux density or its equivalent material magnetization. Via reciprocity, the induced voltage measurement is a method to find out the magnetization variation inside a sample.

To measure the inductive voltage, the magnetic sample is placed on a coplanar waveguide, which carries an alternating magnetic field to excite the magnetic sample. Then it picks up a voltage as sample dynamic response $\mathrm{d}M/\mathrm{d}t$. We consider $\mathrm{d}M/\mathrm{d}t$ provides information about the permeability spectrum and so the resonance frequency.

This was a summarized explanation of PIMM method. Subsequently, it is discussed in elaborate detail.

To start, the equation (3.1) is written in another form for a detected flux originating from a magnetic substance on top of a CPW with thickness δ, length l and width w in the center of a CPW and far from the edges [131]:

$$\begin{aligned} \Phi &= \frac{\mu_0}{I}\int\int\int_{\text{sample}} H_y(I;x,y,z)M_x(x,y,z)\mathrm{d}x\mathrm{d}y\mathrm{d}z \\ \text{with}\quad H_x(I;x,y) &= \frac{1}{\pi}\frac{I}{2w}[\arctan(\frac{(w/2)+x}{y}) + \arctan(\frac{(w/2)-x}{y})] \end{aligned} \tag{3.3}$$

where H_y depends on the CPW dimension. It is the component of a magnetic field perpendic-

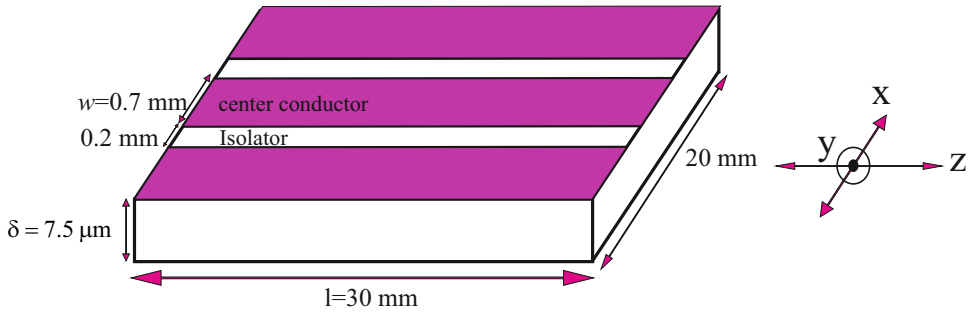

Figure 3.1: The CPW geometry and dimension are specified. The typical values for a CPW dimension used for one of our experimental measurement are shown . In addition Cartesian coordination indicates x and y as IP and z as OOP axis.

ular to the waveguide's longer dimension. The geometry and coordination for the CPW is shown in Fig. (3.1). By substitution of above equations in equation (3.2a), the pick up voltage is obtained:

$$V = \mathrm{g}(\delta, l, w, Z_0, R_{dc}, H_x)\frac{\mathrm{d}M_x}{\mathrm{d}t} \tag{3.4}$$

where g is a time-dependent function of the CPW geometry and its characteristic impedance Z_0. Furthermore, R_{dc} represents dc resistance of the CPW. Finally, by integrating voltage over time, the magnetization component in direction of the pick up is concluded [132]

$$M_x = \frac{1}{\mathrm{g}(\delta, l, w, Z_0, R_{dc}, H_x)}\int V\,dt \tag{3.5}$$

In the subsequent section, it is shown how $\mathrm{d}M_x/\mathrm{d}t$, the permeability spectrum and the resonance frequency for different static bias fields are extracted, when the excitation field in form of a step function through the CPW is applied to the magnetic substance.

The step function is characterized in Fig. (3.2). The rise time is the interval to increase the excitation field $\mathbf{h}(t)$ amplitude from 10% to 90%. The typical value used in our simulation is t_{rise} = 60 ps and then the flat part continues for some ns. In our measurements, the excitation field is applied perpendicular to H_0 and so they do not have any parallel component. However, in Fig. (3.2) it is supposed that H_0 has a small component in direction of h(t) to have a general discussion. This does not make a difference as far as it is very small in comparison with the other component of H_0. The rise time (time-domain) is correlated to the bandwidth (frequency-domain), f_b:

$$t_{rise} = \frac{0.35}{\triangle f_b} \tag{3.6}$$

For instance, for a rise time equal to 60 ps, the bandwidth is 5.8 GHz. It means that the dynamic

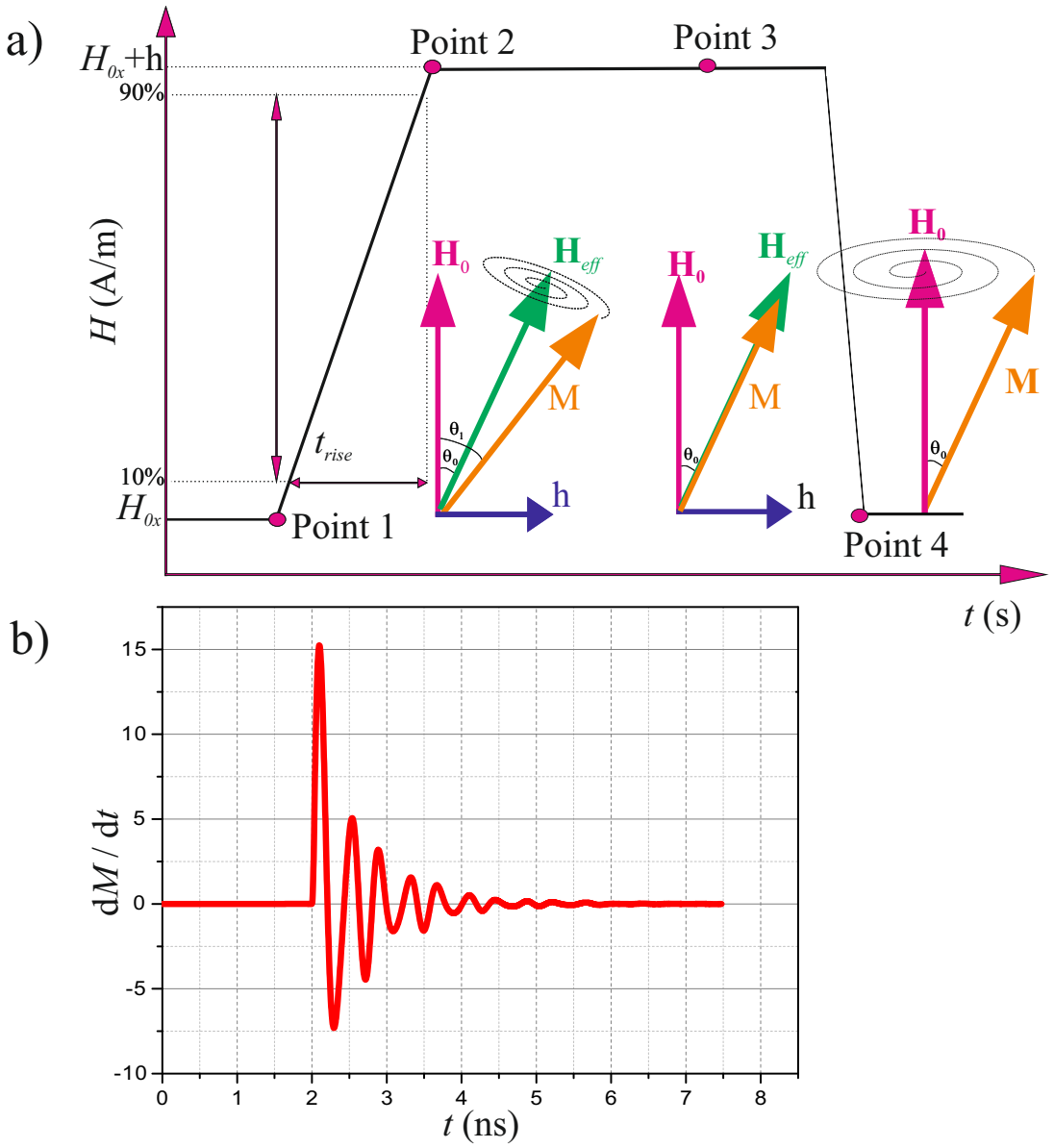

Figure 3.2: a) The step function with amplitude h is shown. To make the rise time clear in this figure , slope of step from point 1 to 2 is underestimated significantly. In addition, relative directions of M, H_{eff} and h are shown as diagram. Partially adopted from [133]. b) The underdamped oscillation of $\mathrm{d}M/\mathrm{d}t$ in response to step excitation is represented.

magnetization responses in this frequency range are detectable. Before excitation, the magnetization is parallel to the static field (effective static field). By applying the excitation step, from point 1 in Fig. (3.2) to point 2, the effective field deviates by the angle θ_0 as the result of a superposition between H_0 and h. Therefore, the magnetization follows this change and deviates by the angle θ_1. It precesses around H_{eff} based on the LL equation in equation (2.33), and because of the damping effect in the LLG equation (2.45) damps on a new effective field as shown in Fig. (3.2 a) [134]. In the end, the step function is removed and the magnetization returns to its initial equilibrium in point 4 [133]. The upper part of the step function between point 2 and 4 should be long enough to prevent interference between the first and second precession of magnetization in the beginning and at the end of excitation [135], [136].

The relevant oscillation is plotted in Fig. (3.2.b) for an exemplary simulated sample, single layer $Co_{40}Fe_{40}B_{20}$ with 50 nm thickness while the static field 4 kA/m is applied perpendicular to the 4 A/m excitation field. As it can be seen the signal is zero before point 1 (indicated in Fig. (3.2.a)), and from point 2 to 3 it shows underdamped oscillation behaviour and then again reaches its equilibrium in zero. The time-dependency of the magnetization angle by applying a step function is formulated as:

$$\Theta(t) = \theta_0 + \beta_0 \sin(\omega t + \theta) e^{-t/\tau} \tag{3.7}$$

where as mentioned above and illustrated in Fig. (3.2 a), the angle θ_0 is the new equilibrium of magnetization after applying an excitation field, β_0 is the amplitude of magnetization rotation and θ defines the phase difference that is considered to be $\pi/2$ and so in comparison to Fig. (3.2.a) $\Theta(t=0) = \theta_1$. Furthermore, τ indicates the relaxation time and depends on the material's damping parameter, and finally $\omega = 2\pi f$ is the angular frequency. The CPW picks up one magnetization component M_x, which is perpendicular to the waveguide length and it is related to $\Theta(t)$ as $M_x = M_s \sin[\Theta(t)]$. This component is calculated analytically by expansion of sin function and then replacing time-dependent cos and sin with their equivalent in the Bessel function form:

$$\begin{aligned} &M_x = M_s \sin[\Theta(t)] = M_s \sin[\theta_0 + \underbrace{\theta_1 \sin(\omega t + \theta) e^{(-t/\tau)}}_{\beta})] = M_s[\sin(\theta_0)\cos(\beta) + \cos(\theta_0)\sin(\beta)] \\ &\mathrm{A}(u) = \sum_n \frac{\mathrm{d}^n \mathrm{A}}{\mathrm{d}u^n} \frac{1}{n!} \quad \text{and} \quad u(t) = \text{ a function with time dependency} \end{aligned} \tag{3.8}$$

where A is the cos function for even value of n = 0,2,4,... or the sin function for odd value of n = 1,3,5,... If we assume $\beta_0 e^{(-t/\tau)} \ll 1$ and the magnetization in analogy with the mechanical oscillator is an underdamped oscillator ($\omega\tau \gg 1$), we can ignore higher order than 3 in β_0 and $d^{(-t/\tau)}$ and we obtain the following equation

$$\frac{\mathrm{d}M_x}{\mathrm{d}t} = \omega M_s [\cos(\theta_0)\beta_0 e^{-t/\tau} cos(\omega t) + \underbrace{\sin(\theta_0)\frac{\beta_0^2}{2} e^{-2t/\tau} \sin(2\omega t)}_{\text{Second Harmonic Distortion}} + \underbrace{\cos(\theta_0)\frac{\beta_0^3}{8} e^{-3t/\tau} \cos(3\omega t)}_{\text{Third Harmonic Distortion}}] \tag{3.9}$$

This analytical solution makes it possible to obtain τ and so the damping parameter in addition to the fundamental frequency, $f = \omega/2\pi$, by fitting equation (3.9) to measured results after applying the step function to the sample [132].

In equation (3.9), the third harmonic distortion is always very small as it is third order of both angle β_0 and exponential function of the damping parameter τ. But the second harmonic distortion can be significantly large even in comparison with the first term, provided that the excitation

field is able to rotate the magnetization normal to H_0. This leads to $\theta_0 = \pi/2$.

On the other hand, if the static field is applied parallel to the easy axis and the excitation field is small in comparison to H_{eff}, the angle θ_0 will also be small too and therefore, the second harmonic distortion is ignorable. In this situation, fast Fourier transformation (FFT) is used instead, since the fitting method mentioned above and FFT have the same results [132].

The FFT method transfers the obtained signal $\mathrm{d}M/\mathrm{d}t$ in the time-domain to its counterpart in the frequency-domain $\mu(\omega)$. To be more precise about the experimentally measured data, the discrete Fourier transformation, DFT, is utilized. The resolution in the f-domain should be small enough to detect all of involving resonance frequencies. This resolution, Δf, depends on a number of points (data points) forming a t-domain signal. Therefore, one way to improve the resolution is adding more point with zero value (new equilibrium after applying excitation field) to the end of signal. This method is called zero-padding and is mathematically allowed because as it can be seen in Fig. (3.2 b), the dynamic response of magnetization damps to zero value at the end of the signal. After applying DFT, the permeability spectrum is extracted in the f-domain, similar to what was explained by Fig. (2.14). As it was mentioned before, the imaginary part's peak or the real part's zero-crossing frequency indicates the resonance frequency, f_r.

3.1.2 Experimental Measurements

The experimental set up is indicated in Fig. (3.3). There are two coils providing a static magnetic field in two IP directions normal to each other, named as x and y direction. The coils are connected to different sources, which are able to feed the coils by applying a current. A digital sampling oscilloscope, Lecroy Wave Expert 100 H, supplies voltage into the system . It has two time domain reflectometry modules, TDR modules. Its bandwidth is 20 GHz and it is able to supply a step pulse with a rise time as fast as 50 ps. The maximum amplitude of the pulse by this oscilloscope is 260 mV.

The waveguide converts voltage to excitation magnetic field. In addition, it acts as a magnetic sensor and picks up the dynamic response of magnetization from the sample [137]. As it can be seen in Fig. (3.3), the output signal moves throughout the coplanar waveguide, CPW. Afterwards, the response comes to the oscilloscope via another cable. The advantage of this method is that output and input voltage are produced and measured by the same source, the oscilloscope, and so they have same clock. Therefore, it prevents jitter in the time domain. Even a 100 fs difference between the pulses leads to tens of millivolts of error when two pulses, input and transmitted one, are subtracted [137]. This is as large as the measured signal which makes clear importance of

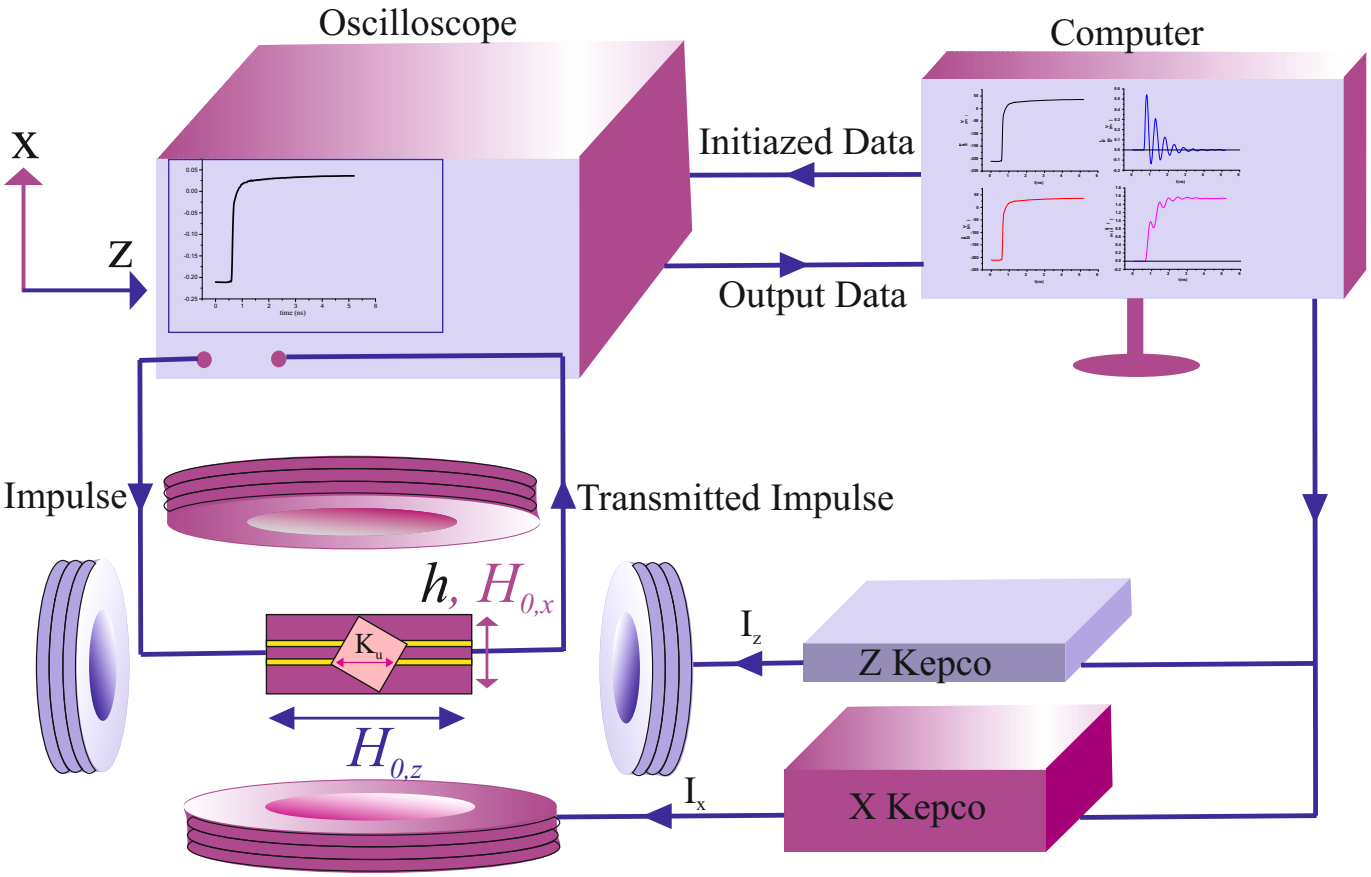

Figure 3.3: The PIMM set up is illustrated. Generally, there are two static fields perpendicular together in $\hat{\mathbf{x}}$ and $\hat{\mathbf{z}}$ direction. The alternative magnetic field is applied via impulse function from the oscilloscope. The magnetic response is transmitted throughout the waveguide and comes back to the oscilloscope to measure. The sample was placed on the waveguide in the way that the easy axis of magnetization is in $\hat{\mathbf{z}}$. We call it easy axis measurement while the anisotropy field axis can be rotated by 90 degree, which is called hard axis measurement. To make figure less full and emphasise on more the important parts of the set up, the wires connecting two coils (the two coils forming a Helmholtz coil are indicated by the same colour) are not drawn.

removing such jitters.

The CPW dimensions determine the magnetic field produced around the waveguide. For instance, we consider the waveguide center conductor width 0.7 mm as introduced in Fig. (3.1). The current in the CPW is (V_{osc}/Z_{CPW} =) 5.2 mA, when the characteristic impedance of the CPW is close to 50 Ω. Therefore, the excitation field's amplitude is about 0.05 Oe:

$$h_x \sim \frac{I}{2w} = 3.7 \text{ A/m} = 0.046 \text{ Oe} \tag{3.10}$$

The above equation is written under the assumption that the CPW's width is much larger in comparison to its thickness.

The sample is placed on the CPW in the way that its magnetic surface touches the CPW conductor. The sample dimension is defined by l and d as length and thickness. The pick up magnetic flux introduced in equation (3.1) is in direct relation to the magnetization component perpendicular to the CPW length [138]. Thus the pick up voltage of a magnetic sample is calculated by Faraday Law in equation (3.2):

$$V = \frac{\mathrm{d}\varphi}{\mathrm{d}t} = \frac{\mu_0 l d}{2}\frac{\mathrm{d}M_x}{\mathrm{d}t} = \frac{\mu_0 l d}{2} i\omega M_x = \frac{\mu_0 l d}{2} i\omega \frac{h_x}{H_{eff}} M_s \tag{3.11}$$

It is assumed that the samples are large enough to cover the central conductor completely.

According to the above equation, for a typical sample's dimension l = 0.01 m, d = 50 nm and the magnetization $\mu_0 M_s$ = 1.48 T, when the effective field is equal to the anisotropy plus bias field, it is considered $H_{eff} = H_K + H_0$=0.946+4 kA/m , the detected voltage in the PIMM measurement is approximately $4.76 \times 10^{-13} \times \omega$ V. This corresponds to the highest amplitude of the output signal as the higher the bias field, the higher the signal amplitude. Therefore, the detected signal amplitude is in the range of 1 μV to a few hundred μV.

3.1.3 Comparison with Other Methods

The experiments done by Stripline, VNA, and PIMM in order to find the FMR linewidth in Permalloy show that these methods produce consistent results [139].

Furthermore, in evaluation of the resonance frequencies, there is a report stating great agreement between TR-MOKE, VNA-FMR, conventional FMR and PIMM for Fe films [140]. Among these methods, it is shown that the effective damping parameter measured by PIMM can produce larger error if the time jitter problem is not fixed, while the obtained results by TR-MOKE denotes 20% lower values than other methods. The possible reason is the limitation of the probed area in TR-

MOKE which is around 1 μ m^2 (in comparison with other methods around 0.4 – 2 mm^2) and so the magnetic properties stay more homogeneous compared to other methods [140].

On the other hand, in another study to detect the optical mode and to distinguish it from the acoustical mode, for double layer NiFe samples in higher fields, the excitation field and the bias field are applied parallel rather than as usual perpendicular to the elongation. The VNA-FMR method is more efficient than PIMM and its detected signal is stronger. The comparison is illustrated in Fig. (2.24) for antiferromagnetic coupling between layers. The results for the ferromagnetic coupling can be found in [47].

Last but not least, it should be mentioned that to measure really high frequency band, the PIMM measurement has some restrictions depending on the sample's substrate. The substrate's material affects the rise time in the step function which is correlated to the frequency band via equation (3.6). This limitation should be considered for instance when detecting perpendicular standing spin waves, PSSWs, in higher order [47]. However, this restriction does not affect the measurements reported in this work, since the rise time equal to 60 ps provides an approximately 6 GHz frequency range which is high enough to detect the samples' dynamic responses.

3.2 Magneto Optical Kerr Effect (MOKE)

3.2.1 Theoretical Explanation

In 1876, John Kerr discovered out that polarity of a linearly polarized light changes to an elliptically one after its reflection from a magnetised surface [141]. This is the principle used in magneto-optical Kerr effect (MOKE) microscopes. The light polarity's variation is calculated by an angle called Kerr rotation which is the rotation of a polarization plane. Experimentally the intensity of the MOKE effect I_k is measured which defines as

$$I_k = I_0 + Qm_x \tag{3.12}$$

where I_0 and m_x show the sample's reflectivity constant and magnetization component, respectively [142], [143]. In addition, Q indicates the linear MO constant and will be introduced in the detail in next page. While light behaviour is considered after transmission from almost transparent magnetized surface (like Garnets), the similar effect, called Faraday effect, plays a role. These two effects comprise odd-order of magnetization. However, just first order magnetization is usually important since higher orders of magnetization are much smaller and difficult to measure.

To explain the MOKE effect, the ordinary refractive index should be substituted by a tensor. For the ferromagnetic materials, their dielectric permittivity in three dimensions is defined as [144]:

$$\mathbf{D} = \hat{\varepsilon}\mathbf{E}$$

$$\mathbf{D} = \left(\varepsilon \underbrace{\begin{bmatrix} 1 & -iQm_z & iQm_y \\ iQm_z & 1 & -iQm_x \\ -iQm_y & iQm_x & 1 \end{bmatrix}}_{\text{Linear effect}} + \underbrace{\begin{bmatrix} B_1 m_x^2 & B_2 m_x m_y & B_2 m_x m_z \\ B_2 m_x m_y & B_1 m_y^2 & B_2 m_y m_z \\ B_2 m_x m_z & B_2 m_y m_z & B_1 m_z^2 \end{bmatrix}}_{\text{Quadratic effect}} \right) \begin{bmatrix} E_x \\ E_y \\ E_z \end{bmatrix} \tag{3.13}$$

where m_i, E_i indicate directional cosines of magnetization and electrical field, respectively. In addition, the complex parameter Q, introduced by Woldemar Voigt, makes a connection between magnetization and gyration vector $\mathbf{g}$ as $\mathbf{g} = Q\mathbf{m}$. If $\mathbf{g}$ and so Q are real, the first tensor in equation (3.13) is Hermitian ($\epsilon_{i,j} = \epsilon_{j,i}$). This means that the ferromagnetic material is lossless. For such materials the MO effect can not be measured as the MO signal intensity depends on the magnetization magnitude and is independent of the applied field [145]. In the above equation, the second term consisting of B_i constant indicates the quadratic MO effect known as the Voigt effect. It is even in magnetization and usually small. Therefore, it will not be considered in detail here and for interested readers these references are suggested [146, 147, 148, 149, 150, 151].

3.2.1.1 Origin of Light Ellipticity in Magneto-optic Kerr Effect

Consider Maxwell equations (2.54 a) with $\mathbf{J} = 0$ and its counterpart for electrical field ($\nabla \times \mathbf{E} = \frac{-\partial \mathbf{B}}{\partial t}$). In these equations, spatial derivative ∇ and time derivative $\dfrac{\partial}{\partial t}$ are replaced by wave vector $\mathbf{k}$ and angular frequency $i\omega$, respectively, for a plane wave 's propagation. Then the relations, $\varepsilon\mu = c^2$ and $\omega/c = n$ are applied where n is the refractive index in the propagation direction. We obtain:

$$\mathbf{D} = n^2[\mathbf{E} - \mathbf{k}(\mathbf{k}\cdot\mathbf{E})] = n^2\mathbf{E} \Longrightarrow \varepsilon \begin{bmatrix} 1 & 0 & 0 \\ 0 & 1 & -iQm_x \\ 0 & iQm_x & 1 \end{bmatrix} \mathbf{E} = n^2\mathbf{E} \tag{3.14}$$

where $\mathbf{k}\cdot\mathbf{E} = 0$ since the propagation axis is normal to the electrical field. In addition, the y axis is assumed to be OOP axis. To simplify, a situation is considered where the magnetization is IP and along $\hat{\mathbf{x}}$ and two other components are zero. Therefore, just two off-diagonal components remain.

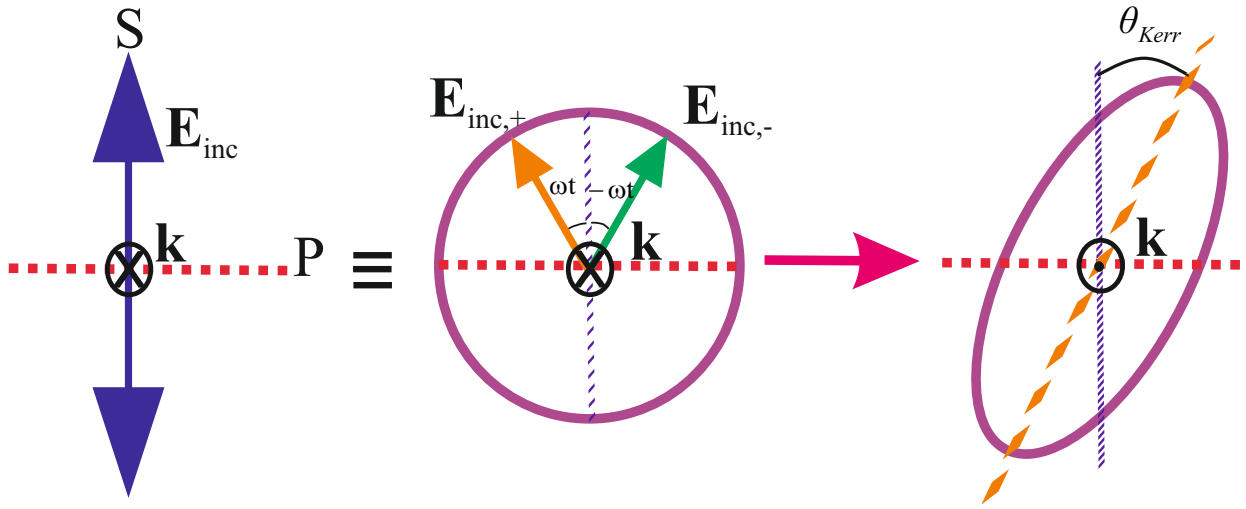

Figure 3.4: The S and P axis indicate S and P polarization while **k** shows the wave vector. In addition, **E** shows the electrical field. To define them, it is supposed that the plane of incidence is perpendicular to the page and their cross section is P axis. The linearly polarized light is equivalent to two circularly polarized ones $E_{inc,\pm}$ in opposite directions with angular momentum $\pm\omega$. After reflection, the major axis of ellipsoid is tilted by θ_{Kerr} .

By solving the above equation, it is obtained:

$$\begin{aligned} &(n^2-\varepsilon)^2+(iQm_x\varepsilon)^2=0 \Longrightarrow n_+^2=\varepsilon(1+Qm_x) \qquad \text{and} \qquad n_-^2=\varepsilon(1-Qm_x) \\ &E_y^+=iE_z^+ \qquad \text{and} \qquad E_y^-=-iE_z^- \end{aligned} \tag{3.15}$$

The first part indicates that the medium is birefringent and so the reflection coefficients $R_\pm$, which depend on the $(n_\pm)$ following equation and correspond to the incidence light with an angular momentum $\pm\omega$, are different:

$$R_\pm=\frac{1-n_\pm}{1+n_\pm} \tag{3.16}$$

The second part of equation (3.15) shows clockwise (right) and anti-clockwise (left) circularly polarized light with + and − signs, respectively.

The linearly polarized incidence light E_{inc} is composed of two circularly polarized lights with the same amplitude and frequency but in the opposite directions as it is illustrated in Fig. (3.4). After reflection, the amplitude along p and s axis is not equal any more and the reflected light is elliptically polarized. In addition, the ellipsoid axe are deviated from the s axis by an angle θ which is called Kerr rotation angle [145], which can be + or −. The mathematical explanation of this effect

MO Effect	m-component	sample surface	incidence Plane
Polar	m_y	$\perp$	$\parallel$
Longitudinal (p-polarization)	m_x	$\parallel$	$\parallel$
Longitudinal (s-polarization)	m_z	$\parallel$	$\perp$

Table 3.1: The orientation of sample surface and incidence plane relative to magnetization are shown. The same coordinate as Fig. (2.18) has been used where m_y is OOP.

is as follow:

$$E_{inc} = \begin{bmatrix} \sin(\omega t) \\ \cos(\omega t) \end{bmatrix} + \begin{bmatrix} \sin(-\omega t) \\ \cos(\omega t) \end{bmatrix} \longrightarrow E_{ref} = R_+ \begin{bmatrix} \sin(\omega t) \\ \cos(\omega t) \end{bmatrix} + R_- \begin{bmatrix} \sin(-\omega t) \\ \cos(\omega t) \end{bmatrix} \tag{3.17}$$
$$\theta_{Kerr} = \frac{R_- - R_-}{R_+ - R_-} = \frac{n_- - n_+}{1 - n_+ n_-}$$

where $n_\pm$ depends directly on the specimen's magnetization through equation (3.16) and therefore higher magnetization of specimen reinforces the Kerr angle and the measured MOKE signal.

3.2.2 Experimental Measurement

In order to determine the components of magnetization, three types of MO effect, longitudinal, transverse and polar MO effect are used. They are defined based on the different orientation between the magnetization vector **m**, electrical field **E** and wave vector **k** of incidence light. In the polar MO effect, the OOP components of the magnetization vector is measured when the plane of incidence is parallel to the magnetization and normal to the sample surface. On the other hand, IP components of magnetization are obtained while plane of incidence light is parallel or perpendicular to the magnetization for the longitudinal or transverse magnetization element, respectively. This information is summarized in the table (3.1) and illustrated in Fig. (3.5). In order to clarify this an example (with Landau configuration) is used . There are different magnetization in each region elongated in the $\hat{\mathbf{x}}$ or $\hat{\mathbf{z}}$ axis. However, in general a magnetic domain might have **m** with non-zero elements. The orange-arrows indicate the sensitivity axis which is defined by plane of incidence and as the name suggests makes measurement sensitive to that axis. Therefore, areas with magnetization along the sensitivity axis either have the highest (white) or the lowest intensity (black) of signal. The areas, whose magnetization is perpendicular, and so do not have any amplitude in the sensitivity axis naturally define zero level of contrast and are shown as grey in magneto-optically measured data. The results are depicted in Fig. (3.5) as well.

The schematic diagram of a MOKE microscope is depicted in Fig. (3.6). The light source is either a pulsed Laser or a high power light eliminating diode, HP LED [152]. The multiple LEDs are used to take simultaneously images in different sensitivities. The images from multiple LEDs are

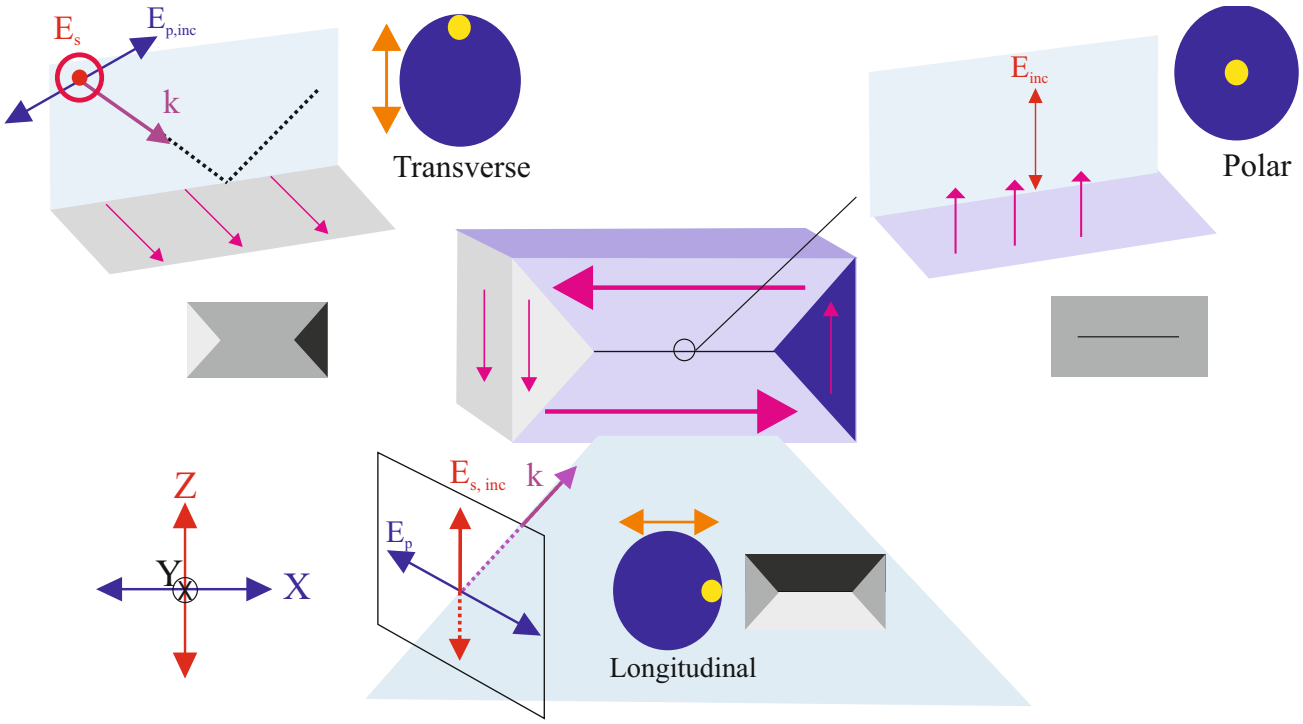

Figure 3.5: The three different MO effects with their corresponding incidence plane are shown. In addition, the position of the fiber light source in the back focal plane (dark blue) in MOKE microscope are illustrated by a yellow circle while the sensitivity axis (in the plane of incidence) is shown by orange two-head arrows. Furthermore, the taken images by MOKE microscope are displayed in grey scale. The middle grey shows the background colour (zero contrast in normalized contrast) while white and black regions have the highest and the lowest contrast level, respectively.

either decomposed through an image splitter [153] or captured by two synchronized cameras. In the late method, light passes the observation path split via dichroitic mirrors. The transferred and reflected light reaches different cameras. To be sure that the image in both cameras is captured at the exact same time, they are synchronized by an external trigger TTL signal [154].

In order to illuminate the wide field of view on the specimen, the Köhler method is used. Through this method, the light source is defocused to obtain even and homogeneous illumination of the sample surface.

In the wide field MOKE, there is a separated path of illumination and observation as it can be seen in Fig. (3.6). The two main parts of the microscope as discussed in the theoretical explanation section are the polarizer in the illumination path in addition to the analyzer to adjust light ellipticity in the observation path. The first lens collects light from the source and is adjusted in the way that LEDs and aperture plane, AP, are in its $2f_L$, where f indicates focal length. In addition, this aperture plane and field diaphragm are on two sides and in the focal length from the condenser lens. Therefore, the light emitted by LEDs after diverges into a field diaphragm, is converged by condenser and reaches the polarizer. To assure polarity of light a quarter-wave plate (converts circularly polarized wave to linear one and vice versa) can be inserted immediately after the polarizer. The third lens in the illumination part of a MOKE microscope is a tube lens through what

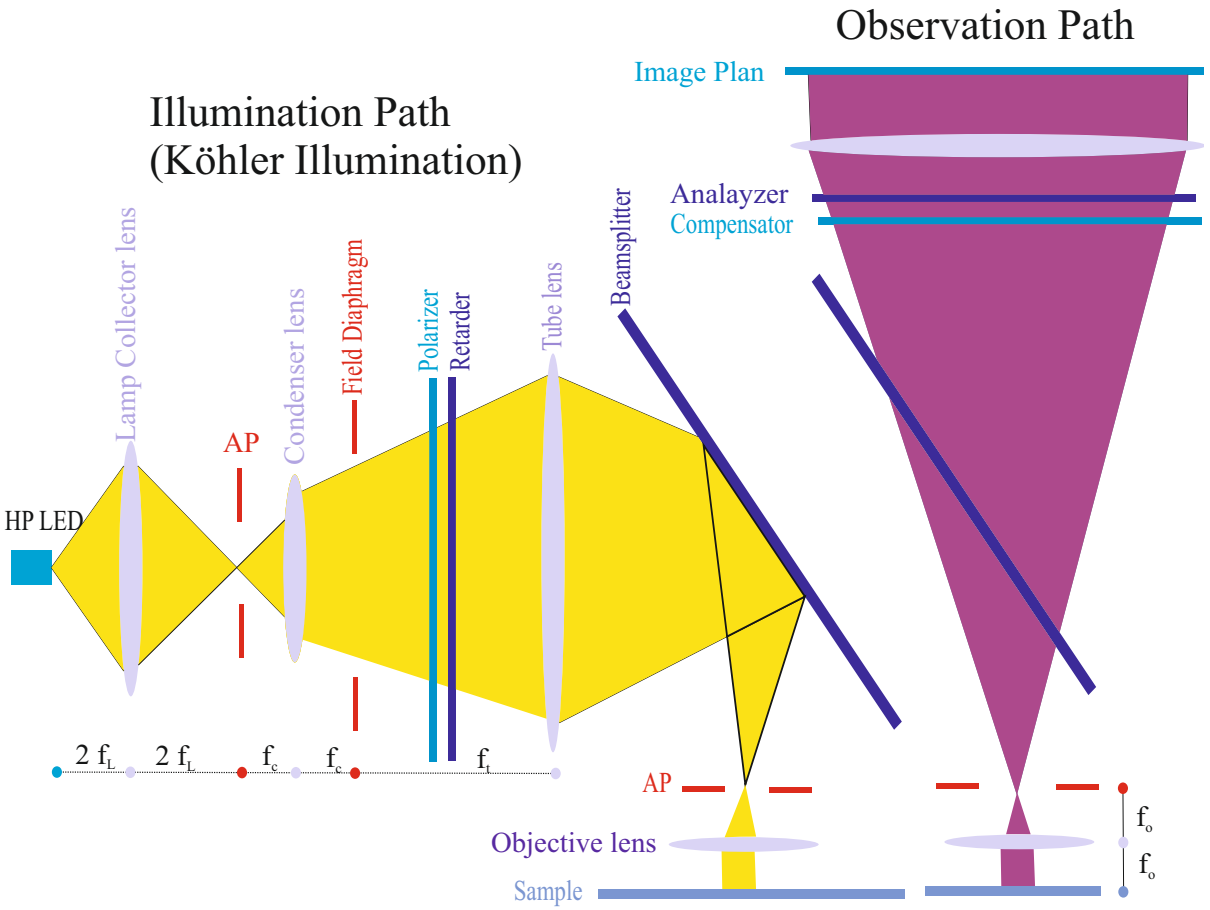

Figure 3.6: The yellow and purple colour indicate light beam, respectively in illumination and observation path[153].

light reaches the beam splitter. As its name suggests, it partially reflects (in illumination) or transmits (in observation) light. The reflected beam diverges in another AP in the back focal plane of the objective lens f_o. This provides a parallel ray via the objective lens to illuminate the specimen homogeneously [153]. The focused reflected beam position in the back focal plane of the objective lens, indicated by a yellow circle in a dark blue one, is shown for different sensitivities in Fig. (3.5).

The reflected beam position in back focal plane of objective lens, indicated by yellow circle in dark blue one are illustrated for different sensitivities in Fig. (3.5). This reflected light from the magnetized sample, now is polarized based on equation (3.17) and is guided via the observation path to the analyzer and then the camera captures the image.

3.2.2.1 Resolution

Based on Lord Rayleigh, two spots in the MO microscope are distinguished while the maximum intensity of one spot meets the minimum intensity of the second one. This is illustrated in Fig. (3.7).

In this situation, intensity difference between the first point's maximum and the valley (formed between two maximum intensities which is indicated in Fig. (3.7) as point A is 80% and therefore,

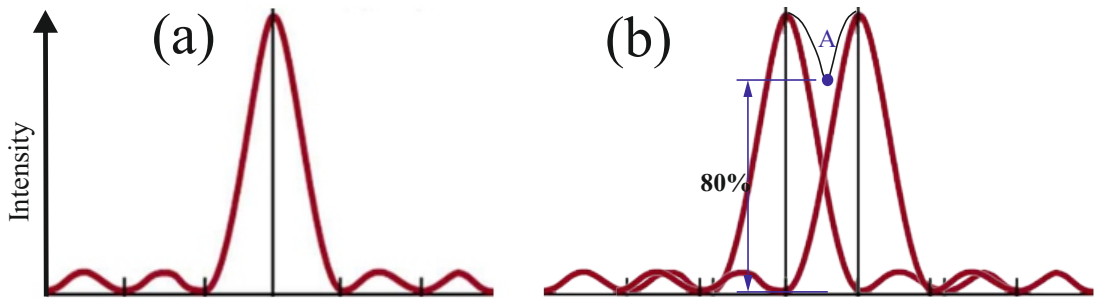

Figure 3.7: (a) One single spot intensity versus radial distance is shown. (b) Two spots intensity are demonstrated when the left one's minimum meets the right one maximum. The two mentioned spots' intensity are superposed and a minimum between them (indicated by A) is formed. It is what can be seen in their image. If the image minimum intensity (point A intensity) is less than 80% of maximum intensity of two spots, based on Rayleigh criterion, these spots are distinguishable.

Magnification	NA	R_{blue}(nm)	R_{green}(nm)	R_{red}(nm)
50 ×	0.8	270-351	306-397	376-488
100×	0.9	240-312	272-352	334-434
20 × Nikon	0.45	-	543-704	-
40 × Nikon	0.6	-	360-468	-

Table 3.2: The spatial resolution is calculated from equation(3.18). There is a range for each source light colour indicating Sparrow (lower) and Rayleigh (upper) criterion. The wavelength for blue, green and red are considered 460, 520 and 640 nm, respectively.

these two points are recognizable in the microscope. This distance between one maximum and one minimum is correlated with the illumination light's wavelength λ. The resolving power R is defined as [155],[153]

$$R = \frac{1.22\lambda}{NA_i + NA_o} = 0.61\frac{\lambda}{NA} \qquad \text{where:} \qquad NA = n\sin\theta \tag{3.18}$$

where the radius of light aperture has been replaced by the lens' numerical aperture in illumination NA_i and observation NA_o. In addition, θ represents the angle of incidence light.

Furthermore, there is another standard defining spatial resolution by replacing the coefficient 0.61 in above equation with 0.47. This is called Sparrow's criterion [155]. For three different light source colours and so different energy, spatial resolution calculated from both criteria is shown in table(3.2).

3.3 Wide Field Time Resolved MOKE

The time-resolved magneto-optical wide field microscope is used to measure the dynamic response of magnetization to a sinusoidal excitation field. All detail about microscope components are explained in Refs [31], [44] and [32]. The principle of MOKE measurements is similar for static, described in the last section, and dynamic MOKE microscope. But one of the main differences is

that a pulsed laser as a light source is used. Therefore, a rotating plate diffuser and a vibrational one should be added to avoid laser-speckles. Besides, the repetition rate of the laser is 50 MHz and this means that the time resolution is restricted to multiples of this value. Furthermore, a time stabilizer controls the pulsed laser repetition. A sinusoidal magnetic field is required to excite magnetization which is provided by a signal generator. This device is capable of generating a magnetic signal with 5 V and 20 GHz as amplitude and frequency, respectively.

To measure dynamic MOKE images, it is necessary that MOKE data in different phases are obtained. Furthermore, because of the oblique plane of incidence, the measurements in every phase should be repeated for three different sensitivities. To achieve optimum quality of the measured data in every phase and each sensitivity, optical measurements are done several times and the average is calculated. For instance, in the measured data in the next chapters, we considered mainly 39 phase points (with 0.17 rad resolution), including one complete period (36 points) and two more extra points, to be sure that one round of data is obtained. Every phase is saved after averaging between 32 MOKE images while every of this image is averaged 16 times. Therefore, the number of measurements is $39 \times 3 \times 32 = 3744$, each is averaged 16 times. This huge number of measurements needs a highly stable system. The mechanical stability is provided by mounting the optical set up including sample stage and focus parts on a massive table. The system is isolated from air flow or any thermal drift, shielding the system from surrounding by keeping it inside a box. Any phase drift between the laser pulse and the excitation field is detected and corrected before every differential image is saved. First, the zero-point of the signal is read out by oscilloscope and the desired phase relative to this new zero-point is calculated [44].

Another important adjustment that has to be done before every measurement is the optical calibration of static MOKE images. In every IP sensitivity, the sample is saturated by applying a high magnetic field and the sample is orientated along different angles, for instance, 0, $\pm\pi/4$,$\pm\pi/2$, $\pm\pi$ rad. Then the corresponding images' intensity is plotted versus angle. This plot, the sensitivity curve, should have sinusoidal behaviour and is fitted easily with a sin or cos function if the sensitivity adjustment is done precisely. To calibrate OOP sensitivity, the same process is applied but obviously, there should be no MOKE intensity variation relative to the magnetic field orientation if the sensitivity is correctly adjusted. There is another method utilizing a known magnetic configuration which is explained in Ref.[31].

In all of the time-resolved MOKE data that are measured and shown in the next chapters, data from five different sensitivities are collocated, including two IP and one OOP sensitivities. The reason is that the oblique plane of incidence in IP sensitivity measurements causes a superposition

between IP and OOP components of magnetization [31],[156]:

$$\begin{aligned} I_{\mathrm{MOKE,p}} &= \pm I_{\mathrm{long}} + \pm I_{\mathrm{trans}} + I_{\mathrm{pol}} + I_{\mathrm{BG}} \\ I_{\mathrm{MOKE,s}} &= \pm I_{\mathrm{long}} + I_{\mathrm{pol}} + I_{\mathrm{BG}} \end{aligned} \tag{3.19}$$

where I indicates intensity, long, trans and pol represent the longitudinal, the transverse, and the polar sensitivities, respectively while p and s display p-polarized and s-polarized light and BG is the abbreviation for background and is non-magnetic information. Moreover, the ± sign refers to the change of the angle of incidence. To select one specific and pure component of magnetization, the two above equations are added together or subtracted [31]:

$$\begin{aligned} I_{\mathrm{MOKE,polar,+}} &= 2I_{\mathrm{pol}} + 2I_{\mathrm{BG}} \text{ and} \\ I_{\mathrm{MOKE,long,-}} &= 2I_{\mathrm{long}}. \end{aligned} \tag{3.20}$$

where + or - show the sum or the subtraction of equations (3.19). Therefore, to precisely measure the magnetization dynamic component, data in 5 different sensitivities is measured, including two s-polarized and two p-polarized sensitivities with ± sign and one polar one.

3.4 Samples

In this work, we consider two categories of samples. They are called antidot and I-dots samples which are described in the following.

3.4.1 Antidots

These samples are made of $Co_{40}Fe_{40}B_{20}$ in single layer with 50 nm thickness and TaN as cap layer, Ta 3 nm/[$Co_{40}Fe_{40}B_{20}$] 50 nm /TaN 5 nm and in double layer with 25 nm for each layer separated by a 0.8 nm Ru, Ta 3 nm/[$Co_{40}Fe_{40}B_{20}$] 25 nm/Ru 0.8 nm/ [$Co_{40}Fe_{40}B_{20}$] 25 nm/TaN 5 nm.The Ru is a metallic material and used as spacer. As it was discussed in section (2.1.2) and shown in Fig. (2.1), this spacer provides RKKY interaction between layers and a weak antiferromagnetic coupling between two ferromagnetic layers because of small and negative $F(\theta)$ and so J in equation (2.6). During a magnetic film's deposition, a magnetic field of H_{dep} = 960-1760 A/m is applied. This field induces an IP uniaxial anisotropy K_u = 700-1300 J/m^3. The samples are patterned via photolithography and then ion beam etching. The antidot sample has dots with different diameters and lattice parameters (the distance between the two nearest neighbour dots' center) for instance 10 and 30 μm, respectively, (equal to 20 μm edge to edge distance). In the following, we refer them as sample

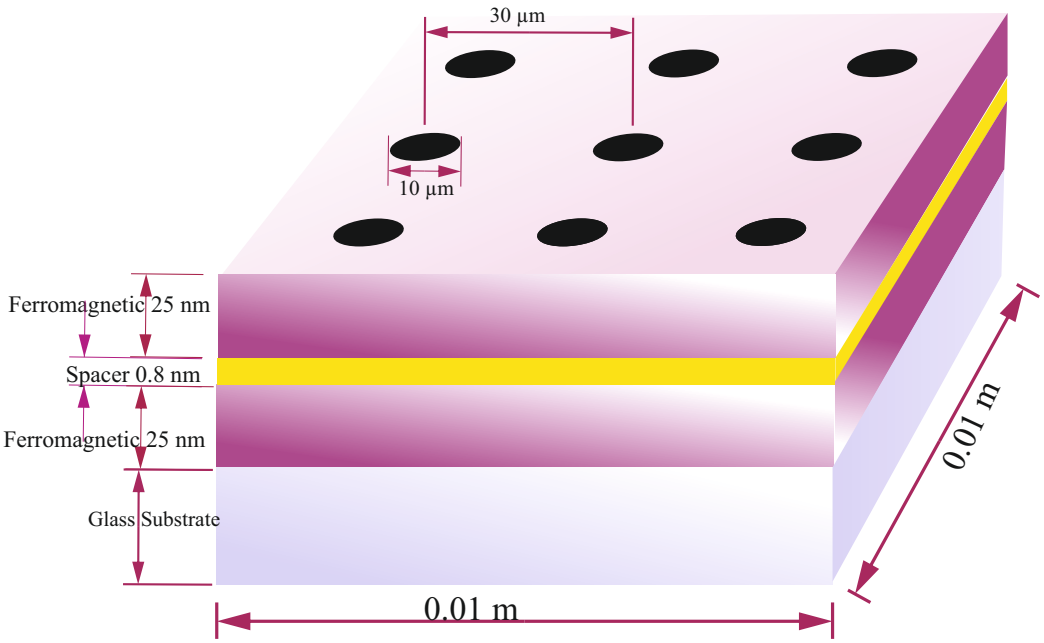

Figure 3.8: The antidot array with 10 μm diameter and 30 μm center to center distance is shown for a double layer structure. They are separated by a Ru spacer and magnetic material is deposited on the glass substrate.

10×30.

The holes' (antidot) diameter and lattice parameter in addition to the magnetic materials features determine the magnetic properties such as remanence, coercivity and general hysteresis shape in easy and hard magnetization direction [157]. The schematic sketch of a double layer antidot array is illustrated in Fig. (3.8). Such antidot structures vary specifically demagnetization field and as a result effective field [30] around the dots locally and therefore this pattern is used as a source to produce spin waves while a uniform microwave magnetic field is applied [158], [50].

3.4.2 Antidot Array with Irradiated Matrix (I-dots)

In order to manufacture the antidot array, rather than lithography and ion etching in the clean room, irradiation with ions is another way to pattern thin films. The wafer is made of $Co_{40}Fe_{40}B_{20}/Ru/Co_{40}Fe_{40}B_{20}$ and then irradiated by Co^{+} beam in presence of a lithographically made mask. The energy of the beam is adjusted based on the required penetration depth. By using Co^{+} ions, the possibility of sample contamination by different ions than the material's substance is avoided.

One of this method advantages in comparison to the etched sample is to avoid a physical border and instead having a magnetic properties' border. In absence of a physical border, the stray field in non-irradiated areas (dots) is reduced in comparison to the antidots areas as a result of shielding them by the adjacent magnetic materials [159].

The initial wafer consists of two layer ferromagnetic material (CoFeB) separated by a Ru spacer

with 0.7 nm thickness. Therefore, they are coupled antiferromagnetically via RKKY type of interlayer exchange coupling. Each layer thickness is 10 nm. Then a lithographic mask is used to avoid irradiation of the dot array and other parts of the thin film (matrix) are irradiated by Co^+ beam. The Co^+ beam carries 80 keV energy with an irradiation dose or fluence of 5×10^{15} Co^+/cm^2. The required energy and dose is calculated via TRIDYN [160], [161]. The beam should be strong enough to penetrate as deep as the spacer depth. The irradiation causes interfacial intermixing between two layers and spacer. Therefore, the dots region keep its double layer structure with antiferromagnetic coupling embedded inside the irradiated, single layer ferromagnetic matrix. However, this single layer's magnetic property is different somehow from a non-irradiated single ferromagnetic layer with the same materials [159]. For instance, the gradient of saturation magnetization in the irradiated samples is investigated in [162]. The complete study on this sample consists of PIMM results, static MOKE measurements are presented in detail in the supplementary material 6. Further, the static magnetization configuration is simulated and the obtained results are compared with measurements' data.

Chapter 4

Spin Wave Excitation, Propagation and Reflection from Domain Walls in 2-D Antidot Arrays in Single Layer CoFeB

4.1 Introduction

By periodically patterning a magnetic full film into an antidot array, the dispersion relation of SWs and as a consequence their propagation velocity can be tuned. In this chapter, one single layer thin film as it was described in section 3.4.1 is characterized. The sample has a size of 1×1 cm^2 in area and is 50 nm thick. The antidot diameter is 4 μm, while the lattice periodicity (dots' center to center) is 16 μm.

In saturation ($\mu_0 M_s$ = 1.48 T), the applied magnetic field is high enough to overcome the high demagnetizing field around the antidots (holes in the magnetic film). Magnetic poles at the edges of the antidots form. Furthermore, the magnetostatic energy corresponding to the mutual interaction between the two magnetic dipoles, P_1 and P_2 in r_{12} (almost equal to the antidot array periodicity) more apart from each other, follows this equation:

$$E_{12} = \frac{P_1 \cdot P_2 - 3(\hat{\mathbf{n}} \cdot P_1)(\hat{\mathbf{n}} \cdot P_2)}{r_{12}^3} \tag{4.1}$$

where $\hat{\mathbf{n}}$ is the unit vector connecting these dipoles.

If it is assumed that all dipoles have the same orientation, for instance at fields slightly under saturation, this energy distribution in a square antidot array is isotropic while the dipole axis follows the effective field axis.

In the absence of an induced anisotropy, there is a four-fold anisotropy with the hard axis along horizontal and vertical axis of the array and the easy axis along the diagonal connection, provided that the antidot array is not tilted [22]. Through a micromagnetic simulation platform, Micromagus [95], the static and dynamic response of the sample is calculated. The magnetization components for every cell are obtained while the data are obtained, for an assumed supercell of 16×16 μm^2. This supercell was divided into 2048×2048 mesh cells in the xz plane. Therefore, every cell size is 7.8×7.8 nm^2. Based on what was discussed before in section 2.2.3, the cell size is important and it should be around the exchange length, having the minimum calculated exchange length from equation (2.28) $\sqrt{2 \times 2.24 \times 10^{-11} \times \mu_0/(1.48^2)} = 5.1$ nm. The uniaxial anisotropy is $K_u = 1300$ J/m^3 and the static domain behaviour along both easy and hard axis of magnetization are calculated.

In the first set of simulations (static simulation), a saturated system as initial magnetization configuration is supposed and then the magnetization is calculated by applying static magnetic field H_0. This field is reduced at equal steps of 80 A/m from 4 to -4 kA/m after a full relaxation for every step is obtained.

4.2 Static Magnetization Configuration

4.2.1 Along Easy Axis of Magnetization

The magneto-optically obtained data on the magnetization configuration in a 1.6 kA/m static field are compared with the simulated static state in Fig. (4.1). The bias and anisotropy field are parallel for both cases, the calculated and the microscope data. The magnetization vectors (every arrow represents 64 discrete cell magnetization) calculated in the simulated mesh are displayed in (c). In addition, to clarify the anti-onion or butterfly state of the magnetization [163] around dots and Néel spikes [164] with tail to tail magnetization on one side and head to head on the other one, the magnetization component parallel to the bias field is colour coded and the total normalized magnetization vectors are displayed on it. The butterfly axis is parallel to both the external and the anisotropy field. Furthermore, in this field, the antidot in the array behaves like an isolated one since there is not yet any connection to the nearest neighbours.

This magnetization configuration around the hole inside the magnetic field is in agreement with other studies [109], [165]. This configuration is symmetric around the film anisotropy and curved DWs in pairs emerge from both sides of the dot. They extend for a few μm inside the magnetic material until they align perpendicular to the induced anisotropy axis. For a bias field

below saturation, the demagnetizing field around the dot dominates and forms magnetic dipoles to reduce the total magnetic energy and reach an energetic minimum. The reduction of the demagnetizing energy E_{dem} is important since, based on calculation results, it has a higher value in comparison to anisotropy E_{an} and exchange energy E_{exch}:

$$E_t = -2.6 \times 10^{-14}\ \text{J} \tag{4.2a}$$

$$E_{exch} = 1.2 \times 10^{-16}\ \text{J} < \quad E_{an} = 2.8 \times 10^{-16}\ \text{J} \quad < E_{dem} = 20.4 \times 10^{-16}\ \text{J} \tag{4.2b}$$

Therefore, the magnetization configuration is formed based on the fact that the magnetic charge density should be reduced as much as possible. The magnetic charge is described as a variation of magnetization in the form of:

$$\nabla \cdot \mathbf{m} = \rho \tag{4.3}$$

where ρ is the magnetic charge density. An analytical model describes this closure domain structure in analogy with vortices on the opposite sides of the antidot along the anisotropy axis [109].

4.2.2 Along Hard Axis of Magnetization

Fig. (4.2 a) shows the magnetization variation by a magnetic field for a single layer antidot 4× 16 μm^2. The difference, in comparison to the last section, is that the anisotropy axis is rotated along $\hat{\mathbf{x}}$ and so it shows hard axis behaviour of magnetization. There are three highlighted points at different magnetic fields 3.18, 0.096 and 1.6 kA/m with the magnetization around 0.8, 0.1 and -0.5 M_s. The simulated data are depicted in addition to the magneto-optically measured data for the three mentioned points in Fig. (4.2 b-d). The first two images in every row clarify calculated components of magnetization, one parallel to static field, m_z, and another along the anisotropy axis, m_x. Furthermore, the magneto-optically measured data are recorded in horizontal sensitivity which is comparable with m_z, when the OOP component of magnetization is so small. To obtain these magneto-optically measured data, the sample is saturated at 20 mT and then it is reduced to the field of interest. It can be seen there is a good agreement between the calculation and experimental measurements.

In Fig. (4.2 b), the magnetic field is reduced from saturation (at 16 kA/m) to 3.18 kA/m. This point is denoted by a purple circle in the MOKE hysteresis. The field is still strong enough to keep more than 80% of the total magnetization in the field direction. The simulation for the other component of magnetization m_x displays small rotation of magnetization inside the matrix and the

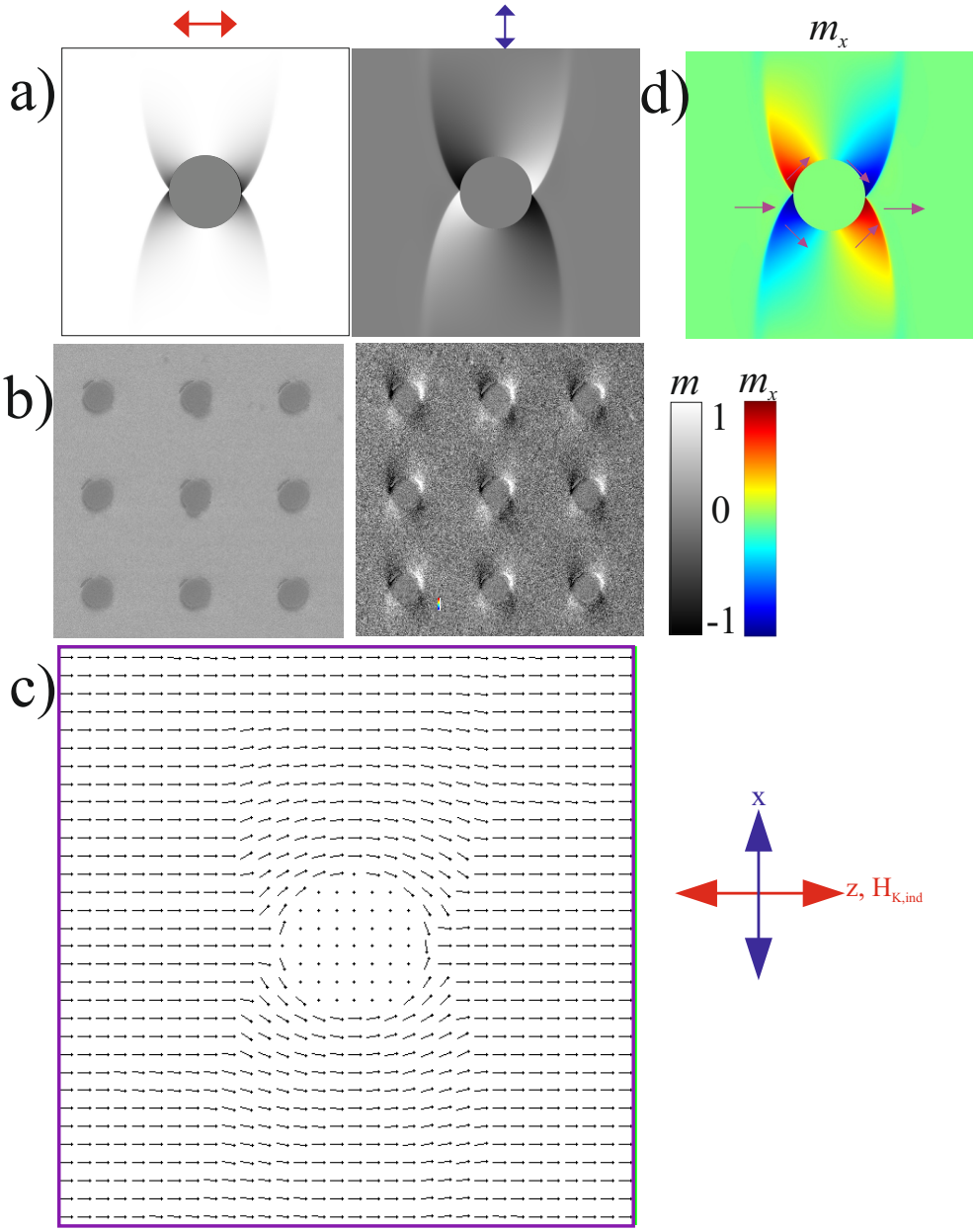

Figure 4.1: The magnetization is illustrated for a single layer antidot array 4×16 μm^2 (antidot diameter × lattice constant) made of CoFeB. Two images illustrate parallel and perpendicular components of magnetization relative to the applied field whose amplitude is 1.6 kA/m in $+\hat{\mathbf{z}}$ direction. As geometry shows the field is applied along magnetic easy axis. (a) The simulated data are shown in grey scale. (b) The measurement via MOKE microscope are illustrated. The calibration bar for these grey scale images is common and from -1 to +1. The two-headed arrows above the images indicate calculation and sensitivity axis for (a) and (b) images, respectively. (c) To clarify, this magnetization configuration is illustrated by vectors. (d) The m_x is coloured to highlight the butterfly pattern while vectors show the total magnetization. The calibration code ranges from dark blue to dark red, corresponding -1 to +1.

formation of magnetic poles in the exact vicinity of dots because of the high shape anisotropy in this area. However, the vertical connection between the first antidot neighbours is still saturated. The magnetic moments are illustrated by arrows in the first image, corresponding to calculated m_z.

Further reduction of the magnetic field, gradually reduces the magnetization component parallel to the field in the matrix and shortly after remanence at 0.096 kA/m, the magnetization along the field drops notably to 0.1 M_s. The corresponding magnetization configuration is shown in Fig. (4.2 c). It is indicated by a blue circle in the hysteresis plot. The magnetization around the antidot is not uniform yet and Néel spikes [164] originating from the dots can be clearly seen. The magnetization vectors depicted around the dots help to recognize the magnetic poles on the top and the bottom of every dot. This rotation of magnetization around the dot reduces the stray field. Moreover, by considering the other magnetical component, a rotation of magnetization can be seen towards the anisotropy axis.

By increasing the magnetic field in the opposite direction, the matrix magnetization follows the magnetic field direction as it can be seen in Fig. (4.2 d). It seems that because of the shape anisotropy coming from the dot edges, the magnetization along the horizontal line connecting the dots stays longer in the anisotropy direction.

As it was discussed in section (4.1), there is an effective four-fold anisotropy because of the square array of antidots with the hard axis connecting the dots and the easy axis along the diagonal connection. This extra anisotropy is the reason in (4.2 b) that the magnetization along a vertical line connecting the antidots remains totally in the saturation field direction. The magnetization along the diagonal line in (4.2 d) rotates faster than the other parts of the matrix toward the field direction.

4.3 The Locally Simulated PIMM, LS-PIMM, for Antidot Array

In the following, the dynamic response of magnetization for antidot pattern shown in the Fig. (4.1) is calculated while the excitation field is step function-like, which was illustrated in Fig. (3.2 a), with 4 A/m in amplitude and 60 ps rise time (providing a 5.8 GHz frequency bandwidth). After this sharp step, the field stays constant for 10 ns. After this period of time, the magnetization is sufficiently relaxed towards the new equilibrium magnetization orientation and is still accounting for slow dynamic processes. To achieve the highest dynamic response, the excitation field is applied perpendicular to the static field which is along the anisotropy axis. The reason is that based on the first term in the LLG equation (2.45b) the maximum torque is achieved while the angle between

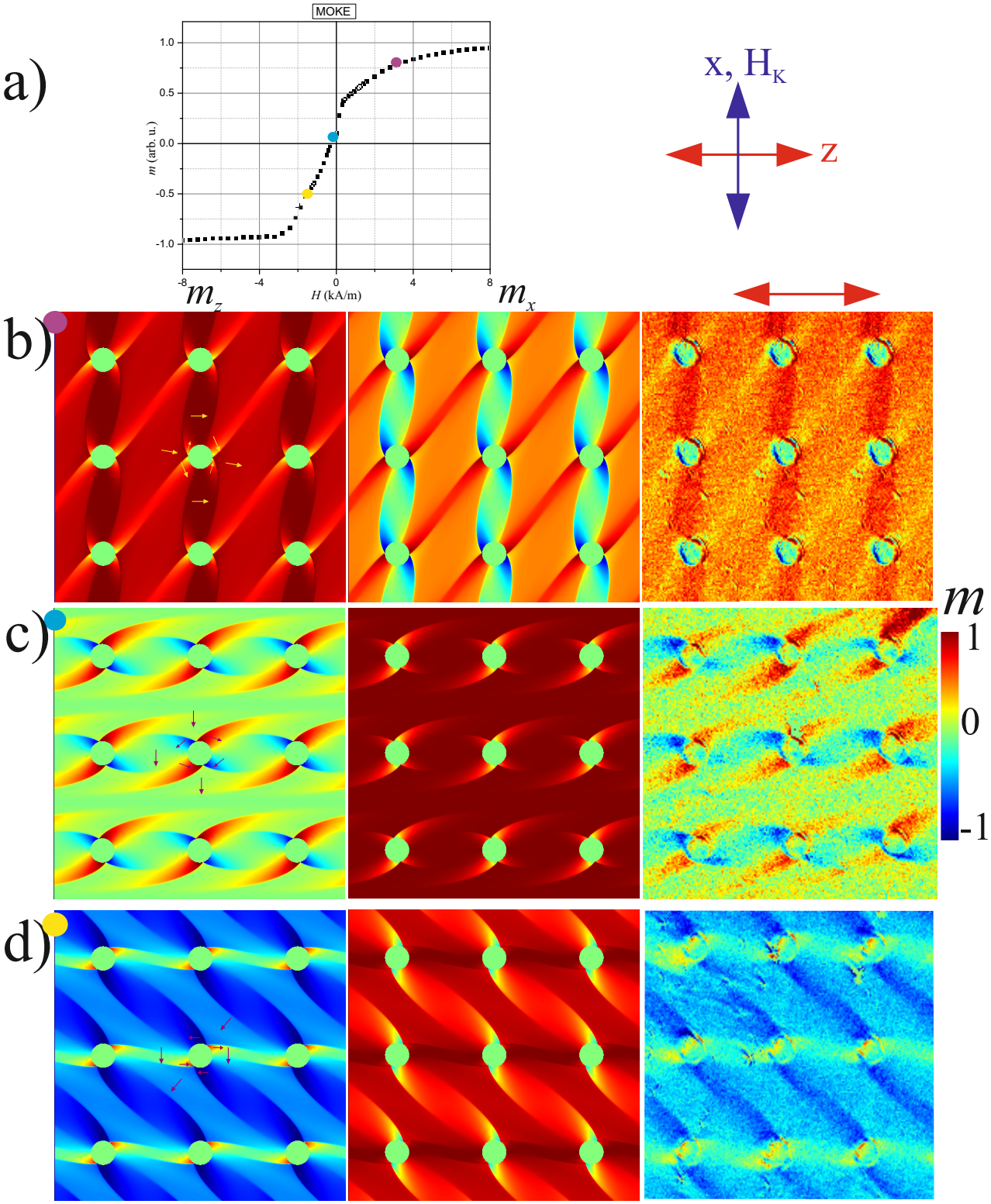

Figure 4.2: (a) The hysteresis obtained from MOKE microscope shows magnetization variations for a single layer anti-dot structure 4×16 μm^2 while applied field and anisotropy axis are perpendicular. (b-d) The simulated magnetization components (two images at the left side) are compared to the results recorded via MOKE microscope at three magnetization configurations which are highlighted on hysteresis via circles by the same colour as in the corner of the images. In these three points, the magnetic fields are equal to 3.18, 0.096 and 1.6 kA/m in the directly measured images.

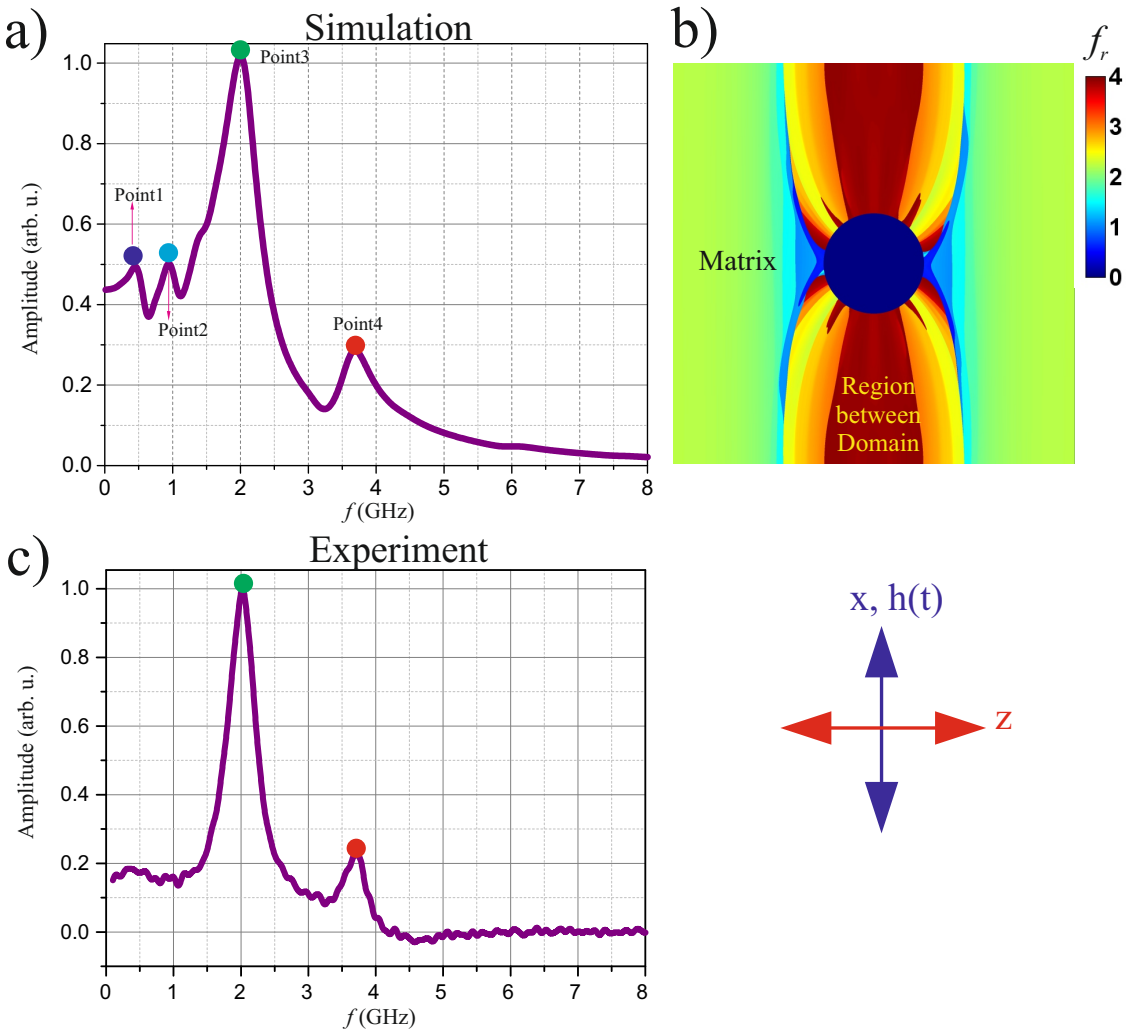

Figure 4.3: (a) The dynamic response of magnetization to a step function is simulated for the static state illustrated in Fig. (4.1). The plot shows the average signal of the whole super cell with 4 peaks (named point 1 to 4) in the calculated susceptibility and corresponds to f_r from different regions. (b) The resonance frequency for every individual simulation cell is displayed. The colour code indicates the resonance frequency. The colour circles above the four points inside plot (a) connect them to the data and the colour code used in (b). For instance matrix and its corresponding peak, point 3, are both green. (c) To confirm LS-PIMM data, the experimentally measured data are plotted as well. Two peaks in this plot are evident at the exact same frequency as for the calculated data.

magnetization and effective field is $\pi/2$.

After the first round of static simulation described in section (4.1), the relaxed system obtained by applying 1.6 kA/m is used as initial magnetization configuration. Here, in the second simulation step, the bias and excitation field are applied normal to each other. Then, the static magnetization configuration is found by minimizing the energy. The process of finding magnetization via e_{min} calculation is repeated after a short time interval which is the time resolution of the calculation, mostly a few ps and in this case 10 ps. So as the excitation field varies by time, the dynamic response is saved after the same time interval.

By saving the dynamic magnetization components as a function of time and position, the local time-domain signal can be extracted for every cell, exhibiting a similar behaviour as an under-

damped oscillator, shown in Fig. (3.2 b). By applying a DFT, the time-domain data of the local magnetization can be transferred to the frequency domain, which is proportional to the permeability spectrum $\mu(f)$. Finally, from this information and based on the discussion in section 2.3.1.4 and Fig. (2.14), resonance local frequencies are obtained.

Fig. (4.3) shows the permeability spectrum for an antidot sample extracted from averaged signals all super cell. There are four peaks indicated as point 1 to 4 which are calculated resonance frequencies. This calculation is comparable and in great agreement to experimentally measured results. In the PIMM, experiment multiple peaks can be detected but it is not possible to make a one by one correlation between peaks and domains. In such a measurement, it is not possible to find the local resonance frequency corresponding to each domain individually, while the simulation provides such opportunity.

The simulation method used here provides us with the possibility to obtain the resonance frequency of each individual cell. The resonance frequencies as a function of position are illustrated in Fig. (4.3) in a colour plot. The process for every cell is the same as explained above for the averaged data. Every cell's permeability spectrum may have multiple peaks, but for Fig. (4.3), only the highest peak is considered. This leads to a sharp variation of f_r in some regions.

There is more than one peak and so more than one f_r in comparison with the structure corresponding to the plotted data in Fig. (2.14). The reason is that Fig. (2.14) indicates calculated data for a single domain while for the structure illustrated in Fig. 4.1, it is obvious that several domains exist. Every domain has a different effective field leading to different f_r based on equation (2.48b). The signal with multi-peaks in the other work is detected by BLS measurement of a much larger structure ($2\times$ 2 $\times 0.01$ μm^3) with one isolated antidot, 100 μm in diameter [30].

Point 1 in Fig. (4.3 a)displays f_r = 0.5 GHz which belongs to the areas denoted in the colour coded image by dark blue in Fig. (4.3 b). It should be mentioned that the minimum local resonance frequency, $f_{r,l}$ belongs to the exact vicinity of and the inside of the DWs. To clarify and individually show these regions, in Fig. (4.4), the permeability amplitude is shown at different resonance frequencies. The permeability amplitude is much higher inside the DWs for low f_r, but in order to enhance contrast the calibration of the colour code is set between zero and one. Depicted are locally simulated PIMM calculations for all f_r found in Fig. (4.3) (0.5, 1, 2, 3.7 GHz) with the addition of two higher frequencies (4, 5 GHz). A comparison between the magnetization pattern in Fig. (4.4) and dynamic magnetization behaviour after applying a harmonic excitation field at different frequencies will be discussed in the next section. A detailed discussion of the dynamic behaviour of a single layer antidot-array will follow in the next section.

The highest amplitude peak in Fig. (4.3) can be observed at 2 GHz. It is located in the matrix

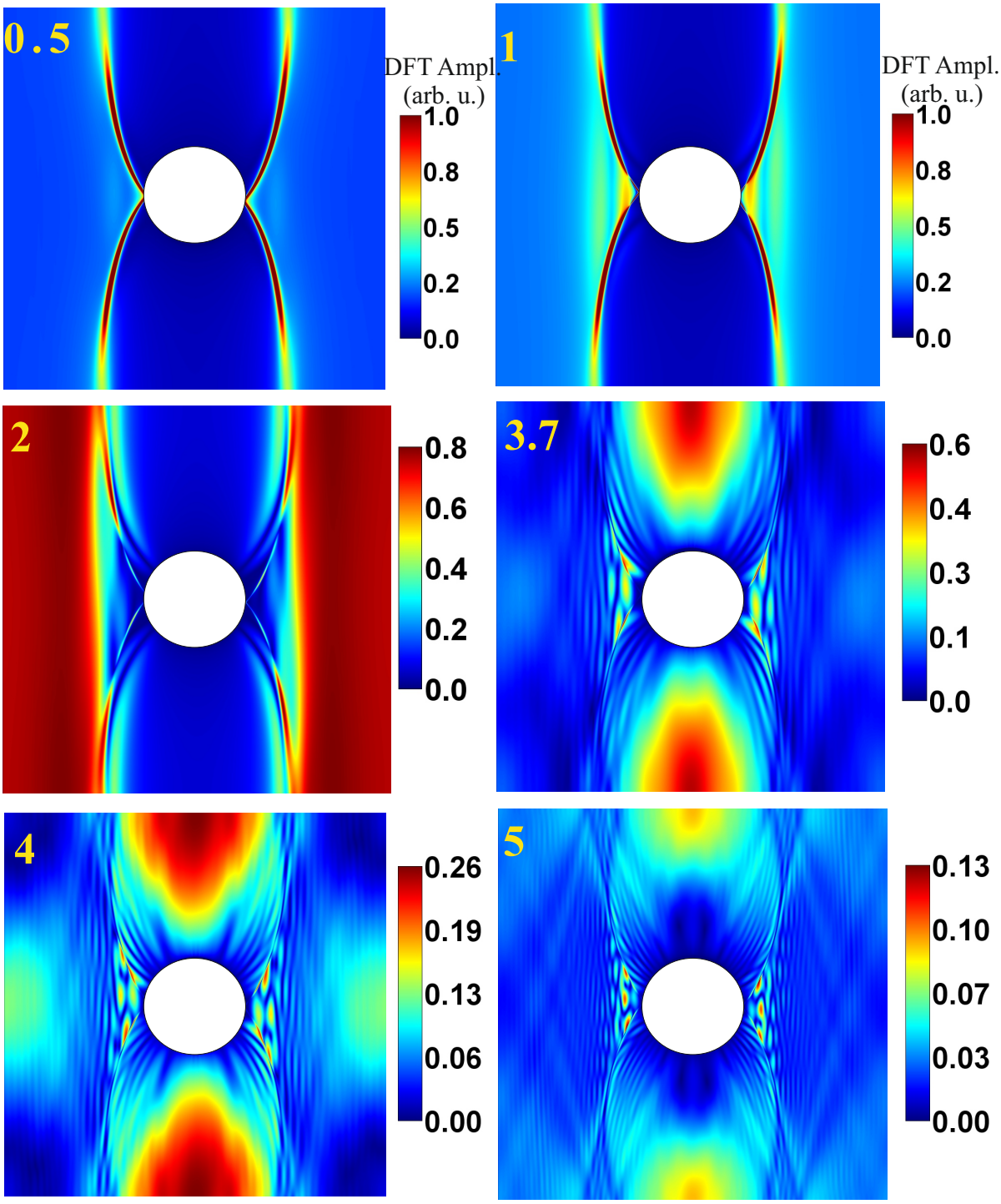

Figure 4.4: The exemplary amplitude for all four peaks denoted in Fig. (4.3 c) in addition to the two higher frequencies, 4 and 5 GHz, are shown. The colour code shows DFT amplitude (dynamic susceptibility) with arbitrary unit. Furthermore, in order to enhance contrast, colour code's range for 0.5 and 1 GHz is restricted between 0 and 1 while the amplitude inside DWs (especially in vicinity of an antidot) is 10 times higher.

and its resonance frequency is the same as for the full film. This region is far enough from the antidot edges and so its effective field is not heavily affected by the demagnetizing field generated around the dot. The magnetostatic field orientation is shown in Fig. (4.5) while every point's vector is normalized to itself in order to make the vectors' direction visible. Inside the matrix, H_{dem} has a lower value in comparison to the area around the dots as it was illustrated before in Fig. (2.16). In addition, in the matrix H_{dem} is antiparallel to the applied field which reduces the effective field in contrast to the area around the dots.This region has the highest f_r = 3.7 GHz and is the region in dark red colour in Fig. (4.3 b). This high frequency arises due to the high effective field as a result of the change in the sign of the demagnetizing field. Normally, the demagnetizing field is antiparallel to the bias field leading to an overall reduction of the H_{eff}, while in the region between Domain walls mentioned in Fig. (4.3 b), H_{dem} and H_0 are parallel and so they sum up, enhancing H_{eff} and therefore f_r.

4.3.1 Comparison with Other Calculation Methods

In Fig. (4.6), the calculated data obtained by three different approaches are compared for our antidot array.

In Fig. (4.6 a), the Kittel formula [166] ($f_r = \gamma/2\pi\sqrt{M_s H_{eff}}$) is applied for the static field along the easy axis orientation of magnetization. This equation is applicable for the single domain structures where effective field and magnetization are parallel. Applying a small excitation field perpendicular to them (magnetization and effective field which are parallel), causes a small deviation and the precession of magnetization around the static effective field. Moreover, the damping inside the material is ignored.

To apply this equation, first the effective fields are calculated, see Fig. (2.16), for an antidot structure at 1.6 kA/m. As expected, the resonance frequency obtained through this method is in excellent agreement with our LS-PIMM method inside the matrix. This can be understood in terms of vanishing demagnetizing fields in the matrix, far from any edges or other magnetic microstructures. Therefore, the magnetic response in this region is similar to the full film response.

On the other hand, in the vicinity of the dots, there are significant differences between the LS-PIMM results and this rough estimation. Another obvious deviation is correlated to DWs. Based on the Kittel mode, they have the highest f_r in contrast to LS-PIMM modelling that reports the lowest f_r, even as low as 0.1 and 0.2 GHz at some points of these regions.

The second method illustrated in Fig. (4.6 b) uses a small perturbation of the magnetization from its ground state to calculate the demagnetizing factors via equations (2.51) to (2.53). This ap-

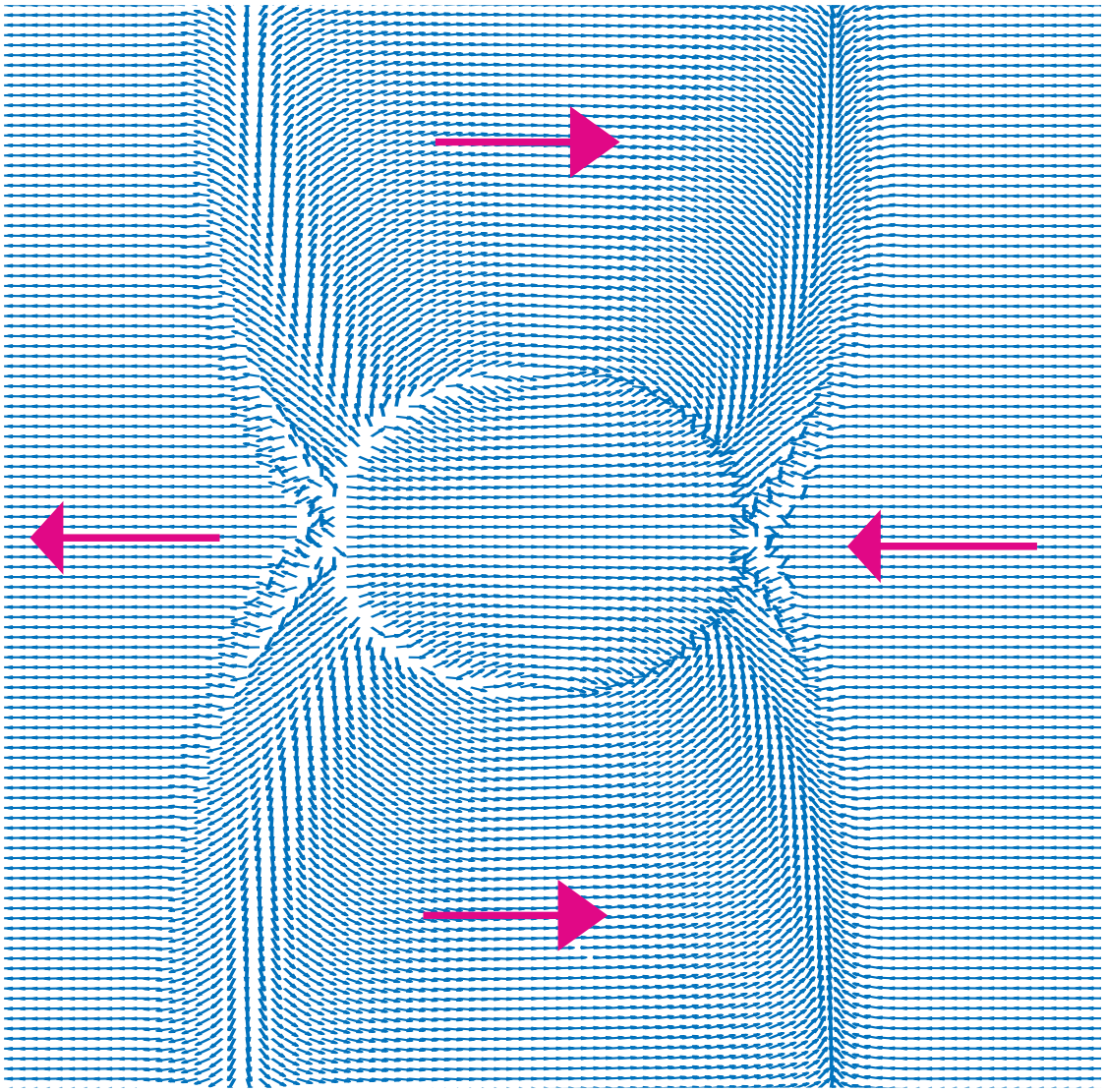

Figure 4.5: Demagnetizing field of the static pattern first shown in Fig. (4.1), represented as a vector plot. The vectors are normalized and show the magnetic moment in the simulated cells. The coloured images in Fig. (2.16) indicate the vector magnitude. The pink arrows are plotted to guide the eye. The static field direction is horizontal from left to right. The variation of this field around the antidot and because of its shape results the inhomogeneity of effective field and magnetization distribution.

proach introduced in [29] has been explained in section (2.3.1.5) and its results for the single layer antidot structure are displayed in Fig. (2.17). Based on our knowledge from LS-PIMM data, the demagnetizing factor inside the matrix and between two DWs should have a different sign which can be seen in N_{zz} in Fig. (2.17). This is the demagnetizing factor parallel to the static field axis. The corresponding plot along the dashed line clearly shows that N_{zz} changes its sign from the matrix to the region confined by DWs. It should be mentioned that two peaks appear in all plots for the DWs. Additionally, there are two discontinuities in the resonance frequency plot. From the mathematical point of view, this is related to the negative value of the radicand in equation (2.50). It leads to pure imaginary values of resonance frequency which is not physically meaningful. Physically, IP demagnetizing factors and therefore their correlated demagnetizing fields are opposed to the

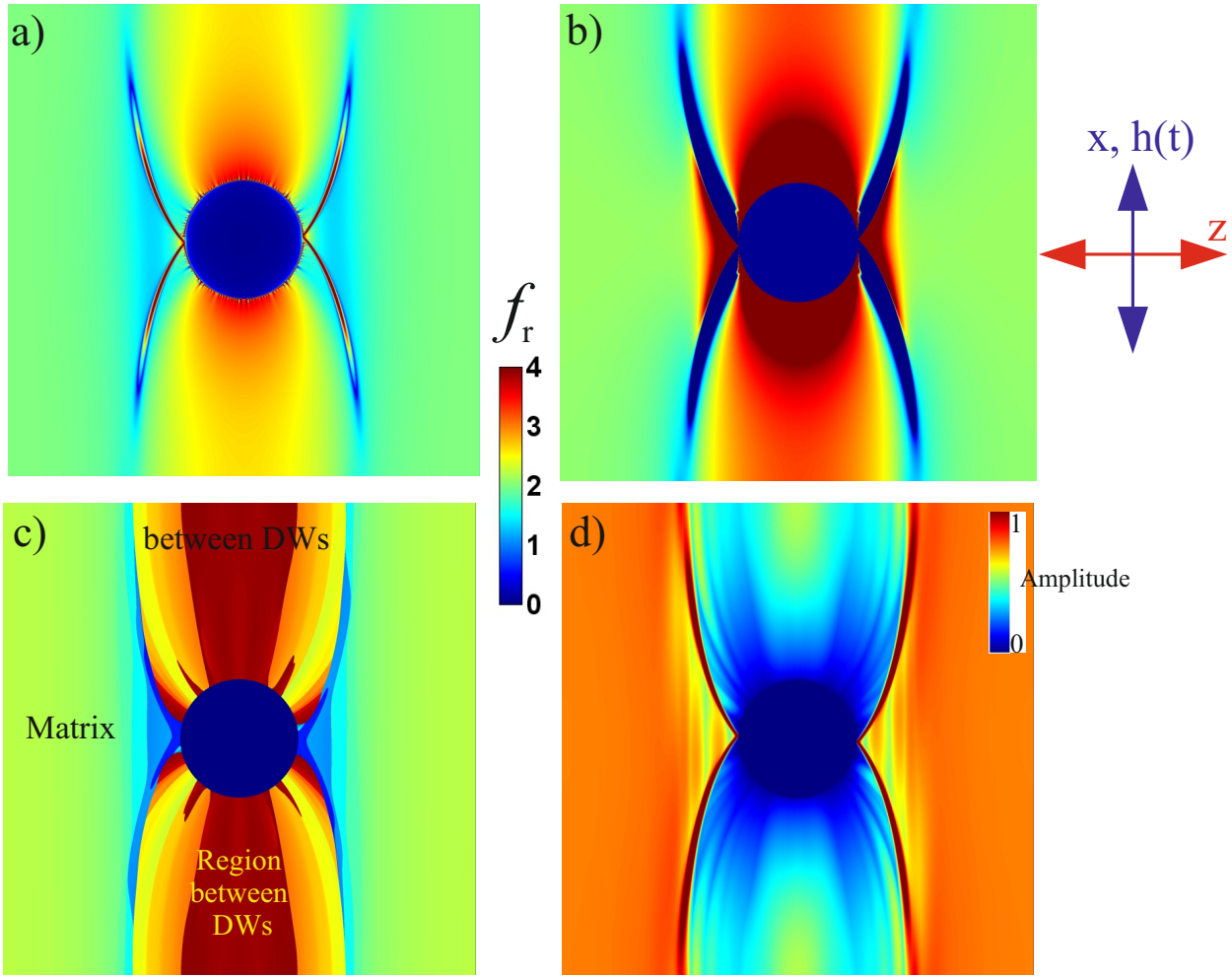

Figure 4.6: The calculated resonance frequencies for every individual cell are illustrated with different methods, (a) the Kittel formula, (b) perturbation and (c) PIMM method. The colour code shows resonance frequencies in GHz. (d) It shows the susceptibility amplitude for every cell in its resonance calculated via LS-PIMM method.

magnetization. However, they are allowed to be parallel. Here, this parallel alignment leads to an imaginary f_r [29].

Last but not least, Fig. (4.6 c) depicts our LS-PIMM data, already shown in Fig. (4.3), repeated for better comparison. In addition, in Fig. (4.6 d) the amplitude of the dynamic response for every cell is indicated if it is excited at its local resonance frequency. It can be seen that the highest amplitude belongs firstly to the exact vicinity of the DWs with a value of 1.1 and secondly to the area inside the matrix. In the next section, it will be shown that the area around DWs plays an important role in emitting SWs, more specifically BVWs because of their low local resonance frequency and the highest dynamic response amplitude.

4.4 Dynamic Magnetization Response to a Harmonic Excitation Field

We consider the static magnetization configuration reported in Fig. (4.1). In this section, dynamic behaviour of this static pattern is calculated. Our sample is a single layer $Co_{40}Fe_{40}B_{20}$ with a thickness of 50 nm that is exposed to the harmonic excitation fields at different frequencies and amplitude. Furthermore, to confirm our simulation results, the dynamic vector response of magnetization is measured directly via TR-MOKE wide field microscopy.

4.4.1 Elastic Waves

Considering the static state discussed in section (4.2.1), in our first measurement we apply a 2 GHz-excitation field with a low amplitude, 56 A/m, to our antidot array with 16 µm lattice constant. The calculated dynamic responses are shown in Fig. (4.7 a). The half period of magnetization evolution by time is displayed to illustrate how magnetization reverses in the full supercell. These four images correspond to minimum, zero, moderate and maximum intensity of full supercell's $\triangle\ m_x$. To calculate them with the highest contrast the frequent images with 180 degree phase differences are subtracted from each other. Their relative phase differences can be followed via a coloured circle in the corner of every image and its counterpart in the plot Fig. (4.7 b).

Moreover, the locally averaged signal from the matrix and the region between DWs (introduced before in Fig. (4.6 c)) are compared in the same plot. It can be seen that their corresponding magnetization precesses with a $\pi/2$ phase difference. However, this leads to the contrast enhancement between the mentioned regions both in the calculated and the measured data. Such a phase shift lowers the full response $\triangle m_x$ (named as total in Fig. 4.7 b)) in comparison with the signal from the matrix. Another point extracted from this phase difference is that the matrix is in $\pi/2$ phase difference with the excitation signal while the region between DWs has another $\pi/2$ phase difference with the matrix. This means, based on the discussion around Fig. (2.14), that $f_{r,l}$ in the region between DWs is much higher than 2 GHz, the matrix f_r. This conclusion is in full agreement with our previous $f_{r,l}$ calculation depicted in Fig. (4.6 c). The last image from Fig. (4.7 a) is shown again in (4.7 c). The utilized colour code type is as the same as before, starting from dark blue to dark red and the antidots are in black. The purpose of this repetition is revealing this image's similarity with our previous calculation in Fig. (4.4) at f_{exc} = 2 GHz. There, we illustrated the amplitude of susceptibility at different excitation frequencies calculated via LS-PIMM. Therefore, the amplitude of susceptibility at one specific frequency display dynamic magnetization response after applying

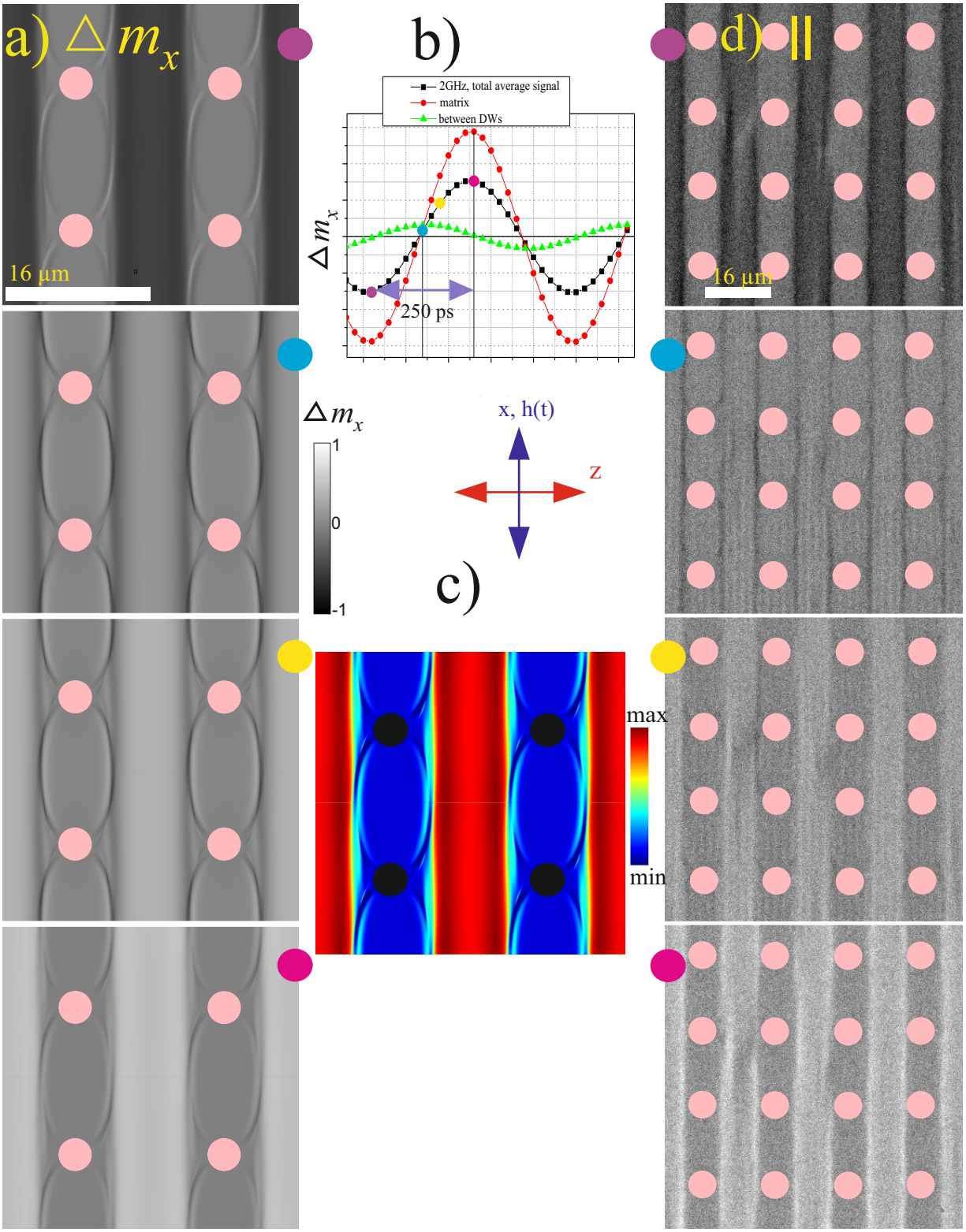

Figure 4.7: (a) The simulation results $\triangle m_x$ are represented by applying a harmonic field 56 A/m, at 2 GHz. (b) The relevant phase of images in (a) is indicated via coloured circles in purple, blue, yellow and pink in the plot. The same set of coloured circles are used in the right corner of simulated images. In addition, the time difference between the first and the last image is shown through a 2-headed arrow which is equal to 250 ps. The time evolution of dm_x form the whole sample, the matrix and the region between DWs (indicated in Fig. (4.6)) are compared via black, red and green curves. (c) We showed one image from (a) in colour to facilitate the comparison between calculated data after applying a harmonic field in (a). The previously obtained results came from PIMM simulation depicted in Fig. (4.4) at 2 GHz. (d) The directly measured images by wide field TR-MOKE are depicted. They are under the same field and frequency as the calculated data and measured with vertical sensitivity parallel to *h(t)*. The elastic waves can be seen as well.

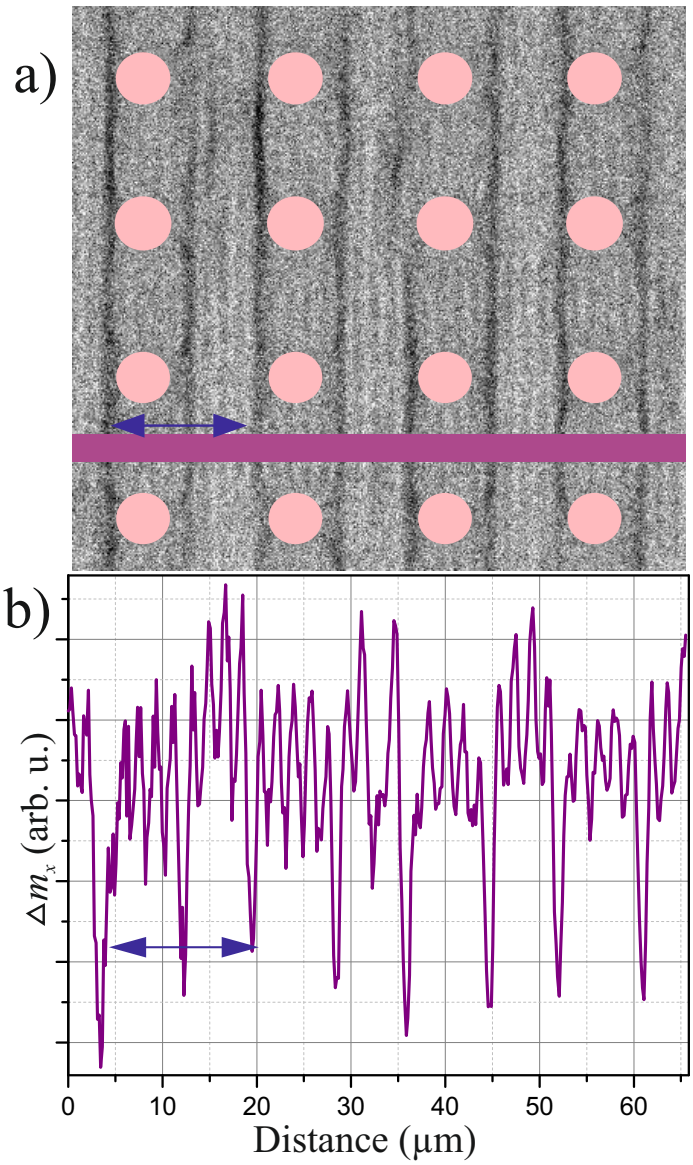

Figure 4.8: (a) The elastic waves from DWs around dots are illustrated. This image is from our measurement shown before for some specific phases in Fig. (4.7 d). (b) To measure them, a 2 GHz excitation field with 56 A/m amplitude is applied. To clarification, magnetization profile along the purple line in (a) is plotted. In addition two-head arrow in (a) corresponds to its counterpart in (b).

the magnetic stimulus at the same frequency. We continue to check this theory for every higher frequency in order to confirm this result and to generalize it.

The measured data via the time resolved MOKE microscope with the same f and amplitude of h_{exc} shown in Fig. (4.7 d) validate our simulated results. Because of the low contrast between antidots (zero in grey scale calibration) and their surrounding, we highlighted them with light pink circles in all images (4.7 a,d).

All of the data in (4.7a) show the differential magnetization component along the excitation field, $\triangle m_x$, in our coordination while the time resolved magneto-optically measured data in (4.7 d) is measured in vertical sensitivity. The required details to extract pure $\triangle m_x$ from the TR-MOKE wide field images can be found in these Ref.s [31], [21],[44].

Considering the static magnetization configuration in Fig. (4.1 a,b), we saw Néel spikes in close vicinity of antidots, while in these regions the demagnetizing field in the matrix rotates and aligns in the opposite direction. Two DWs from the nearest neighbour along the vertical lattice axis of the antidot array extend toward each other. They make a barrier-like border to separate modes inside and outside DWs, which is the matrix. Around these DWs is the area with lowest $f_{r,l} \leq 0.5$ based on the results in Fig. (4.4). There is only one uniform precession of magnetization between the two mentioned DWs and another inside the matrix representing a collective dynamic response.

The comparison between our simulation and time resolved images in Fig. (4.7 a) and (4.7 d) reveals only one difference. In our TR-magneto-optically measured data, waves with a vertical wave front are observed. Their existence is clarified in Fig. (4.8 a). The magnetization variation profile along the purple line is plotted in Fig. (4.8 b) and a two-headed arrow in image and plot displays these waves during one lattice constant. To figure out their origin, we calculate their wavelength. It is around 1.8 µm, at 2 GHz, leading to a phase velocity of approximately 3.6 km/s. This is in the range of elastic waves based on previous study on the same material in Ref. [21].

Based on the above discussion and the fact that these wave fronts are parallel to the DWs' elongation, we conclude that these waves are generated from pinned and overlapped DWs (DWs in each side of antidots overlap) in their first harmonic mode. These were not predicted by our simulation because the magnetostriction effect is not an included feature in our micromagnetic simulator.

To figure out the effective factors on magnetization's dynamic vector response, at the same frequency as before, 2 GHz, the amplitude of the excitation field is increased from 56 to 309 A/m, which is five times higher than in our last simulation. The simulation output is demonstrated in Fig. (4.9 a) for the magnetization component along $\hat{\mathbf{x}}$, $\triangle m_x$. To highlight every detail, the calculated and measured results in Fig. (4.9 a,c) are depicted via colour code. The calibration bar is selected in the way that the images have the best contrast. The four simulated images are correlated to their phases on the plot (4.9 b). Four phases are denoted by purple, blue, yellow and pink in Fig. (4.9 a, b) If this plot is compared to its counterpart in Fig. (4.7 b), it can be concluded that in the similar way the matrix has a higher amplitude than the region between DWs. However, the phase difference is decreased remarkably between these two distinguished areas. This leads to less amplitude difference between the matrix' and the full supercell's (named as total in Fig. (4.9 b)) dynamic response. It can be seen in Fig. (4.9 a) that waves with low amplitude are excited. However, because of superposition between different waves from various sources, one clear wavefront can not be distinguished. They are visible inside the matrix and with much smaller amplitude inside the region confined by DWs. In the latter area, the amplitude of $\triangle\ m_x$ is so small that its colour

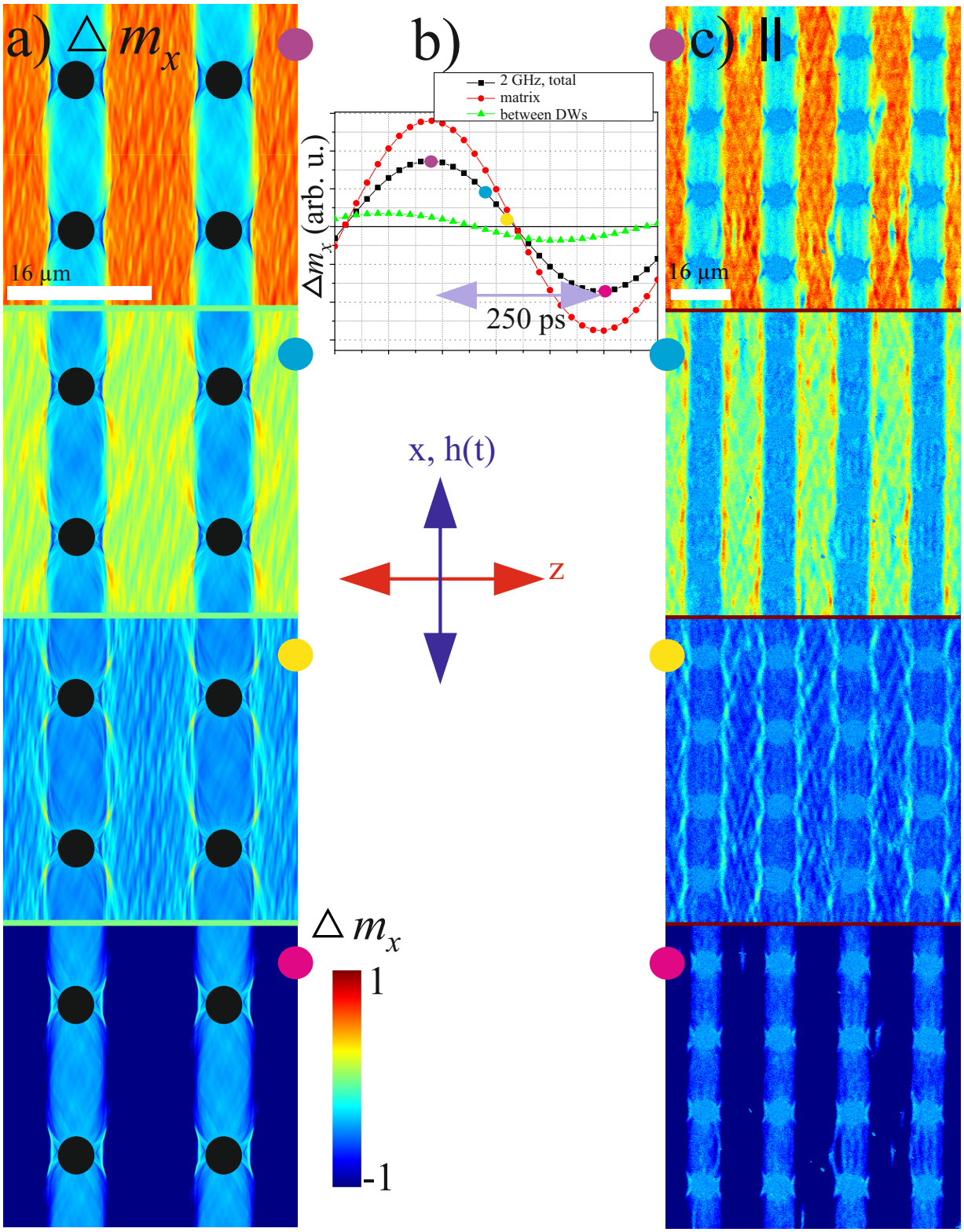

Figure 4.9: (a) The simulated dynamic magnetization response to an excitation field at 2 GHz with 309 A/m amplitude. (b) The diagram is plotted to indicate phase difference between matrix and area confined by DWs (marked in Fig. (4.6)c) in 4 images shown in (a). The time interval between first and last image is indicated by 2-headed arrows. These four phases are indicated via coloured circles in the corner of the images in (a) and their counterpart on the plot. The colour coding here highlights more details as the dynamic response is not so strong. (c) The images directly measured via TR-MOKE wide field microscope are represented in vertical sensitivity along magnetic stimuli ($h(t)$) as it is shown in the above images.

does not change notably throughout all four images. From these simulated patterns, it is clear that every part of the pattern with different $f_{r,l}$ is evoked.

From the plotted amplitude versus time in (4.9 b), it can be seen that the amplitude of the dynamic magnetization response in the area between the DWs is much lower in all phases in comparison with the matrix. Since magnetic waves have a low amplitude, they will not cover the elastic waves. Therefore, these elastic waves can be detected in magneto-optically measured data in this region, as their wave front parallel to DWs is observable in Fig. (4.9 c). The low amplitude of dynamic magnetization response in the area between the DWs can be explained based on LS-PIMM data, shown in Fig. (4.6 c). In this region the local resonance frequency is the highest, at around 3.7 GHz. Therefore, f_{exc} = 2 GHz is far from its f_r especially in comparison to the matrix with $f_{r,l}$ = 2 GHz. This area needs stronger field to be excited.

Based on the calculated local resonance frequency shown in Fig. (4.6 c), the $f_{r,l}$ is 2 GHz in the antidot array matrix. The area between the DWs have even higher $f_{r,l}$ of up to 3.7 GHz. Furthermore, based on our discussion in section (2.3.3) and Fig. (2.19), We concluded that at f_{exc} = 2 GHz BVWs can be emitted from areas with low $f_{r,l}$ = 0.1 GHz, which is a really small area in an antidot array. In addition, this wave is stopped soon after confronting an area with high $f_{r,l}$.

To sum up, 2 GHz excitation frequency is not high enough to excite BVWs or surface waves in their resonance mode with the highest amplitude of response. But applying an excitation field with the amplitude 5 times higher than before, forces almost every point (with higher natural f_r) to oscillate with a detectable amplitude since there is a direct correlation between applied field and response amplitude even far from the resonance based on equation (2.44b).

4.4.2 Prospective SWs' Sources

To understand what happens in the structure, we specified some regions in Fig. (4.10 a) as prospective areas to generate magnetic waves and we then averaged f_r inside these regions. They are marked by numbers in (4.10 a). The averaged signal all over these regions is indicated in Fig. (4.10 b), named as total in the plot. The other regions are categorized in Fig. (4.10 c-e) based on their similarity in dynamic magnetization response to an exerted step function with an amplitude of 4 A/m and t_{rise} equal to 60 ps. Moreover, for every region, the relative orientation of magnetization (indicated in Fig. (4.1)) and the observed wave vectors at higher modes up to 5 GHz (depicted in Fig. (4.4)) are similar.

From Fig. (4.10 b) four distinguishable peaks can be found. The peak at 2 GHz with the highest amplitude is correlated to the matrix, while the first peak at the lowest frequency of 0.5 GHz

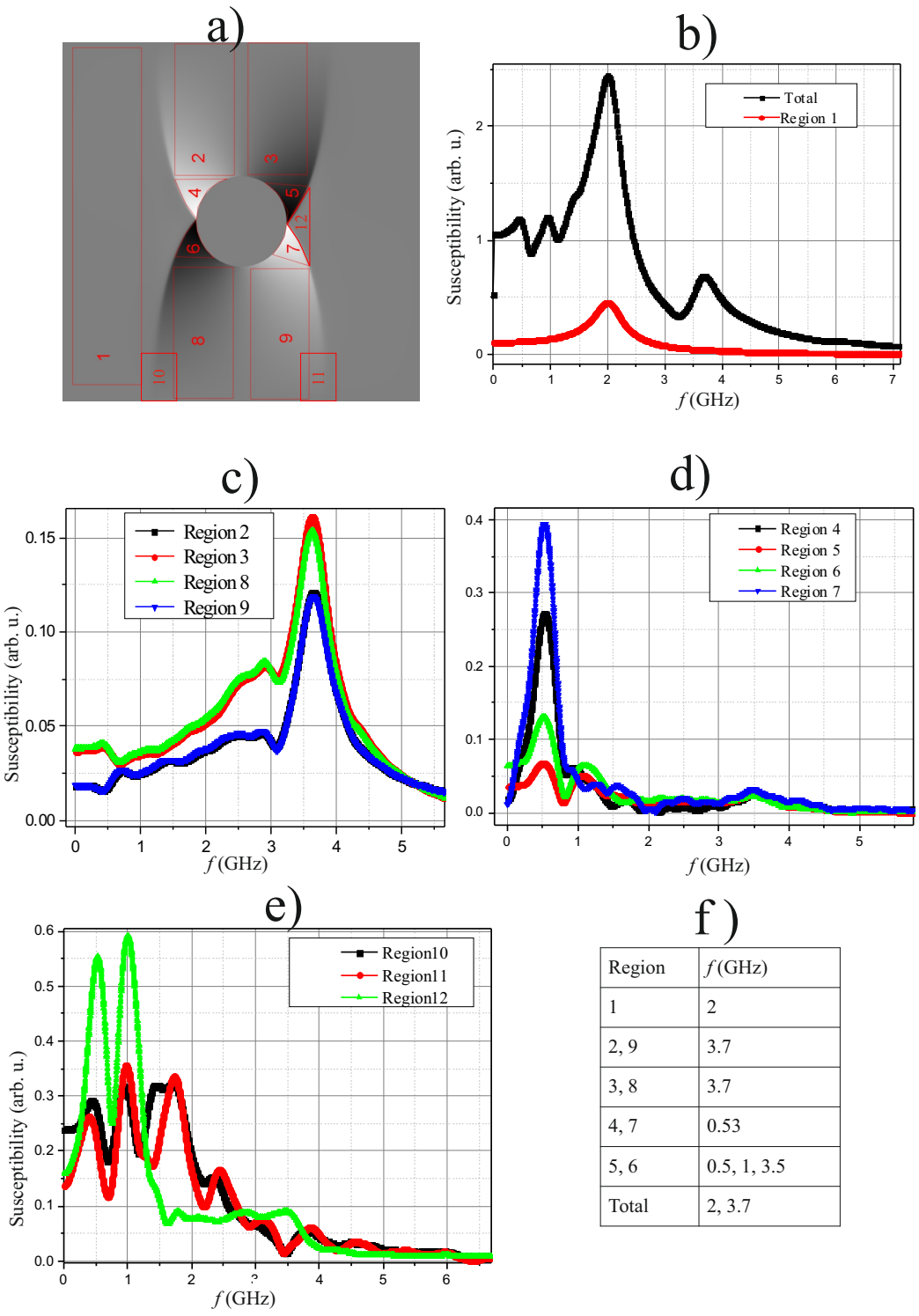

Region	f (GHz)
1	2
2, 9	3.7
3, 8	3.7
4, 7	0.53
5, 6	0.5, 1, 3.5
Total	2, 3.7

Figure 4.10: (a) The 12 regions are marked. (b-e) The averaged signal via LS-PIMM method is calculated for the mentioned regions in (a) an antidot array. They are categorized based on the similarity in their dynamic response. (f) In addition, for some regions their dominant f_r is collected via a table.

belongs to the regions 4-7, indicated in (4.10 d), and partially region 12, indicated in (4.10 e). We discussed in section (2.3.3) that the backward volume waves, BVWs' generation and propagation from these regions are expected in the low k regime at $f \geq$ 2 GHz. For low f_{exc} as we saw at 2 GHz, BVWs can be excited only from regions with f_{exc} = 0.1 GHz, with the wave vector of approximately 2.5 μm^{-1}, which is a limited region of two point-like areas on the left and the right sides of the antidot. To stimulate BVWs from a region with $f_{r,l}$ = 0.5 GHz, the excitation field's frequency should be higher than 4.5 GHz in order to emit SWs with a detectable wavelength.

The next peak at 1 GHz is attributed to the regions 5, 6 and 10-12, denoted in Fig. (4.10 e). Even though, in the low excitation field's frequency, regions with $f_{r,l}$ = 1 GHz do not emit SWs with a detectable wavelength. These moderate $f_{r,l}$ can facilitate propagation of waves coming from neighbouring areas with the lowest $f_{r,l} \leq$ 0.5 GHz. This idea can be confirmed by transient part simulation. It shows that the point poles, on the left and right side of every antidot, which has lowest $f_{r,l}$, are excited even at low frequency (as low as 2 GHz). Their neighbourhood's local resonance frequency is approximately 1 GHz, therefore SWs with vertical wave front (plane-wave like) are emitted. But this wave can not propagate far to the neighbour area with higher $f_{r,l}$ and will stop propagation before the matrix, since the matrix resonance frequency $f_{r,m}$ is equal 2 GHz all over it. The wave from pole points behave as stimuli and all of the magnetic moments in the matrix precess together. By f_{exc} enhancement, the mentioned point source's wave propagate further inside the matrix. Moreover, the first neighbours on the left and right side along the horizontal axis of the antidot lattice, follow the same mechanism. This means that every pole is a SWs source for neighbours and so this leads to multiple reflections of SWs.

Following the above discussion, we expect that an increase in f_{exc} causes emergence of new areas as potential sources of magneto static waves, MSWs. These areas in addition to the previously excited regions, which now oscillate with higher wavelength, make an interesting image of superposition between SWS.

4.4.3 Spin Waves' Emission

In Fig. (4.11 a) dynamic magnetization evolutions $\triangle m_x$ are depicted in response to a harmonic excitation field with 105 A/m amplitude at 3 GHz frequency. The corresponding phase difference between the images is illustrated via a plot in Fig. (4.11 b). The images in (4.11 a) are selected in the way that the supercell's averaged signal varies from its minimum to maximum.

The plot shows phase differences (time evolution) in three different areas. The black curve is calculated from data all over the supercell (named as total) while the green and red ones denote

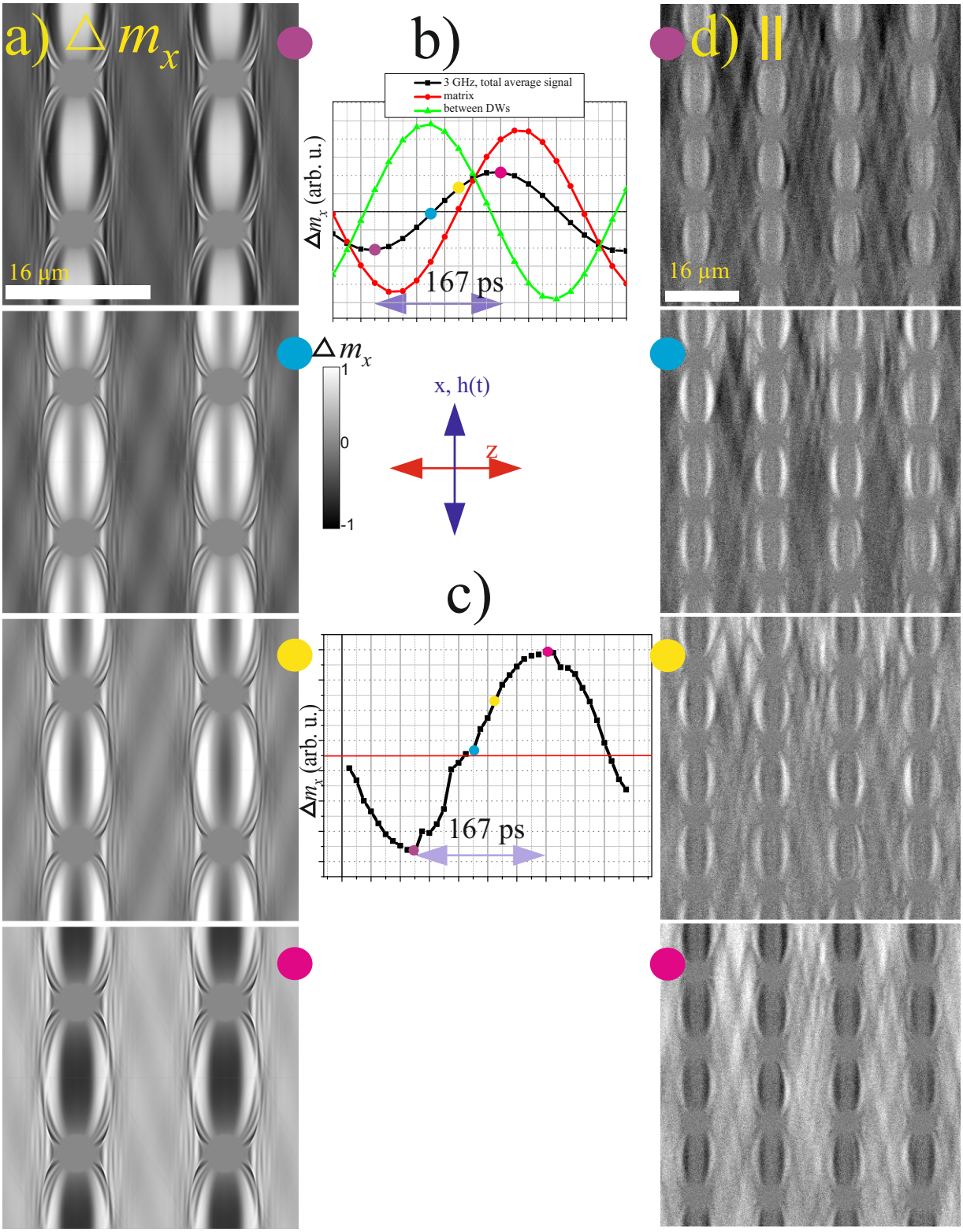

Figure 4.11: (a) The time evolution of magnetization exposed to a harmonic excitation field with 309 A/m amplitude and 3 GHz frequency is calculated and shown for four different phases. (b) The black, red and green curves compare the $\triangle m_x$ from complete supercell, the matrix and the area between DWs (indicated in Fig. (4.6 c)). Moreover, the coloured circles in the corner of images in (a) connect them to their correlated phase in plot (b). (c) The counterpart plot from direct measurement via microscope is depicted. (d) The corresponding measured images with the same phases as in (a) represent the great agreement with the simulated data.

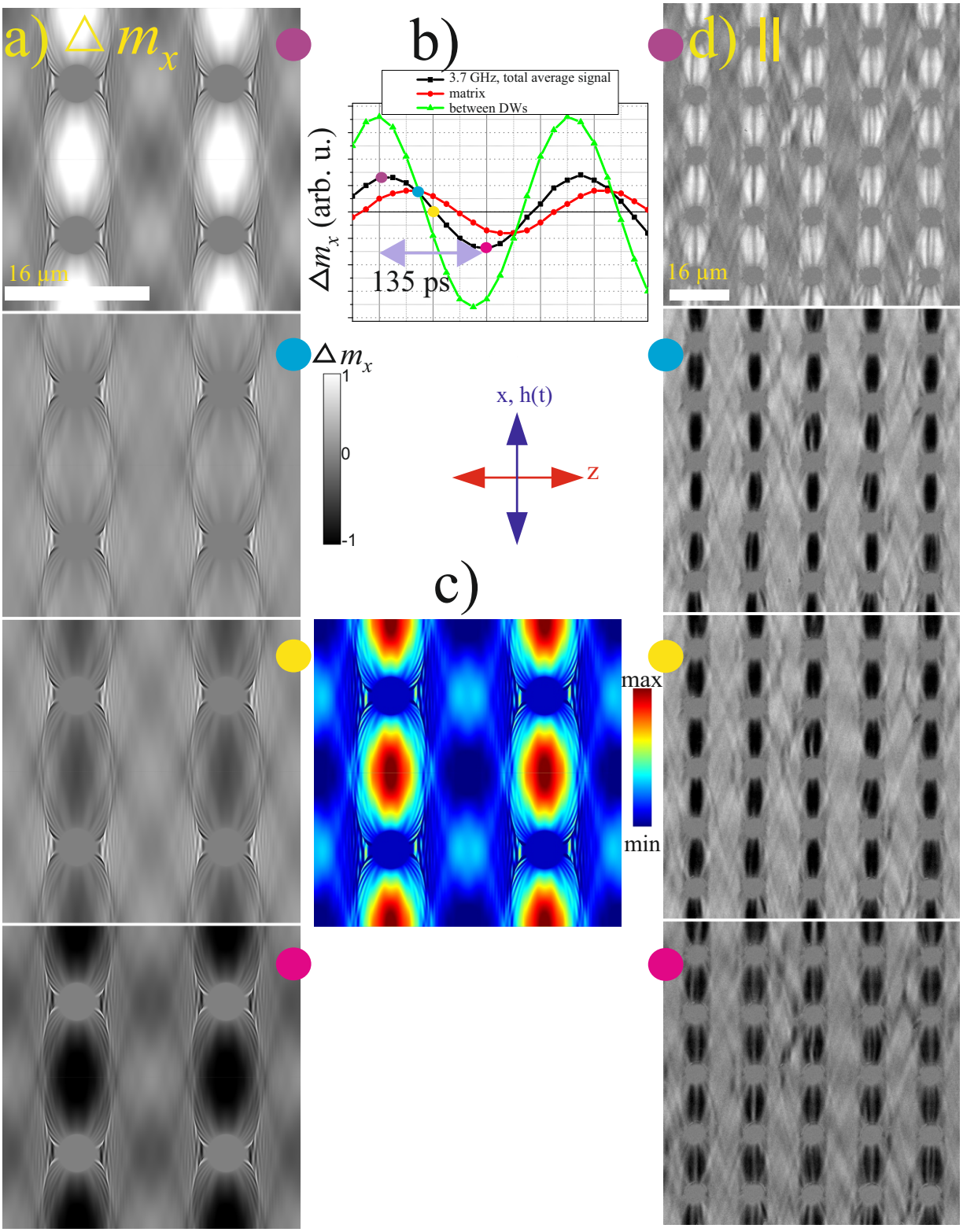

Figure 4.12: (a) The antidot array's dynamic response is calculated for different phases by applying f_{exc} = 3.7 GHz. The amplitude of this excitation field is 28 A/m, half the previous simulations. The relevant grey scale is included as well. (b) The phase differences between images in (a) are indicated by coloured solid circles. The three areas know as total, matrix and between DWs are almost in phase. (c) The first image of (a) is coloured to make comparison easy with Fig. (4.4) at 3.7 GHz. (d) The measured images in the same phases as (a) are depicted. They are measured via TR-MOKE wide field microscopy.

data from regions between dots and inside the matrix, respectively. Every coloured circle on the plot shows the phase related to its counterpart image with the same coloured circle in the right top corner of image. In can be seen that there is an almost 180 degree phase difference between signals obtained from the region confined by DWs and matrix which is more noticeable in the first and the last images, corresponding to maximum and minimum of the over all signal. This phase difference leads to a lower overall signal amplitude since the signal from different regions partially cancel each other. In addition, the phase difference highlights the fact that 3 GHz is neither $f_{r,m}$ nor $f_{r,DW}$.

The data obtained via TR-MOKE wide field microscope is measured for a complete period of time. The phase shown in plot (4.11 c) is comparable to the black curve for the simulated data (4.11 b). Four corresponding images in four phases (denoted by coloured circles on the plot) are indicated in Fig. (4.11 e). They are recorded under the same conditions as for the simulation, exerting a harmonic excitation field at 3 GHz to the antidot array. As 3 GHz is lower than $f_{r,l}$ = 3.7 GHz in the area between the DWs, this region is not excited yet, but the SWs originating from DWs change the pattern relative to the uniform precession recorded in Fig. (4.7).

The calculated dynamic magnetization component is illustrated for the antidot array in Fig. (4.12 a) after the harmonic stimuli's frequency is enhanced to 3.7 GHz. As the harmonic field's frequency is equal to $f_{r,l}$ inside DWs regions, the simulation results are obtained by applying 28 A/m. This is the half of previously used amplitude. This low amplitude prevents the variation of the static magnetization pattern during the transient part in our simulation. The grey scale calibration indicates minimum to maximum intensity with a black to white spectrum. Like before, the time evolution of the magnetization component parallel to the excitation field, $\triangle\ m_x$, in the half time period is shown in the plot (4.12 b) where the averaged signal from full supercell, matrix and region between DWs are compared via a black, red and green sinusoidal curve respectively. The coloured circles on the averaged signal from the full supercell determine the phase corresponding to every image in (4.12 a). This calculation manifests newly excited SWs around the dots. In addition, a diamond like pattern forms inside the area limited by DWs.

It can be seen in Fig. (4.12 b) that the amplitude of the dynamic response in the region between DWs is much higher than matrix and full cell's signal. Furthermore, the phase shift of the region between DWs, which is in $\pi/2$ phase difference with the excitation field, and the matrix is much smaller than before, less than $\pi/4$. Both of these facts can be explained through our knowledge from $f_{r,l}$ calculation. This stimuli frequency is equal to $f_{r,l}$ for the region between DWs, therefore, this area responds with the highest amplitude. Moreover, this frequency is close to 4 GHz which is twice $f_{r,m}$ and leads to second mode excitation there.

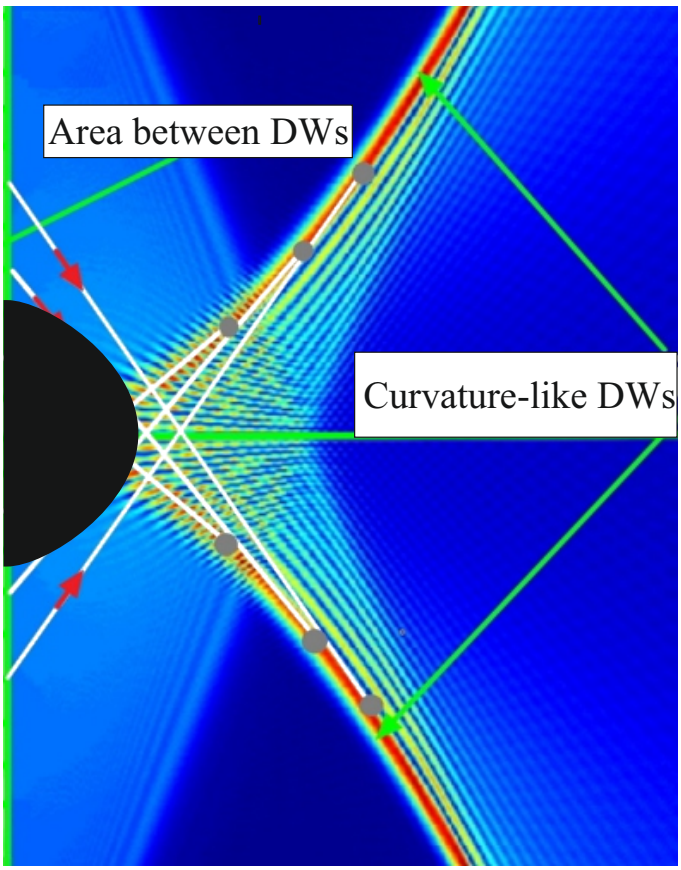

Figure 4.13: The red curves display the surface emitting waves. They are comparable with two DWs on one side of the antidot shown in Fig. (4.1). Adopted from [167].

Furthermore, to compare the calculated data by applying a harmonic excitation field and simulation data via PIMM method, the maximum total response indicated by purple circles in Fig. (4.12 a) is shown in (4.12 c) with the same colour spectrum as Fig. (4.4) at 3.7 GHz. There is an excellent agreement between the images from the dynamic response of magnetization to a harmonic excitation and the achieved amplitude of the calculated permeability spectrum at the same frequency for every cell.

To evaluate our simulation, the images are recorded via TR-MOKE wide field microscope in one full period of time. The plot in Fig. (4.12 d) shows the time resolution between these images in addition to the corresponding images in four phases (the same phases as in the images in (a)) indicated by coloured circles on the plot. These images are depicted in Fig. (4.12 b).

4.4.4 Caustic Waves Because of Reflection from DWs

We expect by considering the lower f_{exc} = 3.0 and 3.7 GHz the analysis is simpler because just BVWs from areas with $f_{r,l} \leq 0.5$ GHz are excited. However, the obtained simulated pattern is not simple. One reason is that the excited areas, mostly around DWs, are curved.

Two DWs in every side of one antidot are similar to the semicubical parabola (cuspidal cubic)

function in mathematics. This function is defined with this general equation:

$$x^2 - a^2 z^3 = 0 \qquad \text{for } a > 0 \tag{4.4a}$$

$$\text{and so:} \qquad x = \pm a z^{\frac{3}{2}} \qquad \text{for } z \geq 0 \tag{4.4b}$$

which is written in our coordination. The point $(0,0)$ is called singularity (cusp) which is a point where an imaginary object moving on the curve changes its movement direction. This point is comparable to the magnetic poles formed on both sites of the antidot in the discussed magnetic structure. It is possible, mathematically, to confirm the generation of waves from these curved surfaces via caustic engineering. The surfaces which reflect waves are found for a given image consisting of waves through a caustic engineering process. This is done via division of the surface into smooth micro-surfaces. An exemplary symmetric caustic wave is shown in Fig. (4.13). The curved surfaces shown in red in this figure are similar to the DWs of the antidot pattern shown in Fig. (4.1). Furthermore, comparison between these symmetric caustic waves and results achieved from LS-PIMM for frequencies higher than 2 GHz as illustrated in Fig. (4.4) shows similarity. Patches in the mentioned data obtained via LS-PIMM confirm reflected waves interference from DWs.

4.4.5 Higher Excitation Frequencies, Higher Modes

We continue to increase the excitation field's frequency to 4 and then 5 GHz. The results are illustrated in Fig. (4.14) and (4.15), respectively, where in every figure part (a) includes the simulated pattern displaying the dynamic response of the magnetization component $\triangle m_x$. This component variation during time is plotted in (b) for one full period. The phases corresponding to the four images in (a) are indicated on this plot by colour circles. The frequency enhancement above the highest $f_{r,l}$ = 3.7 GHz reduces the phase difference between the signals from the matrix and the region between the DWs. At f_{exc} = 4 GHz, while the matrix has $\pi/2$ phase difference with stimuli, the area between DWs is a bit behind than the matrix signal phase. This is not the case at f_{exc} = 5 GHz where, matrix, DWs area and full supercell signal (red, green, black curves in (4.14 b) and (4.15) b) are all in the same phase. In (c), one image from (a) is shown via colour code to facilitate comparison with our simulation throughout PIMM method, denoted in Fig. (4.6). At both of the mentioned frequencies, 4.0 GHz and 5.0 GHz, the coloured images are completely in agreement with the magnetization configuration pattern predicted by the LS-PIMM method. The dynamic magnetization component is measured by microscope in vertical sensitivity under the same condition (the same frequency and amplitude of *h(t)*). The magnetization time evolution versus time

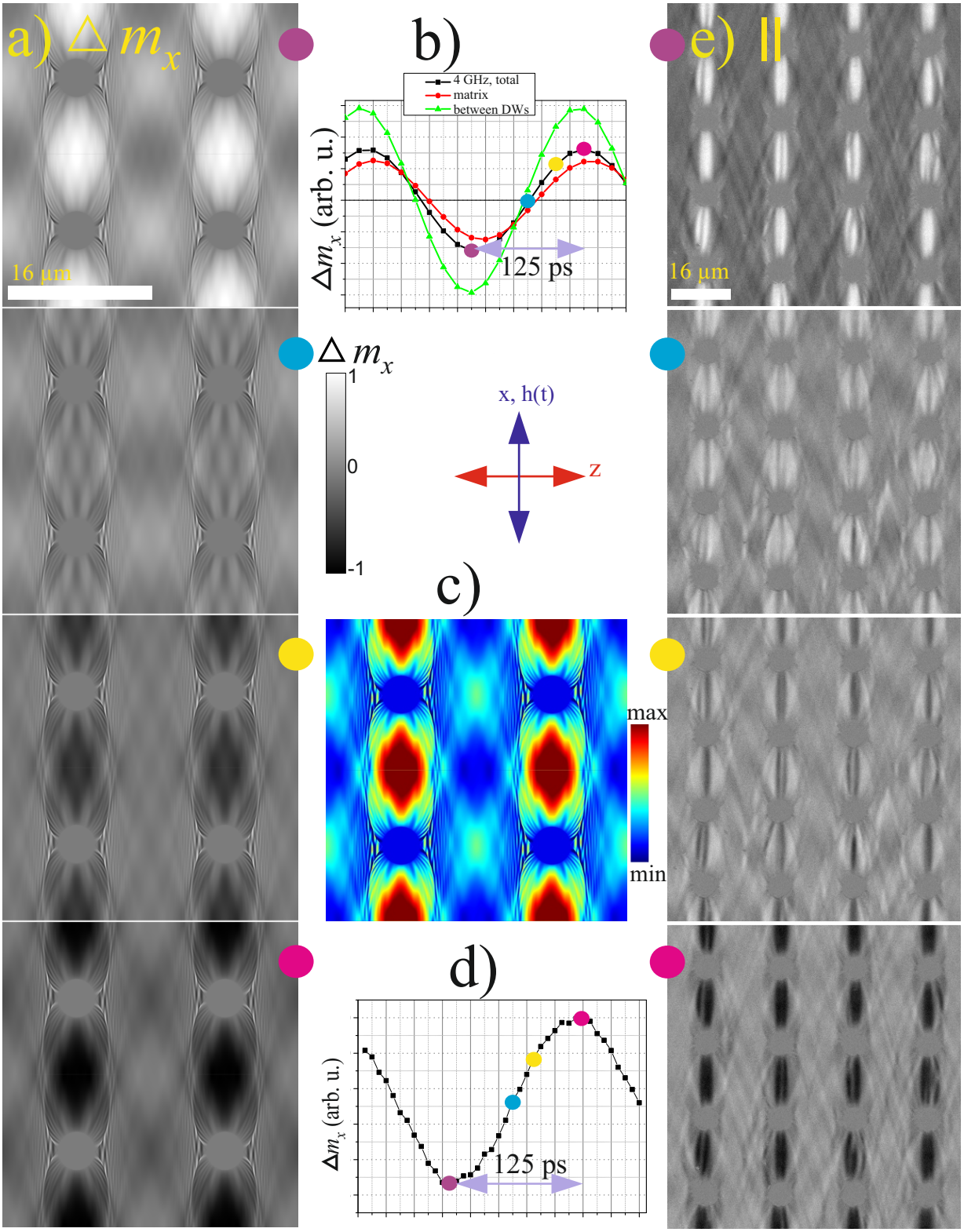

Figure 4.14: (a) The calculated data are obtained under application of a magnetic field stimuli at f_{exc} = 4 GHz with an amplitude of 56 A/m and specified in the grey scale with calibration next to them. (b) The images' phase are displayed in the plot with the same coloured circles as in the corner of images. (c) The first image in (a) is coloured to be comparable with Fig. (4.6) at 4 GHz and the calibration code is shown as well. (d) The counterpart plot for directly measured image via TR-MOKE wide field microscope is demonstrated. Furthermore, the time scale is illustrated via a two-headed arrow in (b) and (d). (e) For indicated phase point in (d) corresponding images are represented.

is indicated for all measured points during one full period in (d) and for four points in the phase diagram, highlighted by circles. The corresponding measured data via microscope are illustrated in (e) for the same phases as simulated results in (a).

The agreement between simulated and measured MOKE image is great. As excitation frequency increase to 5 GHz, the area between DWs splits into two branches in sides and one in the middle. This splitting is more evident at f_{exc} = 5 GHz rather than at f_{exc} = 4 GHz and we will see a diamond-like shape there, indicated in Fig. (4.15 a,e). Based on simulation, the contrast from the matrix is lower than from the DWs region. Therefore splitting in this area is generally better visible in the magneto-optically measured data. Moreover, the patches in the magnetization pattern are results of waves' reflection from the curved part of DWs exactly in the vicinity of the antidot. This reflection and so symmetric caustic waves propagation from DWs in every side of the dots and then their superposition make a mirror-like image from the area between dots inside the matrix.

We refer to our discussion in section 2.3.3 and 2.3.4 about the relation between f_{exc}, $f_{r,l}$ and excited BVWs' wavelength.

To complete our calculation, the calculated data in this excitation frequency is displayed in Fig. (4.16 a) for different phases indicated in the plot (4.16 b).

From our simulation, the wavelength of SWs in the vicinity of dots decreases by increasing f_{exc} but as the regions with the lowest $f_{r,l}$ are closely connected to each other, the SWs with different wavelength are superposed and thus the separation between BVWs is not possible. Here, we utilized DFT in time and space to distinguish existing waves.

4.4.6 DFT in Space and Time

Based on elaborated information represented in Fig. (4.6), there is variety of natural resonance frequencies. In Fig. (4.17 a) four different lines are indicated and shown inside one of our previously simulated images. The DFT method is utilized along these lines and the corresponding results manifest the relation between frequency and wave vector which is shown in Fig. (4.17 b) and (4.18). Every graph is plotted based on simulation data after applying a harmonic excitation field at a specific frequency in the range of 0.1 to 6.0 GHz. Every row in both Fig. (4.17 b) and (4.18) includes information along one line while every column demonstrates one frequency's data. To get the idea about the detected wavelengths, the top horizontal axis display wavelength in nm and the bottom one illustrates the wave vector, $k/2\pi$ in $1/\mu$m. Moreover, to facilitate comparison, graphs in every row (for one line at different frequencies) has exact same axis scale, either vertical or horizontal axis. The colour code calibration is shown next to every graph, indicating DFT

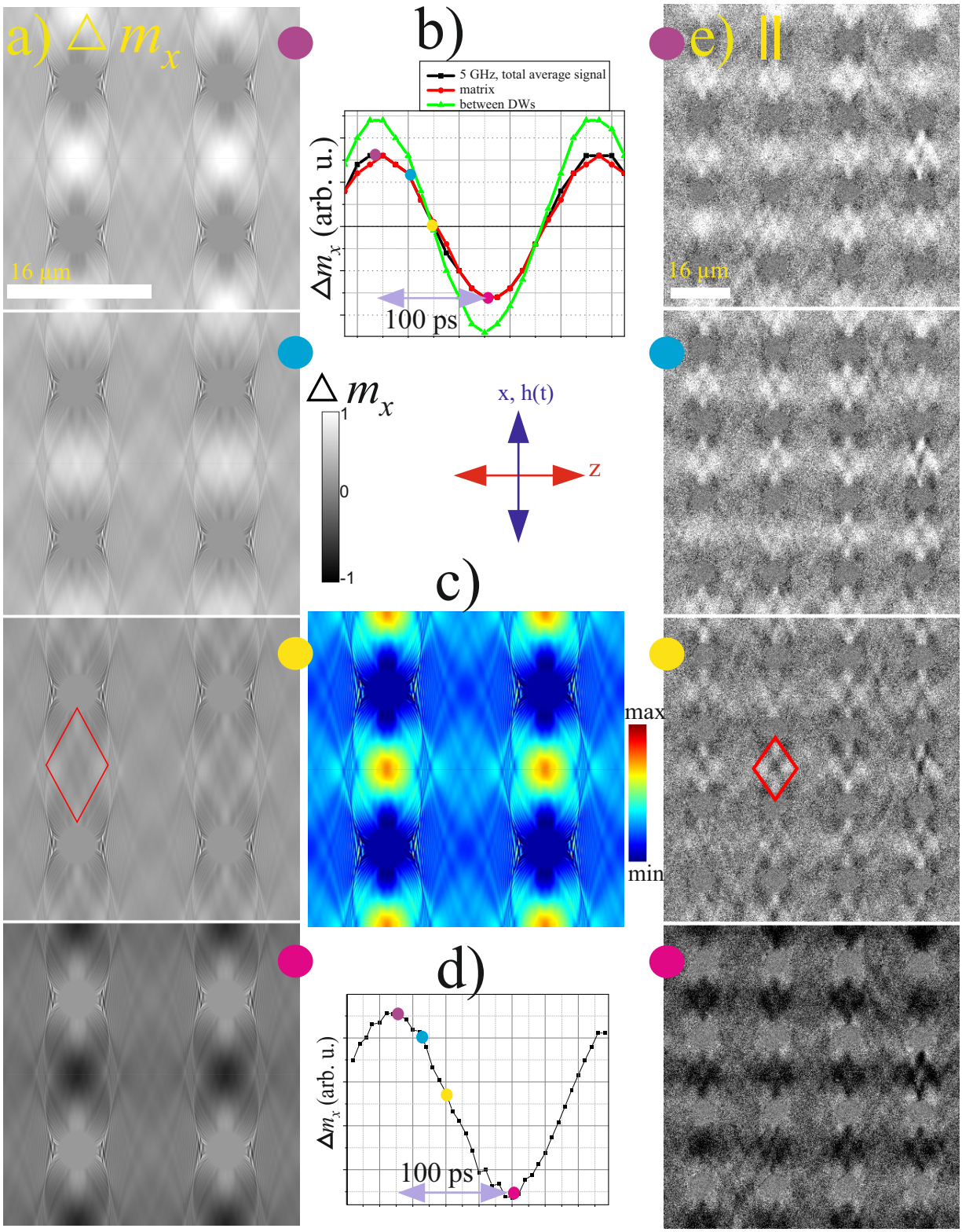

Figure 4.15: (a) The dynamic magnetization response component dm_x is simulated under application of 56 A/m harmonic field with a 200 ps period. The results are specified in the grey scale with the calibration code next to them. (b) Every image's phase is displayed in the plot to the same coloured circles as in the corner of the images. (c) The first image in (a) is repeated in colour to make it comparable to Fig. (4.6) for 5 GHz. The corresponding calibration code is shown next to the image. (d) The counterpart plot for directly measured image via TR-MOKE wide field microscope is demonstrated and its corresponding images are represented in (e). Furthermore, the time scale is illustrated via two-head arrow in (c) and (d).

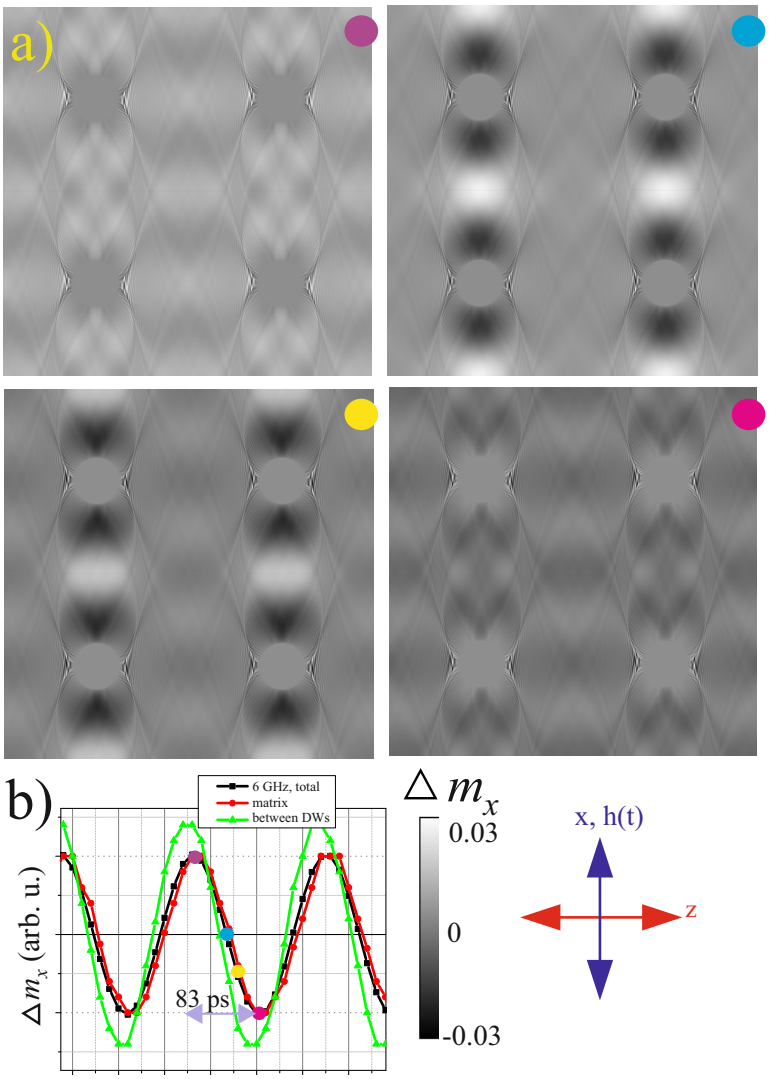

Figure 4.16: (a) The images are calculated by applying harmonic excitation field with 6 GHz frequency and 56 A/m amplitude. Their grey scale calibration is displayed as well. (b) The simulated images' phase differences are plotted. The coloured circles in the corner of the images connect them to their correlated phase in (b). The time scale is illustrated by a two-headed arrow to estimate time differences between images in (a).

intensity.

The purpose of DFT is to determine and highlight dominant wave vectors at each exerted frequency. The dominant wavelength in every plot (and so every individual frequency) can be seen as a point in dark blue. Furthermore, in some plots, the most probable wave vectors (with higher DFT intensity in blue and yellow colour) form one horizontal line. This dispersionless relation between f and k means that group velocity is zero (zero slope in f(k)) which is a feature of standing waves. These lines' existence can be attributed to the nonuniformity of the local resonance frequency. When there is a remarkable variation of $f_{r,l}$ between two neighbouring areas and the excitation frequency is in the range $f_{r,l,lower} < f_{exc} < f_{r,l,higher}$, the region with $f_{r,l,lower}$ is excited and its neighbour with $f_{r,l,higher}$ is not.

The similar dispersionless modes are observed experimentally via BLS for a square dot array

with different size, 2× 0.2 μm and 1× 0.1 μm with a thickness of 40 nm in Ref. [168], see Fig. 7 showing dots array and Fig. 18-20. Their corresponding calculated data in the mentioned reference are DE modes, see equation (11).

Such a dispersionless relation in our case can be seen more pronounced along line 3. Along this line, two areas with different $f_{r,l}$ meet, one area in exact vicinity of the dot with $f_{r,l} \leq 1$ and the other, which is matrix with $f_{r,l} = 2$ GHz. Along the other lines, line 1 and 2, a similar behaviour can be found, however at more than one frequency. The reason is that these lines involve higher modes coming from their border with the lowest $f_{r,l} \leq 0.5$ GHz.

The antidot square array is more complicated, the behaviour is not simple but the above summarized information can provide more detail to understand the system. For instance, the high similarity can be seen between area 1 and 2 at all studied frequencies. Another point is that along line 4, there are other dominant wave vectors, beside one which is equal to 1/(lattice constant = 16 μ m). Furthermore, for $f_{exc} \geq 3$ GHz, there are several waves at different frequencies propagating parallel to line 1 and 2.

4.4.7 Caustic Waves Because of Diffraction from Antidot

The previous studies manifest the possibility of focusing SWs in ferromagnetic materials [169],[30],[158]. The approach to find magnon's focusing pattern is similar to the ones for phonons and magnetoplasmon polarization in Ref. [170]. The method is based on the theory of magnetostatic waves (leading to permeability tensor definition) and Walker equation (to obtain features of the propagating waves). Afterwards, the slowness surfaces are calculated for the frequencies above the natural resonance frequency of the material. They are curves in k plane for a specific frequency. The focusing pattern is found by calculation of normal to these curves in every point. These normals determine the energy flow direction [169]. This energy magnitude is connected to the curvature (c) of the slowness surface reversely ($e \propto c^{-1}$) and so for flat surfaces, we have caustic waves. The corresponding results for BVWs and surface wave are predicted theoretically in Fe and YIG full films in Ref.[169].

The conclusion is that to create a caustic wave, we need a kind of point source and a horizontal part in dispersion relation (isofrequency curve). The first requirement can be fulfilled through an antidot pattern in ferromagnetic materials.

There are studies confirming caustic waves generation by a single antidot via BLS measurements [27] and [30]. The antidot breaks the translational symmetry of the full film and therefore, for a specific frequency, there are different k. This paves the way to have an isofrequency curve.

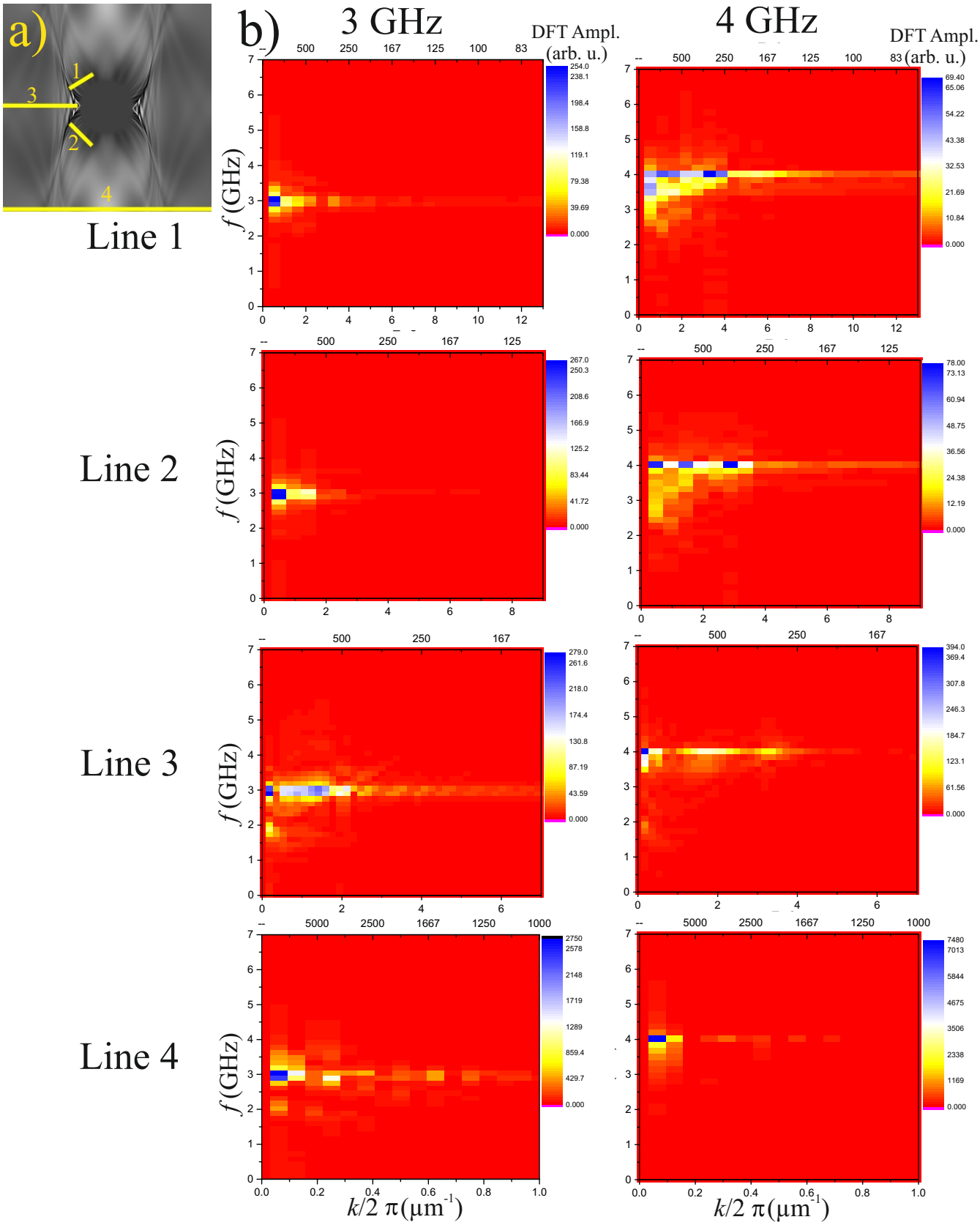

Figure 4.17: (a) The four lines are marked in one of the simulated patterns for an antidot array. (b) The DFT method is applied along the mentioned line in (a) to calculate dominant wave vectors two excitation field's frequencies via contour plots. The colour calibration for every individual plot can be seen next to it, without normalization. It shows DFT amplitude with arbitrary unit. Every column is specified for one frequency and every row for one line. The lower and upper horizontal axis display wave vector (k/2π) in μm^{-1} and wavelength in nm, respectively.

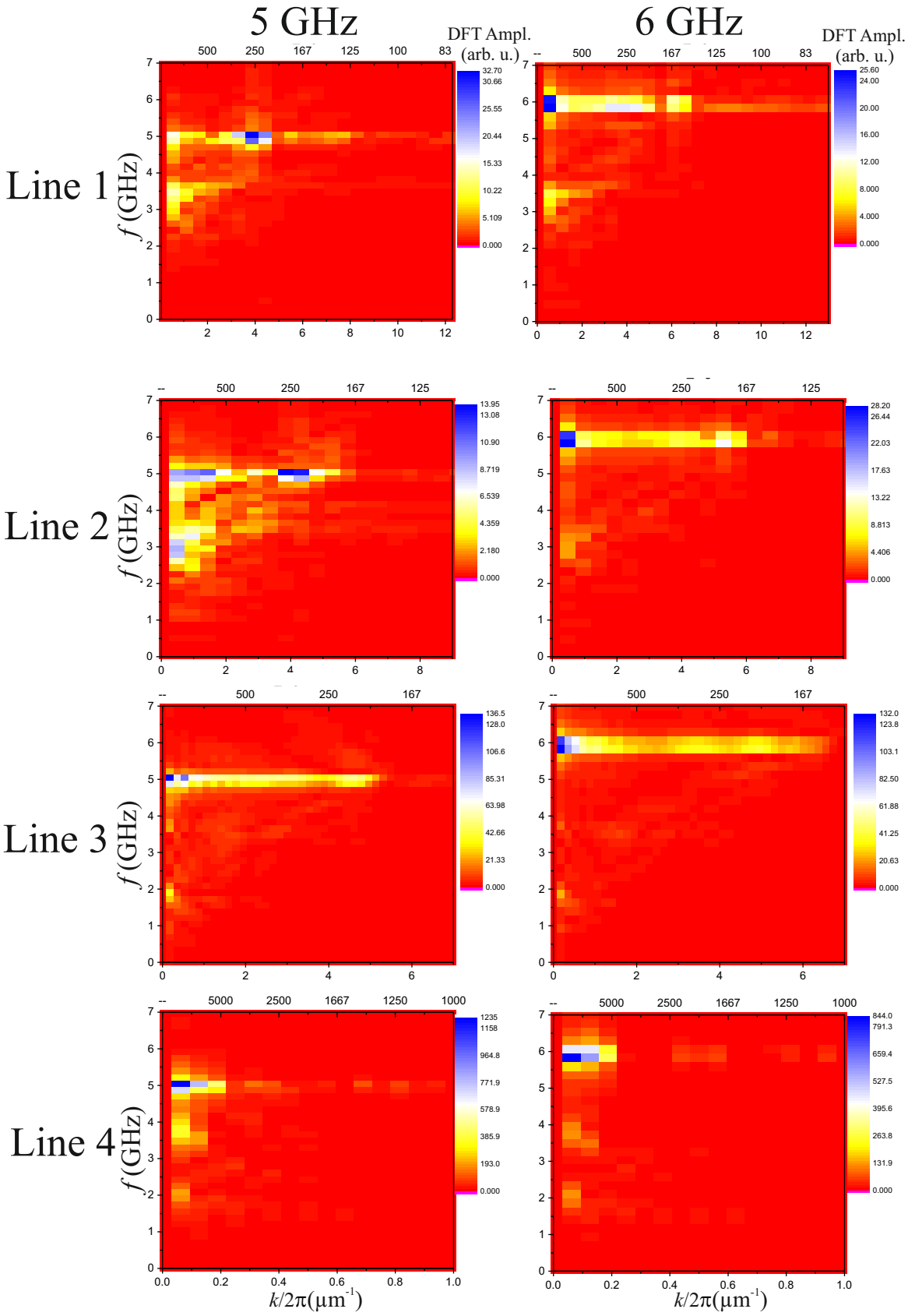

Figure 4.18: The DFT method is used to calculate dominant wave vectors at two excitation field's frequencies 5.0 and 6.0 GHz via counter plots along four lines marked in Fig. (4.17 a). The colour calibration for every individual plot can be seen next to it without normalization. It shows DFT amplitude with arbitrary unit. Every column is specified for one frequency and every row for one line. The upper and lower horizontal axis display wave vector ($k/2\pi$) in μm^{-1} and wavelength in nm, respectively.

In Ref. [27], a microstrip antenna located on one side of the sample produces a RF (radio frequency) magnetic field. This electromagnetic field incidents the sample physical edge and plane SWs travel toward the antidot. For specific frequency, SWs partially pass antidot and make caustic beams while the other part is diffracted and reflected backward (toward RF source) from the antidot.

In Ref. [30], the microstrip antenna is directly under sample so that a single antidot is in the center of antenna. The demagnetizing field calculation makes it evident that nonuniformity in the internal field around the antidot leads to plane SWs scattering from it.

Back to our sample, we have an antidot array with 4 μm in diameter and lattice constant of 16 μm. In the mentioned references with a single antidot, SWs occur from one side to the antidot and a caustic or semicaustic beam on other side can be seen (see for instance Fig. 3 in Ref. [30]). In our case, every antidot acts as a source to produce caustic waves for neighbours and thus, there is a full symmetry in the dynamic magnetization pattern because of 2D symmetry in the antidot array.

In addition, our calculated demagnetizing field shows a non-uniform effective field and as a result a variation of local resonance frequency around every antidot (see Fig. (4.3 b)). In Ref. [158], SWs emission from a single antidot on a thin film made of permalloy-like material is simulated after applying a harmonic stimuli field. It is shown (see Fig. 2 and its following discussion) that there is a tendency to emit caustic waves in a 40 nm film rather than in a much thinner one (6 nm). Therefore, our sample with a thickness of 50 nm is thick enough to focus SWs provided that the stimuli frequency is tuned correctly.

To emit a caustic wave, the f_{exc} should be at least higher than $f_{r,m}$ in the antidot samples [158] and [30]. Naturally, this required frequency is higher than $f_{r,l}$ of a continuous film with the same material and features.

When the harmonic field's frequency is 3 GHz and higher, a mechanism similar to Ref. [30] and [158] is activated in the region between DWs, distinguished in Fig. (4.3). The stimuli frequency elevation up to 5.0 and 6.0 GHz, which is above the highest $f_{r,l}$ throughout our supercell, increases the chance of caustic wave detection. This accompanies with the excitation of BVWs in the areas with $f_{r,l} \geq 0.5$ GHz. Moreover, the area with $f_{r,l}$ up to 3.7 GHz (highest $f_{r,l}$) can be excited with its highest amplitude of response. Last but not least, the area around DWs can be an emitter of surface waves while the caustic beam production mechanism is still active.

4.4.8 Last Hints

There are two important differences between our sample and above mentioned references and so the their results, besides differences in materials and physical sizes. The first one is the existence of DWs around the antidot and as we confirm via our calculation, this leads to non-uniform $f_{r,l}$ more pronounced than for one isolated antidot because of local changes in H_{dem}. Another important dissimilarity is that every antidot is surrounded by four first and four second nearest neighbours in the square array. Therefore, reflection from them and coupling between them even in static pattern can make big differences and lead to a highly complex system.

Furthermore, in the high static magnetic field, there is the possibility of detecting perpendicularly standing spin waves, PSSW, at higher frequencies. For instance, in reference [50], propagation of PSSWs are detected at a frequency range of 10 to 20 GHz for either full film or antidot array 0.7×3.5 μm^2 in 50 nm thick CoFeB when a magnetic field up to 150 mT is applied. In addition, to uniform precession and PSSWs, an extra DE mode has been measured by patterning film as antidot [50]. In PIMM experiments, our goal is to measure the dynamic behaviour in small fields around remanence up to the minimum field required to saturate. Therefore, PSSWs are not expected.

In ferromagnetic materials, the spin waves refraction index depends highly on the magnetization direction. If antidot array periodicity is smaller or equal to the wavelength of spin waves, from nm to a few μm, this artificially made structure is defined as a meta material. For such a structure, the dispersion relation of magnons is different. In addition there is a band gap for waves propagation [113]. Because of our structure's periodicity of 16 μm, our samples are not considered as meta materials.

4.5 Summary

A square array of antidot made of $Co_{40}Fe_{40}B_{20}$ was investigated while a static magnetic field lower than the saturation field was applied. Then the dynamic magnetization response of the sample at different frequencies in the range of 0.5 to 6.0 GHz was simulated via a PIMM method. The dynamic simulation results at the frequency range 2 to 5 GHz by application of a harmonic magnetic field' stimuli were compared with their counterpart measured via wide field TR-MOKE microscopy. The simulation was confirmed at all mentioned frequencies by the measurements' result.

There is more than one mechanism of spin wave propagation in this system. First, based on the

discussion in section 2.3.3, 2.3.4 and 4.4.2, there is a possibility of combination of DE and BVWs in different modes. It is not possible to formulate magnetization dynamic behaviour as a function of time and space coordination as it has been done for spin waves propagation in magnetic material stripes [171], [172]. Therefore, the DFT method is used to find all possible waves at different frequencies. Furthermore, elastic waves were detected at low f_{exc}.

The other involving factor in the formation of the observed pattern for dynamic vector response of the magnetization is caustic waves, either their reflection from DWs and antidot neighbours or their creation because of diffraction from every antidot and then reflection from neighbouring antidots.

Chapter 5

The Magnetic Wave Excitation in Two Antiferromagnetically Coupled Layers Patterned into Antidot Arrays

In this chapter, a double layer antidot array is discussed that was introduced in section (3.4.1). The sample is a double layer $Co_{40}Fe_{40}B_{20}$. Each layer's thickness is 25 nm and they are separated by 0.8 nm of Ru. This interlayer induces antiferromagnetic coupling between the layers by RKKY interaction (see section 2.1.2). In addition, our thin film is patterned as a square antidot array of $4\times$ 12 μm^2 , with a diameter of 4 for every dot and 12 as antidot array's lattice constant.

In the following, the static domain configuration is considered and then the dynamic response to a global, homogeneous excitation field applied via a very wide CPW to the antidot double layer. The various magnetization configuration corresponding on different points in the sample hysteresis are studied in order to make a complete image of static and dynamic behaviour, specifically where the layers have either partially or completely antiparallel magnetization alignment. Every point's behaviour is unique in comparison with both single layer antidot samples, investigated in the last chapter, and double layer samples that are ferromagnetically coupled.

The film thickness is 50 nm and therefore, in the experimentally measured images with wide field TR-MOKE, we observe both layers response together and a separation between the layers' response is not possible. In order to obtain the individual layer's behaviour, static and dynamic simulation are utilized as a powerful tool for all cases with the help of the micromagnetic simulator, Micromagus [95], [173].

Measuring via wide field TR-MOKE microscopy is always challenging as a higher amplitude of the excitation field can lead to a higher signal to noise ratio and therefore, the recorded data as

images are of higher quality. On the other hand, high excitation field can cause changes in the static pattern due to the variation in the local effective field. Therefore, in all of the measurements, we try to make a balance between these two involving factors and apply the signal in such a way that it does not influence the static domain pattern.

Fig. (5.1 a) illustrates the inductive measurement displaying the magnetization variation $\triangle m_z$ along the magnetic bias field. The magnetic anisotropy axis and the static magnetic bias field are parallel. The measurement started by applying 8 kA/m, which is enough to saturate our sample. The field is reduced to zero and further decreased to -8 kA/m. This makes one branch of hysteresis in Fig. (5.1 a). It can be seen that the static magnetization along the magnetic bias field is approaching zero upon reduction of the absolute magnetic bias field towards the remanent magnetization state. The corresponding magneto-optically measured data are shown in Fig. (5.1 b) for the highlighted points in the hysteresis. These images depict the sample's static magnetization configuration after a magnetic field is reduced from saturation, at + 8 kA/m, to 0.48 kA/m, 0, -0.48 kA/m and -1.6 kA/m, respectively. In addition, the other component of magnetization in $\hat{\mathbf{x}}$ direction is reported in Fig. (5.2) for the same magnetic field values which are mentioned above for every image. The coloured circles in the right corner of the images correlate to their corresponding points in the magnetic hysteresis. Moreover, the grey scale calibration next to the magneto-optically measured data indicates the normalized magnetization amplitude.

5.1 Parallel and Antiparallel Magnetization Between Layers

5.1.1 Static Domain Behaviour

In this section, we consider the first point indicated by a purple circle in both hysteresis and in the magneto-optically measured data in Fig.(5.1 a,b) and (5.2). From, the magnetic hysteresis, it can be seen that the sample is no longer saturated at 0.48 kA/m parallel to the magnetic field and the magnetization rotates in some areas along the horizontal axis of the antidot array. However, the matrix is still saturated.

In addition, Fig. (5.3 a,b) shows the calculated static magnetization components along $\hat{\mathbf{x}}$ and $\hat{\mathbf{z}}$ for every layer in the same bias field. There are four distinguishable regions marked as R1 to R4. The colour code is common for these four images and shows a normalized magnetization amplitude from -1 to +1, corresponding to dark blue and dark red, respectively. Moreover, to clarify the magnetization rotation between the marked regions, the magnetization moments are displayed via vectors in (5.3 a). The magnetization angle relative to the applied field direction $+\hat{\mathbf{z}}$ is indicated

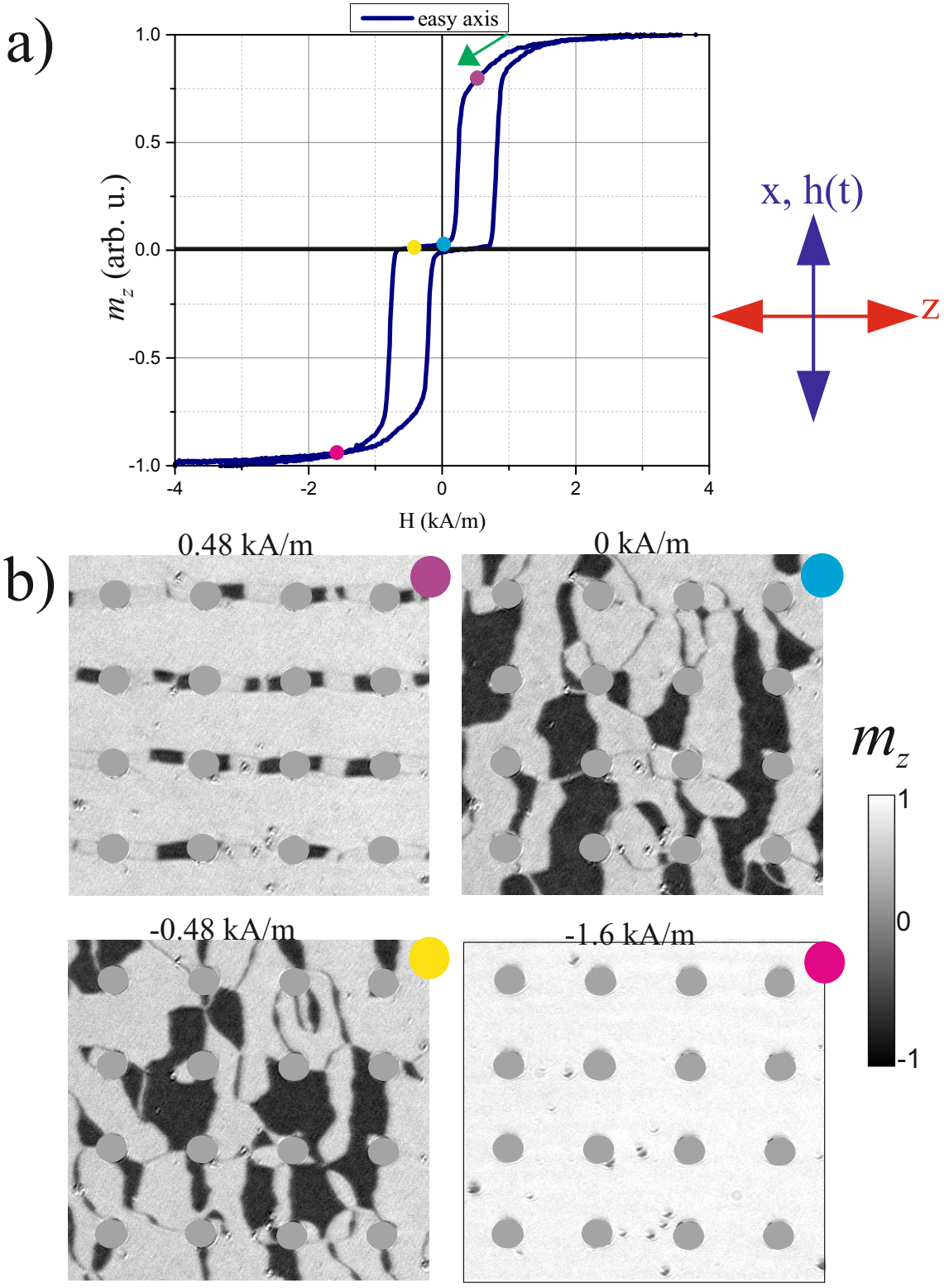

Figure 5.1: (a) The magnetization variation is measured and plotted in the direction of the applied field $\hat{\mathbf{z}}$. This is the easy axis of magnetization. The green arrow indicates the sweep direction. (b) In four points indicated via coloured circles on the hysteresis, the static magneto-optically measured data are shown for the same component of magnetization. The coloured circles in the image corners connect them to their corresponding points in the hysteresis plot. The numbers above the images represent the applied bias field in kA/m.

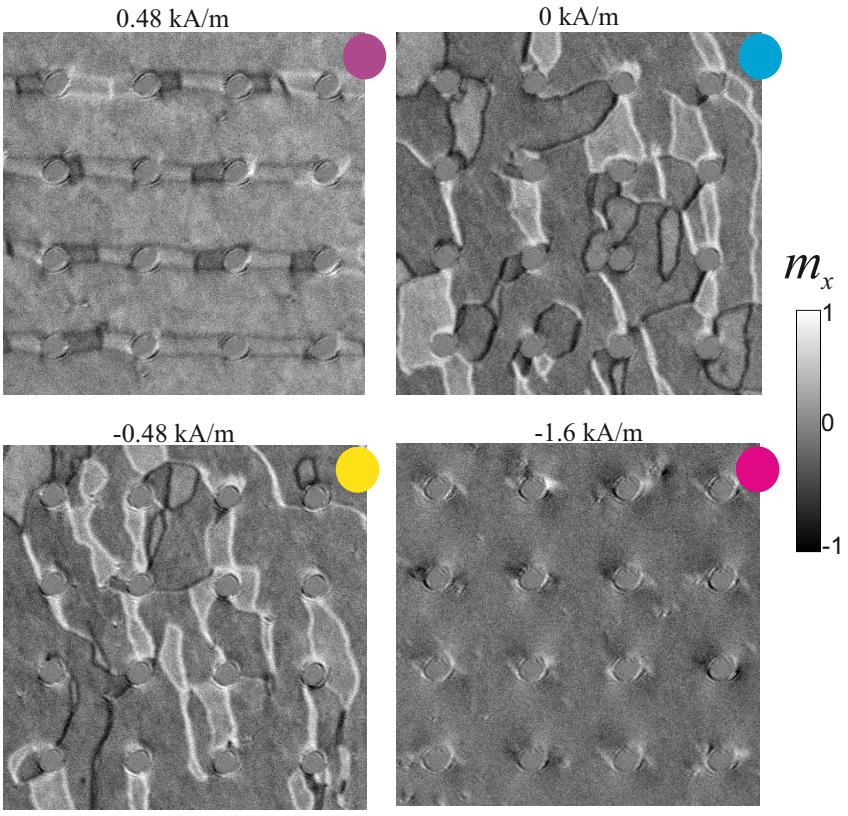

Figure 5.2: The component of IP magnetization in $\hat{\mathbf{x}}$ is illustrated for the same fields indicated in the last Fig. (5.1 b). The value above every image represents the bias field in kA/m. The coloured circles in the corner of images are connected to their corresponding counterparts in Fig. (5.1 a,b).

via colour-coded images for every layer in Fig. (5.3 c).

From the magneto-optically measured data shown in Fig. (5.1) and (5.2) in H_{bias} = 0.48 kA/m, it can be seen that the horizontal connection between dots sometimes has the magnetization configuration like R3 area, sometimes like R4 or a combination of them switching between R3 and R4. In order to make comparison easier, the measured component of magnetization along $+\hat{\mathbf{x}}$ is shown in (5.3 d) in the small area, where we see the frequent switch of magnetization between two dots, which is in great agreement with what is predicted by simulation. In (5.3 d) a rectangular is drawn around one dot with the same size as the calculation supercell to make (5.3 b) and (5.3 d) comparable.

The magnetization is mostly aligned parallel to the applied field and the magnetic anisotropy axis $\hat{\mathbf{z}}$. This parallel alignment between layers can be seen in two regions, R1 and R2 marked in Fig. (5.3). In contrast, the magnetization in R3 and R4 is antiparallel between the layers and at their border. Inside the DWs, the magnetization has a perpendicular component in the $\hat{\mathbf{x}}$ direction. This is illustrated through the transverse magnetization component m_x in Fig. (5.3 b).

Patterning magnetic samples change their demagnetizing field locally and as a consequence their local effective field and dynamic response of magnetization. Therefore, before dynamic mag-

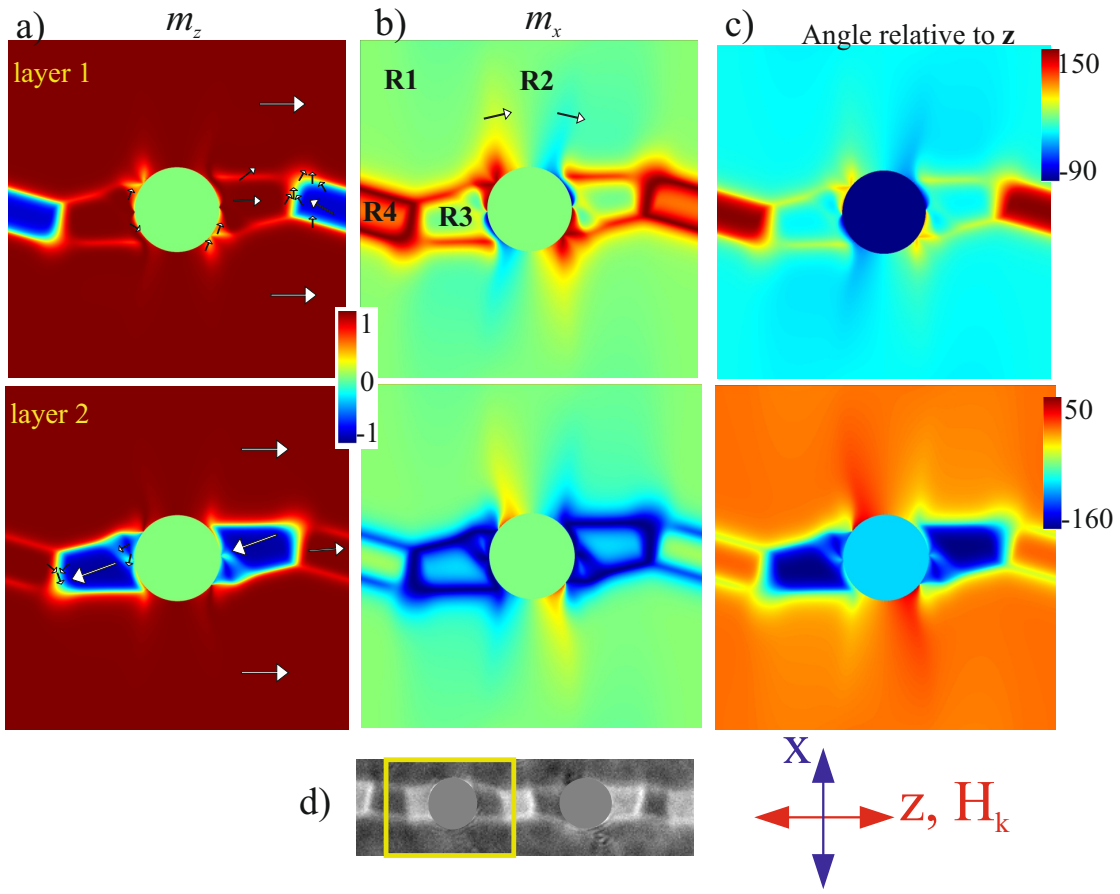

Figure 5.3: (a), (b) The calculated static behaviour of a double layer antidot array is shown in parallel (a) and perpendicular (b) direction relative to the bias field. It is applied in $\hat{\mathbf{z}}$ direction and is decreased from saturation to 0.48 kA/m . The colour code shows normalized the magnetization amplitude and is common between all magnetization components for both layers. The arrows display the magnetization moments. Some regions are denoted as R1- R4. In these areas, the dynamic behaviour is interesting and will be discussed soon. (c) The angle of every simulated cell relative to $\hat{\mathbf{z}}$ is shown via colour coding and the calibration code is in degree. (d) In addition, the measured component of magnetization in $\hat{\mathbf{x}}$ direction is shown to highlight the great agreement with the simulation results.

netization consideration, it is important to have information about the effective fields. The exchange and demagnetizing fields are indicated in Fig. (5.4) and (S-A1) in two directions, parallel $\hat{\mathbf{z}}$ and perpendicular $\hat{\mathbf{x}}$ to the bias field.The exchange field component along $\hat{\mathbf{x}}$ has high variation around DWs since the magnetization vector is rotating in very narrow areas and this increases drastically the corresponding exchange energy. These DWs play an important role in dynamic magnetization behaviour's discussion since they can be a source to emit SWs. Furthermore, the demagnetizing field component along $\hat{\mathbf{z}}$ (shown in Fig.(S-A1)) in the R2 area increased notably and reaches the highest amplitude around dots. This feature is similar to the single layer antidot array and discussed before in Fig. (4.5).

5.1.2 Dynamic Response of Magnetization

One of conclusions from the last chapter was that the amplitude of the permeability spectrum in every specific frequency (obtained from LS-PIMM method) predicts the dynamic response of mag-

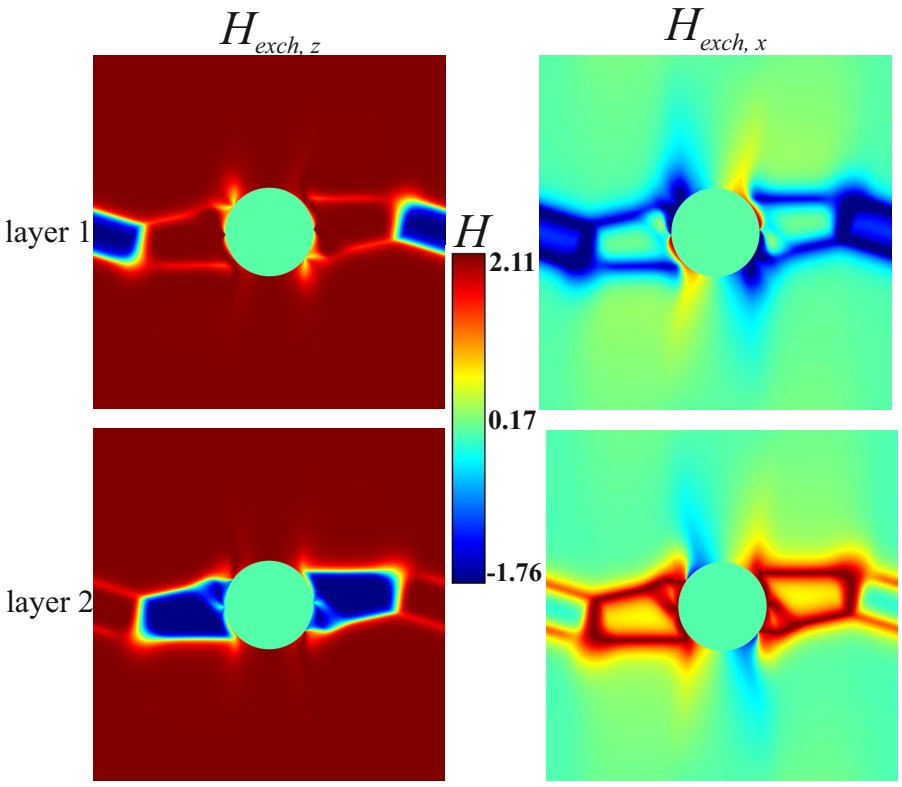

Figure 5.4: The exchange field components are displayed for both layers of a double layer antidot in $\hat{\mathbf{z}}$ direction parallel to 0.48 kA/m applied field and $\hat{\mathbf{x}}$ perpendicular to it. The calibration bar manifests field amplitude in MA/m. The similarity of these pattern with Fig. (5.3a,b), indicating the magnetization components, are evident.

netization to a harmonic excitation with this frequency. This is used in the following to predict the dynamic behaviour in the frequency range from 0.1 up to 6.0 GHz. Then simulated data are then confirmed through experimentally measured data. Consider the static magnetization configuration shown in Fig. (5.3). The LS-PIMM method, explained in section 3.1.1, is used to predict the dynamic response of this pattern to a magnetic stimulus which is a step function. It has an amplitude of 4 A/m and continues for 11 ns. The simulated results are indicated in Fig. (5.5) and (5.6). Every cell intensity is displayed through a colour code. The calibration bars are indicated next to the images. The first one in Fig. (5.5) is common for the four first images and the one colour code is shared by the images named 1.6 and 1.9 GHz. From the LS-PIMM method, the permeability spectrum in the frequency domain for every cell is calculated. We manifest this spectrum amplitude at every frequency via calibration codes. Therefore, the area that is excited with the highest amplitude, in dark red based on our colour code, is in its resonance. In addition, the values above every image denote the frequency in which the permeability amplitude has been shown, as it was discussed in chapter (4). With the above information, it is evident that the area around the DW, specifically at the border of R3 and R4, have the lowest f_r in addition to some parts in R4. The other images are selected in order to depict other areas' $f_{r,l}$, for instance 1.3 GHz as $f_{r,l}$ in R1 and partially in R3 and R4, 2 GHz as $f_{r,l}$ at R2 region's sides and 2.8 as $f_{r,l}$ in R2 are specified.

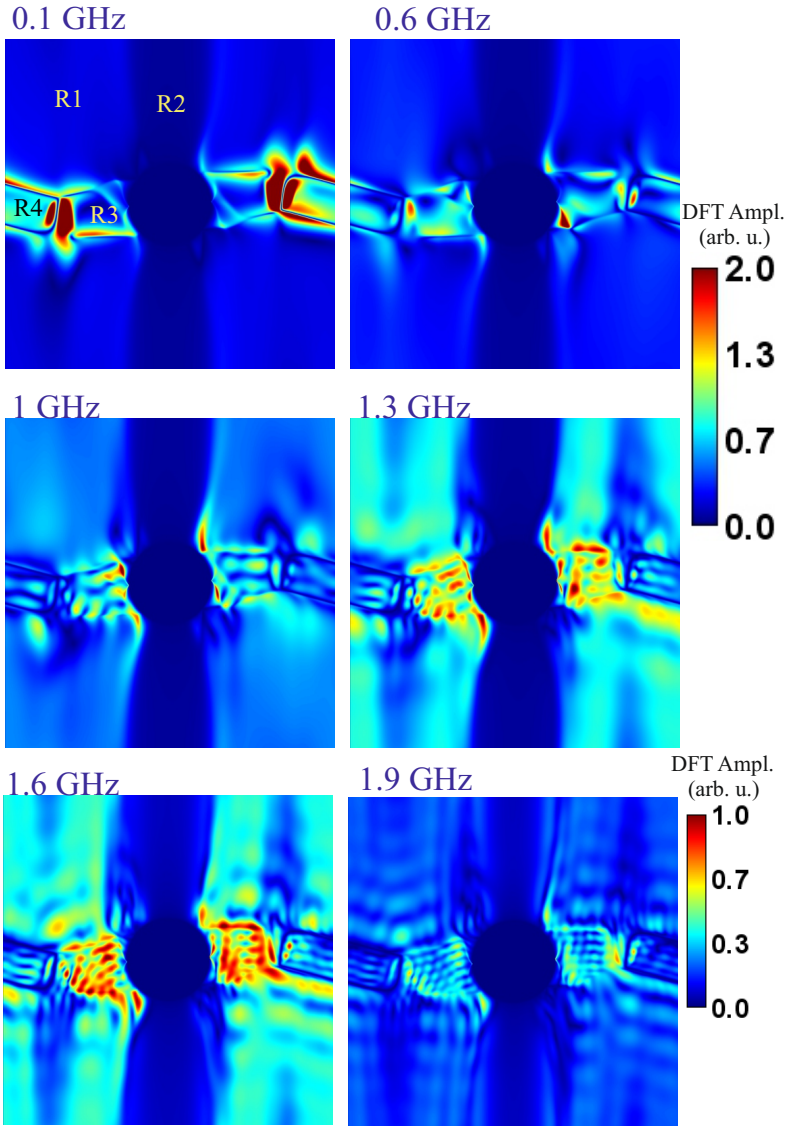

Figure 5.5: The simulated data by LS-PIMM method are shown as anticipated dynamic magnetization response after applying an excitation field with frequencies from 0.1 to 1.9 GHz. All of the data are the dynamic response of magnetization from the first layer, as the second layer has an similar behaviour. There are two colour code calibrations, the first one is common for four upper images and its range is twice as the second calibration code, which is shared for data simulated at f = 1.6 GHz and 1.9 GHz. None of them are normalized.The four areas specified in the first image have unique dynamic behaviour in which SW propagation are detected.

It can be seen from Fig. (5.5) and Fig. (5.6), the highest amplitude of response in addition to the total contrast decrease by frequency enhancement. The contrast between region R1 and R2 increases at f_{exc} = 1.3 GHz since this is the dominant local resonance frequency in the whole area of R1, parts of areas R3 and R4. Thus, this region responds to an external excitation with its highest amplitude. Afterwards, the contrast reduces for higher excitation frequencies higher than 1.6 GHz. Therefore, we consider the dynamic magnetization response to an excitation field at 1.3 GHz with 309 A/m amplitude and simulate it. The calculated data are shown in Fig. (5.7 a) for four different phases. As the second layer has the similar dynamic response as the first one, to avoid repetition, only the simulated results for the first layer are shown. The averaged signal from the full

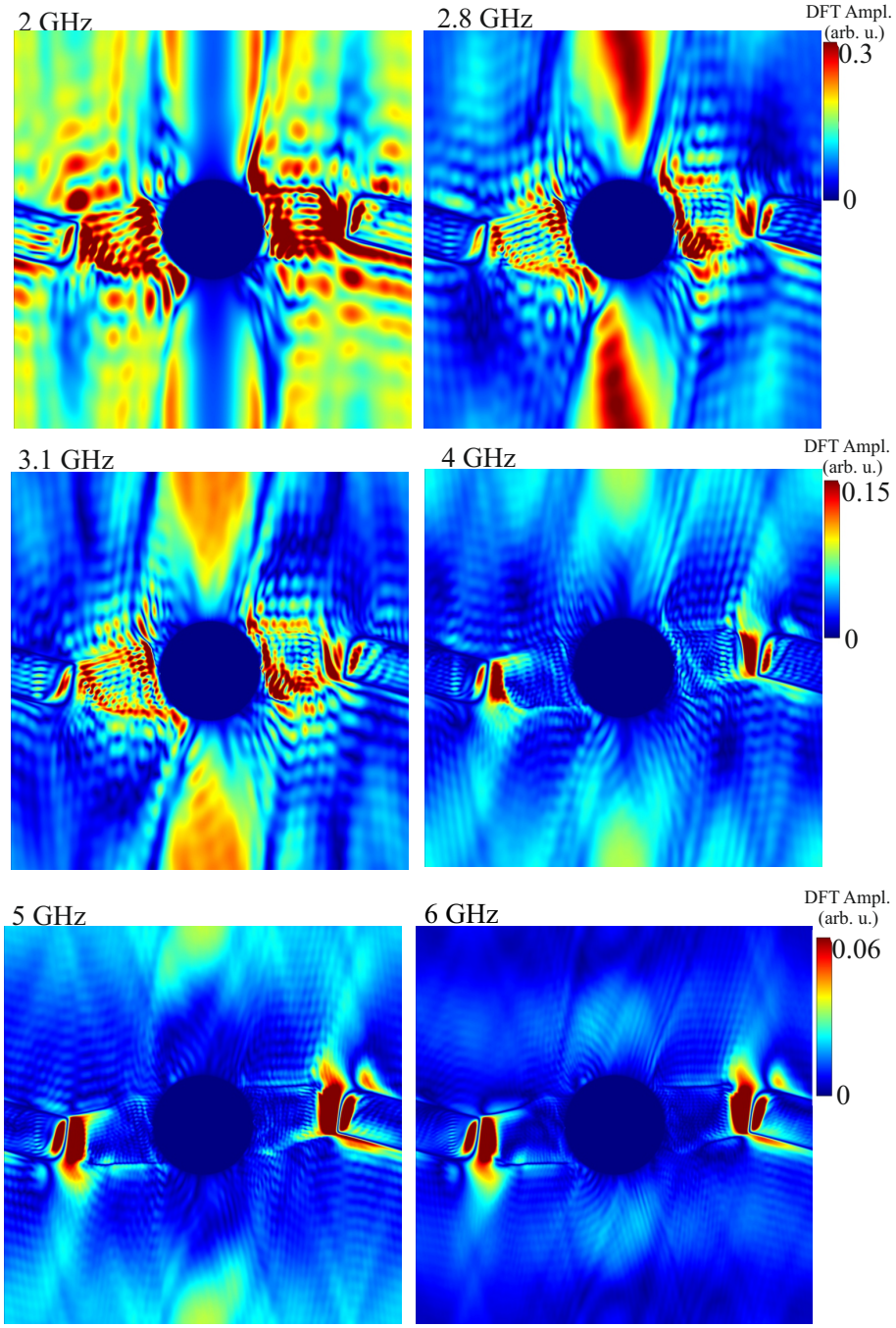

Figure 5.6: The simulated data by PIMM method are shown as anticipated dynamic magnetization response after applying a harmonic excitation field with higher frequencies rather than Fig.(5.5) from 2 to 6 GHz. The correlated frequency is indicated above every image. All of the data are the dynamic response from the first layer, as the second one shows the same behaviour. Every pair of images has a common calibration code. It can be seen from the calibration range that the intensity of the dynamic response decreases with frequency enhancement.

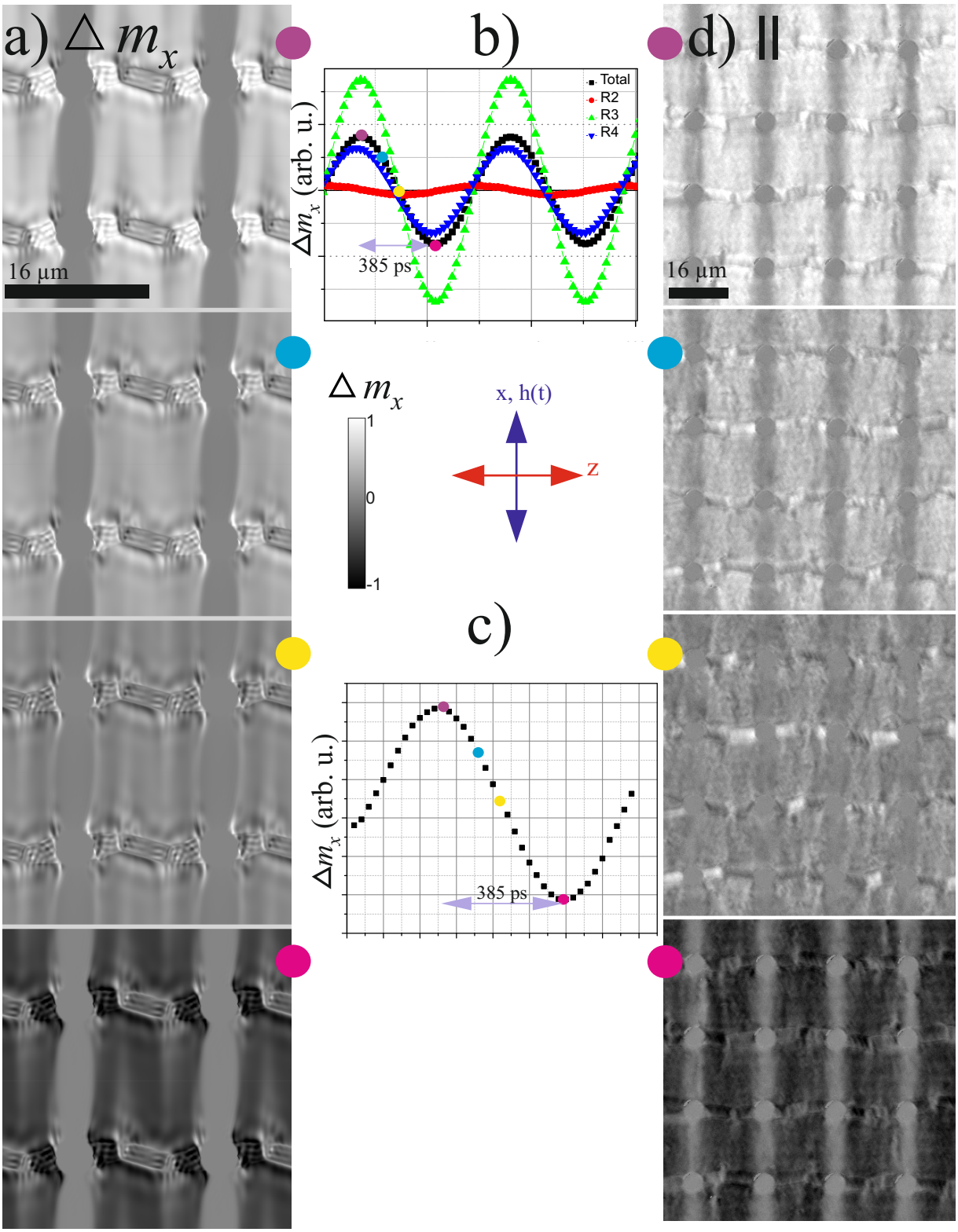

Figure 5.7: (a) The simulated time evolution of $\triangle m_x$ is illustrated via vector response images. The stimulus frequency and amplitude for all data are 1.3 GHz and 309 A/m, respectively. The corresponding phase differences between calculated images are plotted in (a). Furthermore, the averaged signal from three other areas, introduced in Fig. (5.3 b) are added. In addition, the time scale is exhibited in the plot. The coloured circle in the corner of the images refer to their correlated phases on the plot. (c) The similar phase plot is demonstrated from our measurements. (d) We prove our calculation by comparing (a) with its counterpart obtained via wide field TR-MOKE microscopy after applying the excitation field with 309 A/m amplitude. The sensitivity direction is vertical and indicated.

supercell is plotted for one full time period in Fig. (5.7 b) and every image's phase is highlighted by a coloured circle. Moreover, the averaged signal coming from three other regions named as R2, R3 and R4 (indicated before in Fig. (5.3 b)) are calculated and added to the plot. The lowest intensity originates from R2 while the highest one comes from R3. Two regions R3 and R4 are in phase with the total detected intensity while they have an approximately $\pi/4$ phase difference with R2. It is explained with the fact that f = 1.3 GHz is the local resonance frequency, in most parts of supercell. So, R1, R3 and R4 are in phase relative to each other and all have $\pi/2$ phase differences to the excitation field. But $f_{r,l}$ in R2 is much higher, ≥ 2.8 GHz, and so this area is neither in phase with the other area nor oscillates with its highest amplitude. Furthermore, the intensity comes from R2 in comparison with other regions is almost fix. Thus, the contrast between this region and others enhances especially in the first (with maximum total intensity) and the last (minimum total intensity) image, which means better visibility of this area in the simulated and the experimentally taken images.

We measured the dynamic behaviour of the sample at the same f_{exc} = 1.3 GHz via wide field TR-MOKE microscopy for one full cycle, displayed in Fig. (5.7 c). The amplitude of the excitation field applied throughout CPW is 309 A/m in $\hat{\mathbf{x}}$ direction, perpendicular to the bias field and the magnetic anisotropy axis. The corresponding images in the same phases as the simulated data are depicted in Fig. (5.7 d). The circles' colour on the plot correlate to their corresponding image with the same colour in the left corner of images.

The first image in both TR-MOKE Fig. (5.7 a) and simulation (5.7 d) has the highest level of intensity as it can be seen in the plot (b) and (c). For the following images, the intensity gradually decreases until it reaches a minimum in the last one.

We increase the harmonic excitation field frequency to 2 GHz. In the Fig. (5.8), the results from simulation (5.8 a) and TR-MOKE microscopy (5.8 d) are shown for four different phases. To measure experimentally, the antidot sample is exposed to an alternative magnetic field with 154 A/m amplitude which is applied by a CPW and the results with vertical sensitivity are shown as it is indicated in above images. The corresponding phase differences between images are highlighted by coloured circle in the plot shown in (5.8 b) and (5.8 c), respectively, for the calculated and microscopy images. So, the images show the dynamic magnetization evolution with time during one half cycle. The simulated data is confirmed via comparison with the measured images.

Our discussion around the last f_{exc} = 1.3 GHz reveals that the three regions R1, R3 and R4 have similar $f_{r,l}$ and so have the in-phase dynamic response to an harmonic stimulus. Therefore, the averaged magnetization signal originated just from region R2 is added to the plot (5.8 b). It is shown that the amplitude of this signal enhances in comparison with previous data at 1.3 GHz,

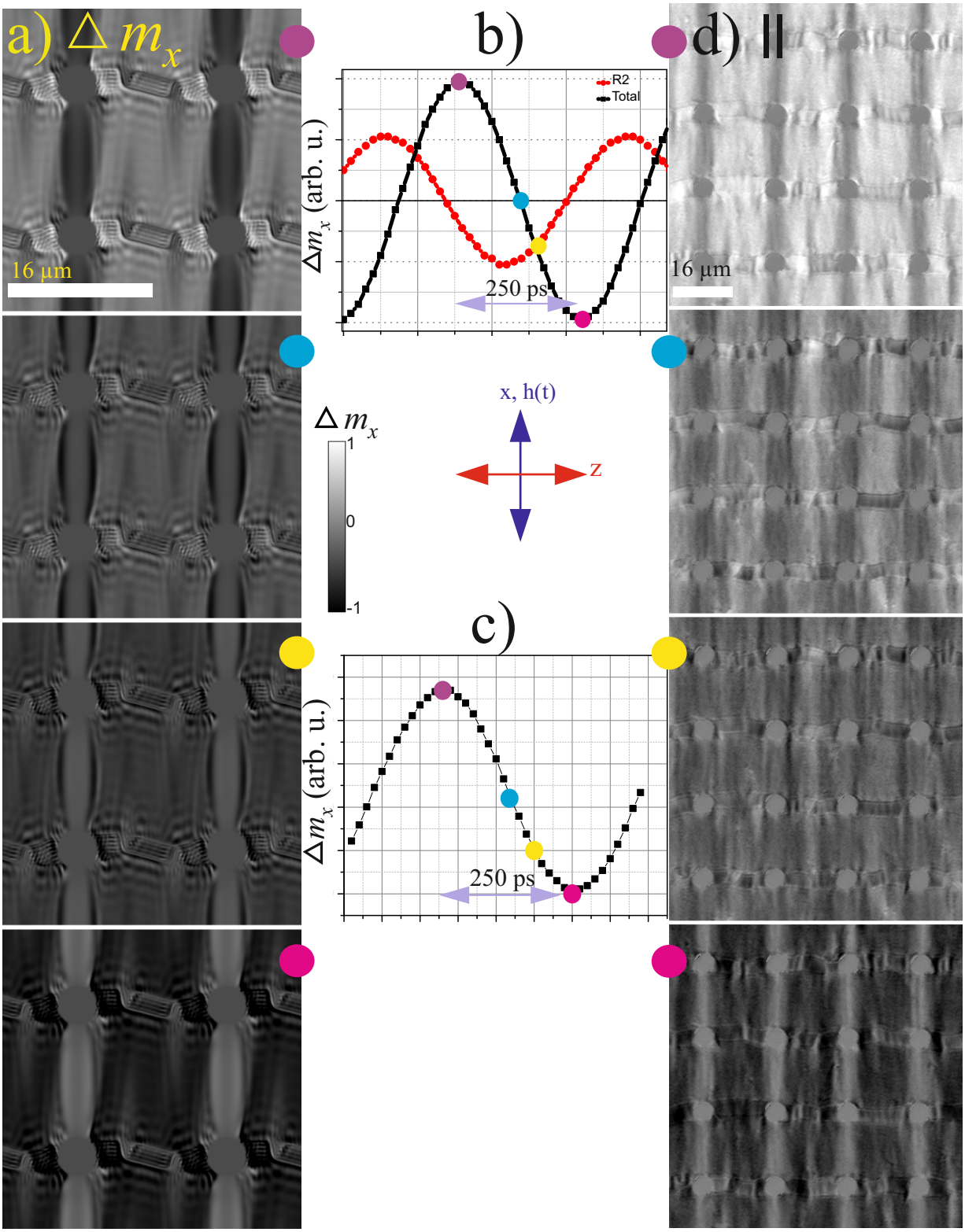

Figure 5.8: (a) The time evolution of magnetization Δm_x for a half period is calculated and illustrated. The stimuli field has a 2 GHz frequency and an amplitude 154 A/m. (b) The time scale and phase difference between the simulated images are displayed and their exact phases are highlighted by the same coloured circles as the ones in the corner of the images. Furthermore, the averaged signal from R2 is added. (c) The corresponding plot from TR-magneto-optically measured data is drawn in (c). The vector dynamic magnetization response with vertical sensitivity is revealed.

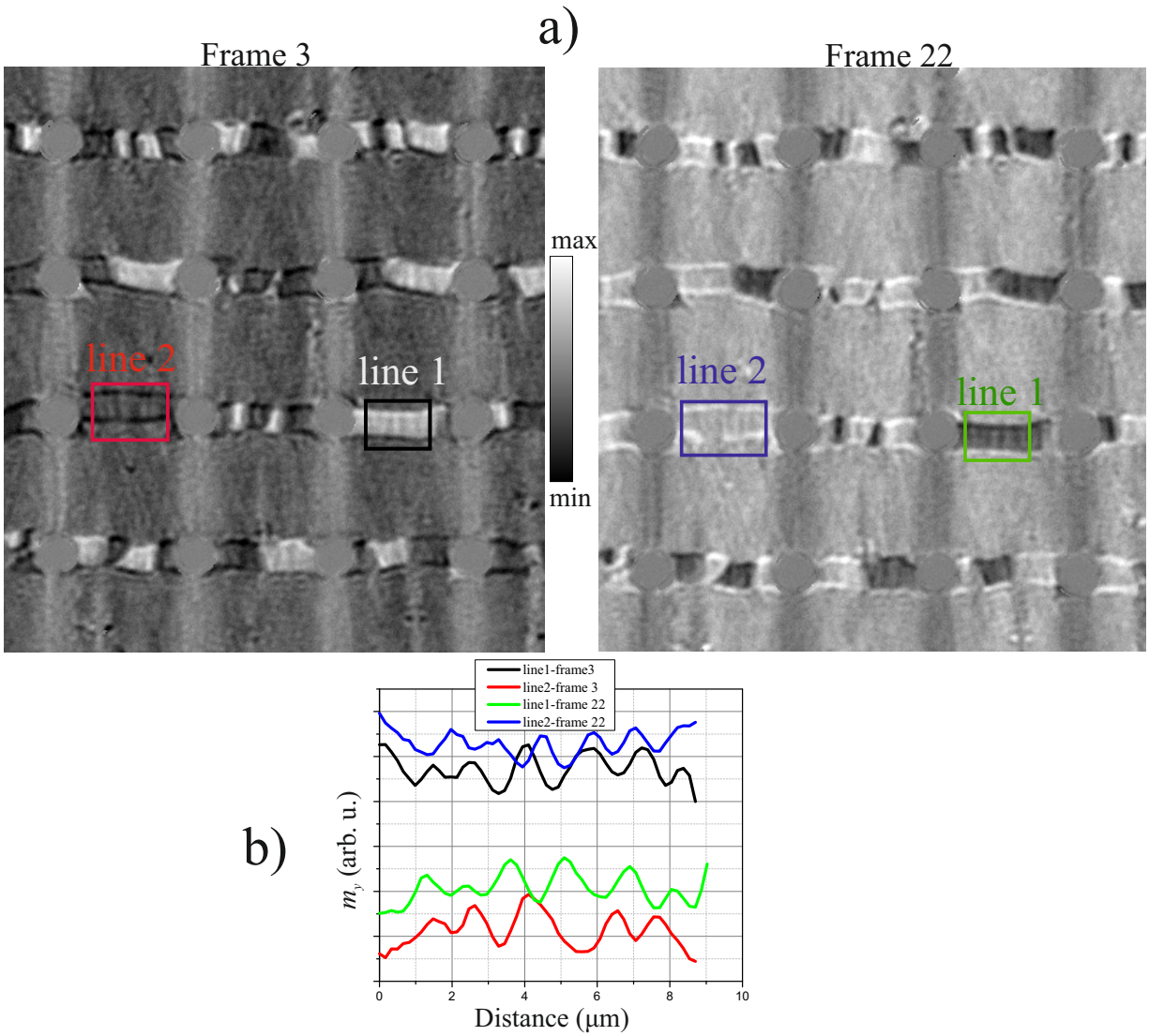

Figure 5.9: (a) The polar (OP) component of magnetization is shown for two phases named as frame 3 and 22. These are in reverse phase. Two regions are selected and marked as line 1 and 2. (b) The magnetization profile along these lines is plotted. The average wavelength of these lines is in the range of 1.3 to 1.6 μm.

however, it has still $\pi/2$ phase difference with average data throughout supercell named as total in the plot. The consequence is that the contrast between R2 and total signal is higher when R1 intensity is highest (first images in (a) and (d)) or when it is lowest (last images denoted by pink circles). There is a point where both plots, named as total and R2 in (b),cross and so contrast and therefore visibility of R2 area is minimum. This point is indicated by the yellow circle either in simulated or measured data and their corresponding plots.

5.1.2.1 Elastic Waves

From the TR-magneto-optically measured data, inside region R3 and R4, the plane wave-like contrast is observed. To figure out their origin, two other images from the same measurement are shown in Fig. (5.9 a). They are measured with polar sensitivity, which displays OOP magnetization

component, and two mentioned frames have 180 degree phase difference. The mentioned waves are better observable in these images. Two lines named line 1 and line 2 are considered and the magnetization profile along them is plotted in Fig. (5.9 b). These waves' wavelength is in the range of 1.3 to 1.6 μm leading to a phase velocity of 2.6 to 3.2 km/s. In addition, their wave front is parallel to the DWs, separating R3 and R4. The conclusion from the elaborated study in Ref. [21] (on the same material), is that these waves' velocity range and wavefront axis, we account them as elastic (shear) waves. The DWs are capable to emit such waves in our magnetostrictive sample, but the signal from them is weak and can be covered by the stronger signal from SWs. In the current measurement, the applied excitation field is neither high, 154 A/m, rather than before 309 A/m, nor at the right frequency (2 GHz is not equal to $f_{r,l}$ in the areas R3 and R4). Therefore, the emergence of SWs' is less probable and this paves the way to detect magnetoelastic waves.

5.1.2.2 Source of Predicted SWs by Simulation

To figure out the source of any SW generation, the dynamic response in the transient part is considered at 2 GHz excitation frequency.

The calculated time evolution of dynamic magnetization, $\triangle m_x$ at 2 GHz is displayed in Fig. (5.10 a) for the transient part. The results correspond to the minimum and the maximum of the averaged signal and they approximately have π phase difference. The coloured circles in the image corners (5.10 a) refer to their correlated phase point on the transient signal in (5.10 b). Moreover, in (5.10 b), the locally averaged domain response for the four areas indicated before in Fig. (5.3 b) are plotted. It is evident that R4 has almost the same behaviour with the overall signal either from phase or amplitude point of view. The R1 and R3 regions response to the harmonic stimuli in the same phase but with higher amplitude. In contrast with the above mentioned domains, R4 oscillates with smaller amplitude and drastic phase shift. Therefore, its reaction to the excitation reduces the dynamic response from the full supercell. Here, only the transient part of the signal is shown while the harmonic oscillation starts after 2 ns from time origin. After a few ns the dynamic response's signal reaches steady state (not shown here), as it was explained before in section (2.3.1.3). In this state the magnetization in the direction of the stimulus field, dm_x , oscillates with the same frequency as its force, which is 2 GHz in this case.

The border of R3 and R4 with R1 has DWs with the lowest $f_{r,l}$, as low as 0.1 GHz, based on calculation shown in (5.5) at 0.1 GHz. In these areas the magnetization vector rotates and in a very narrow region elongates in $\hat{\mathbf{x}}$ direction, perpendicular to the static bias field, as indicated via vectors in Fig. (5.3 a). The simulation results show magnetic waves generation in the R3 and R4

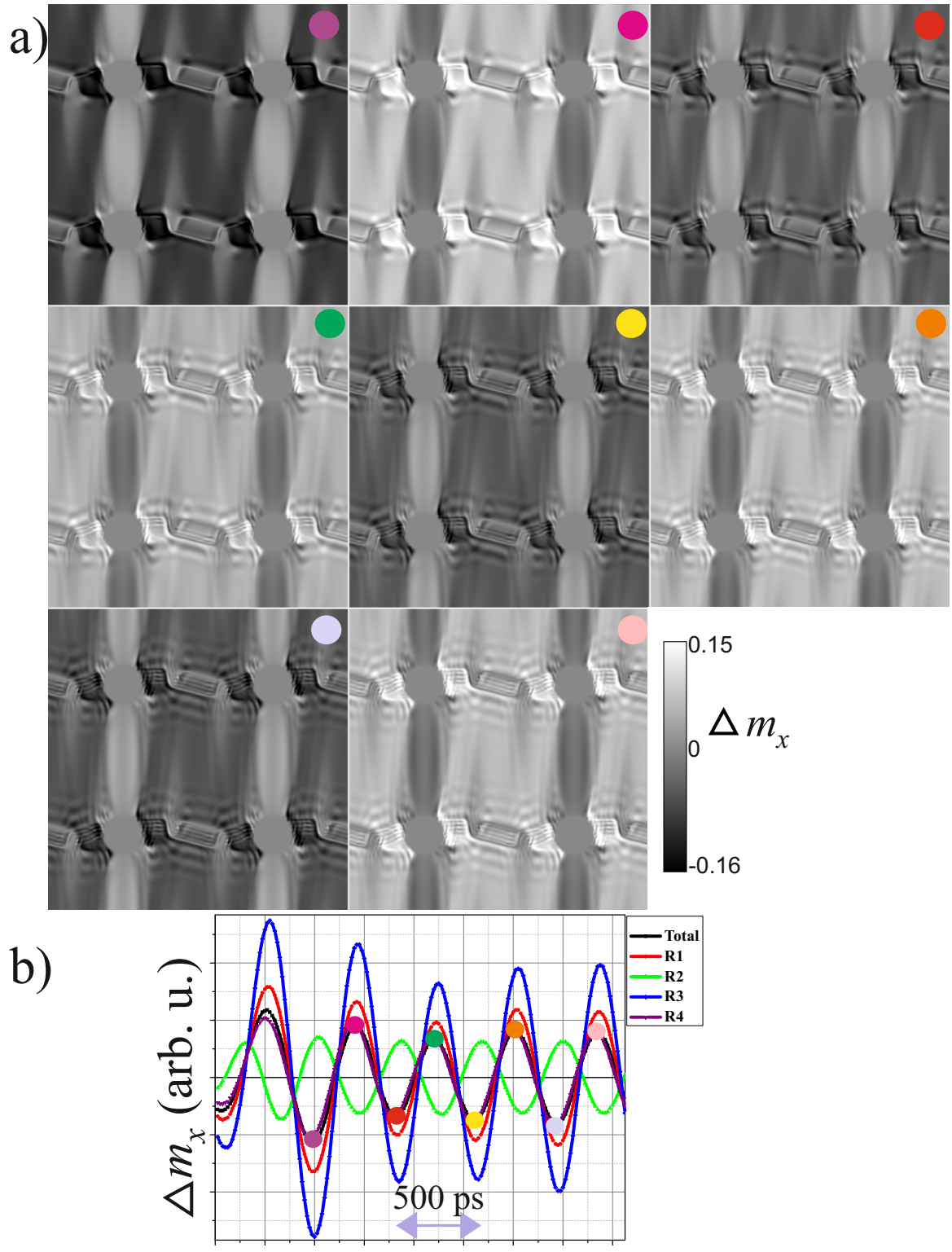

Figure 5.10: The calculated transient part is displayed in different phases after a 2 GHz excitation frequency is applied to the double layer antidot array pattern in 0.48 kA/m in different phases. (b) The locally averaged domain responses, Δm_x, are shown for signal coming from different regions marked in Fig. (5.3 b), named as R1 to R4 in addition to the signal from full frame. The time scale is indicated in the plot as well. It can be seen that R2 has the highest phase difference either with other regions or with the excitation field. The coloured circles in the plot and image corners are utilized to link images and their phases.

area. These waves propagate towards the regions with lower $f_{r,l}$ which are regions R3 and R4.

Moreover, by considering the transient part of the dynamic response signal at frequencies higher than 1.3 GHz in Fig. (S-A2), it can be seen that for all considered frequencies, 1.3, 1.9, 2 and 4 GHz, magnetic waves come from the same mentioned regions with $f_{r,l}$ = 0.1 GHz while the wavefront is propagate parallel to the horizontal DWs.

5.1.2.3 SWs' Detectability in Experimental Measurements

From above discussion, the SWs creation and emission were theoretically predicted inside the R3 and R4 regions. In the following, it is tried to estimate the detectability of such waves in the measurements via TR-MOKE wide field microscopy, either at f_{exc} =1.3 GHz or 2 GHz and even higher frequencies. To be able to detect a wave in the experimental measurement two factors play a role. First, the spatial resolution of the microscope and secondly, the contrast either between different regions or between a wave maximum and minimum peaks. To detect SWs, in addition to have enough contrast from them, their wavelength should be above the limitation of detectable waves via TR-MOKE wide field microscopy. If the average resolving power (R_{green}) is considered around 400 nm, the detectable wavelength is approximately 800 nm based on table 3.2.

One way to get information about SWs and their detectability by a microscope is to consider the relation between their wave vector and the excitation frequency in simulation results. So, the dispersion relation of SWs along four specific lines is calculated. These lines are marked in Fig. (5.11 a). The information provided in Fig. (5.5) and (5.6) is utilized to choose the mentioned lines to study. After applying the DFT method, the dominant wavelength and dominant frequency along the four lines marked from 1 to 4 are obtained. The results are shown via contour plots in Fig. (5.11 b). The DFT intensity manifests the probability of wave propagation with a specific wave vector and frequency which is illustrated via colour code. The points with the highest possibility, red in our selected colour code, determine the dominant wavelength and frequency along every line. These points values indicated in Fig. (5.11 b) correspond to wave vector (in $1/\mu$m), frequency (in GHz) and DFT intensity, respectively. The wavelengths are in the range of a few hundred nanometers. To simplify the results from Fig. (5.11), exemplary waves propagation are displayed in Fig. (5.12) along the same four lines mentioned in Fig. (5.11 a) when 2 GHz excitation frequency is applied. It means that information related to one point (f = 2 GHz) of counter plots is illustrated. Furthermore, their corresponding wavelength is estimated. At 2 GHz, along line 1, there is a damped wave propagation, its equation consists of a sinusoidal function and exponential decay terms, and therefore, the amplitude decreases soon to zero. The wave along this line has a higher wavelength

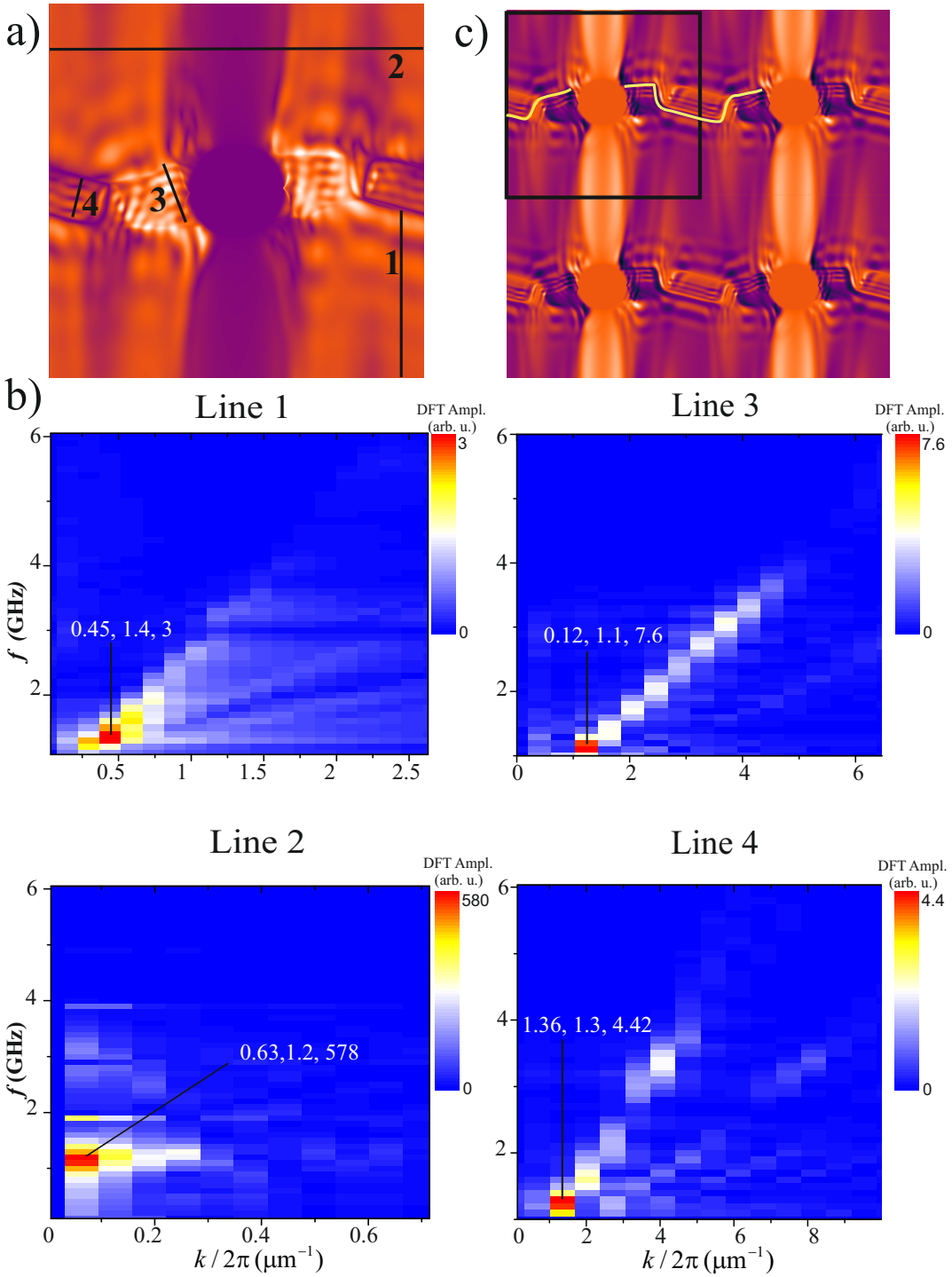

Figure 5.11: (a) The exemplary four lines are drawn inside a supercell calculated at f = 4 GHz applied alternative field. (b) The DFT method in two dimensions, time and space, is used to find dominant frequency and wavelength of propagating waves along introduced lines in (a). The horizontal axis in every contour plot shows $k/2\pi$ in μm^{-1}. In addition, intensity of DFT is illustrated via colour code. The points with the highest intensity, corresponding to the most probable wave vector and frequency, are indicated while the first to the third value shows wave vector $k/2\pi$ in μm^{-1}, frequency in GHz and amplitude of DFT (dynamic susceptibility), respectively. (c) The transient signal is displayed after applying a sinusoidal excitation field at 1.9 GHz. The DWs generating SWs are indicated by a yellow solid line.

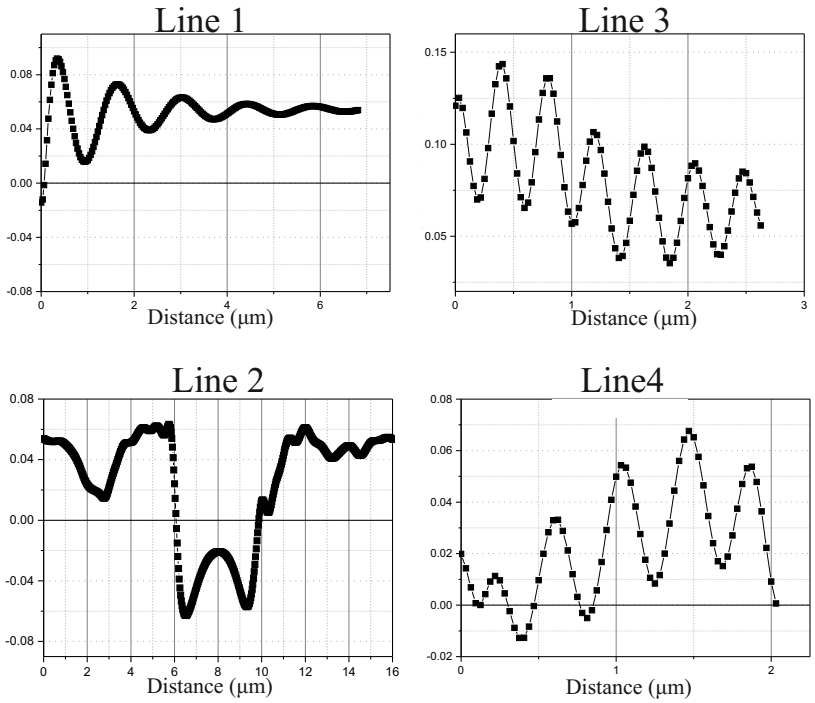

Figure 5.12: The exemplary waves are displayed for just one point in 2D-DFT the counter plot Fig. (5.11 b). This point frequency is 2 GHz and waves are shown along the same lines as Fig. (5.11 b). The vertical axis shows simply intensity of gray scale (arbitrary unit), just to make the comparison of gray scale between different lines possible. The waves along first line damps fast and hard to detect. The second one has in the middle a half cycle sinusoidal like wave which corresponds to contrast from R2. The estimated wavelength along third and fourth line is around 412 and 414 respectively.

than microscope resolution, but the contrast along it is so small in comparison to line 2 which makes detection in the experimental measurement challenging.

Along the second line, the superposition between different sources results in a complicated image at 2 GHz (Fig. (5.12)). In the middle of the plot, the contrast belongs to the R2 region. Moreover, in 2D-DFT contour plots, the dominant wave vectors ($k/2\pi$) equal to 4.45 and 0.63 $\times 10^{-4}$ nm^{-1} is indicated, amongst them is the latter one corresponding to 16 μm which is in the microscope detection range. Furthermore, the amplitude of the response for this line 2 is significantly higher than for other SWs. It can be seen from the intensity of the simulated signal shown in its calibration bar. This dominant dynamic response has the same periodicity as the antidot array and is independent of the frequency. Based on the results shown in Fig. (5.5), this exists even at the lowest excitation frequencies of 0.1 GHz and the f_{exc} enhancement causes other waves excitation inside this region R2. As it was shown in the demagnetizing field configuration in Fig. (S-A1), this originates from the different effective field in this region, R2, in comparison with the neighbours because of the H_{dem} enhancement.

Along line 3 the dispersion relation is linear with the positive slope, Fig. (5.11). Along line 4, the data in the DFT plots consist of few lines illustrating the fact that there is not only one individual propagating wave along the selected lines but one line is more pronounced.

It can be seen that the most probable wave vectors ($k/2\pi$) along lines 3 and 4 are approximately 12.34, 13.6 × 10^{-4} 1/nm, which corresponds to wavelengths of 800 and 735 nm. These dominant wave vectors belong to the frequency range under 2 GHz. Furthermore, *f(k)* is a linear function and frequency enhancement leads directly to a wave length reduction. For instance at f_{exc} = 2 GHz, the wavelength is around 412 nm from Fig. (5.12). This means that SWs detection is not achievable in the region R3 and R4 along these lines, and detecting SWs in these regions by excitation frequency enhancement is even less probable.

In conclusion, in R1 and along line 1, however, the wavelength is above the detectability limitation. Low contrast and highly damped waves make it difficult to see the waves. On the other hand, along line 2, at all excitation frequencies, the contrast from region R2 is observed. The SWs along line R3 and R4 have short wavelength, which attracted a lot of attention recently, therefore, we analyze them in the following with more details.

5.1.2.4 Spin Waves' Non-reciprocity

The DFT along the third and forth line shows a linear behaviour of dispersion relation. If the effective field in j layer, inside the mentioned regions with antiferromagnetic coupling between layers, is considered as [174]:

$$\mathbf{H}_{eff,j} = \frac{2A}{M_s^2}\nabla^2\mathbf{M}_j + \mu_0\mathbf{H}_{ji} \tag{5.1}$$

a linear dispersion relation is obtained, that its slope, velocity of SWs, is calculated with this equation [174]:

$$\begin{aligned} V\left(\phi_k\right) &= \omega_M d\left[\sqrt{\frac{\lambda_{\mathrm{ex}}^2}{d^2}+\frac{1}{12}\left[4+6\frac{d_{\mathrm{s}}}{d}-F\left(\frac{\lambda_{\mathrm{ex}}}{d}\right)\right]}\sin^2\phi_k-\frac{1}{2}\sin\phi_k\right] \\ &\text{with } F(u)=1-12u^2+24u^3\tanh\left(\frac{1}{2u}\right) \end{aligned} \tag{5.2}$$

where ϕ_k is the angle between the magnetization and wave vector $\boldsymbol{k}$, d_s and d correspond to the interlayer and ferromagnetic layer thickness and $\lambda_{exch}^2 = 2A/\mu_0 M_s^2$ shows the exchange length. If both ferromagnetic layers are identical, without applying any bias field the dispersion relation is [175]:

$$\omega_{\mathbf{k}} = \omega_M d\left[\sqrt{\frac{\lambda_{exch}^2}{d^2}+\frac{1}{3}\sin^2\phi_k}+\frac{1}{2}\sin\phi_k\,\mathrm{sign}\,k\right]|k| \tag{5.3}$$

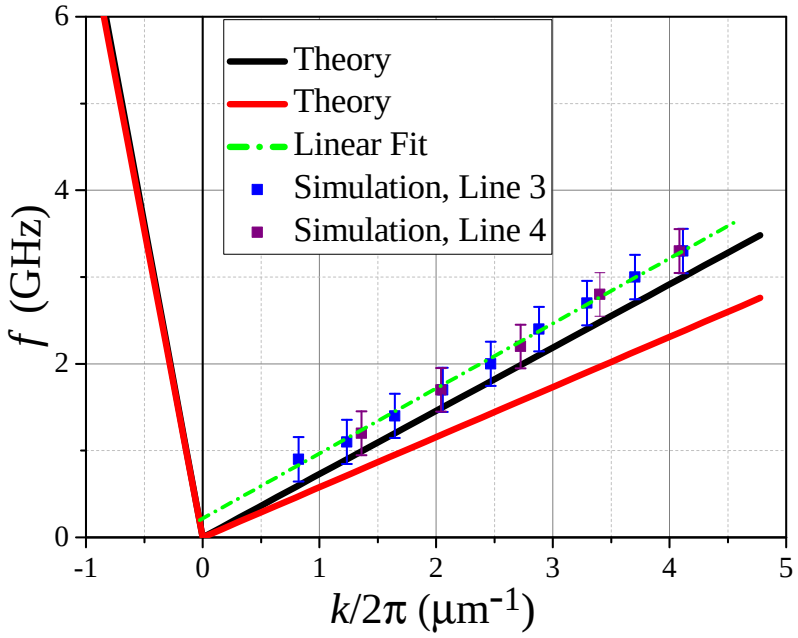

Figure 5.13: The linear dispersion relation are calculated from equations (5.3) and (5.2) and indicated by black and red lines, respectively. The material parameters are exchange constant $A = 2.24\times10^{-11}$ J/m, $M_s = 1.178$ MA/m, $\gamma = 1.76\times10^{11}$ Hz/T, $d = 25$ nm and $d_s = 0.8$ nm and $\phi_k = 3\pi/2$. The squares are the data with higher intensity of DFT signal intensity along line 3 and 4 shown in Fig. (5.11 b) and the dash line has been fitted to these data.

$$\text{sign}(k) = \begin{cases} 1 & \text{if } k > 0 \\ 0 & \text{if } k = 0 \\ -1 & \text{if } k < 0 \end{cases}$$

The plot in Fig. (5.13) compares the calculated linear dispersion from the above equations with the obtained data from our simulation shown in the counter plots in Fig. (5.11). The data with higher DFT intensity from these contour plots are shown by scattered squares. To guide the eye a linear fit on these data is estimated by a dash green line. Furthermore, the black and red lines represent linear dispersion calculation from equations (5.3) and (5.2), respectively. The fitted line has the same slope (and so same phase velocity) as the SWs' in the equation (5.3). There is only a vertical shift between the fitted line and the calculated one from the equation (5.3) that is clarified by extrapolation of the fit line. This shift indicates that for our case $\omega_k(\omega_0 = 0) \neq 0$, while in the equation (5.3) it is assumed that H_0 is zero but in our case and inside R3 and R4, the effective field consists of a non-zero external field and an anisotropy one. Another important point from the equations (5.3) and (5.2) is that SWs are non-reciprocal and therefore, their dispersion and velocity depend on the sign$k$. This is in agreement with our simulated data as it can be seen in Fig. (5.11 c) at 2 GHz and (S-A2)at different frequencies. They show that the observed SWs inside

R3 and R4 come from two DWs, indicated by a yellow line (at f_{exc} = 1.3 GHz). However the other two DWs on the opposite side can emit SWs but their wave vectors k are so small, k/2π < 1 μm in the frequencies under 6 GHz based on the analytical calculation shown in Fig. (5.13) for k<0. Therefore their wavelength is bigger than R3 and R4 regions' width and so can not be observed. On the other side of these DWs, inside R1 and R2 magnetization in both layers is parallel and the above equations can not be applied.

5.2 Antiparallel Magnetization in Remanence

5.2.1 Static Domain Behaviour

The antidot array sample has antiferromagnetic coupling between layers, therefore in low fields and even before bias field cut off, the total magnetization component in the direction of the field collapses to zero. We consider the remanence of the inductive hysteresis where the static field is removed. This is denoted by a blue circle in the static images, measured via MOKE microscopy with horizontal sensitivity (magnetization component along bias field), in Fig. (5.1 b), and with vertical sensitivity, in Fig. (5.2).

The magnetization configuration is complicated. To simulate this microstructure, three prospective magnetization configurations are considered and tried to find the best fitting one based on total energy minimization.

5.2.1.1 First Prospective Microstructure

It seems that DWs around antidots form at higher fields, considered at last section, move and vanish in some parts. Therefore, in these regions, magnetization aligns approximately in $\pm\hat{\mathbf{z}}$. The corresponding magnetization configuration is defined in simulation as completely antiparallel magnetization alignment in each layer relative to the other. This is shown in Fig. (5.14). In this initial magnetization configuration, every layer has a small rotation in the exact vicinity of the antidot which creates two magnetic poles. Moreover, we considered two other possible magnetization configurations.

5.2.1.2 Second Prospective Microstructure

We build the second magnetic microstructure based of other part of sample where DWs are still available. In Fig. (5.15) illustrating magnetization component perpendicular to the field in $\hat{\mathbf{x}}$ can be seen that, there are DWs with highest intensity in $\hat{\mathbf{x}}$ direction. The magnetization rotates by

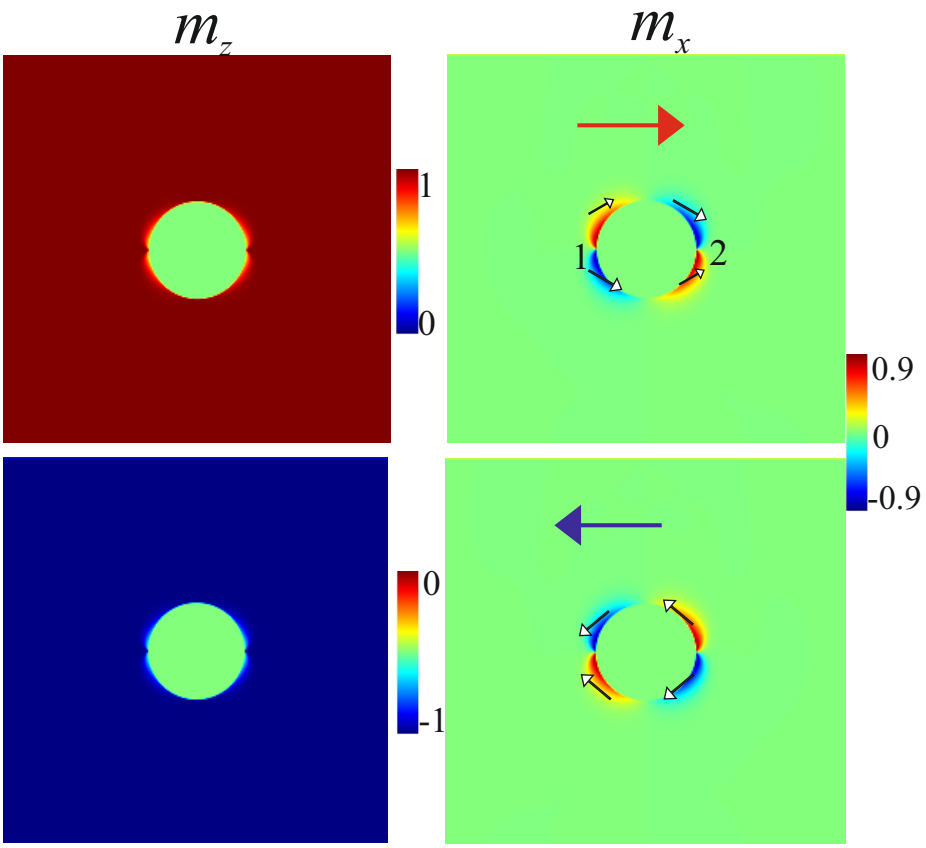

Figure 5.14: The calculated remanence state for double layer antidot array after the static magnetic field is removed from 4 kA/m (saturation) to zero. Two components of magnetization are illustrated. It seems that every layer is almost saturated in $\hat{\mathbf{z}}$. As m_x in the layers is antiparallel, overall magnetization in this direction is zero. There is small m_x around the antidot to reduce stray field energy which is highlighted via arrows. Two points are indicated by 1 and 2 to denote the magnetic poles around the antidot.

180 degree at these walls. To define such a configuration for our calculation, we considered a pattern indicated in Fig. (5.15). Every component of magnetization is depicted for every layer which comprises antiparallel m alignment. The colour code is common for all of the images and the magnetization rotation around the DWs is indicated via arrows. It causes head to head or tail to tail m configuration and inside the DWs the magnetization elongates perpendicular to matrix one.

5.2.1.3 Third Prospective Microstructure

The third magnetization configuration is similar to the second one but DWs move towards the antidot and then stop at the dots' edge since dots act like defects. So, more energy is needed to come out of this dot edge.

The energy distributions correlated to three mentioned microstructures above is calculated in the table (5.1). The energy terms comprise anisotropy, exchange and demagnetizing energy in nJ/m^3.

From this information antiparallel alignment of magnetization in two layers without DWs (Fig.

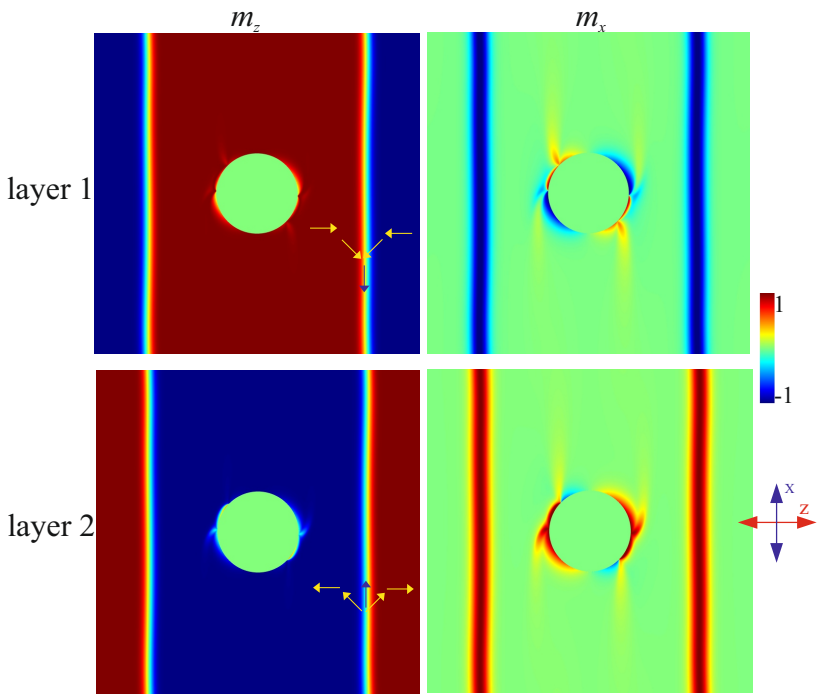

Figure 5.15: The calculated static pattern is illustrated for both normalized magnetization components while the bias field cuts off. Every row indicates one layer's magnetization. The m_z in every individual layer has parallel and antiparallel alignment relative to the saturation field direction. Since the other layer m_z is reverse, total magnetization in $\hat{\mathbf{z}}$ direction, m_z, is zero. The magnetization rotation moderates via DWs that in their core, m_x is equal to m_s. The arrows help to follow this rotation.

Magnetic Microstructure	E_t	E_{ext}	E_{an}	E_{exch}	E_{dem}
Fig. (5.14)	-2.02	0	0.041	-2.37	0.3
Fig. (5.15)	-0.64	0	0.70	-2.10	0.76
DWs exact around dots	-0.84	0	0.53	-2.08	0.71

Table 5.1: The energy distribution is indicated for three different simulations. These prospective magnetization configurations are considered based on experimental measurement by MOKE microscopy and then the magnetization configuration is found with minimum energy by micromagnetic simulator. These energy terms are in nJ/m^{-3}. The magnetic configuration with the lowest energy is considered as initial magnetization configuration to predict the time evolution of magnetization.

(5.14)) has minimum energy with significant difference (-2.02 nJm^{-3}) to the others and thus it is the preferable static microstructure. This configuration reduces magnetic anisotropy and exchange energy. This magnetic configuration is so stable and further enhancement of the static field in opposite direction can not switch the pattern. We used this configuration as initial magnetization configuration in the dynamic simulation to obtain either a permeability spectrum in the frequency domain, via LS-PIMM method, or to simulate the time evolution of the dynamic magnetization after it is exposed to a harmonic stimuli field.

5.2.2 Dynamic Response of Magnetization

As it is shown in Fig. (5.14) at remanent magnetization, the magnetization in two layers is aligned completely antiparallel because of the antiferromagnetic coupling and therefore, the net magne-

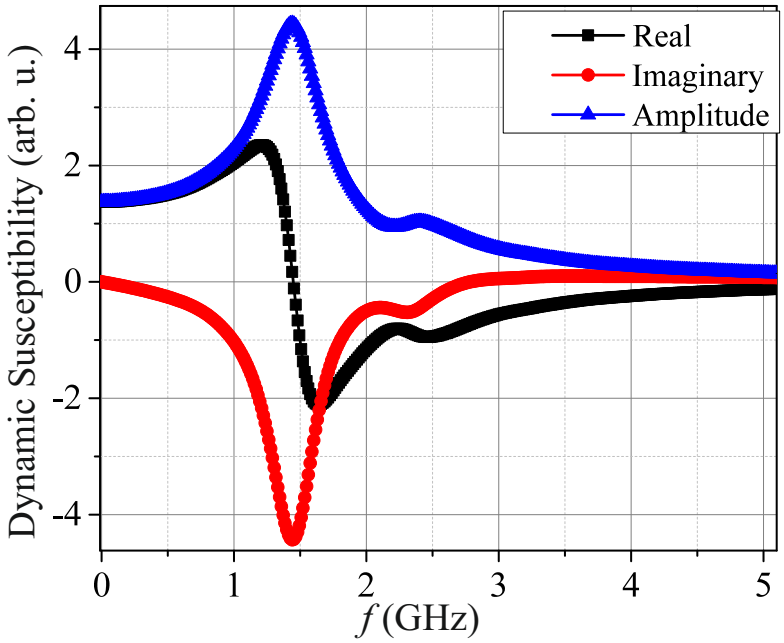

Figure 5.16: A step function is applied to the double layer antidot sample in its remanence state and then the permeability spectrum in the frequency domain is calculated and shown. The signal (from two layers) is averaged all over the supercell and is similar to every layer's permeability behaviour. There is a major peak at 1.4 GHz.

tization is zero. On the other hand, because of demagnetizing field minimization, around the dots the magnetization rotates and the magnetic dipoles form in point 1 and 2 as they are denoted in Fig. (5.14).

5.2.2.1 A Step Function as a Magnetic Stimulus

When a step function is applied to this pattern, both layers respond in the same way. The amplitude of the magnetic stimuli is 5.6 A/m and it needs 30 ps to reach its maximum and then continues for 14 ns, to be sure that every slow magnetization dynamic response is recorded. The averaged signal from the overall supercell is calculated and the permeability spectrum is plotted in Fig. (5.16).

There is a major peak at lower frequencies of around 1.4 GHz in addition to a minor one at higher frequencies of 2.4 GHz with very low amplitude. The major peak in the amplitude graph complies with the imaginary part's peak and real part zero crossing. As it was mentioned, both layers have exactly the same permeability spectrum in the frequency domain and so we showed just the overall signal.

5.2.2.2 Harmonic Excitation as a Magnetic Stimulus

We select a sinusoidal magnetic field at $f_{exc} = 2$ GHz to excite the system. The simulated results are depicted in Fig. (5.17 a). For this calculation, the magnetization pattern is considered to be aligned

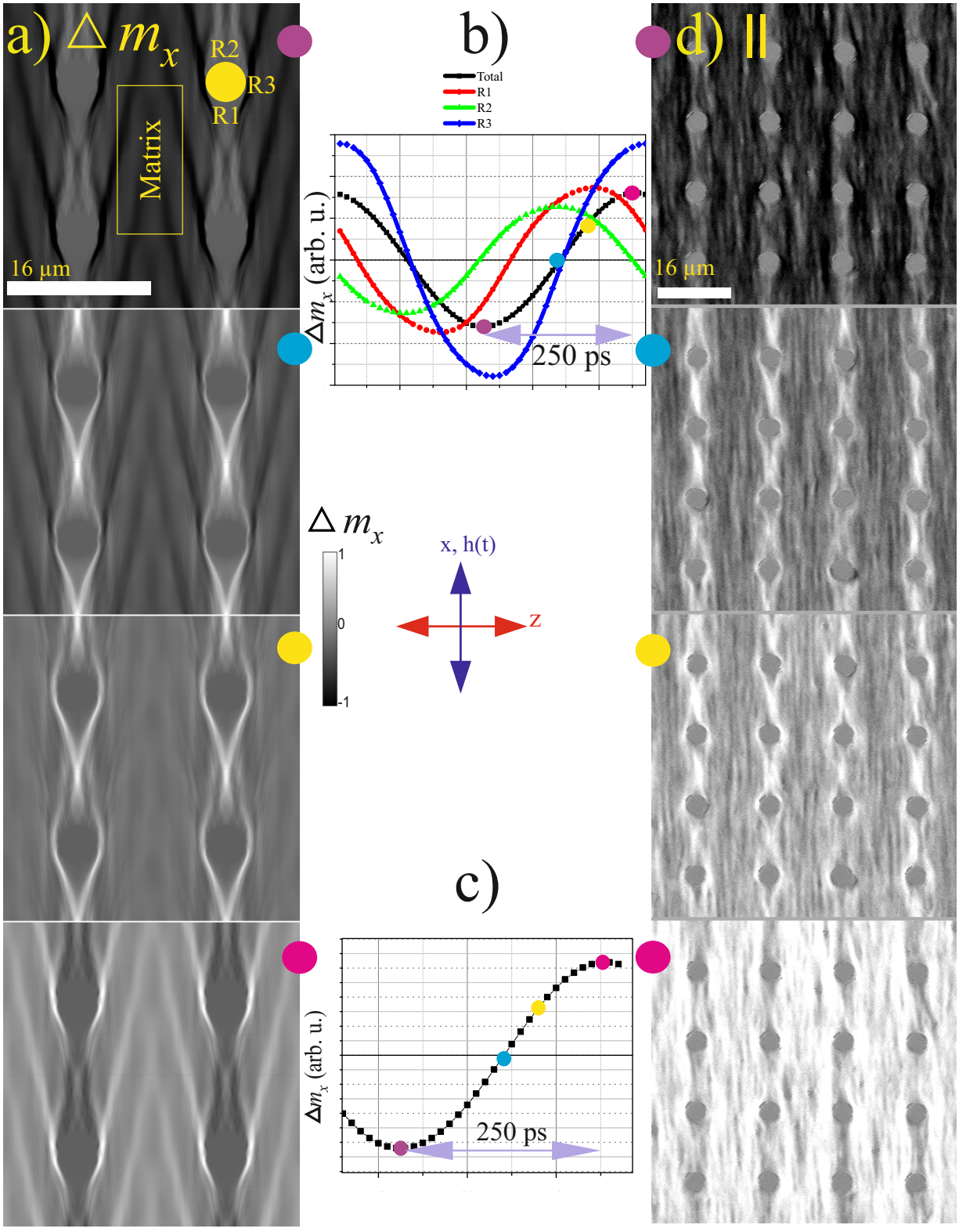

Figure 5.17: (a) The time evolution of magnetization, Δm_x, is calculated under application of a harmonic stimulus at 2 GHz frequency. (b) Its corresponding phases are illustrated on the phase plot via the same coloured circles as in the right corner of the images. In addition to the averaged signal from the entire supercell (named as "Total" in the plot title), the signals from other regions are also shown. (c) For a full cycle, TR-MOKE wide field images are directly measured in vertical sensitivity (Here just half cycle is displayed). (d) For four selected phases (indicated by solid coloured circles) as simulation, microscopy images are shown when the double layer antidot sample is exposed to a magnetic stimulus with 71 A/m amplitude at 2 GHz frequency via a CPW.

antiparallel between layers without any DW as it was shown in Fig. (5.14). Then a sinusoidal magnetic field in the vertical direction $\hat{\mathbf{x}}$ is applied with 309 A/m amplitude and then we wait long enough to reach steady state. The reported results belong to this state. The coloured circles in the corner of images in Fig. (5.17 a) refer them to their corresponding phases on the plot (5.17 b). The four images show the dynamic magnetization response, $\triangle m_x$, during a half cycle. The time scale is shown by a double arrow in the plot. The first to the last image correspond to minimum, zero, half maximum and maximum dynamic magnetization $\triangle m_x$. Furthermore, three areas are named as R1-R2 and R3 in the first image in Fig. (5.17 a), while R1 and R2 are selected based on the dynamic magnetization pattern at higher frequencies. The averaged signals coming from these regions are included in the plot in addition to the averaged signal from the full supercell which is named as "Total". Among these regions, R3 is in phase with the full signal and has a stronger response, while R1 and R2 are neither in phase with each other, nor with the total signal. These regions behaviour leads to a reduction in intensity of the total signal since the $\triangle m_x$ from R3 with higher intensity is partially canceled with R1 and R2 signals, which are in different phases than R3.

Furthermore, we measured a complete cycle of magnetization dynamic response via a TR-MOKE microscopy. The corresponding phase plot (just for half of this cycle) is indicated in Fig. (5.17 c). The colour circles on the plot determine the points (with the same phase as the simulation results in (a)), where the recorded data via microscope are depicted in Fig. (5.17 d). They are measured in vertical IP sensitivity after application of an AC field with 71 A/m in amplitude along the vertical axis $\hat{\mathbf{x}}$ via a CPW.

The agreement between our calculation and the measured data is evident. This confirms the accuracy of our calculation to find the most preferable pattern from an energy distribution point of view out of three different patterns (compared in table (5.1)).

The same process is utilized to observe the time evolution of magnetization after applying a 3 GHz excitation field. The calculated results are shown in Fig. (5.18 a) illustrating the time evolution of magnetization in the direction of the applied excitation field, $\triangle m_x$. The AC field amplitude and frequency are 309 A/m and 3 GHz, respectively. The related phase to every image is indicated in the plot Fig. (5.18 b). The coloured circles in the corner of images link them to their phases on the plot. The averaged signal of the whole supercell is marked as total. In addition, the calculated $\triangle m_x$ variation versus time in some areas (denoted in Fig. (5.17 a)) is added. The dynamic magnetization signals, $\triangle m_x$ from R1, R2 are in phase with each other and with the full signal and the matrix. The matrix is indicated by a rectangle in Fig. (5.18 a) and has the exact same behaviour as the full signal (not shown in the plot). This similar dynamic behaviour of R1, R2 and matrix makes detection of the pattern around the dots (R1 and R2) more difficult in comparison to the 2 GHz case.

The R3, corresponding to a small region including the magnetic pole, has $\pi/3$ phase differences with R1, R2 and the total signal. In addition, the latter area has a higher intensity of response as compared6 to the others, which is similar to what we saw for the 2 GHz excitation.

Moreover, the TR-magneto-optically measured data are measured when the amplitude of excitation signal is 1.5 and 6.5 V, converting to a magnetic of field 71 and 309 A/m. They show the same magnetization evolution with time, therefore to avoid repetition in Fig. (5.18 d), we just included the higher amplitude responses. There is a diamond like pattern inside the matrix in simulated and directly measured images is highlighted by a dashed diamond. In addition, another pattern forms between two neighbouring dots above each other.

5.2.2.3 The Original Static Pattern Excitation at 3 GHz

From the observed magneto optical images, depicted in Fig. (5.1) and (5.2), we proposed three magnetic configurations as possible static patterns for our calculation. The reason was that in the optical images, we observed a combination of magnetization in the first and the second layer. Therefore, simulation with such a random distribution needs a very large supercell that significantly increases the run time. Instead based on table (5.1), antiparallel magnetization between layers was selected as initial configuration. We confirmed our chosen pattern's accuracy via agreement between the dynamic response in simulated and measured data. Now, we illustrate time evolution of magnetization in the same static pattern as measured before. The static pattern before the dynamic measurement starts is shown in Fig. (5.19 a). Afterwards, the specimen is exposed to a 285 A/m field at 3 GHz frequency which is applied in $\hat{\mathbf{x}}$ direction via a CPW. We considered two regions named as A1 and A2 in Fig. (5.19 b) which have almost 90 degree phase difference as it is indicated in the plot (5.19 c). We showed four images correlated to A2's different phases, during which the magnetization reversal in A2 happens. Although recognizing the pure SWs' origin in such measurements is not easy because of high concentration of walls, the similarity of the observed pattern here (especially in the area confined by neighbouring walls like A1 and A2) and the previously simulated area is evident.

From comparison between the static and dynamic images, it can be seen that the excitation field amplitude is carefully selected in order to avoid any DW movement after application of *h(t)*, which is vertical in $\hat{\mathbf{x}}$ direction and normal to the anisotropy axis.

As conclusion, from our knowledge obtained from the single layer antidot chapter, we infer that the observed dynamic magnetization pattern here forms by SWs emission from point 1 and 2 marked in Fig. (5.14). These magnetic poles have the lowest local f_r and at every higher exci-

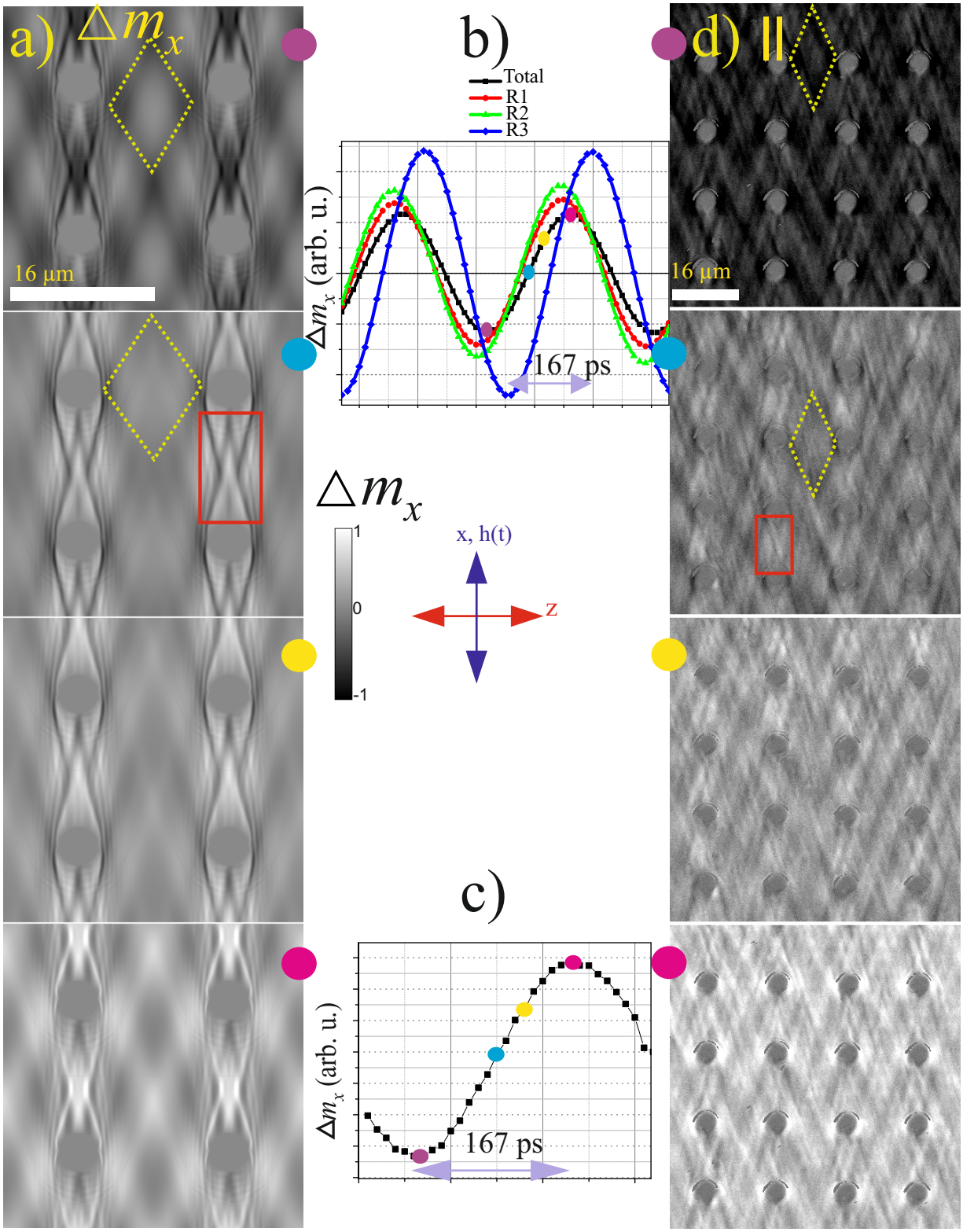

Figure 5.18: (a) The double layer square array antidot is considered after the bias field is cut off. The initial static magnetization is antiparallel between layers. The sample is exposed to a 309 A/m harmonic excitation field at 3 GHz and simulated images are shown. (b) The phase difference between images in (a) are plotted. Every coloured circle on the plot shows the corresponding phase for the calculated image in (a) with the same coloured circle. The total, R1, R2 and R3 in the plot are averaged signals from the full super cell and the regions denoted in Fig. (5.17 a). (c) The measurements under the same conditions as the simulation are done via TR-MOKE wide field microscopy in vertical sensitivity for a full cycle but here half of this cycle is shown. (d) The images are depicted at four points indicated by coloured circles in the plot (c). The geometric shapes in (a) and (d) are drawn to highlight similar patterns.

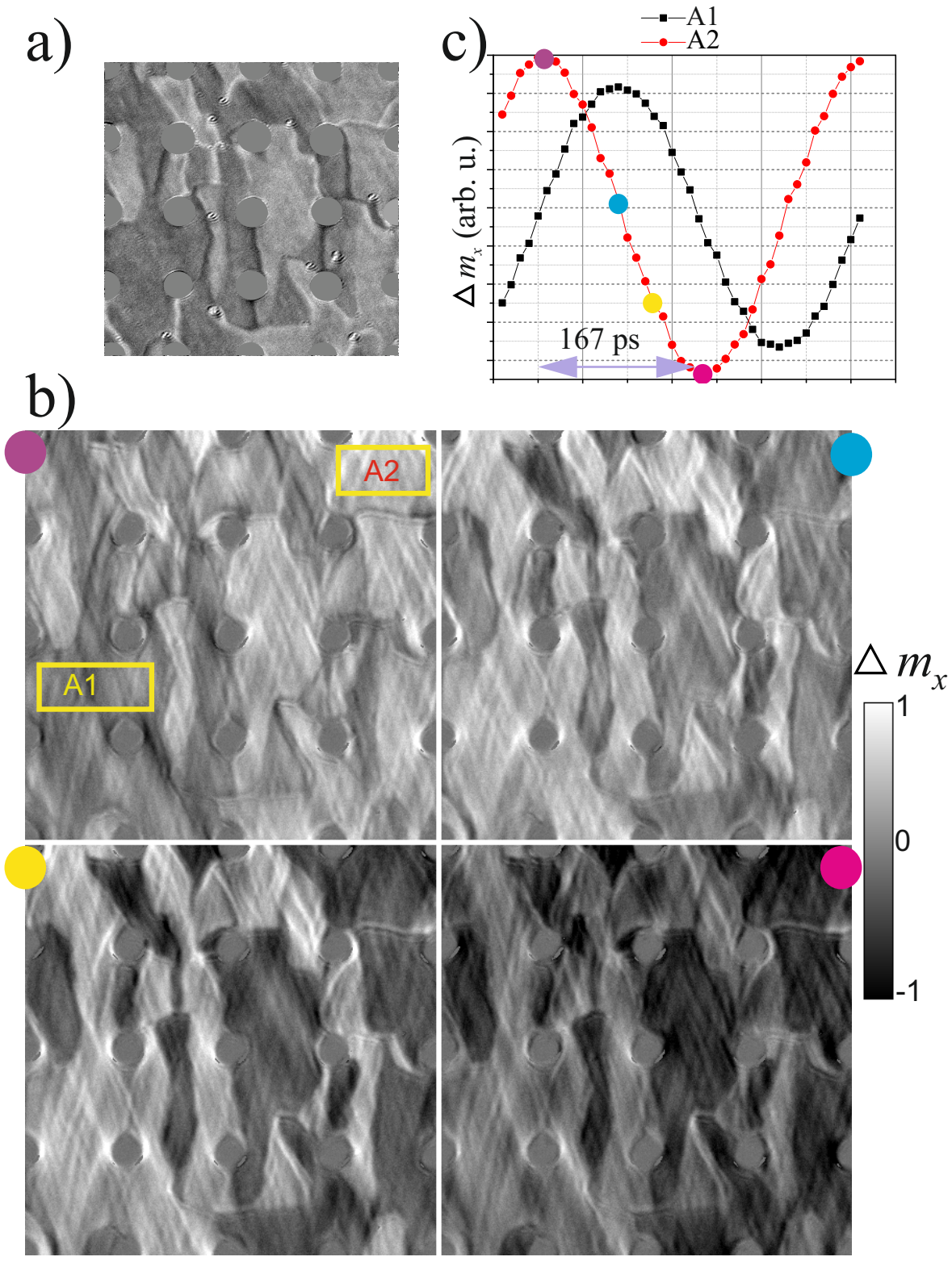

Figure 5.19: (a) The MOKE image after removing the bias field is indicated for the double layer square array antidot. (b) The dynamic magnetization evolution is measured via TR-MOKE microscopy for the static DWs configuration in (a) after applying a 285 A/m (6 V) harmonic excitation field at 3 GHz frequency. The grey scale shows the contrast. In addition, two regions are indicated by R1 and R2 in the first image. (c) The plot shows the variation of magnetization in two mentioned regions. The four points are marked by solid coloured circles in the plot. Their corresponding image in (b) has the same coloured circle in its corner.

tation frequency respond with the highest amplitude in comparison with other areas. Then SWs propagating from neighbouring antidots reflect and interfere. In addition, there is the possibility of caustic wave emission.

5.3 Antiparallel Magnetization at Higher Field

In the last section, the remanence was taken into consideration where antiferromagnetic coupling aligns the magnetization antiparallel between layers. By bias field enhancement in opposite direction to -0.48 kA/m, the static magnetization pattern is still similar to remanence as it can be seen in Fig. (5.1 b) and (5.2). This behaviour is the same in our simulation since the observed pattern remains as before.

In the next step, the initial static magnetization in -0.48 kA/m is used and the permeability spectrum is calculated by LS-PIMM method via applying a step function with the amplitude of 5.6 A/m and rise time equal to 30 ps.

The dynamic magnetization behaviour is not longer similar between layers since their effective field changed. The acquired results from simulation are shown in Fig. (5.20 a) and compared with PIMM measurements results in Fig. (5.20 b). It manifests overall permeability of the specimen with three distinguishable peaks. To find out the origin of these peaks, every layer's permeability is depicted in (5.20 c) and (5.20 d), individually.

It is evident that the first peak at the lowest frequency of around 0.9 GHz comes mostly from first layer. This peak has the highest amplitude of dynamic response in the first layer to step field excitation and is followed by another peak with much lower amplitude. The second layer consideration shows significant enhancement of the peak amplitude approximately at 1.6 GHz. From the plot in (5.20 d), it can be seen that the real part of the signal has wide frequency band. In addition, the imaginary part has two peaks, the first one with lower intensity at the same frequency as dominant frequency of the first layer and the second peak with much higher intensity at 1.6 GHz which corresponds to the real part zero crossing. As conclusion, each of main peaks in Fig. (5.20 a) correspond to dominant $f_{r,l}$ of each layer.

To confirm our simulated results, data from direct PIMM measurement are plotted in Fig. (5.20 b) for the same bias field -0.48 kA/m [48]. The same pattern with two remarkable peaks is evident. Furthermore, as it was predicted by simulation, the second peak at the higher frequency has a higher amplitude. There is a small shift in the detected frequencies in comparison to the simulation. This can be allocated to consideration of uniaxial anisotropy (700 J/m^3) in our calculation, however it can be up to twice higher in real sample. The lower anisotropy decreases the effective

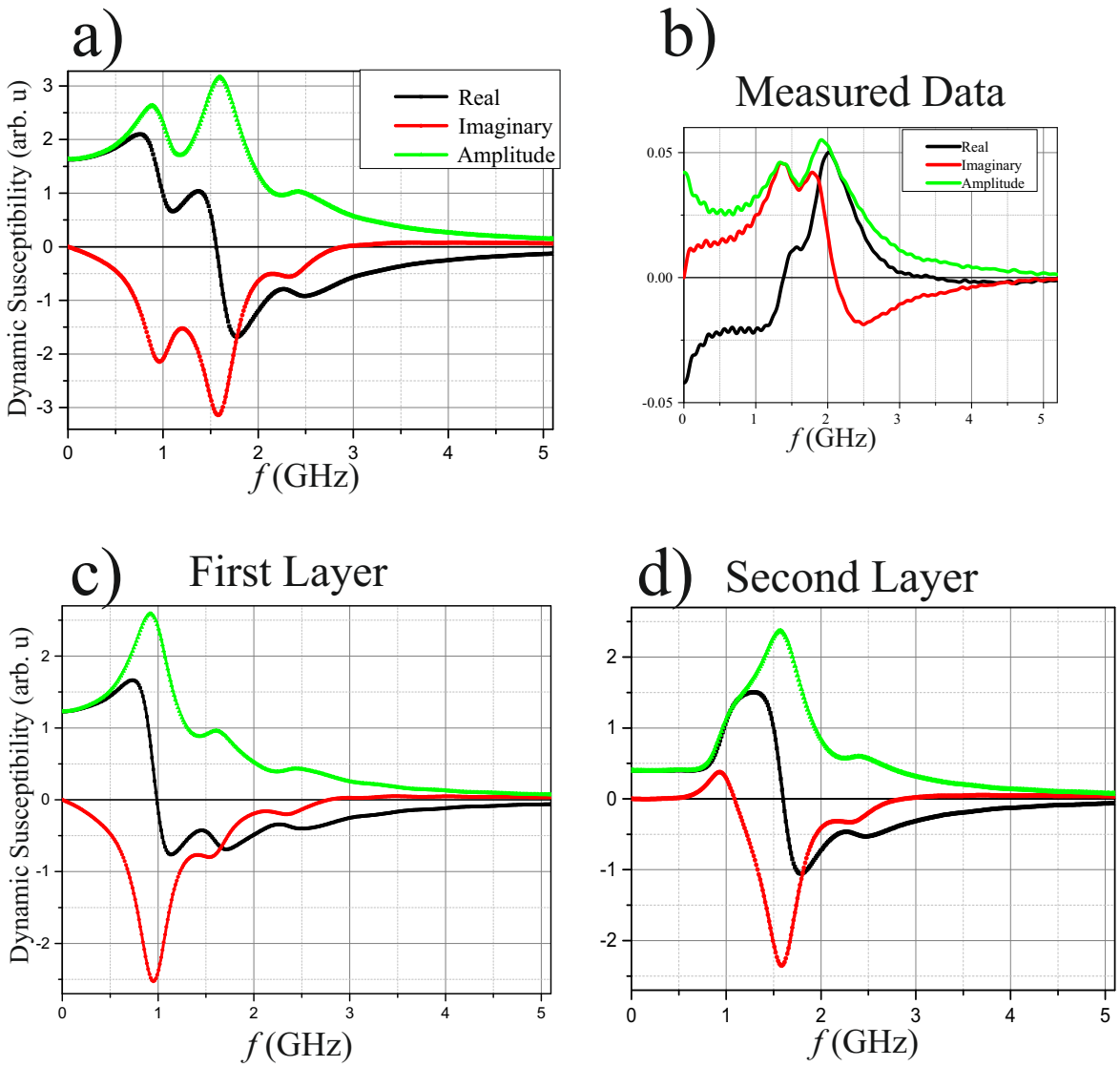

Figure 5.20: (a) The permeability spectrum are calculated in the frequency domain for a double layer antidot. The real, imaginary part and amplitude of the DFT signal are shown with black, red and green graphs. The simulation is based on the initial antiparallel magnetization in layers similar to what was described before in Fig. (5.14). (b) The calculation is compared to PIMM measurement data from [48]. In both calculated and measured data, there are two dominant peaks. (c,d) The permeability is calculated and plotted for every layer individually.

field and as a consequence lowers f_r based on equation (2.48).

The difference in the two layers' resonance frequency corresponds to a difference in their effective field. If a bias field equal to -0.48 kA/m is applied, the anisotropy field in one layer (with higher local resonance frequency) is along the bias field and in another layer (with lower local resonance frequency) is opposite to the bias field. This can be explained by the effective anisotropy field calculation. The effective field is defined as total energy density [77]:

$$H_{eff} = -\frac{1}{\mu_0 M_s}\nabla_{\mathbf{m}} e_{tot}$$
$$e_{an} = -K_u(\mathbf{c}\cdot\mathbf{m})^2 \tag{5.4}$$

where e corresponds to the energy density and $\mathbf{c}$ indicates a unit vector parallel to the easy axis of magnetization. The combination between above equations leads to effective anisotropy calculation:

$$\mathbf{H}_{k,eff} = -\frac{1}{\mu_0 M_\mathrm{s}} \nabla_\mathrm{m} e_{an} = \frac{2K_\mathrm{u}}{\mu_0 M_\mathrm{s}} (\mathbf{c}\cdot\mathbf{m})\mathbf{c} \tag{5.5}$$

Therefore, the effective field is different between layers mostly by H_K. If the Kittel formula, $f_r = \gamma\mu_0/(2\pi)\sqrt{M_s(\pm H_K + H_0 + H_{dem})}$, is used, the layers' resonance frequencies are obtained at f_r = 0.81 and 1.48 GHz which are similar to the simulated results in Fig. (5.20 a). The third peak with low intensity comes from demagnetizing field enhancement around antidots where this field and H_0 are parallel.

Besides, the possibility of perpendicular standing SWs', PSSWs, propagation is investigated. The corresponding dispersion relation from Ref.s [176], [177],[178],[179] is used:

$$f_{PPSW} = \frac{\gamma\mu_0}{2\pi}\sqrt{\left[H_0 + \frac{2A}{\mu_0 M_s}(\frac{p\pi}{d})^2\right]\left[H_0 + \frac{2A}{\mu_0 M_s}(\frac{p\pi}{d})^2 + M_s\right]} \tag{5.6}$$

where $A = 2.4\times10^{-11}$ J/m is the exchange constant and p shows SWs' mode number. If the material saturation magnetization $\mu_0 M_s$ = 1.48 T, each layer thickness d = 25 nm and H_0 = 0.48 kA/m are substituted, f_{PSSW} equal to 0.84 and 31.3 GHz for p = 0,1 is obtained. The first frequency corresponds to Kittel mode and is observed in Fig. (5.20) too, while the second one is much higher than the considered frequency band. From static magnetization simulation, the effective field, $H_{eff} = H_0 \pm H_K + H_{dem}$ in two layers was obtained around 0.48 and 1.43 kA/m. We consider the second layer's effective field and calculate corresponding PSSWs. The obtained results are 1.48 and 31.3 GHz. The first frequency is Kittel mode and the second one is similar to what we obtain for the first layer because the dispersion relation, *f(H0)* for p = 1 is almost a constant line.

There are studies indicating that antiferromagnetic coupling between layers causes an asymmetric dispersion curve in magnonic crystals [54]. It has been mentioned that antiferromagnetic coupling is required to make such asymmetry in comparison with ferromagnetically coupled layers, but it is not enough. Similarly, in our case, it seems that, however, we had such alignment even in remanence, a small bias field is needed to make difference evident by aligning the anisotropy field in layers antiparallel to each other.

Furthermore, the TR-MOKE wide field microscopy is used to measure dynamic magnetization evolution when the static field -0.48 kA/m in $\hat{\mathbf{z}}$ and harmonic excitation in $\hat{\mathbf{x}}$ is applied. The results at 1, 2 , and 3 GHz frequency are similar to the remanence state.

5.4 Parallel Magnetization Between Layers

In this section we consider the last point in Fig. (5.1 a,b) and (5.2), indicated by a pink circle. From an earlier figure that shows the magnetization component in the direction of the magnetic field, it seems that applying -1.6 kA/m results in the system being almost saturated. However, the magnetization component in the other sensitivity shows still small and not saturated areas around dots. These areas form to reduce the high demagnetizing field in this region. To predict the dynamic behaviour of magnetization, a step function is applied as a magnetic stimulus with very small amplitude of 4 A/m along $\hat{\mathbf{x}}$ axis and perpendicular to the static field. With the help of DFT, the simulated signal in the time domain is transferred to the frequency domain and the dynamic susceptibility (or equally permeability) versus frequency is obtained. Then the amplitude of this calculated magnetic permeability in one frequency for every simulation cell is obtained. The results are depicted in Fig. (S-A3) for lower frequencies and in Fig. (S-A4) for frequencies higher than 2 GHz. Consider the area division illustrated before in Fig. (4.6). Here $f_{r,l}$ in the matrix is around 1.7 GHz since the permeability amplitude in this area increases notably at this frequency (Fig. (S-A3)). The area around dots are like Néel spikes and has the lowest $f_{r,l} \leq 0.4$ GHz. They are excited with much higher amplitude in comparison with other areas, however, the colour code range restricted to 1, in order to have best contrast and make the pattern in higher frequencies visible. This calibration is common for all four indicated frequencies in Fig. (S-A3).

Based on above results at 2 GHz and our knowledge obtained from single layer antidot simulation and measurement (see Fig. (4.9) and (4.7)) to excite SWs inside the matrix at this frequency, stronger stimulus (with higher amplitude) are needed. Therefore, we applied the static field at -1.6 kA/m horizontally and a strong harmonic field with 309 kA/m amplitude (base to peak) at 2 GHz. The exemplary data from the wide field time resolved MOKE microscopy are manifested in Fig. (5.21 a). They are recorded in vertical sensitivity ($\triangle m_x \pm$ c m_y where c is a constant and $\hat{\mathbf{y}}$ is OOP axis) and show dynamic magnetization evolution during the half cycle of 250 ps. Their corresponding phase points are indicated via coloured circles on the plot, Fig. (5.21 b).

The calculated result through the LS-PIMM method at higher frequencies Fig. (S-A4) reveals that in the area along the vertical connection between the dots, the highest $f_{r,l}$ of around 3.5 GHz is predicted. This is similar to the single layer case, since this $f_{r,l}$ enhancement is a consequence of the parallel demagnetizing and the bias field alignment in the square antidot array near to the saturation magnetization (see Fig. (4.5)). Therefore, this area responds to the magnetic excitation with higher amplitude, as it can be seen in Fig. (S-A4), at 3.5 GHz. Therefore, a 4 GHz sinusoidal field with 309 A/m is applied in order to follow magnetization precession in this region. The images

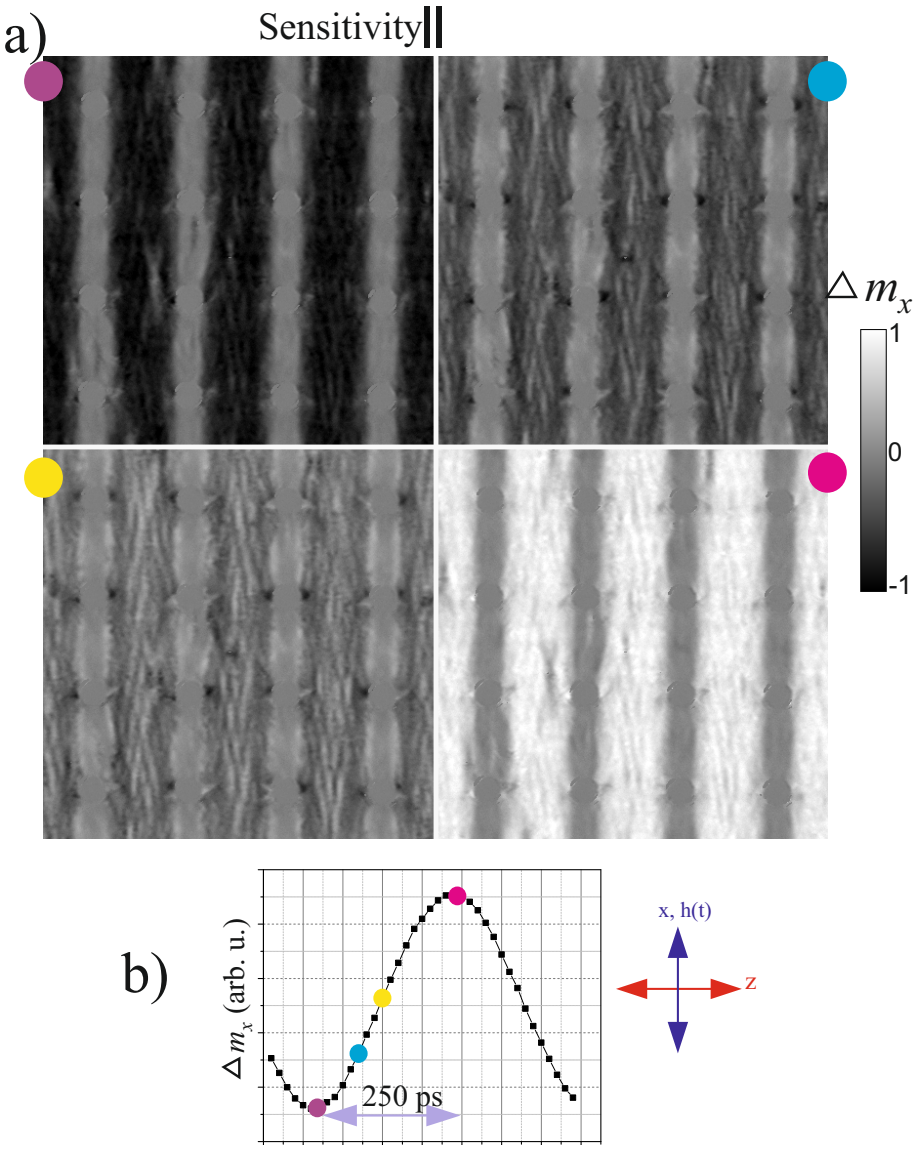

Figure 5.21: The magnetization evolution during the switching process is measured via TR-MOKE wide field microscopy. A harmonic stimulus in the vertical axis at 2 GHz frequency with 309 A/m amplitude is applied at the same time with -1.6 kA/m static field normal to stimuli. All images are measured with vertical sensitivity in the direction of the alternative field. (b) The phase interval during measurement is about 10 degree which corresponds to 14 ps, as it can be seen in the plot, four selected images shown in (a) are highlighted on the plot with colour code.

are shown in Fig. (5.22) in the same phases as in Fig. (5.21 b). This means that the first and the last image correspond respectively to the minimum to maximum $\triangle m_x \pm$ c m_y (c is a constant). It can be seen that the interesting area (vertical connection between dots' area) is in phase with the full dynamic response. Furthermore, the Neél spikes around dots either in simulation or in the dynamic magneto-optically measured data are evident.

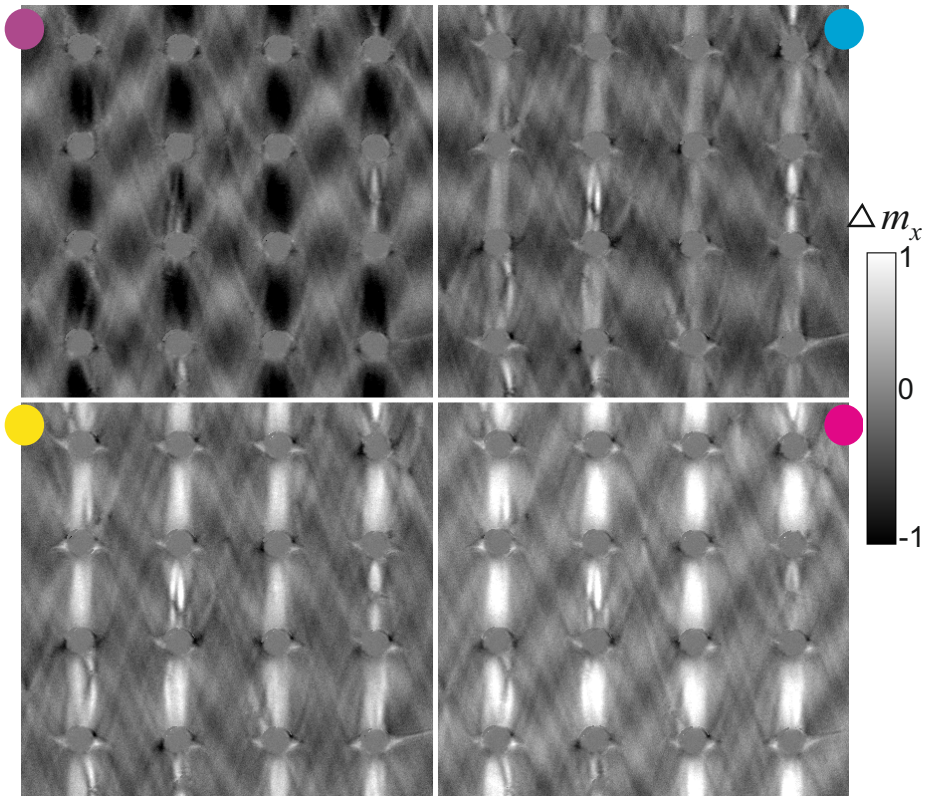

Figure 5.22: The TR-MOKE wide field microscopy is utilized to record images when a sinusoidal magnetic field with 309 A/m in $\hat{\mathbf{x}}$ at 4 GHz frequency simultaneously with -1.6 kA/m static field in $\hat{\mathbf{z}}$ is applied to the double layer antidot sample. The images phase difference is the same as Fig. (5.21 b).

5.5 Summary

We investigated a double layer sample patterned with an antidot array and antiferromagnetic coupling between layers. The static magnetization configuration was investigated via MOKE microscopy and magneto-optical vector imaging via TR-MOKE wide field displayed dynamic magnetization behaviour. In both cases, either the static magnetization microstructure or the dynamic response of $\mathbf{m}$ were simulated and compared with the measurements. The approach to find a prospective SWs' source was $f_{r,l}$ calculation via LS-PIMM, which suggests, based on the discussion in the last chapter, that areas with the lowest $f_{r,l}$ are a prospective source of SWs emittence. Afterwards, this was proved either by agreement between simulation and time-resolved MOKE results or by transient signal simulation. The study included three main magnetization microstructures that have different features in comparison with the single layer, besides two similar ones where the applied magnetic field overcomes antiferromagnetic coupling. In the first case, a magnetic field of 0.48 kA/m was applied, where the antiferromagnetic coupling between layers leads to an antiparallel magnetization alignment between the layers in some part of system. The straight DWs formed along the line connecting two antidots. These DWs are like borders between domains that have antiparallel (R3, R4 in Fig. (5.3)) and parallel (R1, R2 in Fig. (5.3)) magnetization in the two layers,

so we successfully changed magnetization locally . The SW emission from DWs that propagate inside the antiferromagnetically coupled domains was demonstrated by simulation results. The transient signal's simulation reveals the non-reciprocity of the emitted SWs from these walls that shows the band structure and dispersion relation has been locally changed. We used an analytical approach from literature to calculate the dispersion relation of these SWs to explain the unique feature of non-reciprocity. Furthermore, static magnetization configuration after magnetic field reduction to zero and then to -.048 kA/m were studied. The static magnetization configuration is antiparallel between layers and there is no highlighted DW, but the antidots' shape anisotropy led to SW creation when a magnetic stimulus was applied. The static magnetization configuration in 0 (remanence) and with applying -0.48 kA/m seems to be completely similar either via MOKE or time-resolved wide-field MOKE. But the PIMM results, which were comparable to the average signal from LS-PIMM, demonstrate an interesting difference. Via simulation results, it was confirmed that both layers effective fields and therefore f_r are the same in the magnetization remanence, but the layers' behaviour is different after applying a low static field up to -0.48 kA/m. The effective field calculation showed that the uniaxial anisotropy besides antiferromagnetic coupling between layers can explain such a difference. The uniaxial anisotropy supports two possible equilibrium for anisotropy field alignment while the magnetization is still antiparallel between the layers. Thus, in the second layer, the effective field is higher than the first one and this leads to higher f_r rather than natural f_r (FMR) material. Therefore, this asymmetry in dispersion relation ($\omega(H_0)$) can be useful for SWs based devices that need to be sensitive to the field direction. Another advantage can be found when in low fields, we need a higher f_r than the material's natural resonance frequency.

Chapter 6

Summary

A single layer ferromagnetic thin film with a square lattice of antidots was studied. This magnetically engineered pattern varies the demagnetizing field and as a consequence the effective field locally and provides a periodic non-uniform magnetization. When a bias field of 1.6 kA/m was applied, a butterfly-like magnetization configuration (domain patterns of Néel spikes) was observed with two magnetic poles, four curved DWs around the dots. This magnetization pattern was observed via a MOKE microscope. The system's effective field (consists of the demagnetizing, anisotropy, the exchange, and static external field) was calculated via a micromagnetic simulator, Micromagus.

In this work, a numerical method, LS-PIMM, was developed to calculate local resonance frequency distribution $f_{r,l}$. The LS-PIMM provides an approach to predict prospective sources, as the required f_{exc} to emit and propagate SWs via $f_{r,l}$ distribution. This method imitates what happens during a PIMM measurement. The great agreement between the calculated results obtained from this method and the measured data, via PIMM, confirmed the simulation strategy. Furthermore, LS-PIMM was compared with other methods to highlight its accuracy and generality. One advantage of this method is that we calculate the permeability spectrum and so f_r directly when $m(t)$ signal is extracted. Therefore, we neither need to calculate every element of the demagnetizing tensor individually using a complicated process nor apply the Kittel formula with its associated reduction of complexity or restrictions. The LS-PIMM results for the single layer CoFeB showed several maximums in the permeability amplitude, $\mu(\omega)$, at different frequencies, ranging from 0.5 to 3.7 GHz, which corresponds to different effective fields mostly as a consequence of demagnetizing field engineering.

The time-resolved wide-field MOKE investigation revealed the existence of elastic waves originating from DWs around antidots at lower frequencies, about 2 GHz. At higher frequencies, mag-

netic waves were detected. These waves' generation and propagation were controlled via the excitation field frequency and amplitude. However, the magnetic waves in higher frequencies were observed via a time-resolved MOKE microscope, one clear wavefront could not be distinguished. Therefore, to figure out the source of these waves, the dynamic response of magnetization to the harmonic excitation field with different frequencies and amplitudes was simulated. The transient signal consideration confirmed that the DWs with the lowest local resonance frequency ≤ 0.5 GHz are the waves' source. Since the sources, two DWs, exist close to each other on every side of the antidot, the multi-reflections of the waves from curvature-like DWs created a caustic wave pattern in the exact vicinity of DWs. The waves and their reflections are superposed and form a complicated wave propagation pattern.

These magnetic waves have a similar features as the BVWs, not only according to the relative orientation of magnetization and their wave vector around the sources but also regarding the minimum required (threshold) excitation field's frequency. Based on BVWs theory, the abovementioned sources can be excited at low frequencies in the GHz range, ≤0.5 GHz, but they were observed via the wide-field time-resolved MOKE microscope at f_{exc}≥ 3 GHz. Lower than 3 GHz, just the elastic waves were detected. The reason is that the produced waves need to propagate long enough inside a homogeneous magnetic medium to be detected. This propagation depends on the direct neighbour's local resonance frequency, which is based on $f_{r,l}$ distribution's simulation shown in Fig. (4.3), is $f_{r,\,matrix}$ = 2 GHz on one side of DWs. On other side the $f_{r,l}$ is even higher.

To summarize, by applying a static magnetic field to our magnetically engineered pattern, DWs form. They act as a magnetic antenna to emit SWs when they are excited by a magnetic stimulus such as a uniform sinusoidal field. The different distribution of effective field and so $f_{r,l}$ originating from non-uniform demagnetizing field distribution on two sides of the walls, causes nonreciprocity of SWs and even elastic waves. This is another advantage of such a micromagnetic structure since it provides another degree of freedom to control the direction of wave propagation when an asymmetric dispersion is preferable.

Moreover, a double layer thin film with the square lattice of antidots similar to the single layer one was studied. The two ferromagnetic layers were coupled antiferromagnetically via a nonmagnetic layer that modulates RKKY interaction in the interface. This antiferromagnetic coupling between layers increases the complexity of the system. The three different magnetization patterns were considered after applying the static magnetic fields and another pattern in magnetization remanence. The tail-tail and head-head magnetization configuration were obtained in both simulations and from MOKE data by applying a magnetic field of 0.48 KA/m. In this magnetization configuration, antiferromagnetically coupled domains along one of the antidot lattice axis were

observed partially between dots while the matrix in both layers had still parallel magnetization. The local resonance frequencies were simulated via LS-PIMM and the data were utilized to explain dynamic magnetization behaviour measured via the wide-field TR-MOKE microscope. The waves with larger k (shorter wavelength) in the area with antiferromagnetic coupling had a linear dispersion relation and so constant velocity. These waves' behaviour was studied and compared to the data calculated with an analytical approach (from literature, Fig. (5.13)). The transient signal's simulation inside the antiferromagnetically coupled domains revealed that two out of four similar DWs were sources of SWs emittance, see Fig. (5.11 c). The analytical calculation explained this result by an asymmetric dispersion of SWs. Therefore, because of SWs propagation's non-reciprocity, the emitted waves from the the two remaining DWs have a larger wavelength than the width of the antiferromagnetically coupled domain and so they are not detectable.

Furthermore, the magnetization pattern was considered when the magnetic field was removed and antiferromagnetic coupling between layers reduced the total magnetization to zero. To find the static magnetization configuration, the total magnetic energy of three microstructures with and without DWs were calculated and compared by calculating their total magnetic energy. The configuration with the minimum amount of energy was considered as the most stable one and was used as initial magnetization configuration to predict the dynamic response of **m** to a magnetic excitation. The agreement between dynamically simulated data and their counterpart measured via TR-MOKE microscope confirms the whole process.

We compared two magnetic configuration in remanence and H_0 = -0.48 kA/m, that the magnetization between layers orientates antiparallel and therefore, total magnetization is zero. But their permeability spectrum is different in the data collected both via PIMM measurement and LS-PIMM simulation since the magnetic permeability spectrum versus field splits in H_0 = -0.48 kA/m. This splitting in the dispersion graph $\omega(H_0)$ was explained by calculating the effective field. This calculation shows that uniaxial anisotropy (induced during deposition) is mainly responsible to detect different effective fields and thus different f_r in the layers, although they are made of the same material and so have the same magnetic features. Since the magnetization has two equilibrium states and so it can parallel or antiparallel to the applied external field align.

To summarize, it is shown how multiple f_r can be reached by laminating. It should be mentioned that one of the layers' f_r corresponds to the ferromagnetic resonance of material which is lower than the other layer. Therefore, a double-layer structure with antiferromagnetic coupling can be useful when a higher f_r is preferable in small magnetic fields around remanence.

Supplementary A

Double Layer Antidots

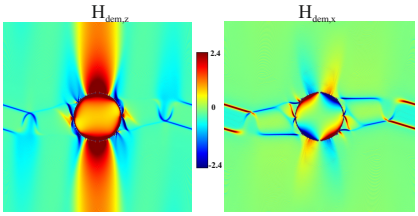

Figure S-A1: The demagnetizing field components for the first layer of a double layer antidot are illustrated under 0.48 kA/m static field is applied. The second layer behaviour is similar, so to avoid repetition just first layer data are shown. The calibration is common between two components and indicates field in kA/m. The area indicated in Fig. (5.3 b) with R2 have the highest value of $H_{dem,z}$ in addition to regions around DWs.

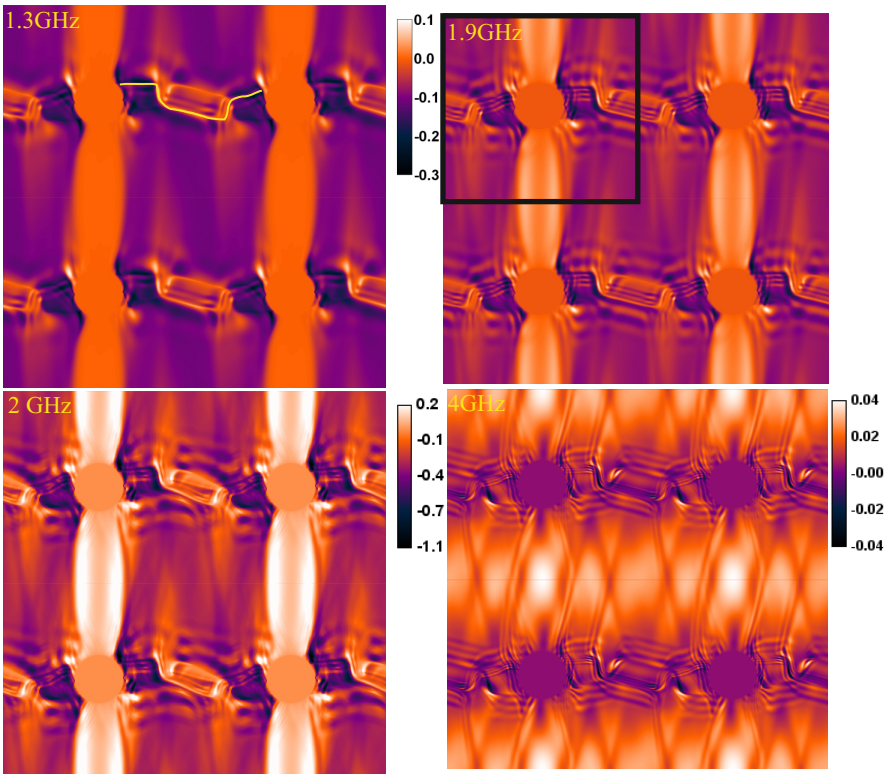

Figure S-A2: The results obtained from simulated transient effect by applying harmonic oscillation are illustrated at different frequencies. The stimuli's frequency is written in the corner of every image. The calibration code for the first row of images is common. Furthermore, to guide the eye the DWs producing SWs are highlighted in the first image by a yellow curve, and a rectangular displays the utilized super cell in the simulation in the second image. The data are calculated results for the first layer, but the second layer behaves totally similar.

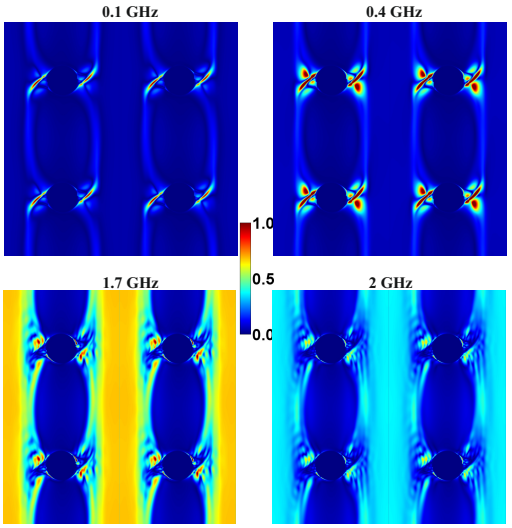

Figure S-A3: The calculated permeability via LS-PIMM method is used and results are depicted at four different frequencies which are indicated above each image. The sample is considered under -1.6 kA/m static along $\hat{\mathbf{z}}$ and a step function as magnetic stimulus with 4 A/m amplitude. The colour code is common for all of images. The area around dots has the lowest local resonance frequency. The matrix $f_{r,l}$ is about 1.7 GHz and therefore, this area has a higher amplitude of response in the mentioned frequency.

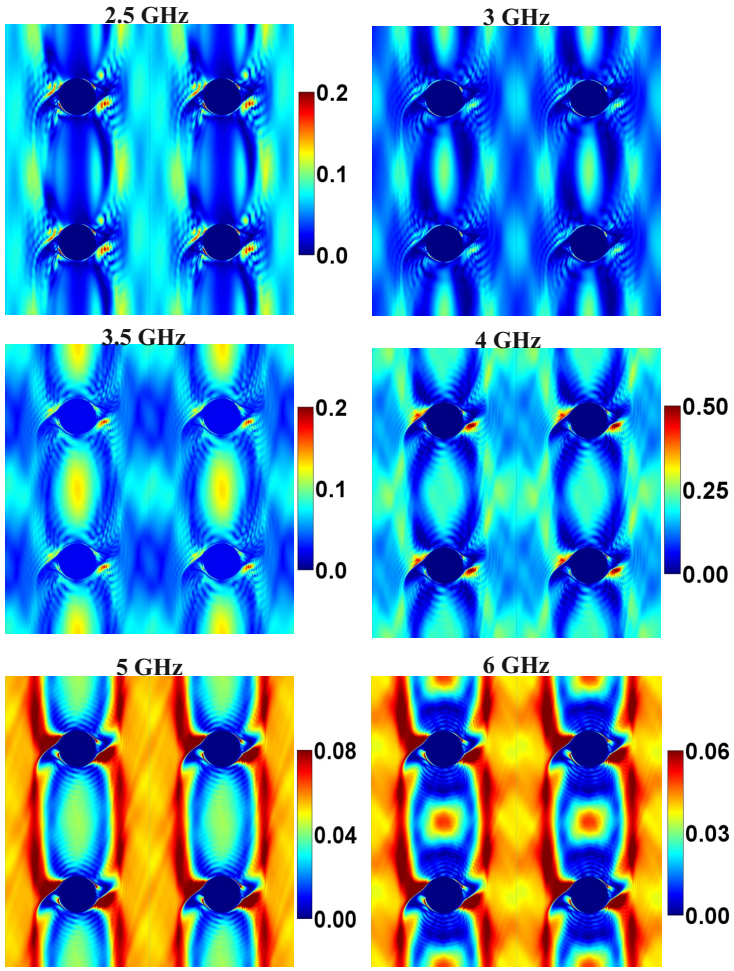

Figure S-A4: The calculated permeability via LS-PIMM method is depicted at the same magnetic fields as Fig. (S-A3) but at the higher frequencies which are indicated above each image. The colour code is common the first raw images and for the other is individual. It can be seen that the calibration range and so the contrast decrease by frequency enhancement. The area between two dots, vertically have high $f_{r,l}$=3.5 GHz in the middle, thus it excited with higher amplitude at 3.5 GHz.

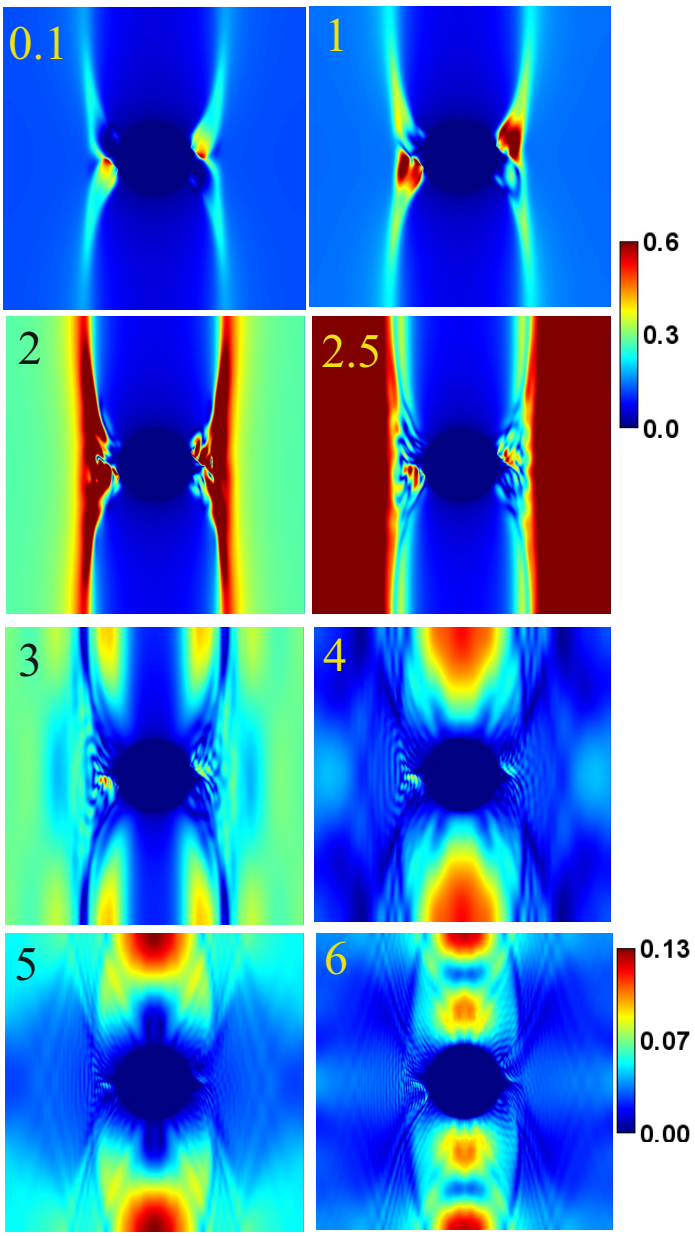

Figure S-A5: The magnetization pattern after applying a step function (LS-PIMM method) are calculated. The amplitude of dynamic responses are displayed in different frequencies. The number in every image indicates its frequency. The calibration bar is the same for frequencies between 0.1 to 4 GHz while this range is different for 5 and 6 GHz cases. The calibration range is reduced significantly to obtain enough contrast and make the magnetic pattern observable. As it can be seen matrix magnetization is 2.5 GHz, while the vertical region between dots have higher frequency around 4 GHz. The measurement will be difficult in higher frequencies than 4 GHz, as magnetization response will reduced almost as 5 times as lower frequencies.

Supplementary B

Antidot Array with Irradiated Matrix (I-dots)

In this chapter, we characterize the I-dots sample introduced in section (3.4.2). It is a double layer CoFeB sample, each layer is 10 nm which are separated by 0.7 nm of Ru. This interlayer enables antiferromagnetic coupling between the layers, by which the whole sample is irradiated except to the dots. The irradiation leads to interlayer removal through interfacial intermixing. Therefore, the only remaining area with antiferromagnetic coupling is an area of dots that have zero overall magnetization and acts like antidots. A big difference between this structure and antidots is that, here, the magnetic properties have been changed without any physical edge at the border of antidot and matrix. The I-dots array is arranged square, consisting of dots with 10 μm diameter and 30 μm center to center distance between neighbours, which is called lattice parameter. In this chapter, these sizes are shown in one symbol 10×30.

In the following, we discuss the static and dynamic features obtained from direct measurements via MOKE microscopy and PIMM measurement.

S-B1 PIMM Measurements

The PIMM method was described elaborately in section (3.1). A CPW is used both to apply a step function as a dynamic stimuli and to pick up the dynamic response of magnetization from the sample. The first step of measurement is to record a so called background from the sample. To record it, a high bias field is applied in order to saturate the sample. We suppose that a 8 kA/m bias field saturates the sample either in the easy or hard axis of magnetization. The result signal is plotted in Fig. (S-B1 a). In the second step, a specific bias field is applied. For instance, the data plotted in the Fig. (S-B1 b) are measured by applying the static bias field equal to 300 A/m along $\hat{\mathbf{z}}$ while the easy axis of magnetization is normal to the bias field, along $\hat{\mathbf{x}}$. All of the shown signals are saved after averaging over 64 times individual measurements. Now the experiment is completed

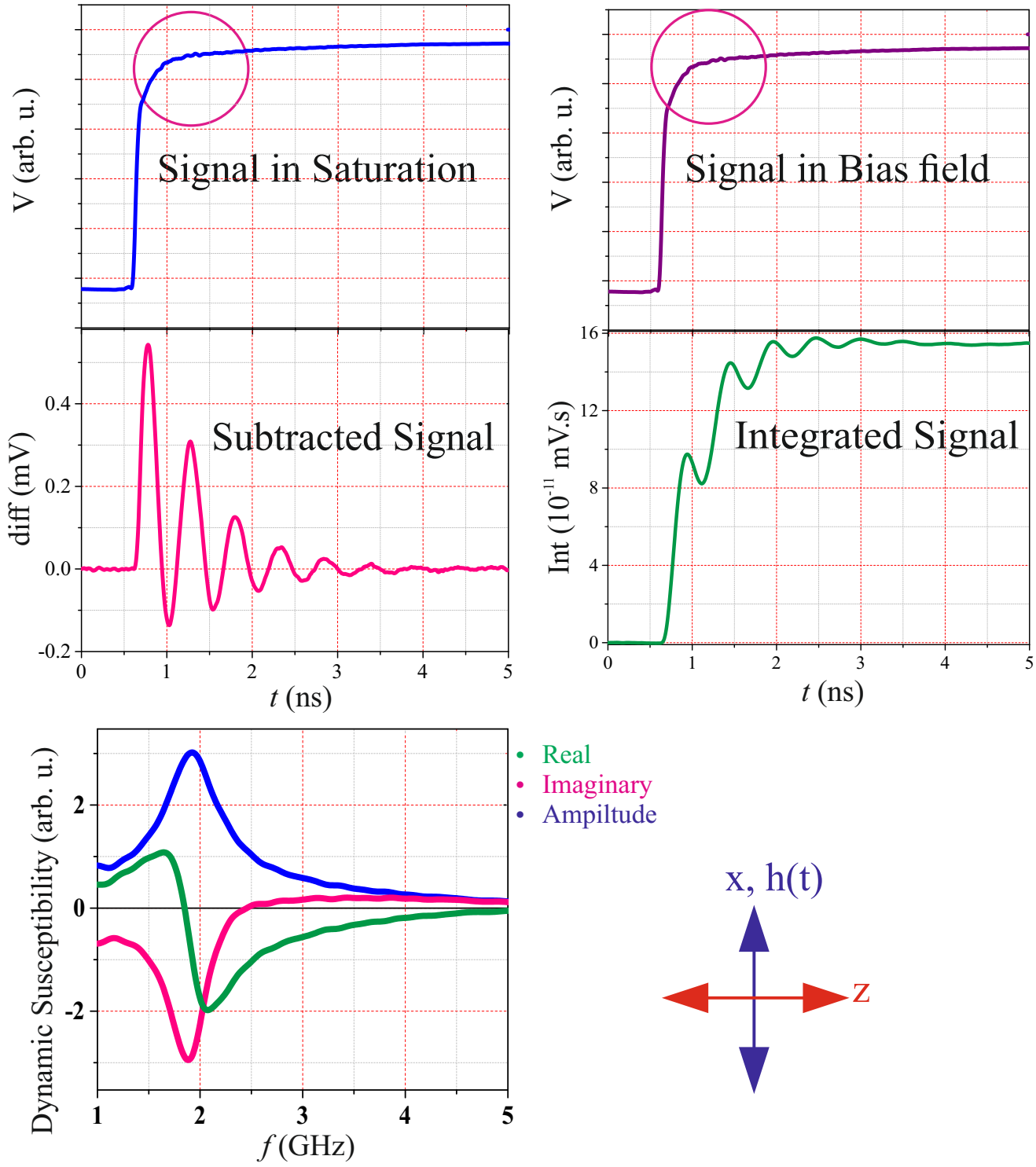

Figure S-B1: The exemplary PIMM data are shown via direct measurement for an I-dot sample with 10×30 array size. A step function is applied through a CPW as magnetic stimuli and the reflected signal is picked up again by CPW in two following situations. (a) The sample is saturated by applying an 8 kA/m bias field. (b) A static field is applied equal to 300 A/m along the magnetic hard axis. (c) The subtracted signal shows a difference between (a) and (b) coming mostly from the regions highlighted by circles. It is proportional to the magnetization dynamic response dM/dt via Faraday Law. (d) The magnetization variation is plotted versus time by calculating integral dM/dt. (e) The DFT method transfers data to the f-domain. The result shows the permeability behaviour by varying frequency. The permeability amplitude is $\sqrt{Re^2 + Im^2}$ and its peak determines resonance frequency.

and the obtained signals are processed.

The difference between signals illustrated in Fig. (S-B1 a) and (S-B1 b) is obtained by subtracting two signals provided that there is not any jitter in the time or voltage signal. The subtracted signal is indicated in Fig. (S-B1 c), which is proportional to the dynamic magnetization response dM/dt. Therefore, by calculating the integral of the subtracted signal in the time domain, the magnetization response is obtained as is shown in Fig. (S-B1 d).

To extract the materials' permeability spectrum in the frequency domain, the subtracted data in the time domain is transferred to the frequency domain via the DFT method. Before DFT, an important point in processing the data is to select first point of the subtracted signal correctly. This first point determines the signal zero base. To show this selection importance, if the time resolution is about 10 ps and the first point is selected just by one point off, the phase would be shifted by $\omega\Delta t = 6.28 \times 10^{-2}$ radian in the GHz regime. Another measure is to utilize, before DFT, the zero padding method to enhance the frequency resolution.

The result, the permeability spectrum, is plotted in Fig. (S-B1 e). As it is discussed before, the amplitude peak ($\sqrt{Re^2 + Im^2}$) shows f_r, which matches the real part zero-crossing and the imaginary part peak because of the material's low damping, see equation (2.48a).

S-B1.1 Hard Axis

The process described above is repeated for the different bias fields, from 3.2 to -3.2 kA/m with 40 A/m resolution. The results are illustrated in a contour plot in Fig. (S-B2). The information provided before in Fig. (S-B1 e) forms one vertical column in this contour. The highest intensity in every column determines resonance frequency. It can be seen that f_r drops at low bias field, -1 ≤ H ≤+1 kA/m. In this range, the sample is not single domain. Formation of domains decreases the overall magnetization component in the direction of the applied field and so the signal from the sample is weaker.

S-B1.2 Easy Axis

If we rotate the sample by 90 degree, bias field and anisotropy would be aligned in $\hat{\mathbf{z}}$ while magnetic stimuli in the form of a step function are still perpendicular to them in $\hat{\mathbf{x}}$ direction. The measurement is done in the same range of bias field as before (in the hard axis of magnetization measurement). The results are reported in a contour plot in Fig. (S-B3). The colour code is used to illustrate the DFT amplitude intensity. The maximum intensity's frequency is f_r and it is approximately between 1.2 to 2.75 GHz in the considered range of bias fields. In the contrast with our

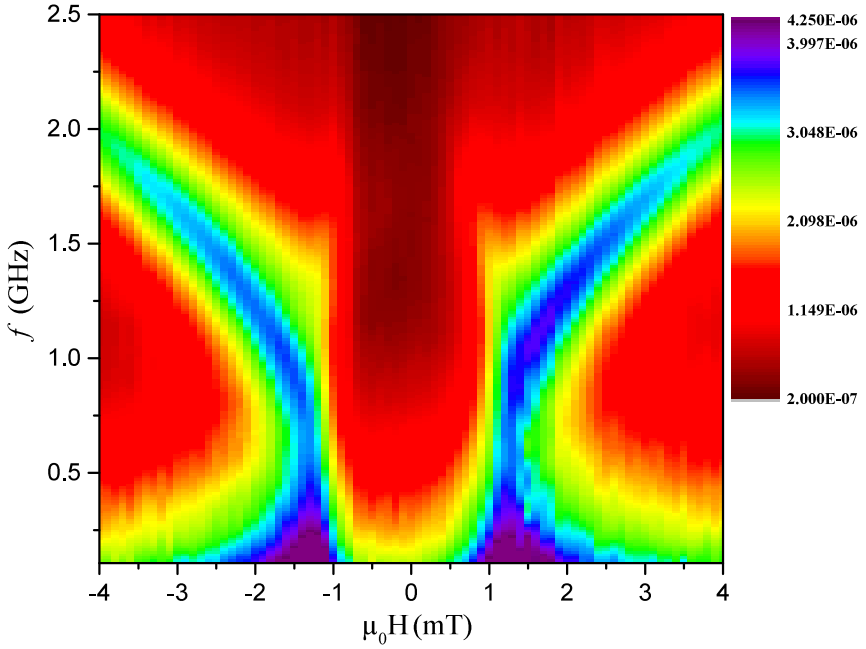

Figure S-B2: The PIMM results are displayed by a contour plot. The sample is an I-dots square array with 10 × 30 μm^2, diameter × lattice constant. The static magnetic field is applied normal to the anisotropy axis of magnetization, while a step function along easy axis provides alternative stimuli by time. The permeability spectrum is calculated based on measured data for every bias field. This spectrum (like shown before in Fig. (S-B1 e) forms one vertical column in above plot while the amplitude of DFT (dynamic susceptibility) is displayed via colour code. The calibration is next to the contour plot its maximum (in blue or purple) indicates resonance frequency in each static field. In the vicinity of the remanent state, the magnetization signal is low and a resonance frequency is not evident. The f_r is under 2 GHz in the higher fields near to saturation magnetization.

previous measurements in the hard axis of magnetization, it can be seen that around remanence state, the f_r is detectable, because after H cuts off, the anisotropy field is still available.

In the above mentioned measurements either for easy or hard axis of magnetization, the dynamic magnetization background is taken at $+H_{sat}$, afterwards the bias field decreases from $+H_{sat}$ to H. In Fig. (S-B4), we show a unique way to record stronger signal in the low bias fields based on change in the magnetization history. In the first round of measurement data, the sample is saturated at +4 mT and then the field reduces to a bias field and data is recorded. The process is repeated for -4≤ H ≤ +4 mT, the data is indicated. The range of -2≤ H ≤+1 mT corresponds to the magnetization reversal and so the effective field and the magnetization along the field direction drop. This leads to dm/dt signal reduction.

In the second round of measurement, the sample is saturated at -4 mT and then the field is reduced to the target bias field. The measurement results are collected and shown in Fig. (S-B4). From the magnetization hysteresis can be seen that magnetization reversal happens in the range of -2 ≤ H ≤1.5 mT. For this field range, we already have collected information during the other hysteresis' branch measurement.

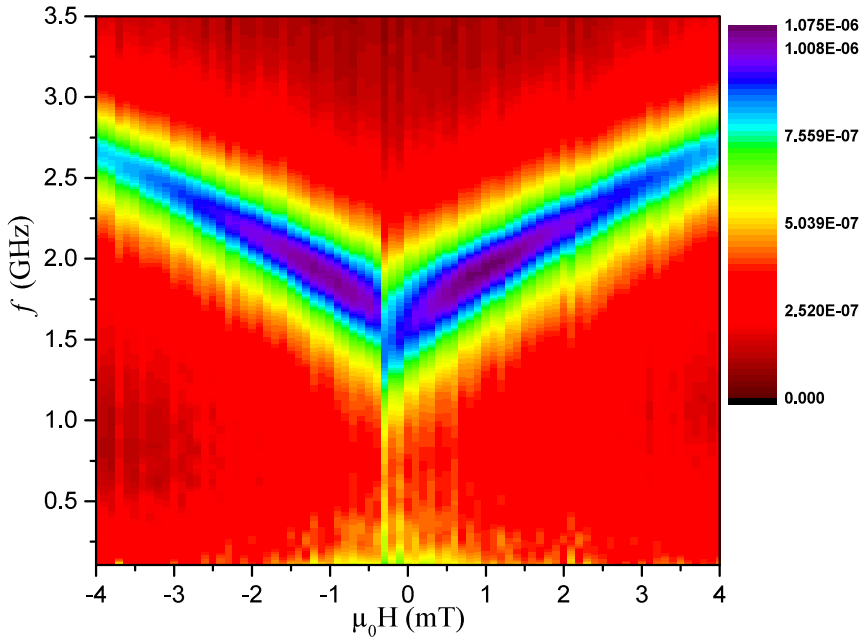

Figure S-B3: The PIMM results are displayed through a contour plot. The sample is an I-dots square array with 10 × 30, diameter × lattice constant. The static magnetic field and anisotropy axis are normal to an exerted step function. The DFT method converts measured differential magnetization in time to susceptibility or permeability of material in the frequency domain. The exemplary signal is demonstrated in Fig. (S-B1 e). This creates data for one vertical column in above plot while the amplitude of signal or DFT (dynamic susceptibility) is displayed via colour code. The calibration is next to contour plot. The resonance frequency, which corresponds to the maximum in colour code calibration, is distinguishable even in the magnetic fields around remanence state. The sample f_r is mostly in the range of 1.5 to 2.75 GHz, which is higher in comparison with the hard axis measurement because of the higher effective field, anisotropy and bias field add together.

Therefore, with two set PIMM measurements corresponding to two branches of hysteresis, it is possible to obtain complete information about the dynamic magnetization response.

S-B2 Anisotropy Estimation

One application of PIMM measurements is to find dynamic anisotropy [180], [181] which can differ from the static anisotropy because of an additional field's involvement. In Fig.(S-B5), the data are taken into consideration from both measurements on the easy and hard axis of magnetization and $f^2(H)$ is plotted. It can be seen that for higher fields, the plots are linear, indicating the regions for which Kittel formula (Kittel mode) is applicable. In this condition, the applied bias field is enough to saturate the sample and so the single domain assumption of this equation is valid. Therefore, the Kittel formula is applicable from equation (2.48 b) and (2.49), in the linear part of the plots. In an exemplary f^2, the difference between these two measurements is equal to 2 H_k. This estimation is shown by a pink double arrow at $f^2 = 4$ GHz^2 in Fig. (S-B5) which is approximately equal to 1.35

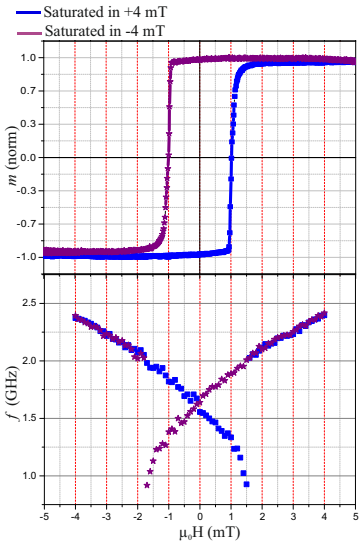

Figure S-B4: The inductive hysteresis measurement by BH-looper (above) and the dynamic measurements results by PIMM are illustrated in two paths for an I-dots square array 2 × 6 μm^2 in which 2 is the dots' diameter and 6 shows the separation distance between two dots' center. The bias field for all measurements is parallel to the anisotropy axis of magnetization. The blue and purple branches indicate, respectively, measurements starting by saturating the sample at - 4 and +4 mT.

mT for the I-dots sample 10×30. In addition, a line is fitted on the easy axis data. By extrapolation of this line, the crossing point with the field axis is obtained and denoted as $H_{k,p}$ in the graph which is -μ_0 $H_{k,p}$ = 2 mT. It is obviously higher than the estimated anisotropy from the same set of data via Kittel formula. The difference between these two obtained anisotropies provides the additional anisotropy field term μ_0 H_{add}=0.65 mT. This is an extra field which is added to the effective field, $H \longrightarrow H + H_{add}$ [107].

Another application of PIMM measurement is determining the effective damping parameter α from the LLG equation (2.45) [182], [183]. It is calculated by fitting an exponentially decay function (exp(-α ωt)) on the subtracted signal, indicating magnetization variation by time, like what was shown in Fig. (S-B1 c). Therefore, it is possible to estimate the effective damping parameter in every bias field, provided that the signal is strong enough and shows underdamped oscillation behaviour. Based on our calculation, effective damping α_{eff} is around 0.008 to 0.01.

S-B3 MOKE Measurement

The hysteresis for I-dots 10 × 30 is measured inductively and shown in Fig. (S-B6). The magnetic field applied in $\hat{\mathbf{z}}$ is perpendicular to the anisotropy axis in $\hat{\mathbf{x}}$. There are some marked points of the graph indicated by solid colour circles, starting from the positive saturation to the negative one. We are going to discuss the static domain configuration at these selected points via MOKE microscope measurements. The required field to saturate the sample is much higher than 2.5 kA/m, but the

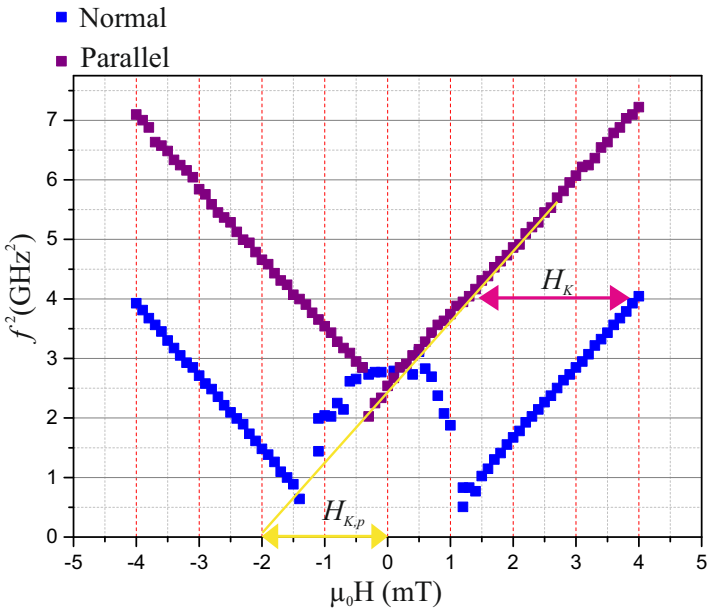

Figure S-B5: The PIMM measurement results are displayed for a sample with a square I-dots array in which the dot diameter × lattice constant is 10 ×30 μm. The vertical axis is the frequency square in GHz^2. The linear behaviour happens in the Kittel mode. The measurement is done by applying a static bias field between 4 and -4 mT while the required stimuli is provided via a step function normal to static field. In order to calculate the anisotropy field, this measurement is repeated for the case that the bias field is either parallel or normal to the magnetization anisotropy axis, respectively, denoted by purple and blue points in the plot. The field difference between these two plots is highlighted at one point of the vertical axis, f^2= 4 GHz^2. This difference corresponds to the double anisotropy field. Furthermore, the extrapolation of data measured in the magnetization easy axis is exhibited by a yellow line. This line intercept manifests the anisotropy plus an additional field.

plotted graph is zoomed in to benefit from the higher resolution.

The magneto-optically measured data are illustrated in Fig. (S-B7), they are recorded in the highlighted points on magnetization hysteresis and indicated by the same colour circle in the middle of pair images as hysteresis. They are differential images after subtracting the background image. The background image's field should be high enough to saturate the sample and as a result, it does not remain any variation in magnetization throughout the sample and therefore no contrast. The images are categorized in pair and their corresponding sensitivity axis are indicated by red and blue double arrows above the images, indicating oblique plane of incidence light. The horizontal sensitivity indicates the components of magnetization parallel to the bias field $m_z$and the vertical sensitivity shows m_z. If the OOP component is small, horizontal and vertical sensitivity present, the magnetization components along the bias field and the anisotropy axis, respectively. The values inside the images are the magnetic field in kA/m. As it is indicated in the magnetic loop Fig. (S-B6), all of the measurements belong to one branch of the hysteresis, starting from saturation at + 32 kA/m. This high static field is needed to completely saturate the dots that have antiferromagnetic coupling with the next layer. Afterwards, the field is reduced to reach every specified field.

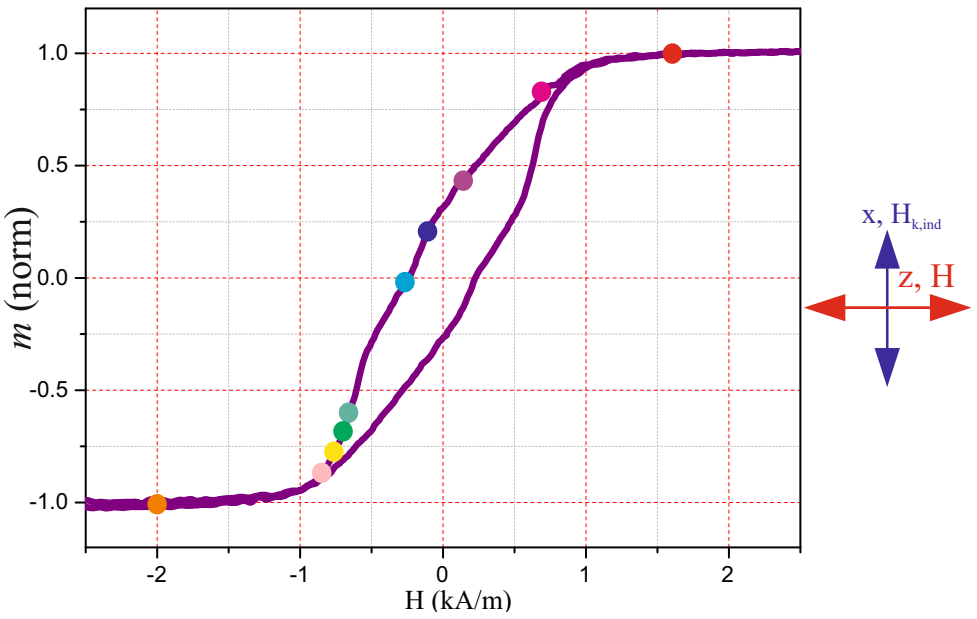

Figure S-B6: The magnetization variation is measured inductively along $\hat{\mathbf{z}}$ direction versus applied magnetic field for an I-dots square array in which the dots' diameter × lattice constant is equal to 10× 30 μm . The magnetic anisotropy is perpendicular to the static field and therefore, measurement is in magnetic hard axis. The solid circles indicate specific magnetic fields, in which magneto-optically measured data are recorded and will be shown in the following.

Furthermore, static magnetic field, $\hat{\mathbf{z}}$, anisotropy axis, $\hat{\mathbf{x}}$, and the square I-dots array axis are illustrated in Fig. (S-B8 a). The anisotropy has been induced to the sample during deposition and the anisotropy axis deviates relative to the I-dots arrays' axis. Thus, in Fig. (S-B7), to obtain the horizontal and vertical sensitivity parallel to, respectively, magnetic field and anisotropy axis, sample and its I-dots array is rotated by 25 degree. The rotation of the antidot lattice relative to the applied field makes a big difference in the magnetization pattern as it was shown through micromagnetic simulation for an antidot sample in [163]. The I-dots array deviation varies the distance between inhomogeneity around neighbouring antidots.

With magnetic field reduction from saturation to 1.6 kA/m, the array is not fully saturated anymore. This can be seen from the vertical sensitivity measurement by a red circle in Fig. (S-B7) and in Fig. (S-B8 b). The high shape anisotropy field around the dots and antiferromagnetic coupling in dots rotate magnetization in this region. This magnetization rotation is illustrated by orange arrows in Fig. (S-B8 b). The demagnetizing field is calculated via micromagnetic simulation in the same static field and illustrated in Fig. (2.16). This butterfly structure is calculated for a similar structure, the square array antidot 4× 12. But the difference is that, here, the dot lattice is tilted relative to the bias field. It is expected that the butterfly axis stays orientated along $\boldsymbol{H}+\boldsymbol{H}_{k,ind}$. The anisotropy field is around 1.08 kA/m, based on measurements via PIMM method. Therefore, under a rough estimation, the superposition between bias field 1.6 kA/m and this anisotropy has a 35 degree angle relative to the $\hat{\mathbf{x}}$ axis. These superposed vectors are shown with purple colour in the schematic part of Fig. (S-B8 b). Moreover, the demagnetizing field based on calculation in

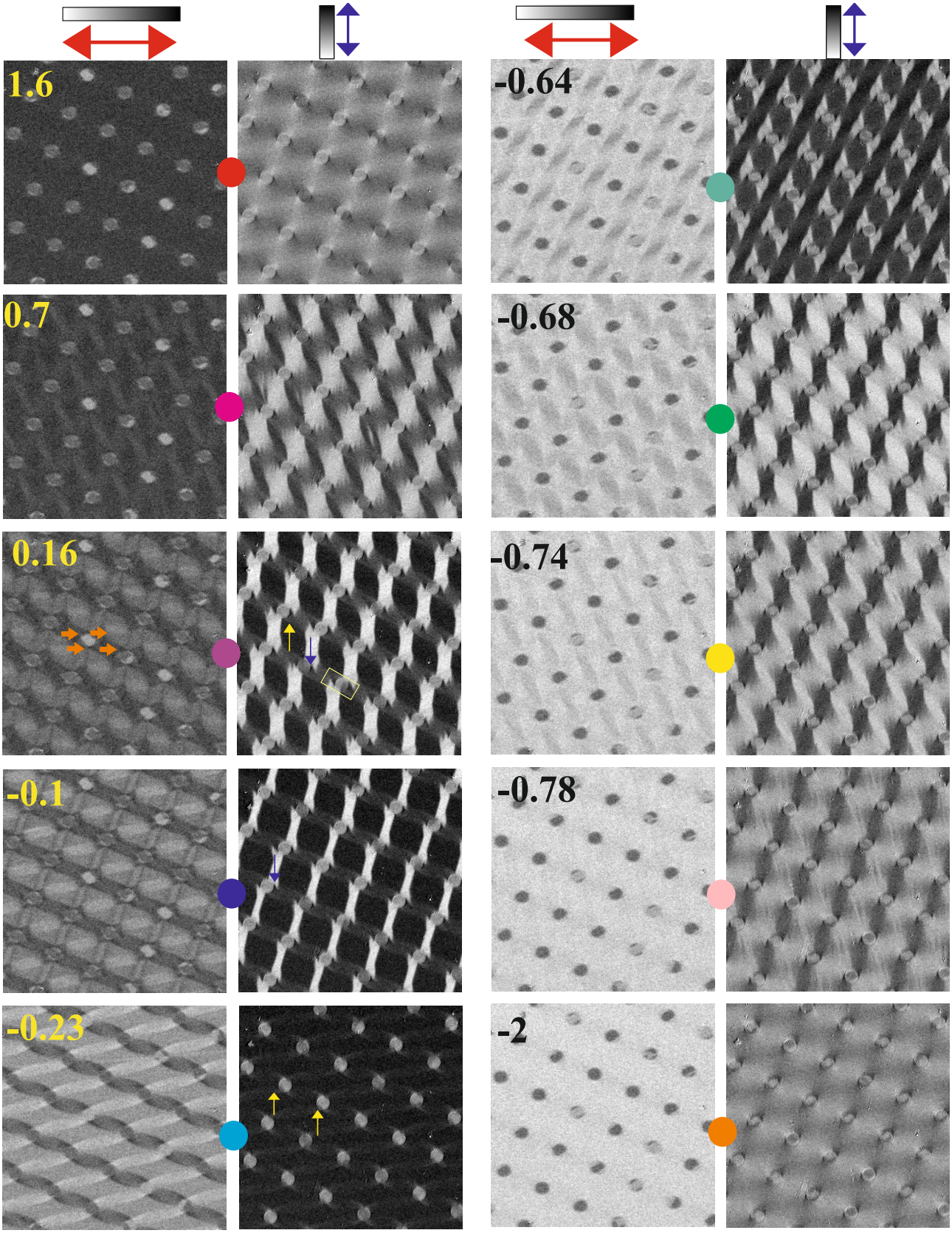

Figure S-B7: The static magneto-optically measured data are shown for both sensitivities at different bias fields. The colour circles between every pair of images connect them to their counterparts on the magnetic hysteresis in Fig. (S-B6). The sample is magnetically patterned via irradiation. The non-irradiated part is an antidot as its total magnetization is zero. The I-dots diameter is 10 μm while the lattice parameter is 30 μm. The I-dot square array are rotated in the way that the anisotropy axis is vertical and the magnetic field is applied perpendicular to it. The static magnetic fields are indicated in every image in kA/m. The longitudinal and transverse sensitivity relative to the magnetic field are shown by red and blue two-head arrows, respectively. In addition, the grey scale next to every sensitivity axis indicate white and black colour regions' magnetization direction in the magneto-optically measured data.

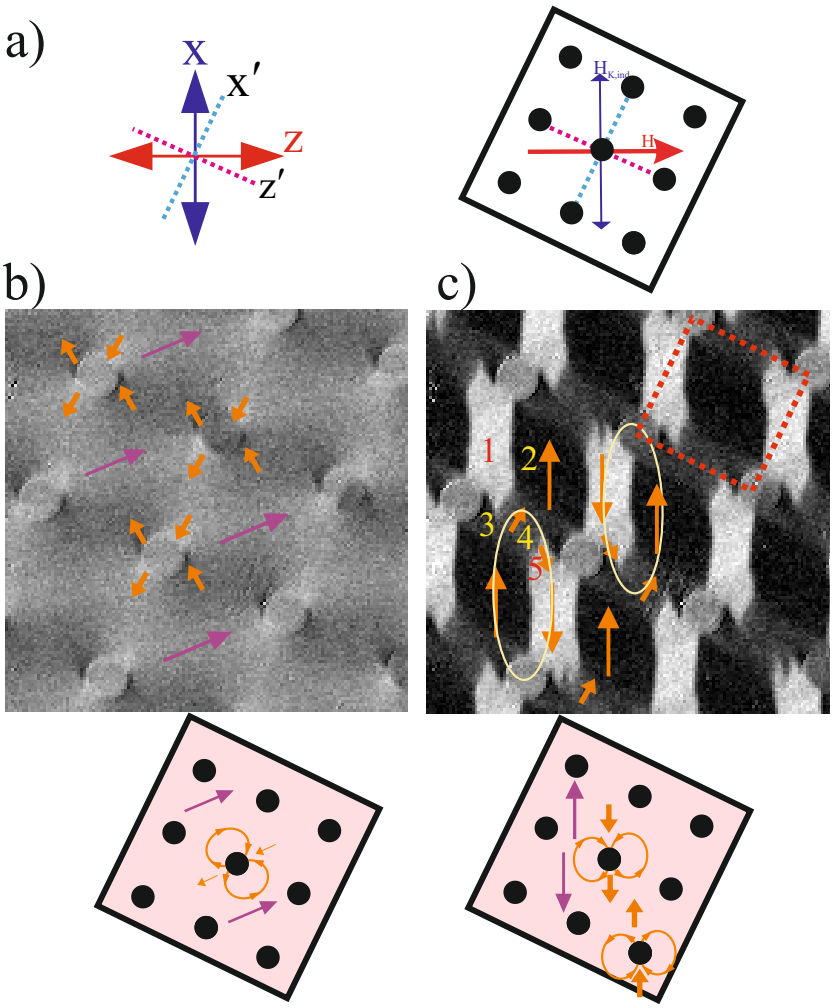

Figure S-B8: (a) The coordination indicates static field $\hat{\mathbf{z}}$, anisotropy $\hat{\mathbf{x}}$ and array ($\hat{z}'$-$\hat{x}'$) axis for an I-dots sample 10×30. The array is deviated from x-z coordination by 25 degree. (b) In order to clarify the magnetization behaviour a schematic diagram is added to the magneto-optically measured data when a static field equal to 0.16 kA/m is applied. (c) The static magnetization pattern is shown in remanence state. Inside the MOKE image, magnetic moments are illustrated via arrows when ovals guide to observe the magnetization rotation. Furthermore, the different domains are marked by numbers and the I-dots array is highlighted by a dash square. In schematic part of (b) and (c), the orange arrows show H_{dem} around an isolated antidot in the same effective field as it is indicated by purple arrows.

Fig. (2.16) is shown in schematic part by orange vectors for an individual antidot in a square array while the butterfly axis is rotated.

The magnetic field reduction to 0.7 kA/m, which is smaller than the induced anisotropy field ($H_{k,ind}$=1.08 kA/m) leads to a magnetization component enhancement along the anisotropy axis. It can be seen in Fig. (S-B7) that the matrix is not saturated anymore in horizontal sensitivity. The magnetization component along the field starts to rotate along one diagonal of the I-dots array. This diagonal has a small angle with $\hat{\mathbf{x}}$ and $H_{k,ind}$ axis. In addition, the magnetization inhomogeneity of neighbouring dots starts to link together along one axis of the array as indicated by $\hat{z}'$ in Fig. (S-B8 a).

In a low bias field 0.16 kA/m and near to the remanence, the anisotropy field determines the magnetization direction mostly inside the matrix. Therefore, the whole matrix's magnetization is

orientated along the anisotropy field either upward ($H_{k,+x}$), inside black domains, or downward ($H_{k,-x}$), inside white domains, in the transverse magneto-optically measured data of Fig. (S-B8 c). This magnetization configuration minimizes the demagnetizing field in the whole sample even in comparison to the pattern in which the magnetization orientates just in one anisotropy direction. The schematic image in Fig. (S-B8 c) shows H_{dem} around two isolated antidots when they are under application of an effective field equal to the anisotropy field. H_{dem} and $H_{k,ind}$ are indicated via orange and purple arrows. The H_{dem} in our structure can be different from an isolated antidot because the I-dots array is tilted and as a consequence its fourfold anisotropy is deviated. In addition, interaction between every I-dot with its first and second neighbour contributes to differences between the array and the isolated antidot structure. The magnetic moment is drawn based on the MOKE observation in Fig. (S-B8 c). In addition, the array of antidot is highlighted by a red dash square and the magnetization rotation is illustrated by ovals as guide to the eyes and the regions with different orientation of magnetization are marked by numbers from 1 to 5. The region 1 and 2 are aligned, antiparallel relative to each other, along the anisotropy axis and connect the first and second neighbour, respectively. The region marked as 3 forms because of strong shape anisotropy around the dots. This region pattern is tilted relative to the pattern around an isolated I-dot because of the oblique array. In a small distance from the dots (region 2), this demagnetizing field is not effective any more and the magnetization is oriented along $H_{k,ind}$. The area 4 and 5 intermediate rotation of magnetization between regions 2 and 1. The contrast among region 5 and 1 is visible in MOKE image with horizontal sensitivity in Fig. (S-B7). The magnetization in remanence is not zero. The magnetization has a small angle with $H_{k,ind}$ between the dots along $\hat{x}'$ because of the anisotropy field. This part has high intensity, as it can be seen in Fig. (S-B7), in the vertical sensitivity component and shown by a blue dashed rectangular in Fig. (S-B9). In addition, magnetization moments are drawn for other areas. For instance, the diagonal connection between I-dots is highlighted by a red dashed rectangular. The pattern around an I-dot is separated by the white curve. The magnetization rotation can be seen by following the arrows from blue, pink, red, orange to white. To reach $m_z = 0$, the enhancement of the field in opposite direction is needed. From Fig. (S-B7), the coercive field is around -0.23 kA/m and $m_z = 0$ while m_x reaches a peak as it can be seen in Fig. (S-B7) in vertical sensitivity. The magnetic moments are illustrated in Fig. (S-B9 b) in addition to a dash circle to guide the eye following the magnetization rotation around the dots. In the schematic image, orange and purple arrows depict respectively, the demagnetizing and the effective field. This configuration of magnetization forms to reduce the high demagnetizing field.

This magnetization configuration is preferable in the coercive field for an I-dots structure even if the lattice constant changes from 30 nm to 40 nm. The magneto-optically measured data in both

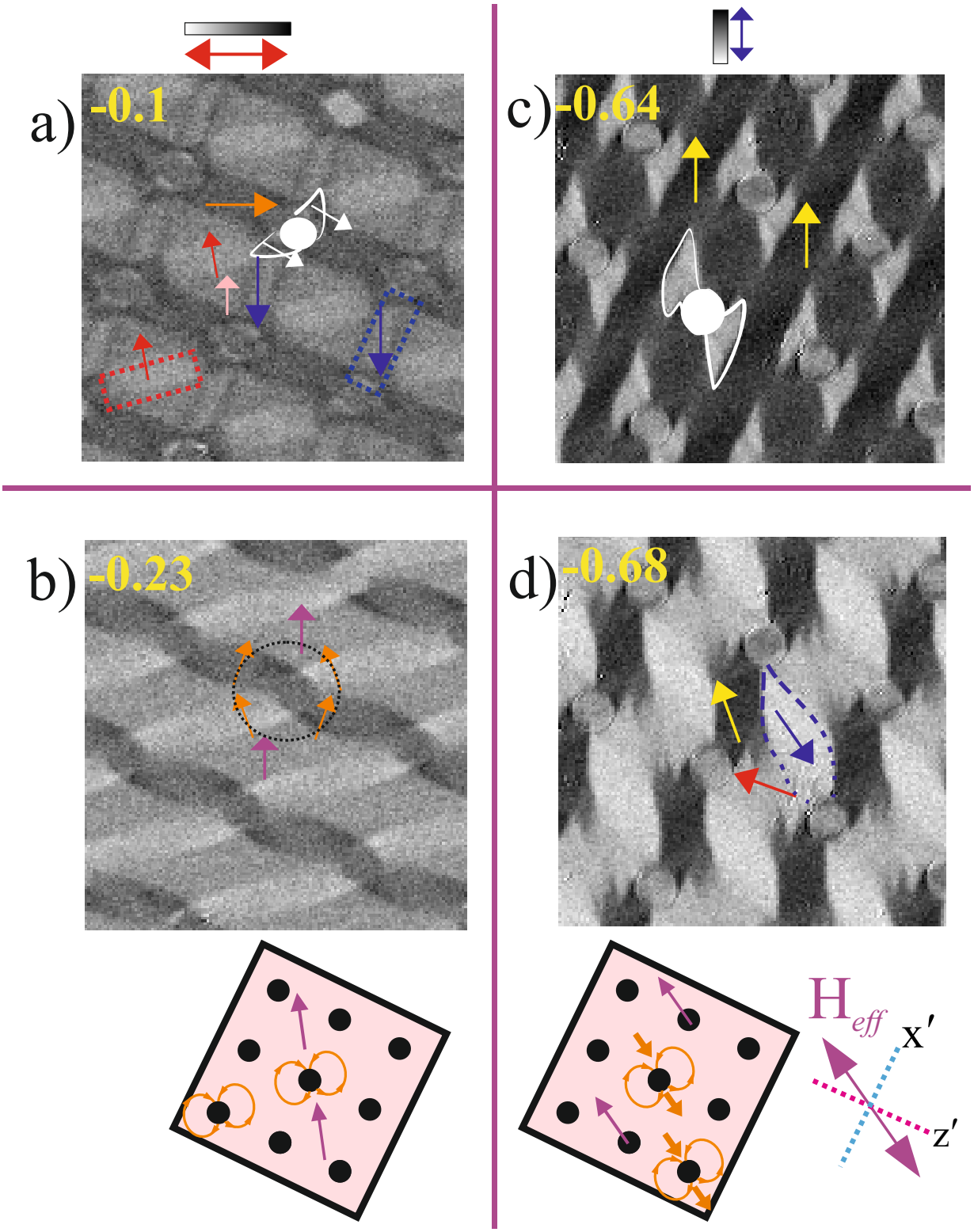

Figure S-B9: The magnetization inside different domains is illustrated under application of different magnetic fields, which are written in the right corner of the images. (a), (b) The magneto-optically measured data are used with horizontal sensitivity. (c), (d) These images are measured in vertical sensitivity. (b), (d) In the schematic part, the effective field is drawn by purple colour, it is the superposition of the anisotropy and the bias field. In addition, the demagnetizing field is illustrated by orange arrows for an isolated antidot at the same effective field.

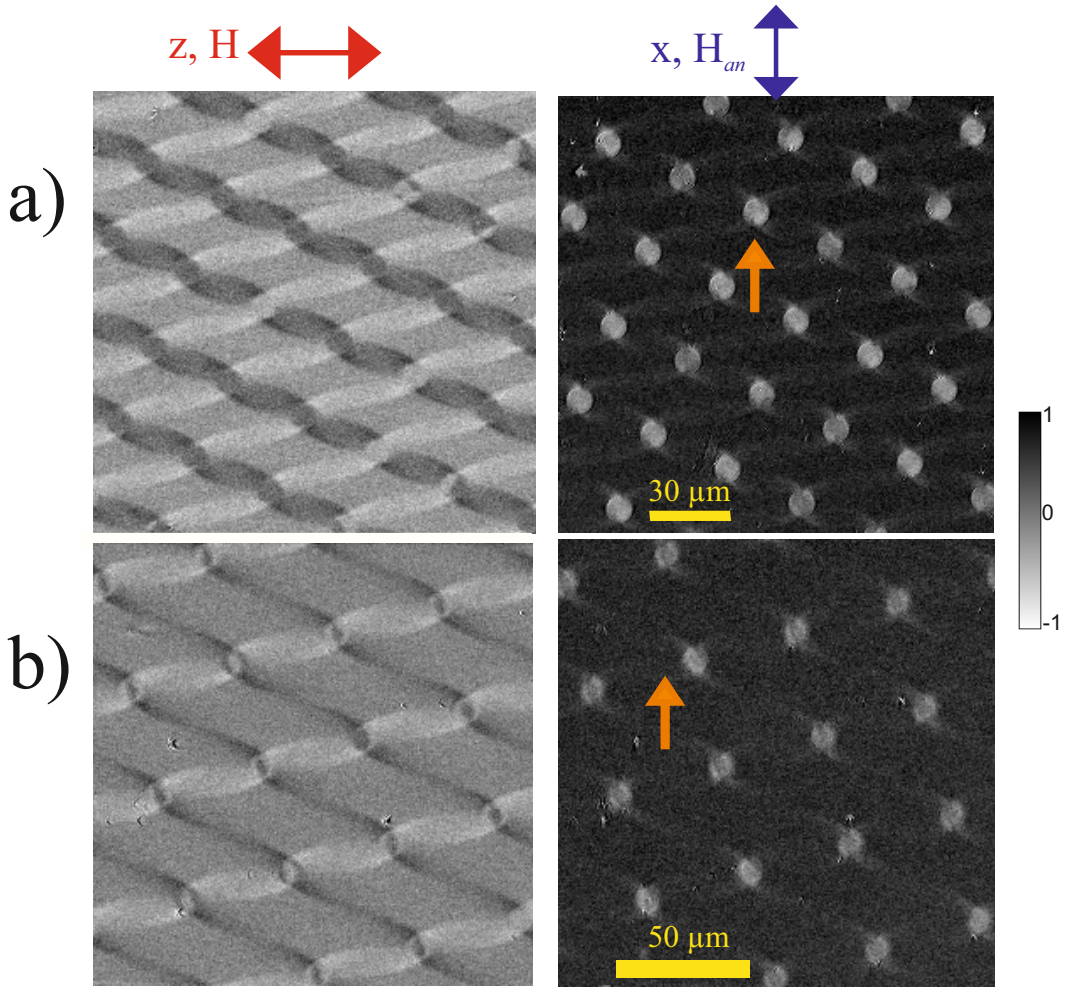

Figure S-B10: (a) The magneto-optically measured data are shown for the I-dot samples 10 × 30 at -0.23 kA/m in both horizontal and vertical sensitivities. (b) In order to compare data with (a), images recorded via a MOKE microscope are depicted for another I-dots sample 10×40 by applying -0.68 kA/m. The two images correspond to the samples magnetic coercivity. The double arrows indicate the sensitivity axis while the orange arrows illustrate the magnetization vector inside the matrix. Furthermore, scale bars are shown.

sensitivities for another sample, 10 × 40, is shown in Fig. (S-B10) to compare with sample 10 × 30. The similarity is obvious between these two measurements.

When the magnetic field is enhanced to -0.64 kA/m, the anisotropy is not the only dominant field around the dots anymore. This leads to emergence of domains in the vicinity of I-dots. The butterfly-like pattern, which forms in this area, is highlighted in Fig. (S-B9 c). However, other areas in the matrix deviate in small angle from the anisotropy axis, the region between antidots and along $\hat{x}'$ axis stays still along $+\mathbf{H}_{k,ind}$. The magnetic moment in this area is indicated in Fig. (S-B9 c) via yellow arrows. The magnetization configuration in -0.64 kA/m is unstable. Thus, the domain configuration changes by a small field enhancement to -0.68 kA/m as it is shown in Fig. (S-B7) and (S-B9 d). Now, the superposition between two fields, $\mathbf{H}+\mathbf{H}_{k,ind}$, is deviated by 35 degree approximately from $+\hat{\mathbf{x}}$ and 30 degree relative to $\hat{z}'$. Therefore, the inhomogeneity around dots that is a consequence of H_{dem} rotates to align axis parallel to the effective field. H_{eff} and H_{dem}

are illustrated schematically in Fig. (S-B9 d), respectively, by purple and orange colour arrows.

The magnetic inhomogeneity from the first neighbouring dots join together along $\hat{z}'$ axis and the magnetization aligns itself in the direction of the applied magnetic field in this area, which is shown by a red arrow in Fig. (S-B9 d). Another result of H_{dem} around the dots is that the magnetization along the array's diagonal flips from $+H_{k,ind}$ (indicated by black in MOKE contrast) to $-H_{k,ind}$ (indicated by white). In addition, the magnetization in the area between dots along $\hat{x}'$ is deviated by a small angle from $+H_{k,ind}$, indicated by a yellow arrow in Fig. (S-B9 d).

The further enhancement of magnetic field reinforces competition between the applied static field and the anisotropy to affect the effective field and so the magnetization direction. The static field at -0.78 kA/m is still below the anisotropy field. The superposition between the anisotropy and applied field, $\mathbf{H}+\mathbf{H}_{k,ind}$ have a 38 and 27 degree angle relative to $\hat{\mathbf{x}}$ and $\hat{z}'$, respectively. Further enhancement of the magnetic field saturates the matrix completely at -2 kA/m. The dots, because of antiferromagnetic coupling between the layers are not saturated at this field value.

S-B4 Simulation

The domain configuration described above is complicated because in addition to anisotropy, bias and demagnetizing field that play a role in the magnetization pattern formation, the symmetry of the square array is affected because of k_u axis deviation relative to the vertical and horizontal axis. To find out how domain behaviour changes, in the following, we are going to simulate a sample with the same features while the dot array is symmetric without any deviation from the usual horizontal and vertical axis.

The supercell contains one I-dot in the center and to avoid edge effects, the 2D periodic boundary condition is applied. Thus a full sample is simulated. The mentioned supercell is 30 × 30 μm^2 which is separated into 2048 × 2048 mesh cells in the xz plane. To obtain interlayer coupling between the layers, interlayer exchange coupling is site dependent. It is supposed that inside the I-dot, interlayer exchange coupling is -0.06 and outside (inside the matrix) is 0.94. As it is mentioned before in equation (2.7), negative exchange value related to antiferromagnetic coupling.

The magnetic field is applied in the $\hat{\mathbf{z}}$ direction, while the magnetic anisotropy axis is normal to it. The initial magnetization is supposed to be saturation and then the field decreases by 0.08 kA/m at every step from 2.4 kA/m to -2.4 kA/m. The simulated results are shown for both IP magnetization components in Fig. (S-B11) while the field values are written in kA/m on the left side of every image. Every column corresponds to one component of magnetization along the field or anisotropy axis, respectively, m_z or m_x. The difference between this simulation and directly mea-

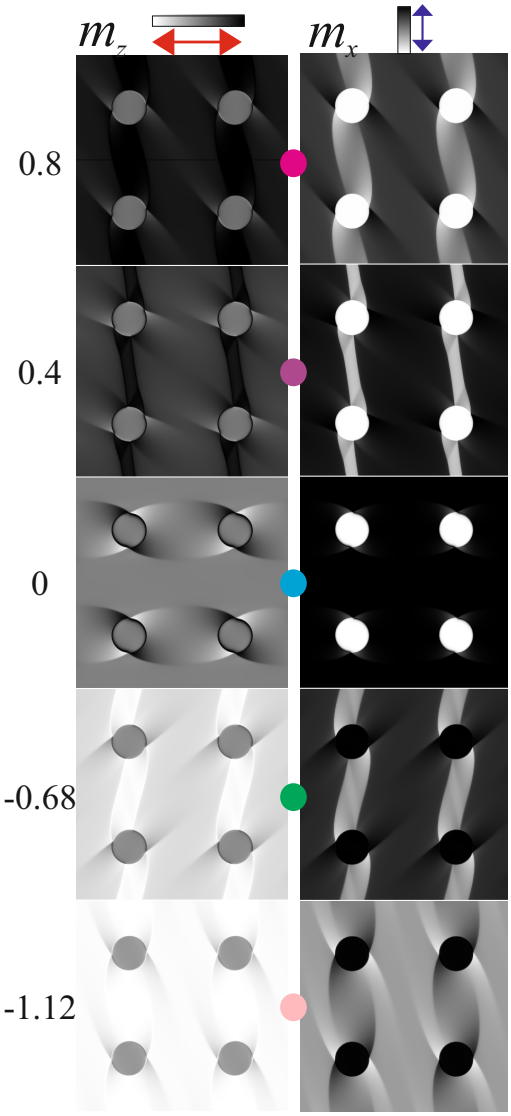

Figure S-B11: The simulated results are shown for a square array of I-dots with 10×30 μm (diameter × lattice constant) size in different fields in kA/m which are indicated on the left side of the images.They are all for the first layer as the second layer results (not shown here) are similar except inside dots because of strong antiferromagnetic coupling of layers. The components of magnetization are illustrated along the field, m_z, and along the anisotropy axis, m_x. The coordination is x-z plane that is displayed before in Fig. (S-B8), while the magnetic field and the anisotropy axis are, respectively, along $\hat{\mathbf{z}}$ and $\hat{\mathbf{x}}$. In order to compare these result with MOKE measurements in Fig. (S-B7), the same coloured circle is used here for a similar pattern.

sured images via MOKE microscope is that here, the square array of dots is not deviated and so field and anisotropy axis match the horizontal and vertical connection between the dots. Therefore, what were described as $\hat{z}'$ and $\hat{x}'$ in the last section (experimental magneto-optically measured data) matches $\hat{\mathbf{z}}$ and $\hat{\mathbf{x}}$, respectively.

The coloured circle between every pair of images connects them to magneto-optically measured data with the same colour in Fig. (S-B7). They are selected based on similarity in their magnetization. For instance, the first row of images, indicated by a pink circle, are simulated by applying 0.8 kA/m magnetic field and $m_z = 0.8$ M_s while their corresponding images in Fig. (S-B7) are measured at 0.7 kA/m field and $m_z = 0.7$ M_s. For them, the magnetization components are

similar in the experimental measurement and the simulation. When m_z starts rotating in the area along the array diagonal, the matrix magnetization rotates towards the anisotropy axis in the area along the vertical connection between dots.

In the next row, the calculated data with an applied field 0.4 kA/m (m_z = 0.5 M_s) is compared with the magneto-optically measured data measured at 0.16 kA/m (m_z = 0.45 M_s). In contrast to the general agreement between simulated and measured m_x, the demagnetizing field around the dots in the MOKE image for m_z is more complicated as it was discussed before.

The array deviation affects the magnetization domains and varies the orientation H_{dem} around the dots. This is evident when a comparison is done between magnetization remanence (here, magnetic remanence and coercivity match) in Fig. (S-B11) and coercive field point, at -0.23 kA/m, in Fig. (S-B7). It is obvious that domains around the dots (formed because of the demagnetizing field) rotate in a tilted array in the magneto-optically measured data relative to the simulated array.

When a -0.68 kA/m magnetic field is applied, the calculation shows magnetization along the dots' vertical connection aligns with the induced anisotropy while this happens in the magneto-optically measured data along the diagonal connection between the dots.

The magnetic field enhancement to -1.12, saturates the matrix in both cases, but there is a small domain structure around the dots which can be seen in the m_x component. The difference between simulation and MOKE microscope results is the array titillation, affects mentioned pattern and is rotated in MOKE results rather than the symmetrical pattern in the simulation.

S-B5 Summary

A magnetically patterned I-dot square array of CoFeB was characterized. The PIMM method was utilized as a tool to find out the dynamic magnetization response of the sample to a step function as a magnetic stimuli. The averaged resonance frequency is obtained in every applied static field either along easy or hard axis of magnetization. It was discussed in the Fig. (2.24) that around remanence state and coercive field, it is not easy to record signal via PIMM.

Furthermore, through optical measurement via Kerr microscope, the complexity of a magnetically patterned system was in detail investigated, when the symmetry of shape anisotropy in a square array was broken as sample was tilted throughout MOKE measurement. The symmetric pattern behaviour was simulated to compare its results with experimentally measured ones and see the variation of magnetization configuration because of this broken symmetry.

In the future applications, when such complex magnetic structure is not essential, the tilted anisotropy relative to array axis can be fixed through annealing sample and then applying higher

field to align anisotropy in the goal axis.

Bibliography

[1] VV Kruglyak, SO Demokritov, and D Grundler. “Magnonics”. In: *Journal of Physics D: Applied Physics* 43.26 (2010), p. 264001.

[2] György Csaba, Ádám Papp, and Wolfgang Porod. “Perspectives of using spin waves for computing and signal processing”. In: *Physics Letters A* 381.17 (2017), pp. 1471–1476.

[3] Sang-Koog Kim, Ki-Suk Lee, and Dong-Soo Han. “A gigahertz-range spin-wave filter composed of width-modulated nanostrip magnonic-crystal waveguides”. In: *Applied Physics Letters* 95.8 (2009), p. 082507.

[4] Alexandr V Sadovnikov et al. “Magnonic beam splitter: The building block of parallel magnonic circuitry”. In: *Applied Physics Letters* 106.19 (2015), p. 192406.

[5] SV Vasiliev et al. “Spin wave interferometer employing a local nonuniformity of the effective magnetic field”. In: *Journal of Applied Physics* 101.11 (2007), p. 113919.

[6] MP Kostylev et al. “Spin-wave logical gates”. In: *Applied Physics Letters* 87.15 (2005), p. 153501.

[7] Ki-Suk Lee and Sang-Koog Kim. “Conceptual design of spin wave logic gates based on a Mach–Zehnder-type spin wave interferometer for universal logic functions”. In: *Journal of Applied Physics* 104.5 (2008), p. 053909.

[8] Alexander Khitun and Kang L Wang. “Nano scale computational architectures with spin wave bus”. In: *Superlattices and Microstructures* 38.3 (2005), pp. 184–200.

[9] Alexander Khitun et al. “Logic devices with spin wave buses-an approach to scalable magneto-electric circuitry”. In: *MRS Online Proceedings Library* 1067.1 (2007), pp. 1–6.

[10] Yina Wu et al. “A three-terminal spin-wave device for logic applications”. In: *Journal of nanoelectronics and optoelectronics* 4.3 (2009), pp. 394–397.

[11] Thomas Schneider et al. “Realization of spin-wave logic gates”. In: *Applied Physics Letters* 92.2 (2008), p. 022505.

[12] Alexander Khitun, Mingqiang Bao, and Kang L Wang. “Magnonic logic circuits”. In: *Journal of Physics D: Applied Physics* 43.26 (2010), p. 264005.

[13] Alexander Khitun and Alexander Kozhanov. “Magnonic logic devices”. In: *Nanomagnetic and spintronic devices for energy-efficient memory and computing, edited by J. Atulasimha, S. Bandyopadhyay (Virginia Commonwealth University, US)* (2016), pp. 189–219.

[14] Yuri K Fetisov and Carl E Patton. “Microwave bistability in a magnetostatic wave interferometer with external feedback”. In: *IEEE transactions on magnetics* 35.2 (1999), pp. 1024–1036.

[15] MP Kostylev et al. “Resonant scattering of spin waves from a region of inhomogeneous magnetic field in a ferromagnetic film”. In: *arXiv preprint arXiv:0705.4191* (2007).

[16] Jakob Walowski et al. “Energy equilibration processes of electrons, magnons, and phonons at the femtosecond time scale”. In: *Physical review letters* 101.23 (2008), p. 237401.

[17] J Goulon et al. “X-ray detected magnetic resonance at the Fe K-edge in YIG: forced precession of magnetically polarized orbital components”. In: *Journal of Experimental and Theoretical Physics Letters* 82.11 (2005), pp. 696–701.

[18] Claudia Hengst et al. “Acoustic-domain resonance mode in magnetic closure-domain structures: A probe for domain-shape characteristics and domain-wall transformations”. In: *Physical Review B* 89.21 (2014), p. 214412.

[19] Mikihiko Oogane et al. “Magnetic damping in ferromagnetic thin films”. In: *Japanese journal of applied physics* 45.5R (2006), p. 3889.

[20] Haiming Yu et al. “High propagating velocity of spin waves and temperature dependent damping in a CoFeB thin film”. In: *Applied Physics Letters* 100.26 (2012), p. 262412.

[21] Rasmus B Holländer et al. “Magnetic domain walls as broadband spin wave and elastic magnetisation wave emitters”. In: *Scientific reports* 8.1 (2018), pp. 1–11.

[22] CT Yu et al. “The magnetic anisotropy and domain structure of permalloy antidot arrays”. In: *Journal of Applied Physics* 87.9 (2000), pp. 6322–6324.

[23] Kai Wagner et al. “Magnetic domain walls as reconfigurable spin-wave nanochannels”. In: *Nature nanotechnology* 11.5 (2016), pp. 432–436.

[24] Antonio Lara et al. “Information processing in patterned magnetic nanostructures with edge spin waves”. In: *Scientific reports* 7.1 (2017), pp. 1–12.

[25] Korbinian Perzlmaier et al. “Spin-wave eigenmodes of permalloy squares with a closure domain structure”. In: *Physical Review Letters* 94.5 (2005), p. 057202.

[26] Mathis Lohman, Babak Mozooni, and Jeffrey McCord. “Homogeneous microwave field emitted propagating spin waves: Direct imaging and modeling”. In: *Journal of Magnetism and Magnetic Materials* 450 (2018), pp. 7–12.

[27] R Gieniusz et al. “Single antidot as a passive way to create caustic spin-wave beams in yttrium iron garnet films”. In: *Applied Physics Letters* 102.10 (2013), p. 102409.

[28] S Tacchi et al. “Brillouin light scattering studies of 2D magnonic crystals”. In: *Journal of Physics: Condensed Matter* 29.7 (2016), p. 073001.

[29] CS Davies, VD Poimanov, and VV Kruglyak. “Mapping the magnonic landscape in patterned magnetic structures”. In: *Physical Review B* 96.9 (2017), p. 094430.

[30] CS Davies et al. “Generation of propagating spin waves from regions of increased dynamic demagnetising field near magnetic antidots”. In: *Applied Physics Letters* 107.16 (2015), p. 162401.

[31] Rasmus B Holländer et al. “Component selection in time-resolved magneto-optical wide-field imaging for the investigation of magnetic microstructures”. In: *Journal of Magnetism and Magnetic Materials* 432 (2017), pp. 283–290.

[32] Babak Mozooni, Thomas von Hofe, and Jeffrey McCord. “Picosecond wide-field magneto-optical imaging of magnetization dynamics of amorphous film elements”. In: *Physical Review B* 90.5 (2014), p. 054410.

[33] J Douglas Adam et al. “Ferrite devices and materials”. In: *IEEE Transactions on Microwave Theory and Techniques* 50.3 (2002), pp. 721–737.

[34] Young-Yeal Song, César L Ordóñez-Romero, and Mingzhong Wu. “Millimeter wave notch filters based on ferromagnetic resonance in hexagonal barium ferrites”. In: *Applied Physics Letters* 95.14 (2009), p. 142506.

[35] X Yang et al. “A wide-band magnetic tunable bandstop filter prototype with FeGaB/Al2O3 multilayer films”. In: *Applied Physics Letters* 107.12 (2015), p. 122408.

[36] CS Tsai et al. “Tunable wideband microwave band-stop and band-pass filters using YIG/GGG-GaAs layer structures”. In: *IEEE transactions on magnetics* 41.10 (2005), pp. 3568–3570.

[37] Chen S Tsai, Jun Su, and Chin C Lee. “Wideband electronically tunable microwave band-stop filters using iron film-gallium arsenide waveguide structure”. In: *IEEE transactions on magnetics* 35.5 (1999), pp. 3178–3180.

[38] Erwan Salahun et al. “Correlation between magnetic properties of layered ferromagnetic/dielectric material and tunable microwave device applications”. In: *Journal of applied physics* 91.8 (2002), pp. 5449–5455.

[39] N Cramer et al. “High attenuation tunable microwave notch filters utilizing ferromagnetic resonance”. In: *Journal of Applied Physics* 87.9 (2000), pp. 6911–6913.

[40] I Harward, RE Camley, and Z Celinski. “On-wafer magnetically tunable millimeter wave notch filter using M-phase Ba hexagonal ferrite/Pt thin films on Si”. In: *Applied Physics Letters* 105.17 (2014), p. 173503.

[41] Bijoy Kuanr, Z Celinski, and RE Camley. “Tunable high-frequency band-stop magnetic filters”. In: *Applied Physics Letters* 83.19 (2003), pp. 3969–3971.

[42] Bijoy K Kuanr et al. “Magnetically tunable micro-strip band-stop filter: Design optimization and characterization”. In: *Journal of applied physics* 97.10 (2005), 10Q103.

[43] Aimad Saib et al. “Unbiased microwave circulator based on ferromagnetic nanowires arrays of tunable magnetization state”. In: *Journal of Physics D: Applied Physics* 38.16 (2005), p. 2759.

[44] Rasmus Bahne Holländer. “Dynamics of Functional Magnetic Microstructures”. PhD thesis. 2019.

[45] P Grünberg. “Magnetostatic spinwave modes of a ferromagnetic double layer”. In: *Journal of Applied Physics* 51.8 (1980), pp. 4338–4341.

[46] A Layadi. “Effect of biquadratic coupling and in-plane anisotropy on the resonance modes of a trilayer system”. In: *Physical Review B* 65.10 (2002), p. 104422.

[47] M Belmeguenai et al. “Frequency-and time-domain investigation of the dynamic properties of interlayer-exchange-coupled Ni 81 Fe 19/ Ru/ Ni 81 Fe 19 thin films”. In: *Physical Review B* 76.10 (2007), p. 104414.

[48] Babak Mozooni. “Characterization of Magnetization Dynamics in Structured Magnetic Films”. PhD thesis. 2019.

[49] Laura J Heyderman et al. “Magnetization reversal in cobalt antidot arrays”. In: *Physical Review B* 73.21 (2006), p. 214429.

[50] Henning Ulrichs, Benjamin Lenk, and Markus Münzenberg. “Magnonic spin-wave modes in CoFeB antidot lattices”. In: *Applied Physics Letters* 97.9 (2010), p. 092506.

[51] Alexander G Gurevich and Gennadii A Melkov. *Magnetization oscillations and waves*. CRC press, 1996.

[52] Jilei Chen et al. “Excitation of unidirectional exchange spin waves by a nanoscale magnetic grating”. In: *Physical Review B* 100.10 (2019), p. 104427.

[53] Yves Henry et al. “Unidirectional spin-wave channeling along magnetic domain walls of Bloch type”. In: *Physical Review B* 100.2 (2019), p. 024416.

[54] Kai Di et al. “Enhancement of spin-wave nonreciprocity in magnonic crystals via synthetic antiferromagnetic coupling”. In: *Scientific reports* 5 (2015), p. 10153.

[55] Edoardo Albisetti et al. “Optically inspired nanomagnonics with nonreciprocal spin waves in synthetic antiferromagnets”. In: *Advanced Materials* 32.9 (2020), p. 1906439.

[56] Russell K Hobbie and Bradley J Roth. *Intermediate physics for medicine and biology*. Springer Science & Business Media, 2007.

[57] Ashutosh Pramanik. *Electromagnetism: Theory and Applications*. PHI Learning Pvt. Ltd., 2008.

[58] Yehuda B Band and Yshai Avishai. *Quantum mechanics with applications to nanotechnology and information science*. Academic Press, 2013.

[59] Alberto P Guimarães and Alberto Passos Guimaraes. *Principles of nanomagnetism*. Vol. 7. Springer, 2009.

[60] Nicolaas Bloembergen. *Encounters in Magnetic Resonances: Selected Papers of Nicolaas Bloembergen (with Commentary)*. Vol. 15. World Scientific, 1996.

[61] John MD Coey. *Magnetism and magnetic materials*. Cambridge university press, 2010.

[62] Richard M Martin. *Electronic structure: basic theory and practical methods*. Cambridge university press, 2004.

[63] Carmen-Gabriela Stefanita. *From bulk to nano: the many sides of magnetism*. Vol. 117. Springer Science & Business Media, 2008.

[64] Nicola A Spaldin. *Magnetic materials: fundamentals and applications*. Cambridge University Press, 2010.

[65] Bernard Dennis Cullity and Chad D Graham. *Introduction to magnetic materials*. John Wiley & Sons, 2011.

[66] Göran Engdahl and Isaak D Mayergoyz. *Handbook of giant magnetostrictive materials*. Vol. 107. Elsevier, 2000.

[67] AC Hsiao et al. "Nanocrystalline and Amorphous Magnetic Materials-Magnetic Properties and Crystallization Kinetics of a Mn-Doped FINEMET Precursor Amorphous Alloy". In: *IEEE Transactions on Magnetics* 37.4 (2001), pp. 2236–2238.

[68] Soshin Chikazumi and Chad D Graham. *Physics of Ferromagnetism 2e*. Vol. 94. Oxford University Press on Demand, 2009.

[69] K Suzuki et al. "Magnetic domains and annealing-induced magnetic anisotropy in nanocrystalline soft magnetic materials". In: *Journal of Applied Physics* 103.7 (2008), 07E730.

[70] Jack Vanderlinde. *Classical electromagnetic theory*. Vol. 145. Springer Science & Business Media, 2006.

[71] Munir H Nayfeh and Morton K Brussel. *Electricity and magnetism*. Courier Dover Publications, 2015.

[72] Silvia Viola Kusminskiy. *Quantum Magnetism, Spin Waves, and Optical Cavities*. Springer, 2019.

[73] John Clarke Slater and Nathaniel Herman Frank. *Electromagnetism*. Courier Corporation, 1969.

[74] Etienne du Tremolet De Lacheisserie, Damien Gignoux, and Michel Schlenker. *Magnetism: II-Materials and Applications*. Springer Science & Business Media, 2012.

[75] H-D Dietze and Harry Thomas. "Bloch-und Néel-Wände in dünnen ferromagnetischen Schichten". In: *Zeitschrift für Physik* 163.5 (1961), pp. 523–534.

[76] Amikam Aharoni. "Energy of One-Dimensional Domain Walls in Ferromagnetic Films". In: *Journal of Applied Physics* 37.8 (1966), pp. 3271–3279.

[77] Amikam Aharoni et al. *Introduction to the Theory of Ferromagnetism*. Vol. 109. Clarendon Press, 2000.

[78] H Riedel and A Seeger. "Micromagnetic treatment of Néel walls". In: *physica status solidi (b)* 46.1 (1971), pp. 377–384.

[79] Alex Hubert and Rudolf Schäfer. *Magnetic domains: the analysis of magnetic microstructures*. Springer Science & Business Media, 2008.

[80] J Fassbender et al. “Introducing artificial length scales to tailor magnetic properties”. In: *New Journal of Physics* 11.12 (2009), p. 125002.

[81] S Middelhoek. “Domain walls in thin Ni–Fe films”. In: *Journal of Applied Physics* 34.4 (1963), pp. 1054–1059.

[82] Jeffrey McCord and Rudolf Schäfer. “Domain wall asymmetries in Ni81Fe19/NiO: proof of variable anisotropies in exchange bias systems”. In: *New Journal of Physics* 11.8 (2009), p. 083016.

[83] Michel Labrune and Jacques Miltat. “Wall structures in ferro/antiferromagnetic exchange-coupled bilayers: a numerical micromagnetic approach”. In: *Journal of Magnetism and Magnetic Materials* 151.1-2 (1995), pp. 231–245.

[84] Amikam Aharoni. “Domain walls and micromagnetics”. In: *Le Journal de Physique Colloques* 32.C1 (1971), pp. C1–966.

[85] William Fuller Brown Jr and Anton E LaBonte. “Structure and energy of one-dimensional domain walls in ferromagnetic thin films”. In: *Journal of Applied Physics* 36.4 (1965), pp. 1380–1386.

[86] Amikam Aharoni. “Two-Dimensional Model for a Domain Wall”. In: *Journal of Applied Physics* 38.8 (1967), pp. 3196–3199.

[87] AE LaBonte. “Two-dimensional Bloch-type domain walls in ferromagnetic films”. In: *Journal of Applied Physics* 40.6 (1969), pp. 2450–2458.

[88] A Hubert. “Stray-Field-Free Magnetization Configurations”. In: *physica status solidi (b)* 32.2 (1969), pp. 519–534.

[89] A Hubert. “Stray-Field-Free and Related Domain Wall Configurations in Thin Magnetic Films (II)”. In: *physica status solidi (b)* 38.2 (1970), pp. 699–713.

[90] Michael J Donahue. “A variational approach to exchange energy calculations in micromagnetics”. In: *Journal of Applied Physics* 83.11 (1998), pp. 6491–6493.

[91] Safa O Kasap. *Principles of electronic materials and devices*. Vol. 2. McGraw-Hill New York, 2006.

[92] Gavin S Abo et al. “Definition of magnetic exchange length”. In: *IEEE Transactions on Magnetics* 49.8 (2013), pp. 4937–4939.

[93] EH Frei, S Shtrikman, and D_ Treves. “Critical size and nucleation field of ideal ferromagnetic particles”. In: *Physical Review* 106.3 (1957), p. 446.

[94] Arne Vansteenkiste et al. “The design and verification of MuMax3”. In: *AIP advances* 4.10 (2014), p. 107133.

[95] DV Berkov, K Ramstöcck, and A Hubert. “Solving micromagnetic problems. Towards an optimal numerical method”. In: *physica status solidi (a)* 137.1 (1993), pp. 207–225.

[96] Anjan Barman and Arabinda Haldar. “Time-domain study of magnetization dynamics in magnetic thin films and micro-and nanostructures”. In: *Solid State Physics*. Vol. 65. Elsevier, 2014, pp. 1–108.

[97] John A Weil and James R Bolton. *Electron paramagnetic resonance: elementary theory and practical applications*. John Wiley & Sons, 2007.

[98] LD Landau and EM Lifshitz. *On the Theory of the Dispersion of Magnetic Permeability in Ferromagnetic Bodies. Reproduced in Collected Papers of LD Landau*. 1935.

[99] Eugene V Dirote. *New developments in nanotechnology research*. Nova Publishers, 2007.

[100] Anil Prabhakar and Daniel D Stancil. *Spin waves: Theory and applications*. Springer, 2009.

[101] John R Taylor. *Classical mechanics*. University Science Books, 2005.

[102] LALE Landau and Evgeny Lifshitz. “On the theory of the dispersion of magnetic permeability in ferromagnetic bodies”. In: *Perspectives in Theoretical Physics*. Elsevier, 1992, pp. 51–65.

[103] Thomas L Gilbert. “A phenomenological theory of damping in ferromagnetic materials”. In: *IEEE Transactions on Magnetics* 40.6 (2004), pp. 3443–3449.

[104] S Iida. “The difference between gilbert’s and landau-lifshitz’s equations”. In: *Journal of Physics and Chemistry of Solids* 24.5 (1963), pp. 625–630.

[105] NX Sun et al. “High-frequency behavior and damping of Fe-Co-N-based high-saturation soft magnetic films”. In: *IEEE transactions on magnetics* 38.1 (2002), pp. 146–150.

[106] Charles Kittel et al. *Introduction to solid state physics*. Vol. 8. Wiley New York, 1976.

[107] Andreas Neudert et al. “Dynamic anisotropy in amorphous CoZrTa films”. In: *Journal of applied physics* 95.11 (2004), pp. 6595–6597.

[108] Charles Kittel. “Ferromagnetic resonance”. In: (1951).

[109] Gabriel Rodríguez-Rodríguez et al. “Closure magnetization configuration around a single hole in a magnetic film”. In: *Physical Review B* 78.17 (2008), p. 174417.

[110] Richard Fitzpatrick. *Maxwell’s Equations and the Principles of Electromagnetism*. Jones & Bartlett Publishers, 2008.

[111] LR Walker. “Magnetostatic modes in ferromagnetic resonance”. In: *Physical Review* 105.2 (1957), p. 390.

[112] BA Auld. “Walker modes in large ferrite samples”. In: *Journal of Applied Physics* 31.9 (1960), pp. 1642–1647.

[113] Benjamin Lenk et al. “The building blocks of magnonics”. In: *Physics Reports* 507.4-5 (2011), pp. 107–136.

[114] John R Reitz, Frederick J Milford, and WM Schwarz. “Foundations of electromagnetic theory”. In: *American Journal of Physics* 29 (1961), pp. 337–338.

[115] BA Kalinikos. “Excitation of propagating spin waves in ferromagnetic films”. In: *IEE Proceedings H (Microwaves, Optics and Antennas)*. Vol. 127. 1. IET. 1980, pp. 4–10.

[116] Jon Mathews and Robert Lee Walker. *Mathematical methods of physics*. Vol. 501. WA Benjamin New York, 1970.

[117] Rf W Damon and JR Eshbach. “Magnetostatic modes of a ferromagnet slab”. In: *Journal of Physics and Chemistry of Solids* 19.3-4 (1961), pp. 308–320.

[118] Daniel D Stancil. *Theory of magnetostatic waves*. Springer Science & Business Media, 2012.

[119] Peter Grünberg. “Layered magnetic structures in research and application”. In: *Acta materialia* 48.1 (2000), pp. 239–251.

[120] P Grünberg. “Magnetostatic spin-wave modes of a heterogeneous ferromagnetic double layer”. In: *Journal of Applied Physics* 52.11 (1981), pp. 6824–6829.

[121] M Vohl et al. “Exchange coupling of ferromagnetic layers across nonmagnetic interlayers”. In: *Journal of Magnetism and Magnetic Materials* 93 (1991), pp. 403–406.

[122] B Heinrich. “Magnetic nanostructures. From physical principles to spintronics”. In: *Canadian Journal of Physics* 78.3 (2000), pp. 161–199.

[123] A Layadi. “Ferromagnetic resonance modes in single and coupled layers with oblique anisotropy axis”. In: *Physical Review B* 63.17 (2001), p. 174410.

[124] Roberto Zivieri, Loris Giovannini, and Fabrizio Nizzoli. “Acoustical and optical spin modes of multilayers with ferromagnetic and antiferromagnetic coupling”. In: *Physical Review B* 62.22 (2000), p. 14950.

[125] M Grimsditch, S Kumar, and Eric E Fullerton. “Brillouin light scattering study of Fe/Cr/Fe (211) and (100) trilayers”. In: *Physical Review B* 54.5 (1996), p. 3385.

[126] Katayun Barmak and Kevin Coffey. *Metallic films for electronic, optical and magnetic applications: Structure, processing and properties*. Woodhead Publishing, 2014.

[127] GM Smith et al. "Quasi-optical cw mm-wave electron spin resonance spectrometer". In: *Review of scientific instruments* 69.11 (1998), pp. 3924–3937.

[128] J Gómez, JL Weston, and A Butera. "Ferromagnetic coupled modes in continuous/granular multilayers: Model and experiments". In: *Physical Review B* 76.18 (2007), p. 184416.

[129] E Lenz. "Ueber die Bestimmung der Richtung der durch elektrodynamische Vertheilung erregten galvanischen Ströme". In: *Annalen der Physik* 107.31 (1834), pp. 483–494.

[130] Uday A Bakshi and Varsha U Bakshi. *Basic Eletrical Engineering*. Technical Publications, 2009.

[131] H Neal Bertram. *Theory of magnetic recording*. Cambridge University Press, 1994.

[132] Thomas J Silva et al. "Inductive measurement of ultrafast magnetization dynamics in thin-film Permalloy". In: *Journal of Applied Physics* 85.11 (1999), pp. 7849–7862.

[133] MM Vopson et al. "High frequency magnetization dynamics metrology using a pulsed field inductive microwave magnetometer". In: *Measurement Science and Technology* 25.1 (2013), p. 015601.

[134] Charles P Slichter. *Principles of magnetic resonance*. Vol. 1. Springer Science & Business Media, 2013.

[135] TM Crawford, Pavel Kabos, and Thomas J Silva. "Coherent control of precessional dynamics in thin film permalloy". In: *Applied Physics Letters* 76.15 (2000), pp. 2113–2115.

[136] M Bauer et al. "Suppression of magnetic-field pulse-induced magnetization precession by pulse tailoring". In: *Applied Physics Letters* 76.19 (2000), pp. 2758–2760.

[137] Anthony B Kos, Thomas J Silva, and Pavel Kabos. "Pulsed inductive microwave magnetometer". In: *Review of scientific instruments* 73.10 (2002), pp. 3563–3569.

[138] John C Mallinson. *The foundations of magnetic recording*. Elsevier, 2012.

[139] Sangita S Kalarickal et al. "Ferromagnetic resonance linewidth in metallic thin films: Comparison of measurement methods". In: *Journal of Applied Physics* 99.9 (2006), p. 093909.

[140] I Neudecker et al. "Comparison of frequency, field, and time domain ferromagnetic resonance methods". In: *Journal of Magnetism and Magnetic Materials* 307.1 (2006), pp. 148–156.

[141] John Kerr. “XLIII. On rotation of the plane of polarization by reflection from the pole of a magnet”. In: *The London, Edinburgh, and Dublin Philosophical Magazine and Journal of Science* 3.19 (1877), pp. 321–343.

[142] Necdet Onur Urs. “Magnetic domain effects in high sensitive, 2-2 composite magnetoelectric sensors”. PhD thesis. 2017.

[143] Wolfgang Rave, Rudolf Schäfer, and Alex Hubert. “Quantitative observation of magnetic domains with the magneto-optical Kerr effect”. In: *Journal of magnetism and magnetic materials* 65.1 (1987), pp. 7–14.

[144] A Hubert and G Traeger. “Magneto-optical sensitivity functions of thin-film systems”. In: *Journal of magnetism and magnetic materials* 124.1-2 (1993), pp. 185–202.

[145] Vladimir Protopopov. *Practical Opto-Electronics*. Springer, 2014.

[146] V Kamberskỳ. “On magnetooptical effects caused by the gradient of magnetization”. In: *physica status solidi (a)* 123.1 (1991), K71–K73.

[147] JF Dillon Jr. “Magnetooptics”. In: *Journal of magnetism and magnetic materials* 100.1-3 (1991), pp. 425–439.

[148] Rudolf Schäfer and Alex Hubert. “A new magnetooptic effect related to non-uniform magnetization on the surface of a ferromagnet”. In: *physica status solidi (a)* 118.1 (1990), pp. 271–288.

[149] R Schäfer et al. “The magneto-optical gradient effect in an exchange-biased thin film: experimental evidence for classical diffraction theory”. In: *New Journal of Physics* 12.5 (2010), p. 053006.

[150] I Banno. “Qualitative explanation for the Schäfer-Hubert effect: A boundary effect at the crossroads of magneto-optics and near-field optics”. In: *Physical Review A* 77.3 (2008), p. 033818.

[151] V Kamberskỳ and R Schäfer. “Magneto-optic gradient effect in domain-wall images: At the crossroads of magneto-optics and micromagnetics”. In: *Physical Review A* 84.1 (2011), p. 013815.

[152] Necdet Onur Urs et al. “Advanced magneto-optical microscopy: Imaging from picoseconds to centimeters-imaging spin waves and temperature distributions”. In: *AIP Advances* 6.5 (2016), p. 055605.

[153] Jeffrey McCord. “Progress in magnetic domain observation by advanced magneto-optical microscopy”. In: *Journal of Physics D: Applied Physics* 48.33 (2015), p. 333001.

[154] Thomas von Hofe et al. “Dual wavelength magneto-optical imaging of magnetic thin films”. In: *Applied Physics Letters* 103.14 (2013), p. 142410.

[155] Randy O Wayne. *Light and video microscopy*. Academic Press, 2019.

[156] Bernell E Argyle and Jeffery G Mccord. “Efficient Kerr Microscopy”. In: *Magnetic Storage Systems Beyond 2000*. Springer, 2001, pp. 287–305.

[157] Alessandra Manzin and Oriano Bottauscio. “Micromagnetic modelling of the anisotropy properties of permalloy antidot arrays with hexagonal symmetry”. In: *Journal of Physics D: Applied Physics* 45.9 (2012), p. 095001.

[158] CS Davies and VV Kruglyak. “Generation of propagating spin waves from edges of magnetic nanostructures pumped by uniform microwave magnetic field”. In: *IEEE Transactions on Magnetics* 52.7 (2016), pp. 1–4.

[159] M Langer et al. “Magneto-optical analysis of stripe elements embedded in a synthetic antiferromagnet”. In: *Physical Review B* 89.6 (2014), p. 064411.

[160] W Möller and W Eckstein. “Tridyn—A TRIM simulation code including dynamic composition changes”. In: *Nuclear Instruments and Methods in Physics Research Section B: Beam Interactions with Materials and Atoms* 2.1-3 (1984), pp. 814–818.

[161] Wolfhard Möller, Wolfgang Eckstein, and JP Biersack. “Tridyn-binary collision simulation of atomic collisions and dynamic composition changes in solids”. In: *Computer Physics Communications* 51.3 (1988), pp. 355–368.

[162] Daniel Marko et al. “Measuring the Saturation Magnetization in Samples With Unknown Magnetic Volume”. In: *IEEE Transactions on Magnetics* 46.6 (2010), pp. 1711–1714.

[163] ON Martyanov et al. “Ferromagnetic resonance study of thin film antidot arrays: Experiment and micromagnetic simulations”. In: *Physical Review B* 75.17 (2007), p. 174429.

[164] Nicholas Kurti. *Selected works of louis neel*. CRC Press, 1988.

[165] C Merton et al. “Magnetic reversal of tapered permalloy bars with holes in the center”. In: *Journal of applied physics* 85.8 (1999), pp. 4601–4603.

[166] Conyers Herring and Charles Kittel. “On the theory of spin waves in ferromagnetic media”. In: *Physical Review* 81.5 (1951), p. 869.

[167] Yixian Qian, Hongxing Mao, and Songtao Lai. “Controllable symmetric caustic beams”. In: *Applied Physics B* 125.4 (2019), p. 59.

[168] Sergej O Demokritov, Burkard Hillebrands, and Andrei N Slavin. “Brillouin light scattering studies of confined spin waves: linear and nonlinear confinement”. In: *Physics Reports* 348.6 (2001), pp. 441–489.

[169] V Veerakumar and RE Camley. “Magnon focusing in thin ferromagnetic films”. In: *Physical Review B* 74.21 (2006), p. 214401.

[170] RL Stamps and RE Camley. “Focusing of magnetoplasmon polaritons”. In: *Physical Review B* 31.8 (1985), p. 4924.

[171] Andreas Krohn et al. “Observation of spin-wave propagation in permalloy microstripes”. In: *arXiv preprint arXiv:0905.2172* (2009).

[172] Philipp Wessels et al. “Direct observation of isolated Damon-Eshbach and backward volume spin-wave packets in ferromagnetic microstripes”. In: *Scientific reports* 6 (2016), p. 22117.

[173] Dmitry V Berkov and Jacques Miltat. “Spin-torque driven magnetization dynamics: Micromagnetic modeling”. In: *Journal of Magnetism and Magnetic Materials* 320.7 (2008), pp. 1238–1259.

[174] Sebastian Wintz et al. “Magnetic vortex cores as tunable spin-wave emitters”. In: *Nature nanotechnology* 11.11 (2016), pp. 948–953.

[175] Roman Verba, Vasil Tiberkevich, and Andrei Slavin. “Wide-Band Nonreciprocity of Surface Acoustic Waves Induced by Magnetoelastic Coupling with a Synthetic Antiferromagnet”. In: *Physical Review Applied* 12.5 (2019), p. 054061.

[176] Huajun Qin, Sampo J Hämäläinen, and Sebastiaan Van Dijken. “Exchange-torque-induced excitation of perpendicular standing spin waves in nanometer-thick YIG films”. In: *Scientific reports* 8.1 (2018), pp. 1–9.

[177] YS Gui, N Mecking, and C-M Hu. “Quantized spin excitations in a ferromagnetic microstrip from microwave photovoltage measurements”. In: *Physical review letters* 98.21 (2007), p. 217603.

[178] Aryan Navabi et al. “Efficient excitation of high-frequency exchange-dominated spin waves in periodic ferromagnetic structures”. In: *Physical Review Applied* 7.3 (2017), p. 034027.

[179] A Conca et al. “Annealing influence on the Gilbert damping parameter and the exchange constant of CoFeB thin films”. In: *Applied Physics Letters* 104.18 (2014), p. 182407.

[180] John P Nibarger et al. “Dynamic and static magnetic anisotropy in thin-film cobalt zirconium tantalum”. In: *Journal of magnetism and magnetic materials* 286 (2005), pp. 356–361.

[181] Michael L Schneider, Anthony B Kos, and Thomas J Silva. “Dynamic anisotropy of thin Permalloy films measured by use of angle-resolved pulsed inductive microwave magnetometry”. In: *Applied Physics Letters* 86.20 (2005), p. 202503.

[182] C Alexander Jr et al. “Frequency-and time-resolved measurements of FeTaN films with longitudinal bias fields”. In: *Journal of Applied Physics* 87.9 (2000), pp. 6633–6635.

[183] Th Gerrits, Michael L Schneider, and Thomas J Silva. “Enhanced ferromagnetic damping in Permalloy/ Cu bilayers”. In: *Journal of applied physics* 99.2 (2006), p. 023901.

Acknowledgments

- Firstly, I'd like to thank my supervisor, Prof. Dr.-Ing. Jeffrey McCord, for his support, guidance, and sharing of his exceptional expertise during my time in the Nanoscale Magnetic Materials, NMM, Group and this research.
- Furthermore, I would like to thank Dr. Rasmus Holländer for extensive reviewing of the whole thesis, for his suggestions and inspiring discussions that widened my horizon of knowledge.
- I would also like to thank Prof. Dr. Martina Gerken for her inspiration, support, and valuable suggestions that brightened my road.
- I'd like to thank Ms. Sigrid Paulsen-McCord who patiently and precisely proofread my whole thesis. I appreciate that extremely. Her warm encouragement, constructive comments were highly valuable to me.
- I want to thank my former colleagues in the NMM group, Dr. Enno Lage, Dr. Necdet Onur Urs for their advice.
- I thank my colleagues Cai Müller for his assistance with TR-MOKE and Simon Jarausch for the German translation.
- Special thanks to my colleagues Dr. Umer Sajjad, Finn Klingbeil, Dr. Matic Jovičević Klug, Malte Römer-Stumm, and Findan Block all provided a great atmosphere for me.
- Finally, my gratitude goes to my family for their endless encouragement and support.

Farzaneh Karimian Jazi